EFFICIENT THERMO-MECHANICAL MODEL FOR SOLIDIFICATION PROCESSES AND ITS APPLICATIONS IN STEEL CONTINUOUS CASTING

BY

SEID KORIC

B.S., University of Sarajevo, 1993
M.S., University of Illinois at Urbana-Champaign, 1999

DISSERTATION

Submitted in partial fulfillment of the requirements
for the degree of Doctor of Philosophy in Mechanical and Industrial Engineering
in the Graduate College of the
University of Illinois at Urbana-Champaign, 2006

Urbana, Illinois

Abstract

A new, computationally-efficient algorithm has been implemented to solve for thermal stresses, strains, and displacements in realistic solidification processes which involve highly nonlinear constitutive relations. A general form of the transient heat equation including latent-heat from phase transformations such as solidification and other temperature-dependent properties is solved numerically for the temperature field history. The resulting thermal stresses are solved by integrating the highly nonlinear thermo-elastic-viscoplastic constitutive equations using a two-level method. First, an estimate of the stress and inelastic strain is obtained at each local integration point by implicit integration followed by a bounded Newton-Raphson iteration of the constitutive law. Then, the global finite element equations describing the boundary value problem are solved using full Newton-Raphson iteration. The procedure has been implemented into the commercial package Abaqus [1] using a user-defined subroutine (UMAT) to integrate the constitutive equations at the local level. Two special treatments for treating the liquid/mushy zone with a fixed grid approach are presented and compared. Other local integration methods as well as the explicit initial strain method used in CON2D for solving this problem are also briefly reviewed and compared.

The model is validated both with a semi-analytical solution from Weiner and Boley [2] as well as with an in-house finite element code CON2D [3,4,7,8] specialized in thermo-mechanical modeling of continuous casting. Both finite element codes are then applied to simulate temperature and stress development of a slice through the solidifying steel shell

in a continuous casting mold under realistic operating conditions including a stress state of generalized plane strain and with actual temperature dependant properties. Mechanical results are then used to predict an ideal taper for different casting speeds.

The model is then improved to add coupling of heat flow and stress generation that are increment-wise coupled through the size of the interfacial gap. Coupled results are first verified with a solidifying slice, and then quantitatively against the CON2D 2D model of billet casting by fully employing Abaqus thermal and mechanical contact capabilities. Another coupled 2D model of bloom beam blank casting with contact, known for a very challenging geometry, is solved for the simultaneous evolution of deformation, temperature, and stress. New knowledge was gained about the complex coupled thermo-mechanical phenomena that take place in this process, especially in the flange region prone to surface and subsurface cracking. Finally, a large scale 3D simulation of a thin slab caster with a funnel is performed to predict for the first time, the fully-3D mechanical state in the solidifying shell of this complex casting process that involves complex geometry and loading conditions. It has provided new valuable insights into a complex mechanical state of transverse and axial stress of the solidifying shell retracted by the funnel geometry.

Acknowledgment

I would like to express my deepest appreciation to my advisor, Professor Brian G. Thomas, for all of his sincere guidance, support, and encouragement over the past five years. I also thank Professors Tucker, Tortorelli, Hilton, and Hashash for all that I learned from them during my graduate study, and for serving on my dissertation committee.

I am indebted to my colleagues at NCSA for all their support, understanding, and for all the cpu-hours that I have used on NCSA supercomputers for this work. I also show my appreciation to my previous colleagues: Dr. Hong Zhu, Dr. Avijit Moitra, Dr. Joong-kil Park, and Dr. Chunsheng Li for their previous work in shell solidification.

Special thanks go to my parents, Suada and Muhamed, who have always believed in me, and who have supported me every step along the way since I was in my cradle. I am grateful to my sons, Tarik and Amar, for inspiring me to undertake this long journey.

Finally, my wife Sanja Koric, a woman of great patience and kindness, deserves my deepest thanks. Without her endless love, support, and patience this work would not have been possible.

Table of Contents

List of Figures

List of Tables

Nomenclature

A	m^2	Surface
A_T	m^2	Temp. Prescribed Surface
A_q	m^2	Flux Prescribed Surface
A_h	m^2	Convection Prescribed Surface
A_u	m^2	Displacement Prescribed Surface
A_Φ	m^2	Traction Prescribed Surface
[B]	1/m	Spatial Derivative of [N]
b		Gen Plane Strain Constant
$\mathbf{b}, \mathbf{b_o}$	N	Volumetric Force Vector
c_j		Constant
c_s		Sign of $\dot{\bar{\varepsilon}}_{ie}$
c_p	J/kgK	Specific Heat
[C]	J/kg	Capacitance Matrix
d_{air}	m	Thickness of air gap
d_{pow}	m	Thickness of powder film
d_{taper}	m	Taper Displacement
$\underline{\underline{\mathbf{D}}}$	N/m^2	4th Order Elasticity Tensor.
E	N/m^2	Elastic Modulus
$\mathbf{F}$		Deformation Gradient
$\mathbf{F}_q$	W	Heat Flow Load Vector
F_z	N	External Mech. Force, Gen. Strain
F_p	Pa	Ferrostatic Pressure
f	1/s	Viscoplastic Law Function
fc	$MPa^{-f3}s^{-1}$	Empirical Constant in Kozlowski III law
$f_{\delta c}$		Empirical Constant in Enhanced Power Delta law
f_1	MPa	Empirical Constant in Kozlowski III law
f_2		Empirical Constant in Kozlowski III law
f_3		Empirical Constant in Kozlowski III law

g		Yield Function
g	m/sec^2	Gravitational Constant
h	W/m^2K	General Film Coefficient
h_{mold}	W/m^2K	Contact heat transfer coefficient on mold side
h_{shell}	W/m^2K	Contact heat transfer coefficient on shell side
h_{rad}	W/m^2K	Radiation heat transfer coefficient
h_T	W/ m^2K	Total Interfacial Heat Transfer Coefficient
H	J/kgK	Enthalpy
Hf	J/kgK	Latent Heat
HR	N/m^2	Isotropic Hardening
$\underline{\underline{\mathbf{I}}}$		4th Order Identity Tensor
$\mathbf{I}$		2nd Order Identity Tensor
$\underline{\underline{\mathbf{J}}}$	N/m^2	Jacobian (Consistent Tangent Operator)
k	W/mK	Thermal Conductivity
k_{air}	W/mK	Thermal Conductivity of Air
k_{pow}	W/mK	Thermal Conductivity of Powder Film
k_B	N/m^2	Bulk Modulus
$\mathbf{k_{uT}}$	N/K	Off-Diagonal Submatrix of fully coupled global stiff. matrix
$\mathbf{k_{Tu}}$	W/m	Off-Diagonal Submatrix of fully coupled global stiff. matrix
$\mathbf{k_{uu}}$	N/m	Mechanical Diag. Submatrices of fully coupled global stiff. matrix
$\mathbf{k_{TT}}$	W/K	Thermal Diag. Submatrices of fully coupled global stiff. matrix
$[K]$	W/K	Tangent Matrix HT
$[K]$	N/m	Tangent Matrix Mech.
L_Z	m	Thickness of 3D domain in casting direction
$M_x M_y$	Nm	External Mech. Moments, Gen. Plain Strain
$[N]$		Element Shape Functions
$\mathbf{N}$	N/m^2	Inelastic Strain Flow Tensor
m,n		Empirical constants used power delta law
$\mathbf{n}$		Surface Unit Vector
p_{cont}	N/m^2	Contact Pressure
$\mathbf{P}$	N	External Force Vector
$\hat{q}$	W/m^2	Prescribed Heat Flux

q”	W/m^2	Interfacial Gap Heat Flux
Q	K	Activation Energy Constant
$\mathbf{R}$	N	Residual Force Vector
$\mathbf{R_u}$	N	Mechanical Residual Vector in Coupled Analysis
$\mathbf{R_T}$	W	Thermal Residual Vector in Coupled Analysis
$\mathbf{S}$	N	Internal Force Vector
t, t_{mold}	sec.	Time spend in mold (bellow meniscus)
t_{ref}	sec.	Reference Plane Time (3D)
T	^oC	Temperature
T_{shell}	^oC	Shell Temperature
T_{mold}	^oC	Mold Temperature
$\hat{T}$	^oC	Prescribed BC Temp.
T_∞	^oC	Ambient Temperature
T_{init}	^oC	Initial Temperature.
T_{ref}	^oC	Reference Temperature
T_{sol}	^oC	Solidus Temp.
T_{liq}	^oC	Liquidus Temp.
TLE		Thermal Linear Expansion
$\mathbf{u,d}$	m	Displacement Vector
V	m^3	Volume
v_c	m/min	Casting Speed
W	m	Mold Width
$\mathbf{x}$	m	Position Vector (initial configuration)
$\bar{\mathbf{x}}$	m	Position Vector (deformed configuration)
z	m	Distance Bellow Meniscus (2D)
Z	m	Local Axial Coordinate (3D)
α	$1/^oC$	Coefficient of Thermal Expansion
β		Constant
γ		Constant
$\boldsymbol{\varepsilon}$		Total Strain Tensor
$\Delta\hat{\boldsymbol{\varepsilon}}$		A guess for Tot. Strain Incr. Tensor
$\dot{\boldsymbol{\varepsilon}}$	1/s	Total Strain Rate Tensor

ε_{max}		Max. Principal Strain
ε_{min}		Min. Principal Strain
$\boldsymbol{\varepsilon}_{el}$		Elastic Strain Tensor
$\dot{\boldsymbol{\varepsilon}}_{el}$	1/s	Elastic Strain Rate Tensor
$\boldsymbol{\varepsilon}_{ie}$		Inelastic Strain Tensor
$\dot{\boldsymbol{\varepsilon}}_{ie}$	1/s	Inelastic Strain Rate Tensor
$\hat{\dot{\boldsymbol{\varepsilon}}}_{ie}$	1/s	Guess for $\dot{\boldsymbol{\varepsilon}}_{ie}$
$\dot{\bar{\varepsilon}}_{ie}$	1/s	Equivalent Inelastic Strain
$\dot{\bar{\varepsilon}}_{ie}^{0}$	1/s	NN Initial Approx. of $\dot{\bar{\varepsilon}}_{ie}$
$\boldsymbol{\varepsilon}_{th}$		Thermal Strain Tensor
$\dot{\boldsymbol{\varepsilon}}_{th}$	1/s	Thermal Strain Rate Tensor
ε_{m}		Emissivity of mold surface
ε_{S}		Emissivity of shell surface
η		Radial Return Factor
$\Delta\lambda$		Plastic Strain Multiplier
μ	N/m^2	Shear Modulus
μ_{v}	Pa-s	Viscosity
μ_{frict}		Friction Coefficient
$\boldsymbol{\sigma}$	N/m^2	Stress Tensor is small strain formulation
$\boldsymbol{\sigma}_{C}$	N/m^2	Cauchy Stress Tensor
$\boldsymbol{\sigma}_{N}$	N/m^2	Nominal Stress Tensor
$\hat{\boldsymbol{\sigma}}$	N/m^2	Guess for Stress Tensor
$\boldsymbol{\sigma}'$	N/m^2	Deviatoric Stress Tensor
$\boldsymbol{\sigma}^{*}$	N/m^2	Trial Stress Tensor
$\bar{\sigma}$	N/m^2	Equivalent Stress
$\bar{\sigma}^{0}$	N/m^2	NN Initial Approx. of $\bar{\sigma}$
$\Delta\bar{\sigma}^{NR}$	N/m^2	Local NR $\bar{\sigma}$ Correction
$\Delta\bar{\sigma}^{max}$	N/m^2	Max. Local BNR $\bar{\sigma}$ Correction

$\bar{\sigma}_{lower}$	N/m^2	Lower Bound for Local BNR
$\bar{\sigma}_{upper}$	N/m^2	Upper Bound for Local BNR
σ_Y	N/m^2	Yield Stress
τ_{crit}	N/m^2	Critical Shear Stress
ρ	kg/m^3	Density
υ		Poisson's Ratio
$\boldsymbol{\phi}$	m	Deformation
$\boldsymbol{\Phi}$	N/m^2	Surface Traction Vector

Chapter 1. Introduction

Many manufacturing and fabrication processes such as foundry shape casting, continuous casting and welding have common solidification phenomena. Probably one of the most important and complex among them is continuous casting. In fact most of the steel made today is produced through continuous casting whose schematic is depicted in Fig. 1.1 [8,9]. Even though the quality of the continuous casting is constantly improving, there is still a significant amount of work needed to minimize the amount of surface defects and to maximize the productivity. Some of the more important issues that are influenced by the casting speed, which in turn influences the productivity and the quality of steel produced by the continuous casting process, are:

- Large axial strains due to oscillations and excessive withdrawal forces can cause transverse cracks and even breakouts
- Large transverse strains due to ferrostatic pressure from the liquid phase applied to a newly solidified shell can cause longitudinal cracks and breakouts.
- Uneven shell growth influences the size of interfacial gap and the gap heat flow, leading to locally hot and thin parts of shell which can be another cause of longitudinal cracks and breakouts.
- Excessive bulging of the strand bellow the mold between the supporting rolls can cause internal cracks too.
- Sloshing of liquid steel in the meniscus due to higher casting speeds can cause later surface quality problems.

Most of these phenomena occur during the early stage of solidification and accurate determination of the distribution of temperature deformation and stress during the early stages of solidification is important for correct prediction of surface shape and cracking problems in processes such as the continuous casting of steel.

The high cost of plant experiments under the harsh operating steel plant conditions makes it appropriate to use all available methods in simulating, optimizing, and designing this process. Even though physical modeling (experiment) of initial solidification has been conducted [10,11,12], the complexity of this process and phenomena that governs it make it difficult to model.

At the same time the increasing power of computers and development of numerical methods in last 20 years has helped researchers to better understand the governing principles of various material processing operations. The continuous casting process is not exception, and it has been subjected to more numerical models than any other process [13]. However, it is a challenging task too, and there is large number of computational difficulties encountered with numerical modeling of thermo-mechanical behavior of the shell in continuous casting. Challenges arise due to the moving solid-liquid interface, complex thermal and mechanical loading, rate-dependent constitutive visco-plastic relationships, temperature dependant material properties, thermal and mechanical contact between the shell and the mold, coupling between the thermal and stress analysis through the changing thickness of the air gap, interaction between metallurgical phase transformations, inelastic strain and thermal stress, relative motion between the casting and the mold, the inherent three dimensional nature of the process, macro segregation and micro segregation and more, just to name some of them. Efficiently including as many as possible of

these phenomena in a single numerical model is still a major topic of many ongoing research projects.

1.1 Steel Continuous Casting-Process Overview

The continuous casting process is a relatively new method in material processing and its widespread use did not start until the mid 1960s after some major technical difficulties were resolved. [14]. It accounts for 90% of all steel produced in the world today, including almost all varieties of steel grades. The continuous casting process is given schematically in Fig. 1.2 [8]. Superheated liquid steel flows from a ladle, through a tundish and then it is poured into the open ended water cooled copper mold through a nozzle, which is submerged into the liquid steel pool. The tundish is designed to hold enough liquid metal to provide continuous flow when ladles are periodically exchanged. When molten metal impacts a chilled mold surface it suddenly freezes against it to form a solid shell. Heat extracted from the liquid steel flows through the partly solidified steel shell, the interfacial gap between the shell surface and the mold, the copper mold wall, and finally is transferred to the cooling water flowing through the outer mold walls. Oil or powder slag is added to the meniscus flowing into the interfacial gap to eliminate extensive friction that accounts for the majority of early solidification shell surface defects, and to protect the steel from the air. The mold oscillates vertically to prevent the shell from sticking to the mold wall allowing a tearing-free withdrawn from the mold. The mold is also tapered to account for the shrinkage of the steel shell by minimizing the occurrence of the gaps which reduce the heat transfer rate and leads to the local hot and thinner spots on the shell. A newly formed shell keeps getting thicker as it moves down the mold withstanding the ferrostatic pressure from the liquid

pool which increases linearly with the submerged height. Very small strains can initiate hot tear cracks at the grain boundaries if liquid from the pool is prevented from feeding through dendrite arms to compensate for the shrinkage. The sources of surface and subsurface cracks that develop later in the mold are: unsteady cooling of the shell, friction between strand and mold, withdrawal forces, microstructure, grain size, and segregation effects.

The strand passes through a series of water sprays and support rolls located below the mold exit where the remaining liquid core solidifies. The shell often bulges in this area of the caster due to the ferrostatic pressure pushing outward the still soft shell between the support rolls. Since the bulging worsenes strain concentration and promote further propagation of the cracks initiated in the mold, it must be minimized by a sufficient number of support rolls to prevent these failures in this final stage of casting. After the liquid core is completely solid, the strand is torch-cut into final slabs or billets of desired length. Due to the generation of residual stresses during the solidification and cooling, there is usually a shape distortion that represents the difference between the section shape of the final slab and the section shape of the mold.

1.2 Objectives

Today's easy-to-use commercial finite-element packages are now fully capable of handling 3D problems, having rich element libraries, fully imbedded pre and post processing capabilities, advanced modeling features such as contact algorithms, and can take a full advantage of parallel-computing capabilities. Unfortunately these commercial packages have given little effort to provide integration schemes that are robust enough to handle the highly nonlinear elastic-

viscoplastic laws arising during casting, so are consequently very slow and prone to convergence problems.

The objective of this work is to implement and validate a robust local viscoplastic integration schemes from an in-house code CON2D [3,5,6,8,9], into the commercial finite element package Abaqus via its user defined material subroutine UMAT. This work aims to open the door for realistic two and three-dimensional computational modeling of complex solidification processes, by substantially improving the efficiency of commercial software available to the wider academic and industrial research communities.

The final objective of this work is to demonstrate application of the model, by predicting thermo-mechanical behavior of the solidifying shell in a wide variety of real world continuous casting applications. These include a solidifying slice in realistic continuous casting conditions, a 2-D generalized plane strain model of billet and beam blank castings, and finally a fully 3-D analysis of casting in a funnel mold. The results obtained from these and future simulations will be available to investigate different practical problems in continuous casting and other solidification processes, including new insights into the failure mechanisms that take place in these complex processes.

1.3 Methodology

The following approach is taken in this thesis to achieve the outlined objectives:

In Chapter 2, most of important previous work in numerical modeling of continuous casting is reviewed. The literature survey of previous numerical models is roughly divided into 3

categories, and all the important aspects in each category are carefully examined. The important previous work review for the applications modeled in this work is included in their chapters.

In Chapter 3, the thermal and mechanical governing equations and their finite-element implementations into Abaqus and CON2D are introduced. Chapter 3 also presents the thermo-viscoplastic constitutive models. The global solution of the boundary value problem is described with two different materially non-linear solution strategies using Abaqus and CON2D.

Chapter 4 provides detailed information on the local integration schemes and their coding. Two special treatments for liquid/mushy zone are introduced in this chapter followed by generalized plain strain assumptions.

In Chapter 5, the new model with a special local integration scheme coded into Abaqus UMAT subroutine is validated against semi-analytical solution and CON2D.

In Chapter 6, a real-world simulation of a typical continuous casting process is performed with both codes using realistic temperature dependant properties and a simple slice domain. The results are compared and CPU times are benchmarked. The mechanical results are then used to predict the ideal mold taper.

In Chapter 7, UMAT is improved to enable thermo-mechanical coupling. The simple slice domain is used one more time for qualitatively validation of coupled results.

In Chapter 8, a 2D coupled thermo-mechanical analysis with contact of billet casting is preformed with our new Abaqus model. The thermo-mechanical results are quantitatively compared to the previous CON2D results.

In Chapter 9, a 2D coupled thermo-mechanical analysis with contact of beam blank caster with complex geometry is performed.

In Chapter 10, a novel 3D uncoupled thermo-mechanical analysis with contact of a thin slab caster with funnel is performed.

In Chapter 11, conclusions and some recommendations for the future utilization and improvement of the tools developed in this work are written.

1.4 Tables and Figures

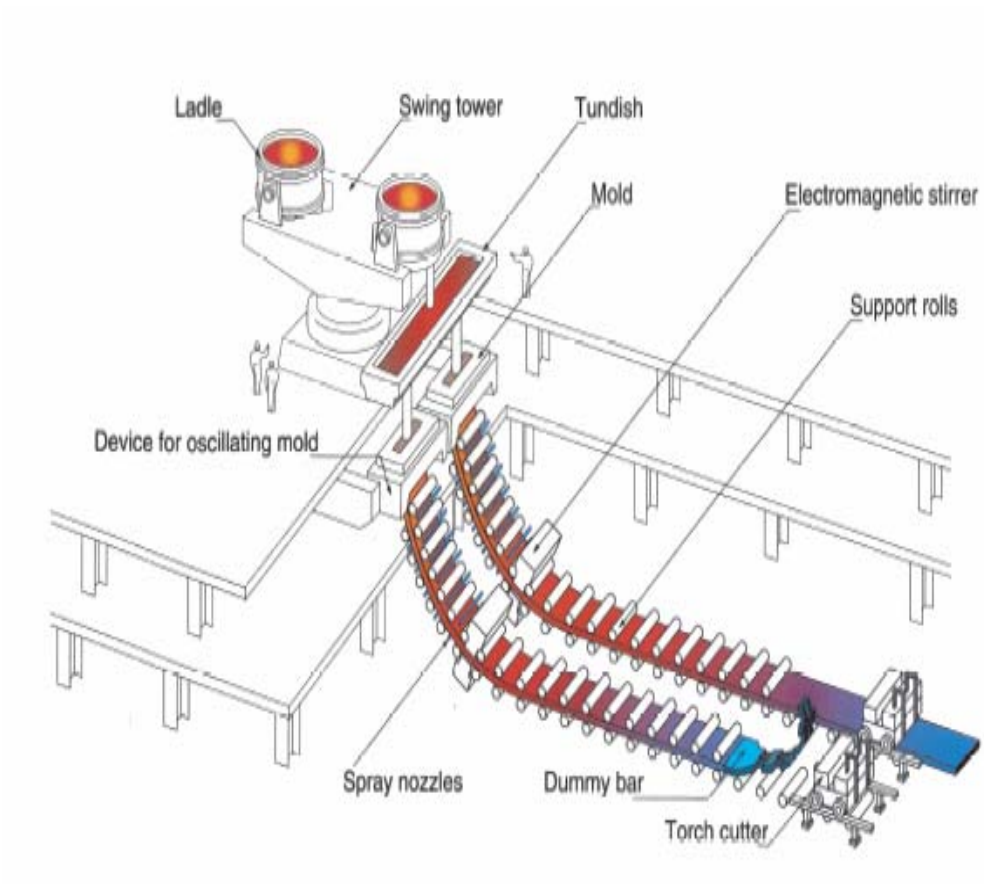

Fig 1.1 3D Scheme of continuous casting process [8]

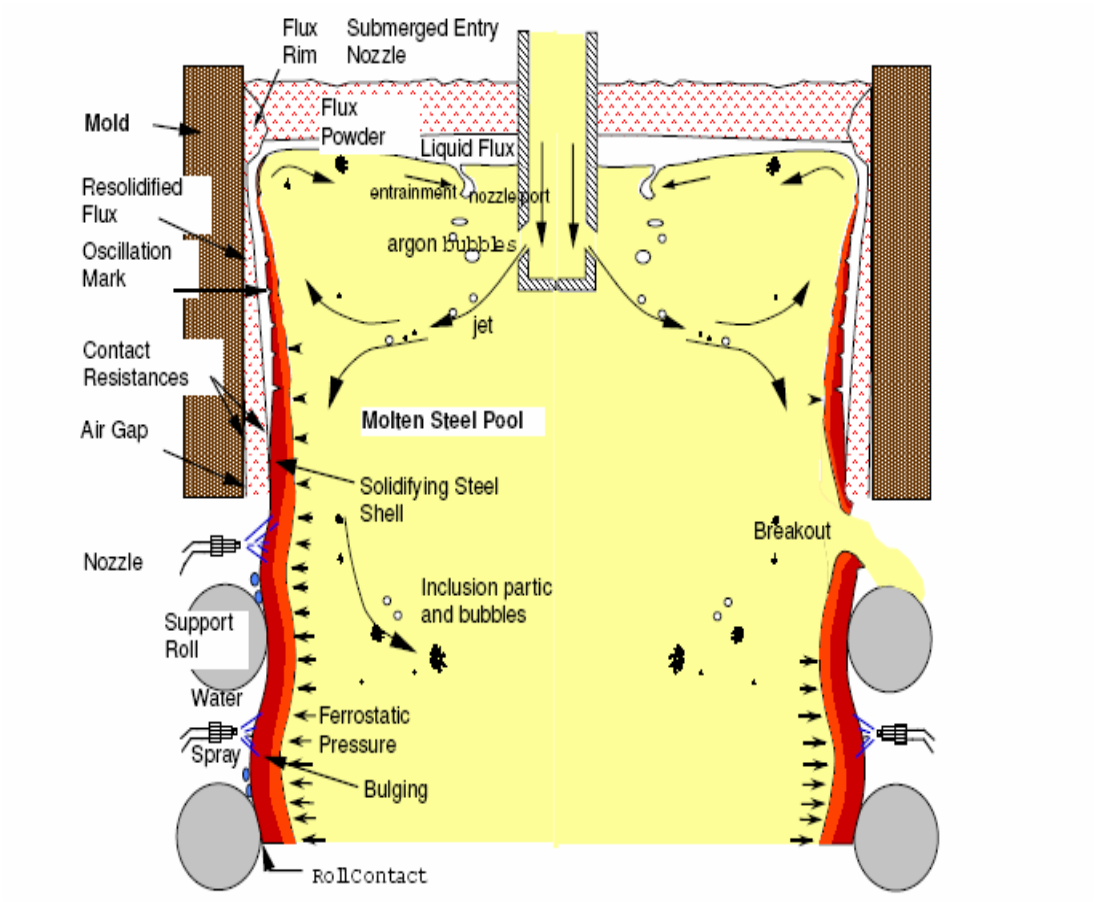

Fig 1.2 Schematic of a longitudinal section through slab caster [7]

Chapter 2. Previous Work Survey

With the rapid advance of hardware, the numerical modeling of thermo-mechanical behavior in a solidifying body has been benefiting the understanding and improvement of material processes such as foundry shape casting, continuous casting, and welding in the last 20 years. Understanding the history of the temperature, shape, and stress helps in the prediction of residual stress, distortion, crack formulation and even porosity formation. A few analytical solutions for stress development in a solidifying body have been developed by Weiner and Boley [2] and by Tien and Kaump [15]. Although these analytical solutions provide valuable benchmark problems for verification of numerical models, they are often limited from practical engineering applications by their oversimplified assumptions for the complex physical phenomena associated with solidification

Various numerical methods have been used to solve the equations governing thermo-mechanical behavior of a solidifying body. Cross [16] and Hattel et al [17], have used control volume finite-difference methods to simulate three-dimensional thermo-elastic stresses in die casting. Recently Jung-Eui Lee and coworkers [18] used a finite volume method for coupled fluid flow, heat transfer, and stress of solidifying shells in beam blank mold. Heinlen and Mukherjee [19] presented a boundary-integral-equation to solve for mechanical behavior for the one-dimensional solidification of an aluminum bar. However, a specially suited method to handle a wide variety of nonlinearities and geometric shapes is the finite-element method, and almost all numerical research in this area has been using the finite-element methods and its tools.

According to the way the following important aspects are handled, the previous work can be divided into the following 3 categories:

- Frame of reference
- Constitutive models for thermo-mechanical behavior and treatment of liquid phase
- Interaction with mold and the treatment of solidification front

2.1 Frame of Reference

Continuous casting is a steady state phenomenon for an outside observer. The support rolls in the lower part of a caster are continuously withdrawing the shell from the mold at a rate or a "casting velocity" that is ideally equal to the flow of incoming molten metal, thus providing a steady state condition. This makes Eulerian approach, which fixes the mesh at spatial points, a natural choice for the frame of reference. However, due to inherited history dependence of the thermo-mechanical behavior, the advective terms are present in Eulerian governing equations and special updating schemes are necessary to handle them. This additional complexity creates further numerical difficulties especially with the visco-plastic constitutive laws and limits the effective implementation of Eulerian approach. Nevertheless, there are a few models based on Eulerian approach. Barber et al. [20] and L. Yu [21] used this approach to model the bulging between the rolls. Kelly et al. [22], Tatsumi et al. [23], and Lee et al. [18] used their Eulerian models to simulate behavior of solidifying shell in the mold.

On the other hand, in a Lagrangian frame of reference computational meshes are moving with the material points eliminating the advective terms and history-dependant variable can be easily updated. Even though the fine meshes or even re-meshing is often needed with this approach, the vast majority of models are based on the Lagrangian frame of reference by tracking the portion of a strand with a variety of 1D slice and 2D domains from the meniscus down the caster. These include early models of Brimacombe and his coworkers [24-27], Rammerstorfer at al. [28-30], Kristiansen et al. [31-32], Kinoshita et al. [33], Wimmer et al. [34]. The more recent models include Thomas and his coworkers [35-39], Park et al. [40-42], Tzeng et al. [43], Mizoguchi et al. [44], Boehmer at al. [45-48], Han et al. [49], and the most recent by Koric and Thomas [50]. While most of them used in-house codes, some have used commercial software [50, 34, 48, 43].

Arbitrary Lagrangina Eulerian (ALE) method have been developed as a combination of Eulerian and Lagrangian approaches in a attempt to overcome the disadvantages of pure Lagrangian and Eularian descriptions by Fachinotti and his coworkers [51, 52]. Even though this hybrid model has computational

advantage over Lagrangian description [52], so far its practical application has been limited to simple geometries only.

2.2 Constitutive Models and Treatment of Liquid Phase

Choosing a realistic model for constitutive behavior is a key for success in mechanical modeling. Both mechanical behavior and thermo-mechanical properties of steels are experiencing a large variation close to their melting points. The constitutive model should be able to reproduce these changes in mechanical behavior observed from various experiments which measure mechanical response over the range of typical continuous casting conditions. Those experiments include uniaxial tests [53-56], creep tests [57], and bending tests [58]. Various constitutive models have been used starting with a simple elastic model by Manes [59]. Elastic-perfectly-plastic model is used by Weiner and Boley [2] followed by simple elastic-plastic models [24,25,27]. Temperature dependant properties are added to elastic-plastic models to get more realistic behavior [46,47,22,23,34]. All of these models are time independent and neglecting important time dependant creep features. Later separate creep models are added to account for it [31,29,45,48]. Lately, with the rapid advance of computer hardware, more computationally challenging elastic-visco-plastic models have been used [42,43,49,18,60] which threat the phenomena of creep and plasticity together since only the combined effect is measurable. In these models the inelastic strain rate is a function of equivalent stress, equivalent inelastic strain, and temperature. An important extra variable, steel carbon content, is added by Kozlowski [61] to the functional dependence of inelastic strain rate, and many new models have already adopted it [38,39,51,52,39,50]. Integration of these time dependant constitutive laws is a very challenging task due to their inherited numerical stiffness. Having efficient and robust integration scheme for constitutive models is essential for successful and time manageable performance of any finite element code modeling solidifying shell behavior, especially with 2D and 3D domains. Integration schemes performed for every material point (local level) range from easy-to-implement but usually slow explicit methods [25,34]; to robust and fast, but hard to implement implicitly based algorithms [2,3]. Complexity of implicit methods comes from the fact that the implicit

implementation leaves a pair of highly nonlinear equations that need to be solved for every material point. It is found in this work that the bounded Newton-Raphson method, originally proposed by Lush et al. [62], and then later implemented into CON2D code by Zhu et al [5], have produced best robustness and efficiency.

Two approaches exist for the treatment of the liquid phase that transmits the ferrostatic pressure to the solidifying shell while providing continuous stress distribution across the solidifying front. First approach is simply avoiding assembling totally liquid elements into the global stiffness matrix [22,45,63,64], however it must have a front-track capabilities which are often based on complicated re-meshing algorithms.

Second and widely used approach is so called "fixed-grid" method which is based on altering properties of liquid with temperature on existing mesh. Providing refined enough mesh to capture the movement of solidifying front, this method can be easily implemented into existing fixed-grid FE codes. There are 3 known variations of altering the properties of liquid the with the fixed-grid method. The simplest one is to model liquid phase as an elastic material with heavily reduced elastic modulus in liquid and mushy zone [65,43,66,67]. This method sometimes introduces non physical stress on the solid part in liquid-solid phase transition zone, as well as numerical ill-conditioning in global stiffness FE assembly. Another method proposed by Zhu et al [5] avoids abrupt changes of elastic properties, and is based on a viscoplastic constitutive relation for liquid/mushy phase in the form of a penalty function that generates inelastic strain in proportion of equivalent stress in the liquid. While this method can provide a useful insight into mechanical behavior in mushy zone, it also introduces even more challenging viscoplastic laws then the solid ones, and requires a highly robust integration scheme that often significantly slows the overall performance of majority of nonlinear FE codes based on a full Newton-Raphson global solution algorithm. Third method proposed in this work [50] is avoiding integration of rate dependant viscoplastic laws. It rather uses a rate-independent elastic-perfectly plastic constitutive law with small enough value for yield stress to effectively eliminate stresses in liquid/mushy zone, but without stress oscillations in the solid part of transition zone. While this method is more efficient than the method with

viscoplastic liquid law, the focus of some future work will be to examine if it can properly model a mechanical behavior in the mushy zone whose results can be used to predict hot-tearing failures.

2.3 Interaction with Mold and the Treatment of Solidification Front

The interaction between mold wall and shell surface consist of mechanical and thermal components. The thermal component includes the heat transfer rate dependence on the size of the interfacial gap, while mechanical component is a contact state between the shell and the mold. These phenomena are closely related and often require coupling between the heat transfer and mechanical models. Even though coupled models require up to ten times more cpu times and often generate more convergence problems, they are more frequently used lately with the increase of computational speed [32,33,3,42,46,48,49,22,18,51,34].

Often an iterative scheme is necessary to solve this coupled model on each time increment level. Based on a gap size from a previous time increment, heat transfer is calculated, and then from its temperature results corresponding strand shrinkage and the mold wall position are determined. This leads to a calculated gap size, and the whole procedure iterates until the gap sizes are within the convergence criteria.

Strong nonlinearity is created from the mechanical contact state, since the contact boundary condition is not known in advance. It is unknown a priori if gap is closed and contact pressure can be transmitted, or if the gap is open preventing contact pressure transmission between the contact surfaces. There are three major contact formulations for finite element codes.

Lagrangian multiplier method [68,69,70] which solves for the value of the contact force needed to keep the penetration of the shell (slave) node into mold exactly zero. While this method provides exact enforcement of contact constrains, it has a complicated implementation and also introduces larger system of equations to be solved.

Penalty method [71,72] uses a stiff spring to prevent the penetration of the shell (slave) surface into the mold. This method is easy to implement and does not change the size of the global stiffness matrix, but

it is an approximate enforcement, and it is prone to convergence problems if a wrong value for spring constant is chosen.

Augmented lagrange method [73-75] which is a combination of above two, with the innermost iteration loop based on a penalty method. It attempts to utilize advantages of two other methods, but it is probably the most complicated to implement.

While many commercial finite software packages are providing all three contact formulations [1,76], in house codes are usually confined to some simplified implementations of the penalty method [4].

In order to distinguish the properties of solid and liquid/mushy elements in a fixed mesh approach, the position of a particular isotherm has to be tracked down. This front is called solidification front, and can depict how much of the finite element domain is solidified at particular time of the simulation. Both thermal and mechanical boundary conditions exist on a solidification front. The thermal boundary condition comes from the superheat from the liquid pool transferred to the solidification front as the liquid flows in the liquid pool. In order to exactly model this phenomenon, the coupled thermo-fluid-mechanical simulation is needed. This is still computationally too expensive and complicated to be performed, though there was an attempt by Kelly et al. [22] who transferred data between CFD and CSM commercial FE packages. Lee et al. is reporting recently that his research group has developed an in-house code that can do thermal-fluid-mechanical coupling for beam blank casting [18,58]. Most of analysis now days are still using enhanced conductivity in liquid to compensate for this effect.

The mechanical boundary condition at the solidification front comes from the ferrostatic pressure from the liquid pool due to gravity. Most of fixed-grid models apply distributed load equivalent to the ferrostatic pressure to the surface of completely solidified elements [32,37,42,48,49,22,18,58,34,50]. There are certain convergence difficulties with this approach if distributed load is applied to the elements in liquid/mushy zone which are soft and prone to uncontrolled deformation under external loads. Tszeng et al. [43] proposed a natural generation of the hydrostatic state of stress in liquid/mushy zone with pure elastic constitutive model by simultaneously lowering elastic modulus while increasing Poisson's ratio. It is not clear how this approach can match properly a linear increase in ferrostatic pressure as strand moves down the mold.

Chapter 3. Governing Equations and their Finite Element Implementations

3.1 Notation

Both standard tensor and indicial notations are used throughout this work. Here is a list of some of important notations and symbols.

	Tensor Notation	Indicial Notation
Fourth Order Tensors	$\underline{\underline{\mathbf{D}}}$	D_{ijkl}
Second Order Tensors	$\boldsymbol{\sigma}, \boldsymbol{\sigma}', \boldsymbol{\varepsilon}$	$\sigma_{ij}, \sigma'_{ij}, \varepsilon_{ij}$
Vectors	$\mathbf{u}, \mathbf{b}$	u_i, b_i
Scalars	T, μ, κ	T, μ, κ
Vector Gradient	$\nabla \mathbf{u}$	$u_{i,j}$
Scalar Gradient	∇T	$T_{,i}$
Divergence of Tensor	$\nabla \cdot \boldsymbol{\sigma}$	$\sigma_{ij,j}$
Identity Second Or. Tensor	$\mathbf{I}$	δ_{ij}
Identity Fourth Or. Tensor	$\underline{\underline{\mathbf{I}}}$	$\delta_{ik}\delta_{jl}$
Inner Products	$\nabla \mathbf{u} : \nabla \mathbf{u}$	$u_{i,j}\, u_{i,j}$
	$\mathbf{F} : \boldsymbol{\sigma}_N$	$F_{ij}(\sigma_N)_{jk}$
	$\underline{\underline{\mathbf{D}}} : \boldsymbol{\varepsilon}$	$D_{ijkl}\varepsilon_{kl}$
Outer Tensor Product	$\mathbf{I} \otimes \mathbf{I}$	$\delta_{ij}\delta_{kl}$

δ_{ij} is Kronecker's delta defined by

$$\delta_{ij} = \begin{Bmatrix} 1 \text{ if } i = j \\ 0 \text{ if } i \neq j \end{Bmatrix}$$

Symmetric second order tensors are often written as column vectors "{}", while symmetric fourth order tensors are written as square matrices "[ ]"- following the Voigt Notation [77].

$$\{\sigma\} = \{\sigma_x, \sigma_y, \sigma_x, \sigma_{xy}, \sigma_{xz}, \sigma_{yz}\}^T \qquad \{\varepsilon\} = \{\varepsilon_x, \varepsilon_y, \varepsilon_z, \varepsilon_{xy}, \varepsilon_{xz}, \varepsilon_{yz}\}^T$$

3.2 Thermal Governing Equations and their Finite Element Implementations

The local form of the transient energy equation is given in equation (1)[78].

$$\rho\left(\frac{\partial H(T)}{\partial t}\right) = \nabla \cdot \left(k(T)\nabla T\right) \tag{1}$$

along with boundary conditions:

Prescribed temperature on A_T $\quad T = \hat{T}(\mathbf{x}, t)$

Prescribed surface flux on A_q $\quad \left(-k\nabla T\right) : \mathbf{n} = \hat{q}(\mathbf{x}, t)$ (1a)

Surface convection on A_h $\quad \left(-k\nabla T\right) : \mathbf{n} = h(T - T_\infty)$

Where ρ is density, k is isotropic temperature dependant conductivity, H is temperature dependant enthalpy, which includes the latent heat of solidification. $\hat{T}$ is a fixed temperature at the boundary A_T, $\hat{q}$ is prescribed heat flux at the boundary A_q, h is film convection coefficient prescribed at the boundary A_h where T_∞ is the ambient temperature, and **n** is the unit normal vector of the surface of the domain.

The commercial finite-element package Abaqus uses the backward-difference algorithm for time integration [80].

$$\dot{H}^{t+\Delta t} = \frac{H^{t+\Delta t} - H^{t}}{\Delta t} \tag{2}$$

After applying the standard Galerkin finite-element method to equation (1) [80], the weak form is established in equation (3) using the common notation for element shape functions and their spatial derivatives $[N]$ and $[B]$ respectively.

$$\int_V [N]^T \dot{H} dV + \int_V [N]^T k(t) \frac{\partial T}{\partial \mathbf{x}} dV = \int_{A_q} [N]^T \hat{q} dA + \int_{A_h} [N]^T h(T - T_o) dA \tag{3}$$

Using equation (2) for time discretization of (3), the following nonlinear system is established

$$\frac{1}{\Delta t}\int_V [N]^T \rho\left(H^{t+\Delta t} - H^{t}\right) dV + \int_V \frac{\partial [N]^T}{\partial \mathbf{x}} k(T) \frac{\partial T}{\partial \mathbf{x}} dV - \int_{A_q} [N]^T \hat{q} dA - \int_{A_h} [N]^T h(T - T_o) dA = 0 \tag{4}$$

Abaqus solves the nonlinear system, Eq. (4), incrementally, i.e. achieving equilibrium balance at every time increment Δt by utilizing the modified Newton-Raphson (NR) iteration scheme given in (5) for each iteration i.

$$\left[\frac{1}{\Delta t}\int_V [N]^T \rho \left(\frac{dH}{dT}\right)_i^{t+\Delta t} [N] dV + \int_V [B]^T k_i^{t+\Delta t} [B] dV - \int_{A_h} [N]^T h [N] dA\right]\left\{\Delta T_i^{t+\Delta t}\right\} = \int_{A_q} [N]^T \hat{q} dA +$$
$$+ \int_{A_h} [N]^T h(T_i^{t+\Delta t} - T_o) dA - \frac{1}{\Delta t}\int_V [N]^T \rho\left(H_i^{t+\Delta t} - H^{t}\right) dV - \int_V \frac{\partial [N]^T}{\partial \mathbf{x}} k^{t} \left(\frac{\partial T^{t}}{\partial \mathbf{x}}\right) dV \tag{5}$$

Equation (5) is solved for $\left\{\Delta T_i^{t+\Delta t}\right\}$ and then used to update the temperature solution, equation (6) until convergence is achieved at every point in the domain at time $t + \Delta t$.

$$\left\{T_{i+1}^{t+\Delta t}\right\} = \left\{T_i^{t+\Delta t}\right\} + \left\{\Delta T_{i+1}^{t+\Delta t}\right\} \tag{6}$$

The term $\left(\frac{dH}{dT}\right)^{t+\Delta t}$ is an effective specific heat which is greatly enlarged over the phase-change temperature interval $T_{sol} < T^{t+\Delta t} < T_{liq}$ owing to the evolution of latent heat H_f. Here T_{sol} and T_{liq} are the solidus and liquidus temperatures respectively. The temperature solution (history) for each material point is stored in a result file that is used in the subsequent mechanical analysis.

CON2D solves Eq. (3) explicitly using the special averaging technique suggested by Lemmon [81] to evaluate the effective specific heat, as given in Eq. (7)

$$\frac{dH}{dT} = \sqrt{\frac{\left(\frac{\partial H}{\partial x}\right)^2 + \left(\frac{\partial H}{\partial y}\right)^2}{\left(\frac{\partial T}{\partial x}\right)^2 + \left(\frac{\partial T}{\partial y}\right)^2}} \tag{7}$$

A three-level time-stepping method proposed by Dupont [82] was adopted for CON2D to explicitly solve Eq. (3). Assuming the current time is t+Δt, the previous two time steps are t, and t-Δt, respectively. The temperature vector $\{T\}$ and its time derivative vector $\{\dot{T}\}$ are given as:

$$\{T\} = \frac{1}{4}\left\{3T^{t+\Delta t} + T^{t-\Delta t}\right\} \tag{8}$$

$$\{\dot{T}\} = \left\{\frac{T^{t+\Delta t} - T^{t}}{\Delta t}\right\} \tag{9}$$

After some rearranging this leads to an explicit matrix equation to be solved for temperature at the current time:

$$\left[\frac{3}{4}[K] + \frac{[C]}{\Delta t}\right]\left\{T^{t+\Delta t}\right\} = \left\{F_q\right\} - \frac{1}{4}[K]\left\{T^{t-\Delta t}\right\} + \frac{[C]}{\Delta t}\left\{T^{t}\right\} \tag{10}$$

where [K] conductance (tangent) matrix, [C] capacitance matrix, and $\{F_q\}$ heat flow load vector are defined as:

$$[C] = \int_V [N]^T \rho \left(\frac{dH}{dT}\right)^{t+\Delta t} [N] dV \qquad [K] = \int_V [B]^T k^t [B] dV \qquad \left\{F_q\right\} = \int_{A_q} [N]^T \hat{q} dA \tag{10a}$$

CON2D incrementally solves Eq. (10) for $\{T^{t+\Delta t}\}$. It couples the transient heat transfer and stress analysis; within each time increment, temperature is solved first and then subsequently used for the stress distribution. This procedure is repeated for every increment.

3.3 Mechanical Governing Equations

In Figure 3.1 two configurations are defined, the initial (reference) configuration and the deformed configuration. After forces are applied to the body in initial configuration, it deforms to the deformed configuration. We identify each particle of the body with its position $\mathbf{x}$ in the initial configuration (Lagrangian coordinates of the particle), and they are being mapped to deformed configuration $\bar{\mathbf{x}}$ by the function ϕ called deformation.

$$\bar{\mathbf{x}} = \phi(\mathbf{x}) \tag{11}$$

The displacement field is defined as:

$$\mathbf{u}(\mathbf{x}) = \phi(\mathbf{x}) - \mathbf{x} \tag{12}$$

To determine how adjacent points in the initial configuration deform we define the deformation gradient $\mathbf{F}$, the derivative of the deformation.

$$\mathbf{F} = \nabla\phi = \mathbf{I} + \nabla\mathbf{u} \tag{13}$$

The tensor $\mathbf{F}^{\mathbf{T}} : \mathbf{F}$ which measures the length of an elementary vector defined over the deformed configuration in terms of its definition in the initial configuration is right Cauchy-Green strain tensor. The local force balance (equilibrium) is originally defined with respect to deformed configuration via Cauchy (physical) stress $\boldsymbol{\sigma}_{\mathbf{C}}(\bar{\mathbf{x}})$.

$$\nabla \cdot \boldsymbol{\sigma}_{\mathbf{C}}(\bar{\mathbf{x}}) + \mathbf{b}(\bar{\mathbf{x}}) = 0 \tag{14}$$

Equation (14) is of little use since the deformed configuration is unknown prior to the solution of the boundary value problem. We can transform (14) [83] to the initial configuration and express the local force balance with respect to initial configuration via nominal stress $\boldsymbol{\sigma}_{\mathrm{N}}$, whose transpose is often called the first Piolla-Kirchoff stress.

$$\nabla \cdot \boldsymbol{\sigma}_{\mathbf{N}}(\mathbf{x}) + \mathbf{b}_0(\mathbf{x}) = 0 \tag{15}$$

where $\mathbf{b}(\bar{\mathbf{x}})$ and $\mathbf{b}_0(\mathbf{x})$ are body force densities with respect to deformed and initial configurations respectively. The relation between Cauchy stress and nominal stress is given in equation (16)

$$\boldsymbol{\sigma}_{\mathbf{C}} = \frac{\mathbf{F} : \boldsymbol{\sigma}_{\mathbf{N}}}{\det(\mathbf{F})} \tag{16}$$

The thermal strains which dominate thermo-mechanical behavior during solidification are on the order of only a few percent, or cracks will form [84]. Several previous solidification models [3,5,6,31,52] confirm that the solidified metal part indeed undergoes only small deformation during initial solidification in the mold. The displacement spatial gradient $\nabla \mathbf{u} = \partial \mathbf{u} / \partial \mathbf{x}$ is small, so $\nabla \mathbf{u} : \nabla \mathbf{u} \approx 1$, $\det(\mathbf{F}) \approx 1 + \nabla \cdot \mathbf{u}$. This leads to the following approximations:

The positions before and after the deformations can be identified ie,

$$\bar{\mathbf{x}} \approx \mathbf{x} \tag{17}$$

The right Cauchy-Green $\mathbf{F}^{\mathbf{T}} : \mathbf{F}$ strain tensor reduces to

$$\mathbf{F}^{\mathrm{T}} : \mathbf{F} \approx \mathbf{I} + \nabla\mathbf{u} + (\nabla\mathbf{u})^{\mathrm{T}} \tag{18}$$

which leads to the definition of the linearized strain tensor [83,77]

$$\boldsymbol{\varepsilon} = \frac{1}{2}[\nabla\mathbf{u} + (\nabla\mathbf{u})^{\mathbf{T}}] \tag{19}$$

Then, the Cauchy stress tensor $\boldsymbol{\sigma}_{\mathbf{C}}$ can be identified with the nominal stress tensor $\boldsymbol{\sigma}_{\mathbf{N}}$ and we use $\boldsymbol{\sigma}$ to denote stress in small-strain formulation.

$$\boldsymbol{\sigma}_{\mathbf{C}}(\bar{\mathbf{x}}) \approx \boldsymbol{\sigma}_{\mathbf{N}}(\mathbf{x}) = \boldsymbol{\sigma}(\mathbf{x}) \tag{20}$$

and the equilibrium equation (14) can be defined with respect to initial configuration

$$\nabla \cdot \boldsymbol{\sigma}(\mathbf{x}) + \mathbf{b}_{\mathbf{o}} = 0 \tag{21}$$

The boundary conditions are:

$$\mathbf{u} = \hat{\mathbf{u}} \quad \text{on } A_u$$

$$\boldsymbol{\sigma} : \mathbf{n} = \boldsymbol{\Phi} \text{ on } A_\Phi \tag{21a}$$

where prescribed displacements $\hat{\mathbf{u}}$ on boundary surface portion A_u, and boundary surface tractions $\boldsymbol{\Phi}$ on portion A_Φ define a quasi-static boundary value problem. The rate representation of total strain in this elastic-viscoplastic model is given by:

$$\dot{\boldsymbol{\varepsilon}} = \dot{\boldsymbol{\varepsilon}}_{el} + \dot{\boldsymbol{\varepsilon}}_{ie} + \dot{\boldsymbol{\varepsilon}}_{th} \tag{22}$$

where $\dot{\boldsymbol{\varepsilon}}_{el}, \dot{\boldsymbol{\varepsilon}}_{ie}, \dot{\boldsymbol{\varepsilon}}_{th}$ are the elastic, inelastic (plastic + creep), and thermal strain rate tensors respectively. Stress rate $\dot{\boldsymbol{\sigma}}$ depends on elastic strain rate and in this case of linear isotropic material and negligible large rotations it is given by (23)

$$\dot{\boldsymbol{\sigma}} = \underline{\underline{\mathbf{D}}} : (\dot{\boldsymbol{\varepsilon}} - \dot{\boldsymbol{\varepsilon}}_{ie} - \dot{\boldsymbol{\varepsilon}}_{th}) \tag{23}$$

$\underline{\underline{\mathbf{D}}}$ is the fourth order isotropic elasticity tensor given by (24)

$$\underline{\underline{\mathbf{D}}} = 2\mu \underline{\underline{\mathbf{I}}} + (k_B - \frac{2}{3}\mu)\mathbf{I} \otimes \mathbf{I} \tag{24}$$

Here μ, k_B are the shear modulus and bulk modulus respectively and are in general functions of temperature, while $\underline{\underline{\mathbf{I}}}, \mathbf{I}$ are fourth order and second order identity tensors.

3.4 Inelastic Strain

Inelastic strain includes both strain-rate independent plasticity and time dependant creep. Creep is significant at the high temperatures of the solidification processes and is indistinguishable from plastic strain [3]. The inelastic strain-rate is defined here with a unified formulation using a single internal variable [85,62], equivalent inelastic strain $\bar{\varepsilon}_{ie}$ to characterize the microstructure. For steel solidification considered here, the equivalent inelastic strain-rate $\dot{\bar{\varepsilon}}_{ie}$ is a function of equivalent stress $\bar{\sigma}$, temperature T, equivalent inelastic strain $\bar{\varepsilon}_{ie}$, and steel grade defined by its carbon content %C.

$$\dot{\bar{\varepsilon}}_{ie} = f(\bar{\sigma}, T, \bar{\varepsilon}_{ie}, \%C) \tag{25}$$

$$\bar{\sigma} = \sqrt{\frac{3}{2}\sigma'_{ij}\sigma'_{ij}} \tag{26}$$

$\boldsymbol{\sigma}'$ is a deviatoric stress tensor defined by

$$\sigma'_{ij} = \sigma_{ij} - \frac{1}{3}\sigma_{kk}\delta_{ij} \tag{27}$$

The mild carbon steels treated in this work are assumed to harden isotropically, so the von Mises loading surface, associated plasticity, and normality hypothesis in the Prandtl-Reuss flow law is applied [86,87]:

$$(\dot{\varepsilon}_{ie})_{ij} = \frac{3}{2}\dot{\bar{\varepsilon}}_{ie}\frac{\sigma'_{ij}}{\bar{\sigma}} \tag{28}$$

$\dot{\bar{\varepsilon}}_{ie}$ has a sign determined by the direction of the maximum principle inelastic strain, as defined in equation (29) in order to achieve kinematic behavior (Bauschinger effect) during reverse loading [3].

$$\dot{\bar{\varepsilon}}_{ie} = c_S\sqrt{\frac{2}{3}(\dot{\varepsilon}_{ie})_{ij}(\dot{\varepsilon}_{ie})_{ij}} \quad \text{where} \quad c_S = \begin{Bmatrix} \dfrac{\varepsilon_{max}}{|\varepsilon_{min}|} & \varepsilon_{max} \geq \varepsilon_{min} \\ \dfrac{\varepsilon_{min}}{|\varepsilon_{max}|} & \varepsilon_{max} < \varepsilon_{min} \end{Bmatrix} \tag{29}$$

3.5 Thermal Strain

Thermal strains arise due to volume changes caused by both temperature differences and phase transformations, including solidification and solid-state phase changes between crystal structures, such as austenite and ferrite.

$$(\varepsilon_{th})_{ij} = \int_{T_0}^{T}\alpha(T)dT\,\delta_{ij} \tag{30}$$

where α is temperature dependant coefficient of thermal expansion, and T_0 is the reference temperature. Thermal strain tensors in this work are calculated from the thermal linear expansion function, TLE [3,5], which will be discussed later.

3.6 Global Solution of Boundary Value Problem, Materially Non-Linear Solution Strategies in Abaqus and CON2D

After applying the standard Galerkin finite element method to the materially nonlinear boundary value problem in equation (21), residual force $\{R\}$ is found, representing the imbalance between internal stress in the body and externally-applied loads from body forces and surface tractions [1, 88, 89, 90].

$$\{R\} = \int_V [B]^T \{\sigma\} dV - \left(\int_V [N]^T \{b\} dV + \int_{A_\Phi} [N]^T \{\Phi\} dA \right) \tag{31}$$

Equilibrium is satisfied when the residual force vanishes (at least within prescribed tolerance). Similarly to its solution of the heat transfer equation (4), Abaqus solves Eq. (31) incrementally. Using the full Newton-Raphson method, equation (32), several "global equilibrium iterations" "i" are needed to achieve equilibrium by the end of every time increment Δt.

$$\left[K_{i-1}^{t+\Delta t}\right]\left\{\Delta u_{i-1}^{t+\Delta t}\right\} = \left\{P^{t+\Delta t}\right\} - \left\{S_{i-1}^{t+\Delta t}\right\} \tag{32}$$

(32) is solved for $\left\{\Delta u_{i-1}^{t+\Delta t}\right\}$ and then used to update the displacement solution, equation (33), until convergence is achieved everywhere at time $t + \Delta t$.

$$\left\{u_i^{t+\Delta t}\right\} = \left\{u_{i-1}^{t+\Delta t}\right\} + \left\{\Delta u_{i-1}^{t+\Delta t}\right\} \tag{33}$$

External Load Vector $\left\{P^{t+\Delta t}\right\}$ at time $t + \Delta t$ is defined as

$$\left\{P^{t+\Delta t}\right\} = \int_V [N]^T \left\{b^{t+\Delta t}\right\} dV + \int_{A_\Phi} [N]^T \left\{\Phi^{t+\Delta t}\right\} dA \tag{34}$$

Internal Force $\left\{S^{t+\Delta t}\right\}$ at time $t + \Delta t$ is defined as

$$\left\{S^{t+\Delta t}\right\} = \int_V [B]^T \left\{\sigma^{t+\Delta t}\right\} dV \tag{35}$$

The tangent stiffness Matrix $\left[K^{t+\Delta t}\right]$ is defined in equation (37) from the consistent tangent operator, or "Jacobian" $[J]$, defined in equation (36), which must be consistent with the local integration method to provide quadratic convergence of Eq. (32) [91,92,93]. Again [B] contains spatial derivatives of the element shape functions [N], while $\Delta\hat{\boldsymbol{\varepsilon}}^{t+\Delta t}$ is a "guessed" mechanical strain increment, based on the current best displacement increment.

$$\underline{\underline{\mathbf{J}}} = \frac{\partial \boldsymbol{\sigma}^{t+\Delta t}}{\partial \Delta\hat{\boldsymbol{\varepsilon}}^{t+\Delta t}} \tag{36}$$

$$\left[K^{t+\Delta t}\right] = \int_V \left[B^T\right][J][B]dV \tag{37}$$

The nonlinear response to a load increment ΔP is shown in Figure 3.2. The global tangent stiffness matrix $K_{iter=1}^{t+\Delta t}$, which is based on its configuration at time t and ΔP, is used to calculate a displacement correction $\Delta u_{iter=1}^{t+\Delta t}$ for the first iteration using the equation (32). The structure configuration is updated to $u_{iter=1}^{t+\Delta t}$ using equation (33). The structure's internal force is calculated from equation (35), and the difference between the total applied load and internal force can be calculated in equation (31) to yield the force residual for the first equilibrium iteration $R_{iter=1}^{t+\Delta t}$. In nonlinear problems the force residual will never be exactly zero, so it compared to a tolerance value. If the force residual is less then this force residual tolerance at all nodes, the code accepts the solution as being in equilibrium. However, Abaqus also has secondary convergence criteria. It checks that the current displacement correction is small relative to the total incremental displacement, which is calculated as a sum of all displacement corrections from all previous iterations in a current increment. Both convergence criteria must be satisfied before a solution is said to have converged for that time increment in Abaqus. The displacement correction convergence check often creates unnecessary convergence problems in mostly uninteresting liquid/mushy zone with the perfectly plastic constitutive law with very small yielding stress. Therefore, the displacement correction convergence is often loosen to enable convergence, while the primary force residual convergence criteria is still sufficient to enforce very correct results in the solid shell part. If the solution from the first iteration is not converged, second iteration is performed to try to bring the internal and external forces into balance. The same procedure is

repeated to calculate the displacement correction for second iteration $\Delta u_{iter=2}^{t+\Delta t}$ along with new force residual $R_{iter=2}^{t+\Delta t}$ that becomes smaller, bringing the system closer to equilibrium. If necessary, Abaqus performs further iterations until the system is brought into the equilibrium with the convergence tolerance.

The complete nonlinear solution strategy in Abaqus used in this work is shown in Figure 3.3. If the tolerance for NR convergence criteria is exceeded, a new NR iteration starts that performs the following tasks:

- New guess for mechanical strain increments is calculated from the current displacement increments.
- Native local integration or UMAT subroutine is called at all material points to perform constitutive model integration (also called local integration, stress update algorithm, or solution to boundary value problem) and returns updated stress, and Jacobian.
- Element internal forces and element tangent matrices are calculated and assembled into the global assembly.
- New global displacement field is calculated from (32) and (33) and convergence criterion is checked again.
- Once the NR convergence criterion is satisfied everywhere, a new increment of loading history is applied, based on the heat transfer solution for the next time step, and the whole process is repeated until the end of the loading history, which is defined as a STEP in Abaqus.

CON2D uses an Operator Splitting Technique [3,94] with fully explicit initial-strain procedure [88,95] to solve equation (31) by alternating between the local and global steps without global iterations or consistent tangent operators [3,5]. First, local integration of the constitutive equations is used to guess the inelastic strain rate $\left\{\hat{\dot{\varepsilon}}_{ie}\right\}^{t+\Delta t}$ and stress at each material point, assuming total strain rate stays constant over the time step. The inelastic strain rate is converted to an initial strain increment as follows [88,96]

$$\left\{\hat{\sigma}\right\}^{t+\Delta t} = \left\{\sigma\right\}^{t} + \left[D\right]^{t+\Delta t}\left(\left\{\Delta\varepsilon\right\}^{t+\Delta t} - \left\{\Delta\varepsilon_0\right\}^{t+\Delta t}\right) \tag{38}$$

$$\left\{\Delta\varepsilon_0\right\}^{t+\Delta t} = \left\{\Delta\varepsilon_{th}\right\}^{t+\Delta t} + \left\{\hat{\dot{\varepsilon}}_{ie}\right\}\Delta t \tag{39}$$

Then, the global equation (31) is manipulated into the following explicit system of linear equations given in equation (40), which is solved for displacement increments only once for each time increment. The tangent matrix on the left hand side of equation (40) is the same as that of linear elasticity.

$$\begin{aligned}\Sigma\int_{V_{el}}[B^T][D][B]dV\left\{\Delta d\right\}^{t+\Delta t} &= \Sigma\int_{V_{el}}[B^T][D]\left\{\hat{\dot{\varepsilon}}_{ie}\right\}^{t+\Delta t}\Delta t dV + \Sigma\int_{V_{el}}[B^T][D]\left\{\Delta\varepsilon_{th}\right\}^{t+\Delta t}dV - \\ -\Sigma\int_{V_{el}}[B^T][D]\left\{\varepsilon_{el}\right\}^{t}dV &+ \Sigma\int_{V_{el}}[N^T]\left\{b\right\}^{t+\Delta t}dV + \Sigma\int_{A_\phi}[N^T]\left\{\Phi\right\}^{t+\Delta t}dA\end{aligned} \tag{40}$$

Finally, the total values of displacement, inelastic strain and total strain are updated as follows.

$$\left\{d\right\}^{t+\Delta t} = \left\{d\right\}^{t} + \left\{\Delta d\right\}^{t+\Delta t}, \left\{\Delta\varepsilon\right\}^{t+\Delta t} = [B]\left\{\Delta d\right\}^{t+\Delta t}, \left\{\Delta\varepsilon_{ie}\right\}^{t+\Delta t} = \left\{\hat{\dot{\varepsilon}}_{ie}\right\}^{t+\Delta t}\Delta t$$

(41)

and stress is updated with equation (42)

$$\{\sigma\}^{t+\Delta t} = \{\sigma\}^{t} + [D]^{t+\Delta t}\left(\{\Delta\varepsilon\}^{t+\Delta t} - \{\Delta\varepsilon_{ie}\}^{t+\Delta t} - \{\Delta\varepsilon_{th}\}^{t+\Delta t}\right) \tag{42}$$

Even though this simplified approach for solving the boundary value problem shows some small stress oscillations which are not found with the full global NR method from Abaqus, this method generally performs well with very low CPU cost.

3.7 Figures and Tables

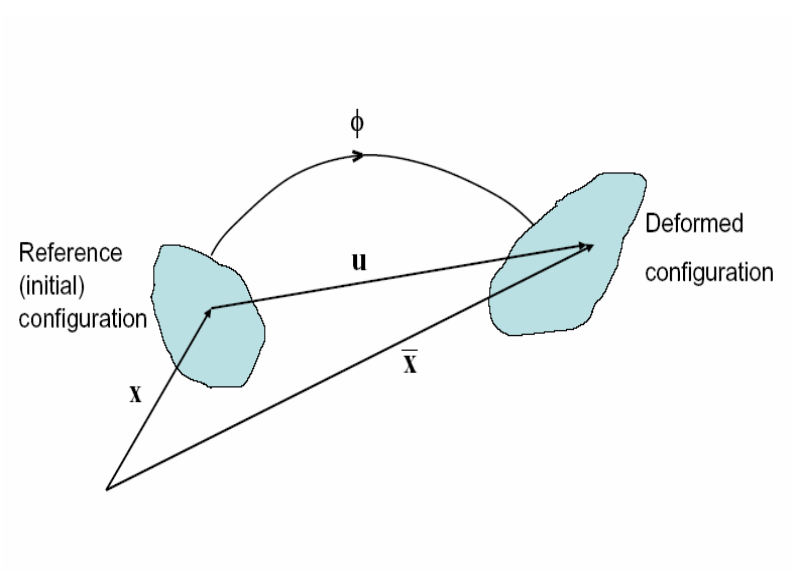

Figure 3.1 Deformation of a body

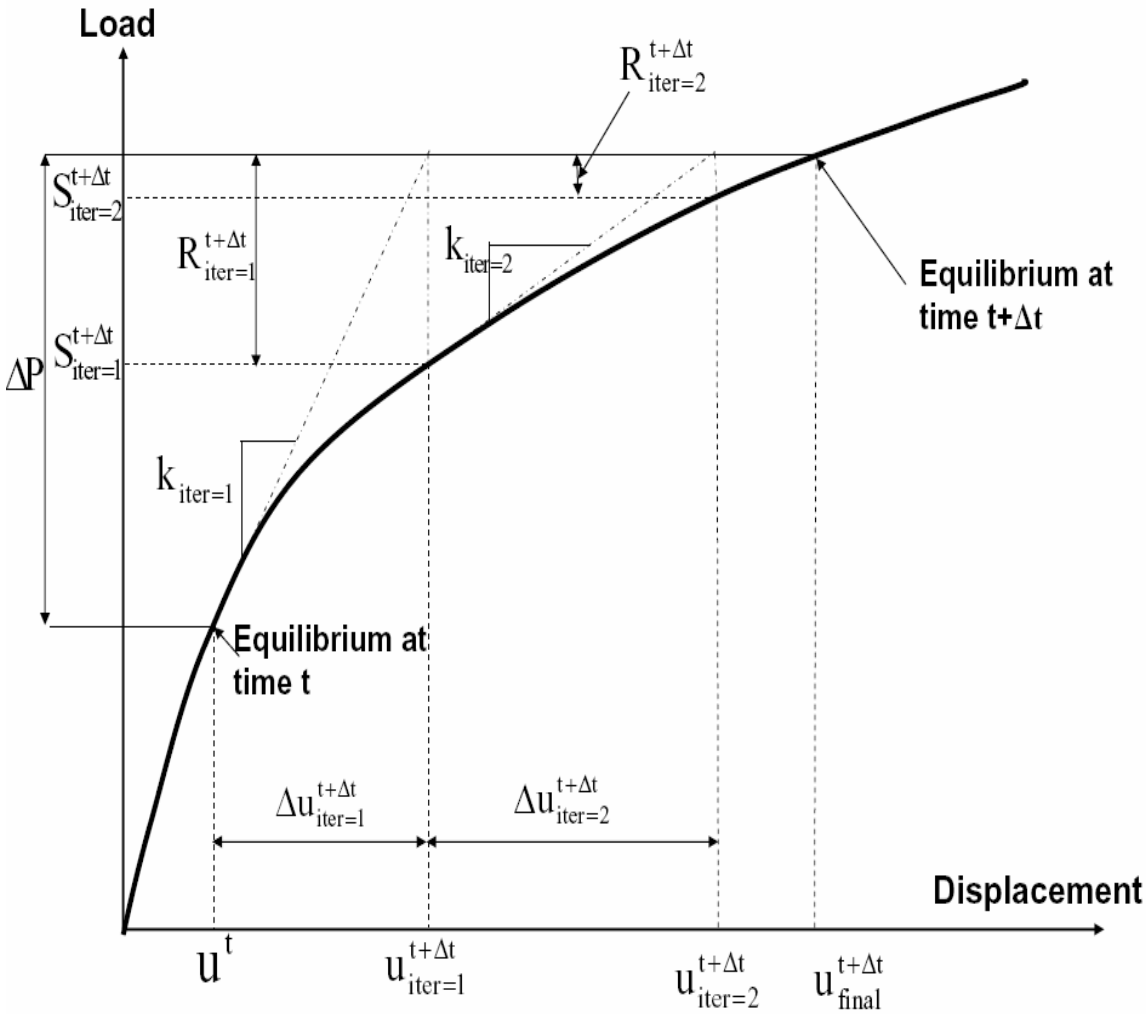

Figure 3.2 Newton-Raphson nonlinear solution strategy

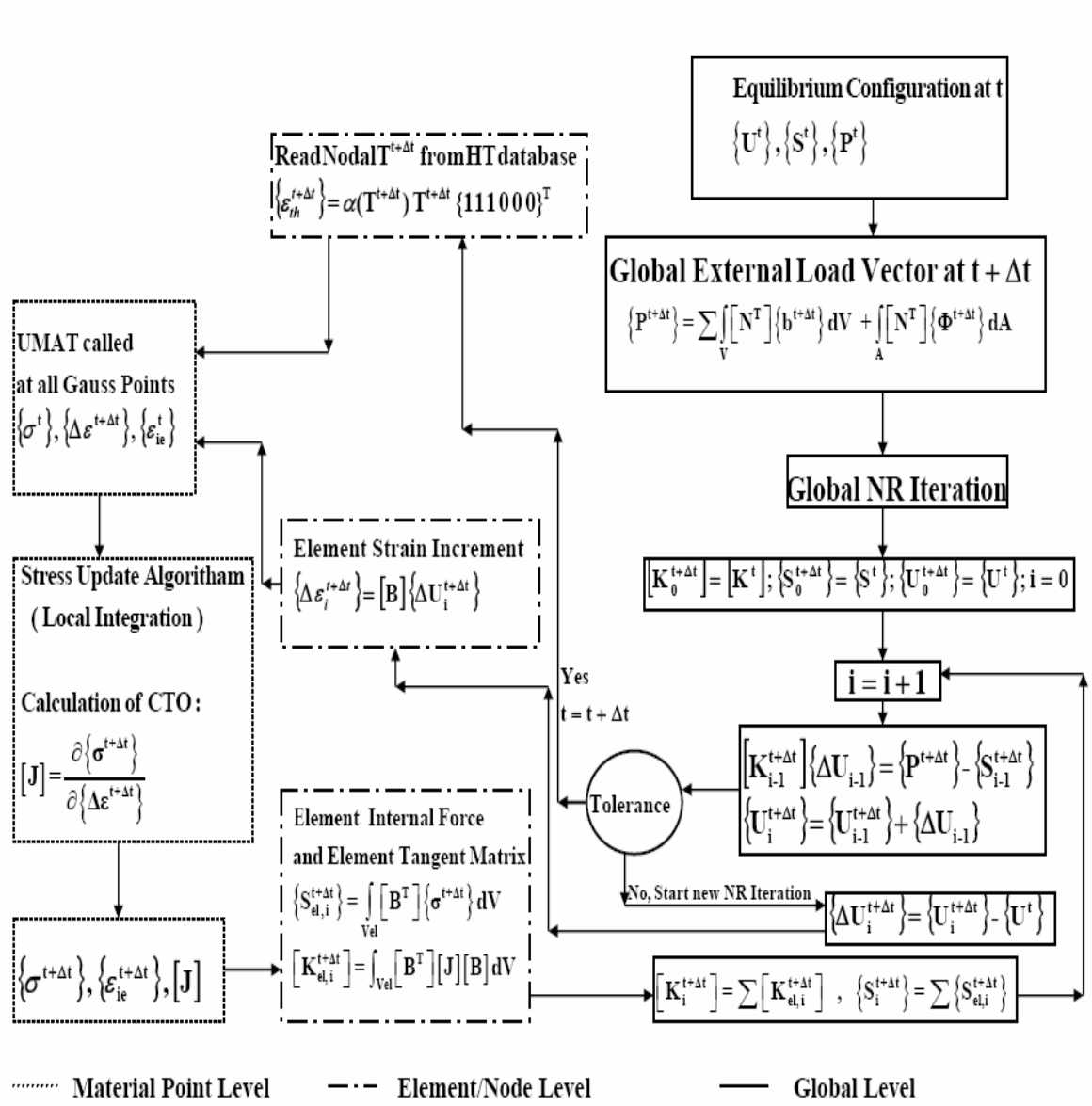

Figure 3.3 Flow chart for Abaqus solution of uncoupled thermo-mechanical problem, including local material-point level calculations in user-defined UMAT

Chapter 4. Local Time Integration of the Constitutive Model

Assuming that the total strain rate at time t is known from the previous time step, equations (23,25,26,27,28,29) constitute a nonlinear system with 15 unknowns (2 tensors and 3 scalars) at every material point for a three dimensional problem. Owing to the highly strain dependant inelastic responses, a robust integration scheme is required to solve this system over a generic time increment Δt. The solution obtained from this "local" integration step from all material (gauss) points is used to update the global finite element equilibrium equation (31), and solved using the finite element procedure from chapter 3.

Four different local integration methods are investigated in this work. Abaqus supports the CREEP subroutine where viscoplastic laws like (25) just need to be coded and Abaqus will integrate them with either its explicit, or implicit built-in algorithm followed by the full local Newton-Raphson scheme [1,97]. Alternatively, implicit CREEP can work together with Abaqus built-in plasticity, which was used here as one approach to model the liquid/mushy zone.

On the other hand, an implicit integration technique based on Lush et al [62], Zabaras et al [98] and later Zhu et al [5] in CON2D [3,4] was used here to reduce the equation system to a pair of scalar equations with just two unknowns. These two equations are then solved with either a local bounded Newton-Raphson scheme or an explicit scheme from Nemat-Nasser [99,100]. Both of these techniques are coded into Abaqus via its user defined subroutine UMAT. The benchmark results from all of these methods are produced and compared in chapter 6.

4.1 Implicit Local Integration (ODE) from CON2D

The system of ordinary differential equations defined at each material point are converted into two "integrated" scalar equations and solved using either 1) bounded Newton-Raphson method; or 2) Nemat-Nasser method.

Knowing the state ($\boldsymbol{\sigma}^{t}, \boldsymbol{\varepsilon}^{t}{}_{ie}$) at time t, the solution marches forward in time to determine the state at $t + \Delta t$, ($\boldsymbol{\sigma}^{t+\Delta t}, \boldsymbol{\varepsilon}_{ie}^{t+\Delta t}$). The Euler backward method of integration is used to convert the system of ODEs at each material point, equation (23), to the following equation system:

$$\sigma_{ij}^{t+\Delta t} = D_{ijkl}^{t+\Delta t}\left(\varepsilon_{kl}^{t} - (\varepsilon_{th}^{t})_{kl} - (\varepsilon_{ie}^{t})_{kl} + \Delta\varepsilon_{kl}^{t+\Delta t} - (\Delta\varepsilon_{th}^{t+\Delta t})_{kl} - (\Delta\varepsilon_{ie}^{t+\Delta t})_{kl}\right) \tag{43}$$

By using equations (28) and (25), and by introducing $\Delta\hat{\varepsilon}_{kl}$, (which is the current best estimate of the total strain increment from the global solution of the nonlinear finite element equations), to replace $\Delta\varepsilon_{kl}^{t+\Delta t}$, equation (43) becomes:

$$\sigma_{ij}^{t+\Delta t} = D_{ijkl}^{t+\Delta t}\left(\varepsilon_{kl}^{t} - (\varepsilon_{th}^{t})_{kl} - (\varepsilon_{ie}^{t})_{kl} + \Delta\hat{\varepsilon}_{kl} - (\Delta\varepsilon_{th}^{t+\Delta t})_{kl} - \frac{3}{2} f(T^{t+\Delta t}, \bar{\sigma}^{t+\Delta t}, \bar{\varepsilon}_{ie}^{t+\Delta t}, \%C)\frac{\sigma'^{t+\Delta t}_{kl}}{\bar{\sigma}^{t+\Delta t}}\Delta t\right) \tag{44}$$

Similarly the evolution of equivalent inelastic strain $\bar{\varepsilon}_{ie}$ equation (25) is integrated in (45)

$$\bar{\varepsilon}_{ie}^{t+\Delta t} = \bar{\varepsilon}_{ie}^{t} + f(T^{t+\Delta t}, \bar{\sigma}^{t+\Delta t}, \bar{\varepsilon}_{ie}^{t+\Delta t}, \%C)\Delta t \tag{45}$$

Given the temperature solution from the Heat Transfer procedure, $\Delta\varepsilon_{th}^{t+\Delta t}$ is easy to find. Therefore, there are 7 unknown scalars for 3-D problems, (6 components of $\sigma_{ij}^{t+\Delta t}$ plus $\bar{\varepsilon}_{ie}^{t+\Delta t}$), and 5 for 2-D problems. Solving nonlinear tensor equation (44) and nonlinear scalar equation (45) for these unknowns is computationally challenging.

Fortunately, Lush et. al. [62] transformed the tensor equation (44) into a scalar equation for isotropic materials with isotropic hardening.

$$\bar{\sigma}^{t+\Delta t} = \bar{\sigma}^{*t+\Delta t} - 3\mu^{t+\Delta t} f(T^{t+\Delta t}, \bar{\sigma}^{t+\Delta t}, \bar{\varepsilon}_{ie}^{t+\Delta t}, \%C)\Delta t \tag{46}$$

where $\bar{\sigma}^{*t+\Delta t}$ is equivalent stress of the trial stress tensor (elastic predictor) $\sigma_{ij}^{*t+\Delta t}$ defined in equation (47)

$$\sigma_{ij}^{*t+\Delta t} = D_{ijkl}^{t+\Delta t}\left(\varepsilon_{kl}^{t} - (\varepsilon_{th}^{t})_{kl} - (\varepsilon_{in}^{t})_{kl} + \Delta\hat{\varepsilon}_{kl} - (\Delta\varepsilon_{th}^{t+\Delta t})_{kl}\right) \tag{47}$$

Equations (45) and (46) form a pair of highly nonlinear scalar equations to solve in the local step for the two unknowns $\bar{\varepsilon}_{ie}^{t+\Delta t}$ and $\bar{\sigma}^{t+\Delta t}$. Two solution methods that showed the best accuracy, convergence, and robustness in previous work [5] are implemented and tested.

4.1.1 Bounded Newton-Raphson Solution of a Pair of Scalar Equations

Lush et. al. [62] and later Zhu et. al. [5] used a two-level iterative scheme to solve (45) and (46) that showed fast and robust convergence using different viscoplastic laws in equation (25). Details of this scheme can be found at [62,5,3] and here is a brief summary.

The main iterative loop, Level 1, solves equation (45) for $\bar{\varepsilon}_{ie}^{t+\Delta t}$. Using this estimate for $\bar{\varepsilon}_{ie}^{t+\Delta t}$, equation (46) is solved for $\bar{\sigma}^{t+\Delta t}$ using a bounded Newton-Raphson iteration scheme, which is called Level 2. The solution $\left(\bar{\sigma}^{t+\Delta t}, \bar{\varepsilon}_{ie}^{t+\Delta t}\right)$ is substituted into equation (45) and the estimate for $\bar{\varepsilon}_{ie}^{t+\Delta t}$ is corrected using a standard Newton-Raphson scheme on Level 1. The whole procedure is repeated until equation (45) is satisfied within error tolerance.

Each Level 2 iteration i, upper and lower bounds are set on $\bar{\sigma}^{t+\Delta t}$. The initial lower bound is always zero. The first upper bound is that $\bar{\sigma}^{t+\Delta t}$ is positive.

$$\bar{\sigma}_i^{t+\Delta t} > 0 \text{ gives } \bar{\sigma}_i^{t+\Delta t} \le \bar{\sigma}^{*t+\Delta t} \tag{48}$$

The second upper bound starts with the condition that f is positive and invertible:

$$f > 0 \qquad \text{gives } f\left(\bar{\sigma}_i^{t+\Delta t}, \bar{\varepsilon}_{ie}^{t+\Delta t}\right) \le \frac{\bar{\sigma}^{*t+\Delta t}}{3\mu\Delta t} \tag{49}$$

$$\bar{\sigma}^{t+\Delta t} = f^{-1}\left(\dot{\bar{\varepsilon}}_{ie}^{t+\Delta t}, \bar{\varepsilon}_{ie}^{t+\Delta t}\right) = f^{-1}\left(f\left(\bar{\sigma}_i^{t+\Delta t}, \bar{\varepsilon}_{ie}^{t+\Delta t}\right), \bar{\varepsilon}_{ie}^{t+\Delta t}\right) \tag{50}$$

Inserting (49) into (50) gives a second upper bound for $\bar{\sigma}_i^{t+\Delta t}$ assuming that f^{-1} is an incremental function with respect to $\dot{\bar{\varepsilon}}_{ie}^{t+\Delta t}$ and $\bar{\varepsilon}_{ie}^{t+\Delta t}$.

$$\bar{\sigma}_i^{t+\Delta t} \le f^{-1}\left(\frac{\bar{\sigma}^{*t+\Delta t}}{3\mu\Delta t}, \bar{\varepsilon}_{ie}^{t+\Delta t}\right) \tag{51}$$

So, the bounds for $\bar{\sigma}_i^{t+\Delta t}$ are given in equation (52)

$$\begin{aligned} \bar{\sigma}_{lower}^{t+\Delta t} &= 0 \\ \bar{\sigma}_{upper}^{t+\Delta t} &= \min\left(\bar{\sigma}^{*t+\Delta t},\ f^{-1}\left(\frac{\bar{\sigma}^{*t+\Delta t}}{3\mu\Delta t}, \bar{\varepsilon}_{ie}^{t+\Delta t}\right)\right) \end{aligned} \tag{52}$$

If $\Delta\bar{\sigma}_i^{NR}$ is the Newton-Raphson correction from the i-th iteration of Level 2, then the maximum allowable correction $\Delta\bar{\sigma}_i^{max}$ is defined by the quasi-bisection rule in (53).

$$\begin{aligned} &\text{if } \Delta\bar{\sigma}_i^{NR} < 0 \Rightarrow \bar{\sigma}_{upper}^{t+\Delta t} = \bar{\sigma}_i^{t+\Delta t} \Rightarrow \Delta\bar{\sigma}_i^{max} = \frac{1}{2}(\bar{\sigma}_{lower}^{t+\Delta t} - \bar{\sigma}_i^{t+\Delta t}) \\ &\text{if } \Delta\bar{\sigma}_i^{NR} > 0 \Rightarrow \bar{\sigma}_{lower}^{t+\Delta t} = \bar{\sigma}_i^{t+\Delta t} \Rightarrow \Delta\bar{\sigma}_i^{max} = \frac{1}{2}(\bar{\sigma}_{upper}^{t+\Delta t} - \bar{\sigma}_i^{t+\Delta t}) \end{aligned} \tag{53}$$

If the absolute value of $\Delta\bar{\sigma}_i^{NR}$ is larger then the absolute value of $\Delta\bar{\sigma}_i^{max}$, then the NR correction is bounded to $\Delta\bar{\sigma}_i^{max}$. Otherwise, the NR correction is used.

Finally $\bar{\sigma}_{i+1}^{t+\Delta t}$ is updated from above correction, ie:

$$\bar{\sigma}_{i+1}^{t+\Delta t} = \bar{\sigma}_i^{t+\Delta t} + \Delta\bar{\sigma}_i^{t+\Delta t} \tag{54}$$

The advantage of the local Bounded NR method versus the full local NR method in solving the Level 2 equation is illustrated graphically in Figure 4.1. In this particular case, the local full NR method is diverging.

4.1.2 Nemat-Nasser Solution of a Pair of Scalar Equations

Nemat-Nasser et. al. [99,100] developed an explicit constitutive algorithm for their isothermal unified model. They observed that most of the deformation in incremental inelastic deformation is due to plastic flow with very small elastic deformation. Therefore, at the beginning of each increment the scalar measure of the total deformation rate can be approximated, with little error, to be due to inelastic deformation. The appealing aspect of this method is its explicit nature, which unlike bounded NR method, means that no iterations are required at the local integration level.

By defining the initial inelastic strain rate $\dot{\bar{\varepsilon}}_{ie}^{t+\Delta t0}$ to equal the total strain rate in equation (55)

$$\dot{\bar{\varepsilon}}_{ie}^{t+\Delta t0} = \frac{\bar{\sigma}^{*t+\Delta t} - \bar{\sigma}^{t}}{3\mu^{t+\Delta t}\Delta t} \tag{55}$$

Equation (46) can be written as:

$$\bar{\sigma}^{t+\Delta t} - \bar{\sigma}^{t} = 3\mu^{t+\Delta t}\Delta t\left(\dot{\bar{\varepsilon}}_{ie}^{t+\Delta t0} - \dot{\bar{\varepsilon}}_{ie}^{t+\Delta t}\right) \tag{56}$$

Initial approximations of the effective inelastic strain and effective stress from equations (45) and (50) are given by:

$$\bar{\varepsilon}_{ie}^{t+\Delta t0} = \bar{\varepsilon}_{ie}^{t} + \dot{\bar{\varepsilon}}_{ie}^{t+\Delta t0}\Delta t \tag{57}$$

$$\bar{\sigma}^{t+\Delta t0} = f^{-1}\left(\dot{\bar{\varepsilon}}_{ie}^{t+\Delta t0}, \bar{\varepsilon}_{ie}^{t+\Delta t0}\right) \tag{58}$$

Function f^{-1} can be approximated at time $t+\Delta t$ by a truncated Taylor series with initial values from equations (56) and (59).

$$\bar{\sigma}^{t+\Delta t} = \bar{\sigma}^{t+\Delta t0} + \frac{\partial f^{-1}}{\partial \dot{\bar{\varepsilon}}_{ie}}\Big|_0 \left(\dot{\bar{\varepsilon}}_{ie}^{t+\Delta t} - \dot{\bar{\varepsilon}}_{ie}^{t+\Delta t0}\right) + \frac{\partial f^{-1}}{\partial \bar{\varepsilon}_{ie}}\Big|_0 \left(\bar{\varepsilon}_{ie}^{t+\Delta t0} - \bar{\varepsilon}_{ie}^{t+\Delta t}\right) \tag{59}$$

Solving equations (45), (56), (57), and (59) together for $\bar{\sigma}^{t+\Delta t}$ and $\bar{\varepsilon}_{ie}^{t+\Delta t}$ gives:

$$\bar{\sigma}^{t+\Delta t} = \frac{\gamma\bar{\sigma}^{t} + \bar{\sigma}^{t+\Delta t0}}{1+\gamma} \tag{60}$$

$$\bar{\varepsilon}_{ie}^{t+\Delta t} = \bar{\varepsilon}_{ie}^{t} + \dot{\bar{\varepsilon}}_{ie}^{t+\Delta t0}\Delta t - \frac{\bar{\sigma}^{t+\Delta t0} - \bar{\sigma}^{t}}{3\mu^{t+\Delta t}(1+\gamma)} \tag{61}$$

where

$$\gamma = \left(\frac{\partial f^{-1}}{\partial \dot{\bar{\varepsilon}}_{ie}} |_0 \frac{1}{\Delta t} + \frac{\partial f^{-1}}{\partial \bar{\varepsilon}_{ie}} |_0 \right) \frac{1}{3\mu^{t+\Delta t}} \tag{62}$$

Equations (55), (57), (58), (60), (61), and (62) give an approximate explicit solution of a pair of integrated scalar equations (45) and (46).

If the material response is essential elastic, which is given by condition $\bar{\varepsilon}_{ie}^{t+\Delta t} < \bar{\varepsilon}_{ie}^{t}$, the alternative solution suggested by Nemat-Nasser et al. [99,100] is:

$$\bar{\sigma}^{t+\Delta t} = \bar{\sigma}^{*t+\Delta t} - 3\mu^{t+\Delta t} f(T^{t+\Delta t}, \bar{\sigma}^{t}, \bar{\varepsilon}_{ie}^{t}, \%C)\Delta t \tag{63}$$

$$\bar{\varepsilon}_{ie}^{t+\Delta t} = \bar{\varepsilon}_{ie}^{t} + f(T^{t+\Delta t}, \bar{\sigma}^{t}, \bar{\varepsilon}_{ie}^{t}, \%C)\Delta t \tag{64}$$

4.2 Treatment of Liquid/Mushy Zone

In this model, elements containing both liquid and solid are generally given no special treatment regarding either material properties or finite element assembly. The only difference is to choose a constitutive law that enforces negligible liquid strength and stress when the current temperature is higher then the solidus temperature. This fixed-grid approach avoids difficulties of adaptive meshing or “giving birth” to solid elements as used in Ansys [76].

Two different approaches are implemented:

- Elastic-Perfectly plastic rate independent model with small yield stress
- Extremely rapid creep rate function in the liquid/mushy zone

4.2.1 Elastic-Perfectly Plastic Model in Liquid/Mushy Zone

The first approach implements an isotropic elastic-perfectly-plastic rate-independent model for liquid or mushy elements, defined when $T > T_{sol}$ for at least one material point. The yield stress $\sigma_Y = 0.03\,\text{MPa}$ is chosen small enough to effectively eliminate stresses in the liquid-mushy zone, but also large enough to avoid computational difficulties. These liquid/mushy elements use the standard radial-return algorithm, which is a special form of backward-Euler procedure. [92,77, 88] given in equation (65)

$$\boldsymbol{\sigma}^{t+\Delta t} = \boldsymbol{\sigma}^{*t+\Delta t} - \Delta\lambda^{t+\Delta t}\,\underline{\underline{\mathbf{D}}} : \mathbf{a}^{t+\Delta t} \tag{65}$$

$\boldsymbol{\sigma}^{*t+\Delta t}$ is elastic stress predictor given by

$$\boldsymbol{\sigma}^{*t+\Delta t} = \boldsymbol{\sigma}^{t} + \underline{\underline{\mathbf{D}}} : \Delta\hat{\boldsymbol{\varepsilon}}^{t+\Delta t} \tag{66}$$

$\mathbf{a}^{t+\Delta t}$ is a flow vector which is a normal to the yield surface given by a function g

$$\mathbf{a}^{t+\Delta t} = \frac{\partial g}{\partial \boldsymbol{\sigma}} \tag{67}$$

In case of Von Mises yield criteria, the yield surface is a circle in deviatoric stress space and the flow vector at enlarged yield surface at trail elastic position $\mathbf{a}^{*t+\Delta t}$ is the same as the flow vector at final position on the yield surface $\mathbf{a}^{t+\Delta t}$ (Fig 4.3). This significantly simplifies the solution

procedure and no iterations are required to get an exact solution. The algebraic equations associated with integrating the model are developed here for a single variable, equivalent inelastic (plastic) strain increment $\Delta\bar{\varepsilon}_{ie}$ which is the same as $\Delta\lambda$, a plastic strain multiplier for von Mises yield surface. The plastic stress corrector, which returns trail elastic solution in radial direction back to the von Mises yield surface, is given in (68) [92, 77, 88].

$$\Delta\lambda^{t+\Delta t}\underline{\underline{\mathbf{D}}}:\mathbf{a}^{t+\Delta t}=\frac{\Delta\bar{\varepsilon}_{ie}^{t+\Delta t}3\mu}{\bar{\sigma}^{*t+\Delta t}}\boldsymbol{\sigma}'^{*t+\Delta t} \tag{68}$$

μ is the shear modulus, $\boldsymbol{\sigma}'^{*t+\Delta t}$ is a deviatoric stress at trial elastic position and $\bar{\sigma}^{*t+\Delta t}$ is its equivalent stress. Splitting the stress update into volumetric and deviatoric parts [92] and using (68) gives

$$\sigma_{ij}^{t+\Delta t}=\frac{1}{3}\sigma_{kk}^{t+\Delta t}\delta_{ij}+\sigma'^{\,t+\Delta t}_{ij}=\frac{1}{3}\sigma_{kk}^{*t+\Delta t}\delta_{ij}+\left(1-\frac{3\mu\Delta\lambda}{\bar{\sigma}^{*t+\Delta t}}\right)\sigma'^{\,*t+\Delta t}_{ij} \tag{69}$$

Since plastic deformation is independent of hydrostatic stress, equating the volumetric components, $\sigma_{kk}^{*t+\Delta t}=\sigma_{kk}^{t+\Delta t}$, equation (69) simplifies to relate the deviatoric stress components as follows:

$$\sigma'^{\,t+\Delta t}_{ij}=\eta\sigma'^{\,*t+\Delta t}_{ij}=\left(1-\frac{3\mu\Delta\bar{\varepsilon}_{ie}^{t+\Delta t}}{\bar{\sigma}^{*t+\Delta t}}\right)\sigma'^{\,*t+\Delta t}_{ij} \tag{70}$$

These deviatoric stresses must satisfy the von Mises yield criterion given by yield function g

$$g^{t+\Delta t}=\bar{\sigma}^{t+\Delta t}(\boldsymbol{\sigma}'^{\,t+\Delta t})-\sigma_{Y}^{t+\Delta t}(\bar{\varepsilon}_{ie}^{t+\Delta t})=\eta\bar{\sigma}^{*t+\Delta t}-\sigma_{Y}^{t+\Delta t}(\bar{\varepsilon}_{ie}^{t+\Delta t})=0 \tag{71}$$

For nonlinear hardening, $HR = \partial\sigma_Y / \partial\bar{\varepsilon}_{ie}$ is not constant so equation (71) is nonlinear and can be solved for $\Delta\bar{\varepsilon}_{ie}^{t+\Delta t}$ by the full Newton-Raphson method. For the present perfect plasticity, HR=0, and (71) gives the simple solution for $\Delta\bar{\varepsilon}_{ie}^{t+\Delta t}$

$$\Delta\bar{\varepsilon}_{ie}^{t+\Delta t} = \frac{\bar{\sigma}^{*t+\Delta t} - \sigma_Y}{3\mu} \tag{72}$$

At the beginning of every increment, a trial stress (elastic predictor) $\boldsymbol{\sigma}^{*t+\Delta t}$ is calculated from (66). $\bar{\sigma}^{*t+\Delta t}$ is then calculated from (27) and (26) and compared with $\sigma_Y^t(\bar{\varepsilon}_{ie}^t)$. If $\bar{\sigma}^{*t+\Delta t} < \sigma_Y^t$ only elastic response is calculated. Otherwise if $\bar{\sigma}^{*t+\Delta t} \geq \sigma_Y^t$, the material yields and $\Delta\bar{\varepsilon}_{ie}^{t+\Delta t}$ is either solved from (71) for a material with hardening, or calculated directly from (72) for perfect plasticity. Once $\Delta\bar{e}_{ie}^{t+\Delta t} = \Delta\lambda$ is found, $\boldsymbol{\sigma}^{t+\Delta t}$ is given from (69), and $\Delta\boldsymbol{\varepsilon}_{ie}^{t+\Delta t}$ is calculated from the flow rule, given by the Prandtl-Reuss equation (73) [86].

$$(\Delta\varepsilon_{ie}^{t+\Delta t})_{ij} = \frac{3}{2}\frac{\sigma'^{t+\Delta t}_{ij}}{\bar{\sigma}^{t+\Delta t}}\Delta\bar{\varepsilon}_{ie}^{t+\Delta t} \tag{73}$$

Finally, plastic strains at the end of the increment $\boldsymbol{\varepsilon}_{ie}^{t+\Delta t}$ are updated.

The Consistent Tangent Operator (Jacobian), consistent with the backward-Euler integration, provides a quadratic convergence of the global equilibrium equations when using the Newton-Raphson method [92,91].

$$\underline{\underline{\mathbf{J}}} = \left(k_B - \frac{2\mu\eta}{3} \right)\left(\mathbf{I} \otimes \mathbf{I}\right) + 2\mu\left(\eta\underline{\underline{\mathbf{I}}} - \beta\boldsymbol{\sigma}'^{*t+\Delta t} \otimes \boldsymbol{\sigma}'^{*t+\Delta t}\right) \tag{74}$$

where $\underline{\underline{\mathbf{I}}}$ and $\mathbf{I}$ are respectively fourth and second order identity tensors and

$$k_B = \frac{E}{3(1-2\upsilon)} \quad \text{(Bulk Modulus)} \tag{75}$$

$$\beta = \frac{3}{2\left(\bar{\sigma}^{*t+\Delta t}\right)^2}\left(1-\eta\right)\left(1 - \frac{\bar{\sigma}^{*t+\Delta t}}{\Delta\lambda\left(3\mu + HR^{t+\Delta t}\right)}\right) \tag{76}$$

4.2.2 Rapid Creep Rate Function in Liquid/Mushy Zone

An alternative way to treat liquid and mushy material is to create a viscoplastic constitutive relation that acts as a penalty function to generate inelastic strain in proportion of the absolute difference between equivalent stress $\bar{\sigma}$ and a small yield stress σ_Y [3,5,6].

$$\dot{\bar{\varepsilon}}_{ie} = \begin{cases} \dfrac{c_S}{\mu_V}\left(\left|c_S\bar{\sigma}\right| - \sigma_Y\right) & \left|c_S\bar{\sigma}\right| > \sigma_Y \\ 0 & \left|c_S\bar{\sigma}\right| \le \sigma_Y \end{cases} \tag{77}$$

c_S is a sign defined in equation (29), while the parameter μ_V^{-1} is a large number. For large values of μ_V^{-1}, which physically match the reciprocal of the viscosity of molten steel $1.5\text{x}10^8$ $\text{MPa}^{-1}\text{s}^{-1}$, numerical difficulties were experienced with Abaqus global NR equilibrium iterations

even when using the robust local viscoplastic scheme from section 4. Thus, much smaller numbers for μ_V^{-1} had to be chosen that were still able to enforce negligible strength and stress in mushy/liquid zone and produce accurate stress results.

The CON2D model handles large μ_V^{-1} without problem. In alloy systems with large mushy zones, the restriction of flow through the dendrite network could generate both stress and hot tearing in the mushy zone [101]. This behavior can be taken into account in this model by choosing the value of μ_V according to the actual permeability of the mushy zone. Further details on this idea are given elsewhere [3].

4.3 Summary of Local Integration Algorithm Applied in UMAT

Starting from an equilibrium at some time t, Abaqus provides subroutine UMAT with time increment Δt, stress vector $\{\sigma\}^t$, total mechanical strain vector $\{\varepsilon\}^t$, inelastic strain vector $\{\varepsilon_{ie}^t\}$ (which is supplied via the array of state variables STATEV), and an initial guess for total mechanical strain increment vector $\{\Delta\hat{\varepsilon}\}^{t+\Delta t}$ calculated from current displacement increments, see Fig. 4.1. Thermal strains at time t, $\{\varepsilon_{th}\}^t$, and increments of thermal strains $\{\Delta\varepsilon_{th}\}^{t+\Delta t}$ are computed from the previous transient heat transfer analysis and subtracted from $\{\varepsilon\}^t$ and $\{\Delta\hat{\varepsilon}\}^{t+\Delta t}$ respectively.

The subroutine UMAT has then to supply Abaqus with a stress vector $\{\sigma^{t+\Delta t}\}$, updated according to the constitutive laws, and the consistent tangent operator defined in equation (36). An accurate Jacobian (CTO) is essential to achieve fast quadratic convergence in the global NR iterations

[91,93]. Also, the updated inelastic strain vector $\{\varepsilon_{ie}\}^{t+\Delta t}$ is carried to the next iteration via updated STATEV array [1].

If the current temperature exceeds T_{sol}, the material point still contains liquid so the elastic-perfectly plastic algorithm from section 4.2.1 may be used. If equation (77) is used for the liquid, or if the material point is solid, then the following 6 steps are used for time integration of the elastic-viscoplastic constitutive law, given in the form of equation (25) for the inelastic strain rate.

Step 1, Calculation of equivalent stress and equivalent inelastic strain at time t

$$\bar{\sigma}^{t} = \frac{1}{\sqrt{2}}\sqrt{(\sigma_x^t - \sigma_y^t)^2 + (\sigma_y^t - \sigma_z^t)^2 + (\sigma_z^t - \sigma_x^t)^2 + 6\left((\sigma_{xy}^t)^2 + (\sigma_{yz}^t)^2 + (\sigma_{zx}^t)^2\right)} \tag{78}$$

$$\bar{\varepsilon}_{ie}^{t} = \frac{\sqrt{2}}{3}\sqrt{(\varepsilon_{iex}^t - \varepsilon_{iey}^t)^2 + (\varepsilon_{iey}^t - \varepsilon_{iez}^t)^2 + (\varepsilon_{iez}^t - \varepsilon_{iex}^t)^2 + 6\left((\varepsilon_{iexy}^t)^2 + (\varepsilon_{ieyz}^t)^2 + (\varepsilon_{iezx}^t)^2\right)} \tag{79}$$

Step2, Calculation of trial stress vector $\{\sigma^*\}^{t+\Delta t}$, deviatoric trial stress vector $\{\sigma'^*\}^{t+\Delta t}$, and equivalent trial stress $\bar{\sigma}^{*t+\Delta t}$

$$\{\sigma^*\}^{t+\Delta t} = [D]^{t+\Delta t}\left(\{\varepsilon\}^t - \{\varepsilon_{ie}\}^t + \{\Delta\hat{\varepsilon}\}^{t+\Delta t}\right) \tag{80}$$

$$\{\sigma'^*\}^{t+\Delta t} = \{\sigma^*\}^{t+\Delta t} - \frac{1}{3}\left(\sigma_x^{*t+\Delta t} + \sigma_y^{*t+\Delta t} + \sigma_z^{*t+\Delta t}\right)\{1,1,1,0,0,0\}^T \tag{81}$$

$$\bar{\sigma}^{*t+\Delta t} = \frac{1}{\sqrt{2}}\sqrt{(\sigma_x^{*t+\Delta t} - \sigma_y^{*t+\Delta t})^2 + (\sigma_y^{*t+\Delta t} - \sigma_z^{*t+\Delta t})^2 + (\sigma_z^{*t+\Delta t} - \sigma_x^{*t+\Delta t})^2 + 6\left((\sigma_{xy}^{*t+\Delta t})^2 + (\sigma_{yz}^{*t+\Delta t})^2 + (\sigma_{zx}^{*t+\Delta t})^2\right)} \tag{82}$$

Step 3, Solve a pair of scalar nonlinear equations (45) and (46) for $\overline{\sigma}^{t+\Delta t}$ and $\overline{\varepsilon}_{ie}^{t+\Delta t}$ by using methods from 4.1.1 or 4.1.2.

Step 4, Calculate radial-return factor $\eta^{t+\Delta t}$, expand stress vector $\{\sigma\}^{t+\Delta t}$, calculate $\{\sigma'\}^{t+\Delta t}$

$$\eta^{t+\Delta t} = \frac{\overline{\sigma}^{t+\Delta t}}{\overline{\sigma}^{*t+\Delta t}} \tag{83}$$

$$\{\sigma\}^{t+\Delta t} = \eta^{t+\Delta t}\{\sigma'^{*}\}^{t+\Delta t} + \frac{1}{3}\left(\sigma_x^{*t+\Delta t} + \sigma_y^{*t+\Delta t} + \sigma_z^{*t+\Delta t}\right)\{111000\}^T \tag{84}$$

$$\{\sigma'\}^{t+\Delta t} = \{\sigma\}^{t+\Delta t} - \frac{1}{3}\left(\sigma_x^{t+\Delta t} + \sigma_y^{t+\Delta t} + \sigma_z^{t+\Delta t}\right)\{111000\}^T \tag{85}$$

Step 5, Calculate increments of inelastic strains from Prandtl-Reuss flow law, update the inelastic strains and store them in STATEV array.

$$\{\Delta\varepsilon_{ie}\}^{t+\Delta t} = \frac{3}{2}\frac{\{\sigma'\}^{t+\Delta t}}{\overline{\sigma}^{t+\Delta t}}\Delta\overline{\varepsilon}_{ie}^{t+\Delta t} \tag{86}$$

$$\{\varepsilon_{ie}\}^{t+\Delta t} = \{\varepsilon_{ie}\}^{t} + \{\Delta\varepsilon_{ie}\}^{t+\Delta t} \tag{87}$$

Step 6, Calculate Jacobian (Consistent Tangent Operator)

The derivation of the Jacobian for this form of constitutive laws is given in [62]. The final expression is given in Eq. (88) in tensor notation.

$$\underline{\underline{\mathbf{J}}}^{t+\Delta t} = 2\mu^{t+\Delta t}\eta^{t+\Delta t}\underline{\underline{\mathbf{I}}} + \left(\kappa^{t+\Delta t} - \frac{2\mu^{t+\Delta t}\eta^{t+\Delta t}}{3}\right)\mathbf{I}\otimes\mathbf{I} - 2\mu^{t+\Delta t}\left(\eta^{t+\Delta t} - c_J{}^{t+\Delta t}\right)\mathbf{N}^{t+\Delta t}\otimes\mathbf{N}^{t+\Delta t} \tag{88}$$

The above variables were defined except normal flow tensor **N** and constant c_J

$$\mathbf{N}^{t+\Delta t} = \sqrt{\frac{3}{2}}\frac{\boldsymbol{\sigma}'^{t+\Delta t}}{\bar{\sigma}^{t+\Delta t}} \tag{89}$$

$$c_J{}^{t+\Delta t} = \frac{1 - \dot{\bar{\varepsilon}}_{ie}^{t+\Delta t}\Delta t}{1 + \Delta t\left(3\mu^{t+\Delta t}\dfrac{\partial\dot{\bar{\varepsilon}}_{ie}}{\partial\bar{\sigma}} - \dfrac{\partial\dot{\bar{\varepsilon}}_{ie}}{\partial\bar{\varepsilon}_{ie}}\right)} \tag{90}$$

The derivatives in (79) are found from the strain rate laws given in equations (77) or (25) evaluated at $t + \Delta t$

4.4 Two Dimensional Problems

In many solidification processes, such as the continuous casting of steel, one dimension of the casting is much longer than the others, and is otherwise unconstrained. In this case, it is quite reasonable to apply a condition of generalized plane strain in the long direction (z), and to solve a two-dimensional thermal stress problem in the transverse (x-y) plane. This condition reasonably allows a two-dimensional computation to produce the complete three-dimensional stress state in the plane section.

The generalized plane strain condition assumes that strain in the undiscretized longitudinal direction z is a linear function of the in-plane coordinates:

$$\varepsilon_{zz} = a + bx + cy \tag{91}$$

The unknown constants (a,b,c) are solved together with the in-plane displacements, adding three extra degrees of freedom to the global system of equations for the entire domain. The associated additional equation for a is:

$$\int \sigma_{zz} dA = F_z \tag{92}$$

where F_z is an external mechanical force acting in the z direction. The two additional equations for b and c are:

$$\int \sigma_{zz} y dA = M_x \tag{93}$$

$$\int \sigma_{zz} x dA = M_y \tag{94}$$

where M_x, M_y are external mechanical moments in the x and y directions respectively.

A simplification of this condition occurs when two-fold symmetry causes the axial strain to be a constant ($\varepsilon_{zz} = a$). In this case, M_x, M_y, b and c all equal zero, and only one additional global equation must be solved for a. Furthermore, the axial force, F_z is set to zero, when there is no axial load or

constraint. The axial strain, a, is generally negative for solidification problems, as it accounts for the average thermal shrinkage of the plane section.

4.5 Figures and Tables

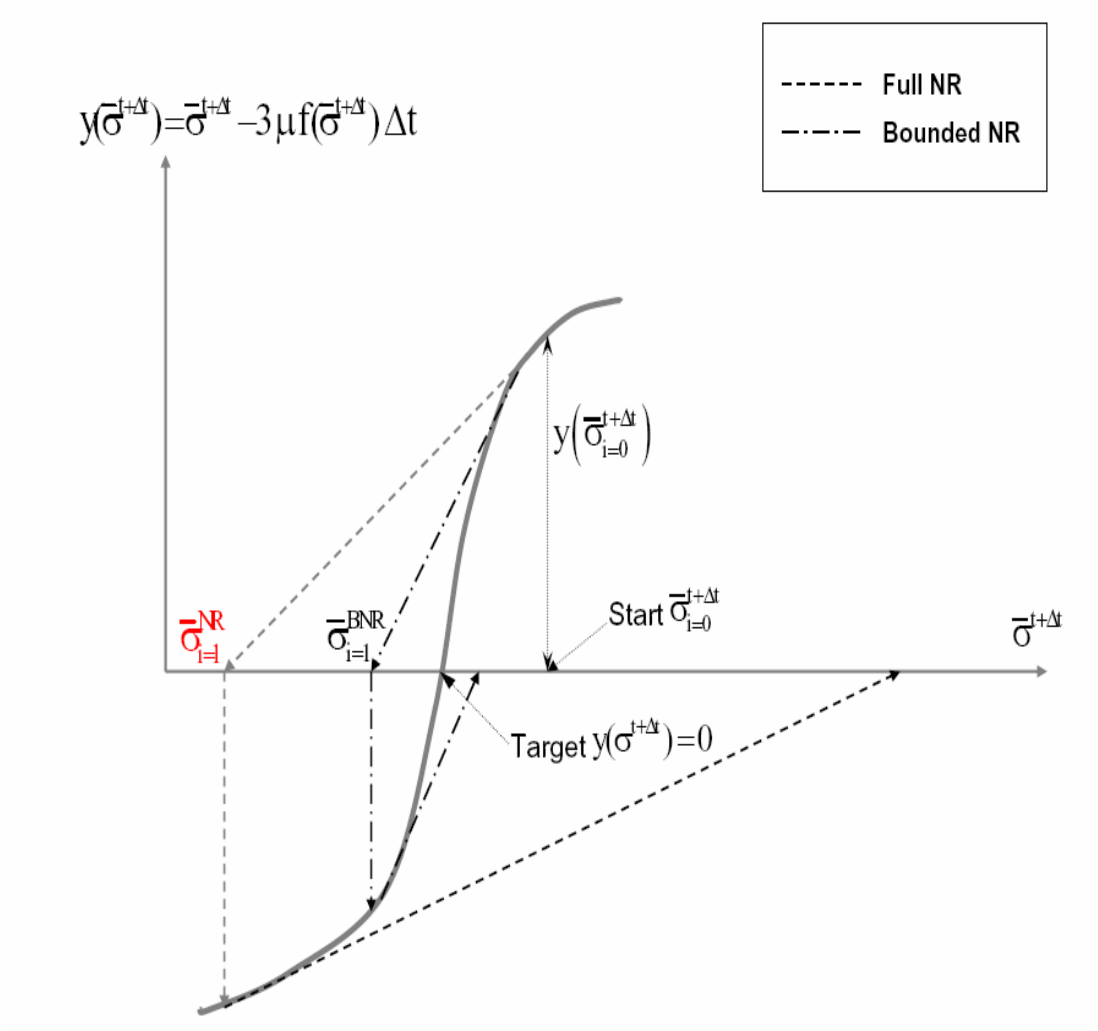

Figure 4.1 Bounded NR Method

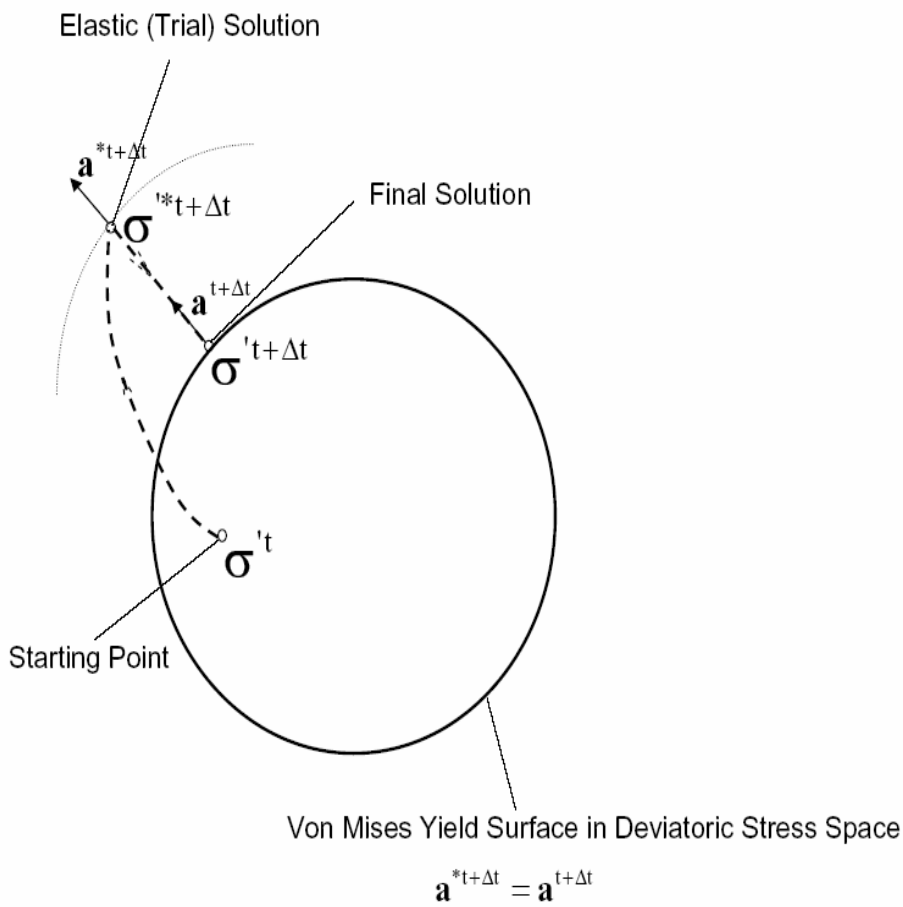

Fig 4.2 Radial-return method for von Mises yield Surface

Chapter 5. Model Validation

A semi-analytical solution of thermal stress in an unconstrained solidifying plate, derived by Weiner and Boley [2] is used here as an ideal validation problem for solidification stress models. This one-dimensional solution takes advantage of the large length and width of the casting. Thus, it is reasonable to apply the generalized plane strain condition, discussed in the previous section, in both the y and z directions, to produce the complete 3-D stress and strain state.

The domain adopted for this problem is a thin slice through the plate thickness using 2-D generalized plane strain elements (in the axial z direction) with zero relative rotation (ie b=c=0 in equation.(91). The domain moves with the strand in a Langrangian frame of reference as shown in Fig. 5.1. In addition, a second generalized plane strain condition was imposed in the y-direction (parallel to the surface) by coupling the displacements of all nodes along the bottom edge of the slice domain as shown in Figure 5.2. This was accomplished using the *EQUATION option in Abaqus [1]. The normal (x) displacement of all nodes along the bottom edge of the domain is fixed to zero. Tangential stress was left equal zero along all surfaces. Finally, the ends of the domain are constrained to remain vertical, which prevents any bending in the xy plane.

The material in this problem has elastic-perfectly plastic constitutive behavior. The yield stress drops linearly with temperature from 20 MPa at 1000°C to zero at the solidus temperature 1494.4^{o}C, which was approximated by 0.03 MPa at the solidus temperature. A very narrow mushy region, 0.1^{o}C, is used to approximate the single melting temperature assumed by Boley and Weiner. All the constants used in this solidification model are listed in Table 4.I

Abaqus with UMAT is tested with both elastic-perfectly-plastic algorithm from section 4.2.1, and a robust viscoplastic algorithm from section 4.1 applied to the rapid liquid strain function equation (77) to emulate elastic-perfectly-plastic behavior. Also, an in-house code, CON2D [3,5,6] code is used to solve this problem as well as the realistic problem from chapter 6. In the latter elastic-viscoplastic model, the constitutive relation was transformed into a computationally more challenging form, the highly nonlinear creep function of Eq. (77) with $\mu_V^{-1} = 1.5\text{x}10^8\ \text{MPa}^{-1}\text{sec}^{-1}$, and σ_Y =0.01 MPa in the liquid.

Figure 5.2 shows the domain and boundary conditions for both the heat transfer and mechanical models. Heat transfer analysis is run first to get the temporal and spatial temperature field. Stress analysis is then run using this temperature field. The domain in Abaqus has a single row of 300 plane 4 node elements in both thermal and stress analysis. CON2D uses a similarly refined mesh with 6-node, quadratic triangular elements.

Figures 5.3 and 5.4 show the temperature and the stress distribution across the solidifying shell at two different solidification times. The semi-analytical solutions were computed with MATLAB by C. Li et. al. [3]. The almost-linear temperature gradient through the shell gradually drops as solidification proceeds. This faster cooling of the interior relative to the surface region naturally causes interior contraction and tensile stress, which is offset by compression at the surface. The changes in slope at ~ -15 and +12 MPa denote the transition from the elastic central region to the plastically-yielded surface and interior. Both lateral stress distributions (y and z directions) are the same for both codes, which is expected from the identical boundary conditions in these two directions. Shear stresses and x-stress are all zero. Identical results were found with the perfectly-plastic and the viscoplastic liquid functions coded in UMAT, so there is a single Abaqus curve representation on the graphs. The original boundary condition prescribed an

abrupt surface quench to 1000 ^{o}C, which causes convergence problems for Abaqus at early times. Instead applying a convection boundary condition with a film coefficient of 250,000 W/m^{2}C alleviated the convergence problems and improved the stress results (under 1% error). CON2D produced similar accuracy with the semi-analytical solution.

CPU times were also similar between CON2D and Abaqus with the elastic-perfectly-plastic (radial return) algorithm. The viscoplastic algorithms from section 4.1 coded in Abaqus were ~10 times slower, and experienced computational difficulties, which required lower μ_V^{-1}, and resulted in ~4% error.

The two CREEP methods supported in Abaqus [1, Y19] were also tested for this problem using a less nonlinear form of Eq. (77) with smaller μ_V^{-1} The implicit CREEP method always failed to converge despite many attempts, even when used in conjuction with Abaqus built-in plasticity alogoritham based on classic radial-return method (section 4.2.1) for an elastic-perfectly plastic liquid/mushy zone. The explicit CREEP also experienced convergence problems, but did converge with the easier, but less accurate lower μ_V^{-1} equation. Although the stress results were comparable, the CPU times with explicit creep were ~20 times larger compared to Abaqus with the UMAT of this work or CON2D.

Abaqus automatically adjusts the time increment size, based on the convergence criteria from the previous time increment [1], starting from an initial time increment of 10^{-5} at 0s, and increasing to 0.3s after 15s. Time increments are specified manually in CON2D to increase logarithmically from 0.001s at 0s to 0.1s at 21s. A formal study of mesh and time increment refinement was conducted for CON2D by Zhu at al. [5], which shows that the 300-node mesh used here is more than sufficient to achieve accuracy within 1% error with a fixed time increment of 0.01s (1000

time increments per 10 s), Figure 5.5. Further convergence studies with CON2D for this problem were performed by Li & Thomas [3], including variable mesh and time increment sizes.

5.1 Figures and Tables

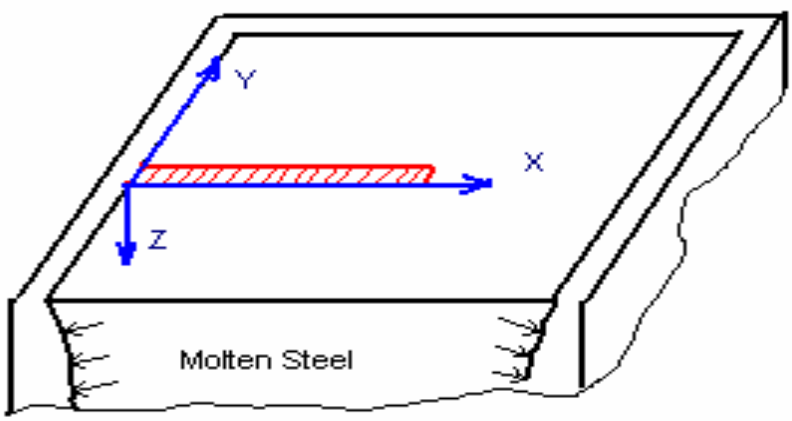

Figure 5.1 Solidifying slice

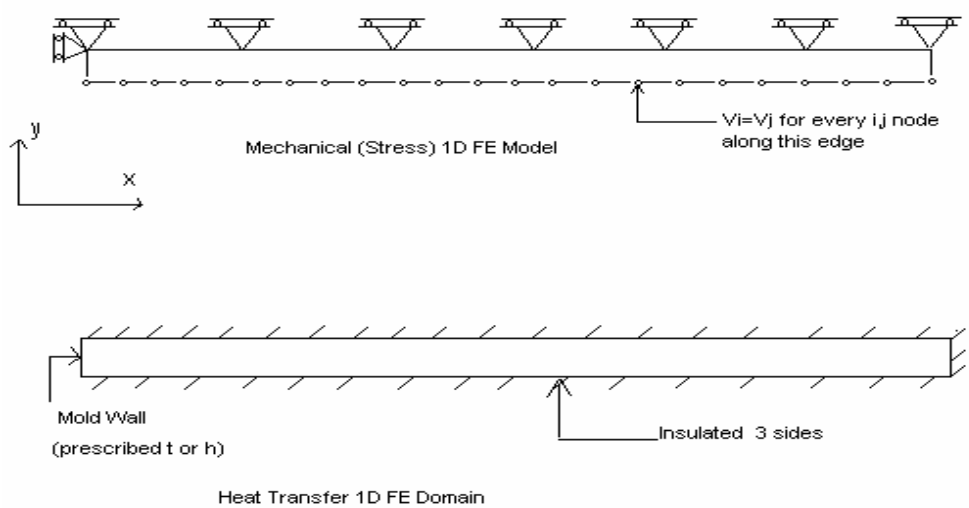

Figure 5.2 Mechanical and thermal FE domains

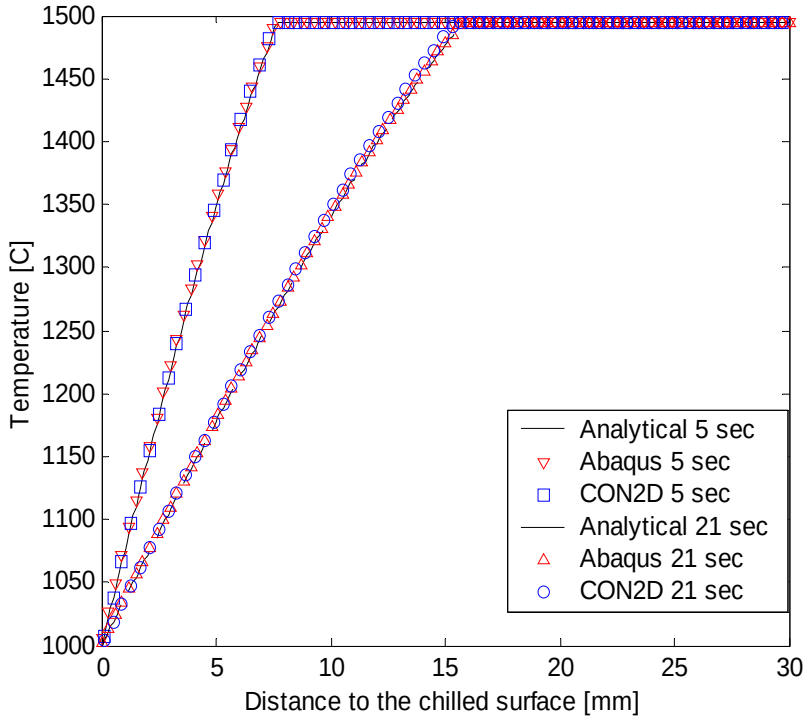

Figure 5.3 Temperature distribution along the solidifying slice

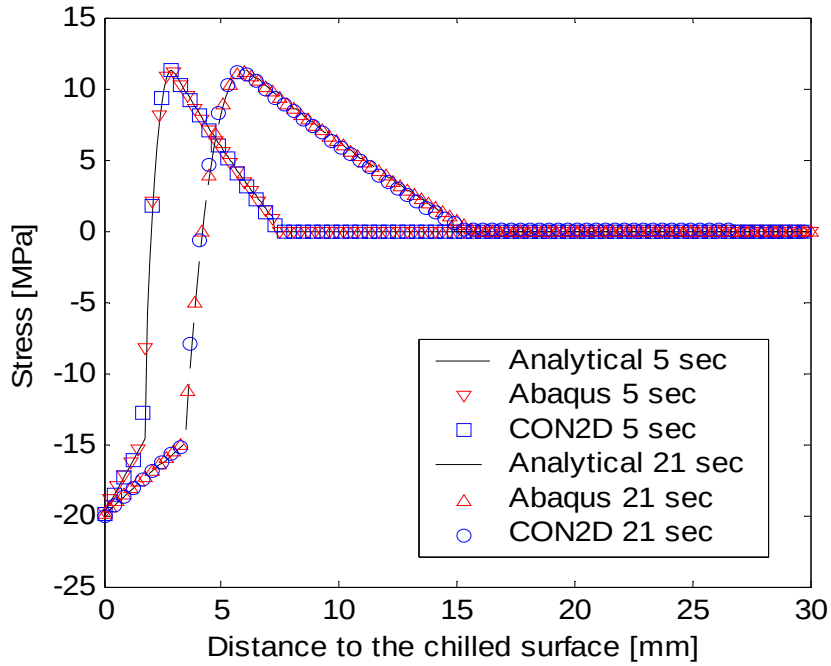

Figure 5.4 Y and Z Stress distributions along the solidifying slice

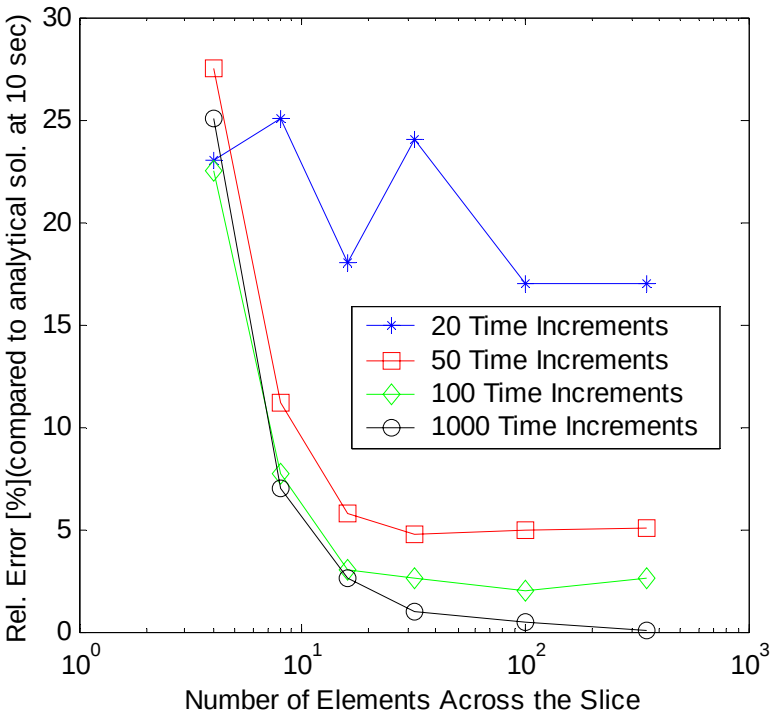

Figure 5.5 Convergence study [5]

Table 5.I Constants used in solidification test problem

Conductivity [W/mK	33.0
Specific Heat [J/kg K]	661.0
Elastic Modulus in Solid [GPa]	40.0
Elastic Modulus in Liquid [GPa]	14.0
Thermal Linear Expansion Coefficient [1/K]	0.00002
Density [kg/m^3]	7500.
Poisson's Ratio	0.3
Liquidus Temperature [^{o} C]	1494.45
Fusion Temperature (analytical) [^{o} C]	1494.4
Solidus Temperature [^{o} C]	1494.35
Initial Temperature [^{o} C]	1495.0
Latent Heat [J/kg K]	272000.0
Reciprocal of Liquid viscosity [MPa^{-1}sec^{-1}]	1.5x10^8
Surface Film coefficient [W/m^{2}K]	250,000

Chapter 6. Uncoupled Analysis of Solidifying Slice in Continuous Casting Mold

6.1 Material Properties, Loads, Constitutive Law

The FE model of solidification of a slice, with the identical mesh of nodes and elements that was validated in the previous section, was next applied to a realistic problem of continuous casting of steel with temperature-dependent properties and boundary conditions matching typical plant conditions. The artificial surface quenching condition was replaced with an instantaneous interfacial heat flux profile that varied with time down the mold according to mold thermocouple measurements [3] and is given in equation (95), and Fig.6.1. This heat flux boundary condition was input to Abaqus using the DFLUX subroutine.

$$\hat{q}\left[\mathrm{MW/m^2}\right] = 6.5\left(t[s]+1\right)^{-1/2} \tag{95}$$

Constitutive Eq. (25) was chosen for solidifying plain-carbon steel in the austenite phase using the rate-dependent, elastic-visco-plastic model III of Kozlowski [61] given in Eq. (96). This model was developed to match tensile test measurements of Wray [53] and creep test data of Suzuki [57].

$$\dot{\bar{\varepsilon}}_{ie}[\sec^{-1}] = f_C\left(\bar{\sigma}[\mathrm{MPa}] - f_1\,\bar{\varepsilon}_{ie}\,|\,\bar{\varepsilon}_{ie}\,|^{f2-1}\right)^{f3}\exp\left(-\frac{Q}{T[K]}\right)$$

where :

$$Q = 44,465$$

$$f_1 = 130.5 - 5.128\times10^{-3}\,T\,[K] \qquad (96)$$

$$f_2 = -0.6289 + 1.114\times10^{-3}\,T\,[K]$$

$$f_3 = 8.132 - 1.54\times10^{-3}\,T\,[K]$$

$$f_C = 46,550 + 71,400\,(\%C) + 12,000\,(\%C)^2$$

This empirical relation relates the equivalent inelastic strain rate $\dot{\bar{\varepsilon}}_{ie}$ with the von Mises stress $\bar{\sigma}$, equivalent inelastic strain $\bar{\varepsilon}_{ie}$, activation constant Q, steel grade %C, and several empirical temperature- or steel-grade-dependant constants f_1, f_2, f_3, f_C.

Another constitutive model, so called enhanced power law model [5] was added to the UMAT lately to simulate delta ferrite phase with relatively higher creep rate than austenite phase, Eq. (96A). The constitutive model given in Equation (96A) is applied in the solid whenever the volume fraction of ferrite is more than 10%. Otherwise, Equation (96) is applied. The calculation of the volume fractions is adopted from CON2D [5,8].

$$\dot{\bar{\varepsilon}}_{ie}\,(1/\sec.) = 0.1\left|\frac{\bar{\sigma}\,(MPa)}{f_{\delta c}(\%C)\left(\frac{T\,(^{o}K)}{300}\right)^{-5.52}(1+1000\bar{\varepsilon}_{ie})^{m}}\right|^{n}$$

$where$:

$$f_{\delta c}\,(\%C) = 1.3678\times10^{4}\,(\%C)^{-5.56\times10^{-2}} \qquad (96A)$$

$$m = -9.4156\times10^{-5}\,T\,(^{o}K) + 0.3495$$

$$n = \frac{1}{1.617\times10^{-4}\,T\,(^{o}K) - 0.06166}$$

Temperature dependent properties were chosen for %0.27C plain carbon steel with T_{sol}=1411.79 ^{o}C and T_{liq}=1500.72 ^{o}C. All temperature dependant material property calculations are an integral part of the CON2D code [3,5,6], and were extracted for Abaqus input. Fig.6.2 shows the fractions of solid phases and liquid for this steel [3], which confirms the assumption of single-phase austenite for the solid over the temperature range of interest.

The enthalpy curve used to relate heat content and temperature in this study, H(T), is shown in Fig. 6.3. It was obtained by integrating the specific heat curve fitted from measured data of R. D. Pehlke et. al. [103]. Abaqus tracks the latent heat Hf=257,867 J/kg separately from the specific heat $c_p(T)$, which is found from the slope of this H(T) curve, except in the solidification region, where c_p is found [78] using equation (97). Equation (97) assumes that the fraction of solid is a linear interpolation between the liquidus and solidus temperatures, while CON2D is using the leveler rule [79] which assumes that the solid develops more slowly when cooling through the higher temperature ranges, and more rapidly as the solidus temperature is approached.

$$c_p(T) = \frac{dH}{dT} - \frac{Hf}{\left(T_{liq} - T_{sol}\right)} \tag{97}$$

The temperature dependent conductivity function for 0.27%C plain carbon steel is fitted from measured data by Harste et. al. [103], and given in Fig.6.4. The conductivity increases in the liquid region by a factor of 6.65 to partly account for the effect of convection due to flow in the liquid steel pool [104]. Density was assumed constant at this work, 7400 kg/m^3, in order to maintain constant mass.

Thermal strain can be calculated from the temperature changes simulated by the heat transfer model and from the unified state function, TLE, thermal linear expansion, which includes the volume change of materials undergoing both temperature change and phase transformation, Fig. 6.5 [3]. The thermal strain in CON2D is expressed by equation (98) [3].

$$\{\varepsilon_{th}\} = \left(TLE(T) - TLE(T_{ref})\right)\{1110\,0\,0\}^T \tag{98}$$

T_{ref} is an arbitrary reference temperature, typically either Tsol or 20°C. This thermal linear expansion function was obtained from solid phase density measurements compiled by K. Harste et. al. [103, 105] equation (99), while in liquid/mushy zone by density measurements by Jimbo and Cramb et. al. [106].

$$TLE = \sqrt[3]{\frac{\rho(T_{ref})}{\rho(T)}} - 1 \tag{99}$$

Abaqus calculates thermal strains from equation (100) [1]

$$\{\varepsilon_{th}\} = \left(\alpha(T)\left(T - T_{ref}\right) - \alpha(T_{init})\left(T_{init} - T_{ref}\right)\right)\{1110\,0\,0\}^T \tag{100}$$

where $\alpha(T)$ is the temperature-dependant coefficient of thermal expansion, T_{init} is initial temperature (pouring temperature), and T_{ref} is a very important reference temperature.

The following expression is used to calculate $\alpha(T)$ from TLE:

$$\alpha(T) = \frac{TLE(T_{ref}) - TLE(T)}{T_{ref} - T} \tag{101}$$

Identical thermal strain results are produced with Abaqus for $T_{ref} = 20^oC$ and $T_{ref} = T_{sol}$, though $\alpha(T)$ curves have totally different shape, see Fig 6.7 and 6.8. This is a clear sign that the expression from equation (101) is correctly calculating $\alpha(T)$ from TLE. Fig.6.7 has $\alpha(T)$ for $T_{ref} = 20^oC$.

Elastic modulus E generally decreases as the temperature increases, although its value at high temperatures is uncertain. The temperature-dependent elastic modulus curve used in this model was fitted from measurements from Mizukami et. al. [107] by Kozlowski [61] as shown in Fig.6.6. Unlike in other models, the elastic modulus of the liquid here was given the physically realistic value of 14GPa. This value also avoids numerical trouble from excessively small values in the stiffness matrix. Actually, the value of the elastic modulus in the liquid has little effect on the stress results, due to the negligible strength of the liquid. Poisson ratio is 0.3 constant. All other material constants are listed in table 6.I.

6.2 Results and Comments

A 21s simulation was performed, which corresponds to 700mm long shell of cast steel at a casting speed of 33.3mm/s (2m/min). The temperature and stress distribution results along the solidifying slice are presented at four times during solidification for both codes in Fig.6.9 and Fig.6.10. The temperature and stress histories are given for two material points in Fig. 6.11 and Fig. 6.12. Temperature and stress contours are constructed from the transient results in Figs. 6.13

and 6.14, and represent the steady-state appearance of the solidifying shell. The shape of the tensile region that forms inside the shell, and the development of surface compression are clearly revealed. These stress distributions are qualitatively similar to that of the semi-analytical solution. The shape changes slightly due to the change in heat flux and properties. The temperature results predicted by Abaqus and CON2D match except near the solidification front, where an unplanned difference in phase fraction evolution causes minor variations. This causes minor variations in the stress results, although there is still a reasonable match. The operator-splitting method in CON2D produced minor oscillations in the stresses, such as the bump at ~1s in Fig. 6.9 and 6.12.

Integration of the enhanced delta power constitutive law from Eq. (96A) is tested with the steel grade 0.10%C. All material properties for the 0.10%C steel grade are first extracted from CON2D. Since 0.10%C steel grade has a strong presence of delta phase [8], the enhanced delta power law is integrated most of the time in solid. The temperature and stress results are compared with the 0.27%C steel grade results in Fig 6.15 and 6.16. The 0.27%C steel grade is used throughout this work and is know for a strong presence of a single austenite phase in solid, and therefore integrating only the Kozlowski III law (96). There are visible differences between the temperature and stress distributions stress, and there is a spike in the stress results for 0.10%C in the transition zone from austenite to delta-ferrite phase observed also in previous work [5,6,8]. Since the enhanced delta power law has much more creep, it takes five times more cpu time to integrate the enhanced power law (96A) compared to the Kozlowski III law (96).

Detailed CPU benchmark results are presented in Table 6.II for all combinations of methods compared. Simulations were performed on an IBM p690 with Power 4, 1.3 Ghz CPU running under AIX 5.1 OS. Abaqus required 2-3 global NR iterations per increment, and 5.6 minutes of

CPU time for the 21s. stress simulation with the elastic-perfectly plastic (radial-return) algorithm for liquid/mush. Depending on severity of the nonlinearity in the strain rate – stress function, (ie value of μ_V^{-1}), between 30 minutes and 2 hours were needed for the same simulation using Eq. (77) for the liquid. Even though Nemat-Nasser is an explicit local solution method, it was only slightly faster then the local bounded Newton-Raphson method. However, benchmarks performed by Zhu et. al. [5] found that the Nemat-Nasser method produced incorrect results for some viscoplastic laws, while the local bounded NR method was reliable in all cases. As found in section 5, Abaqus implicit built-in integration (via CREEP subroutine) failed to converge, while explicit CREEP was very slow. There were no visible differences between any of the Abaqus stress results using the four different local integration algorithms that converged.

CON2D had similar performance to Abaqus for the same local method, showing that the operator-splitting approach is reasonable, if the oscillations can be tolerated.

In conclusion, the implicit viscoplastic integration algorithm followed by the bounded NR scheme at the local level is the best, most robust method for solving solidification problems with highly-nonlinear elastic-viscoplastic constutitive equations. Coding this method into a UMAT enables Abaqus to perform as well as the in-house CON2D code. Either full NR or operator-splitting are effective methods at the global level. The elastic-perfectly-plastic algorithm (radial return) method is an efficient method to handle the liquid/mushy region. The rapid creep-type function for treating liquid (Eq. 77) has the advantage of accurately simulating liquid flow that is important for the quantitative prediction of hot tear cracks between dendrites at the solidification front [3,108]. Using the UMAT, Abaqus is now ready to tackle large-scale finite-element simulations of solidification processes, including multi-dimensional analysis of continuous casting.

6.3 Ideal Taper Based on Shell Shrinkage for Different Casting Speeds

Even though the geometry of the slice model in this chapter is relatively simple, it can be still effectively used to predict the ideal mold taper which compensate for shrinkage of the solidifying strand to maintain good contact and heat transfer between the mold and shell surface without applying extra frictional force. The amount of taper needed varies with steel composition, mold length, casting speed, and type of lubrication. [8].

The transversal strain slice results from this chapter for 0.27%C steel, with all austenite phase using Kozlowski III constitutive law from Eq. (96) and with the heat flux BC from Eq. (95), are used to predict the shell shrinkage, or ideal mold taper, from the narrow mold side assuming the width of the wide mold side to be 1m. Due to the Langrangian frame of reference, the times that the slice spends in 0.7 m long mold are easily calculated for the four different casting velocities. Assuming that the heat flux curve, Fig. 6.1 remains constant with speed, and that all slices along the mold width behave the same, transversal strain histories corresponding to these times are extracted from Abaqus post-processing tool in form of xy data files. Those files are than read into Matlab [110], and the percentage of ideal taper per unit of the mold length is calculated as a function of current time bellow meniscus for each casting velocity using Eq, (101A)

$$(\%\text{taper/m}) = \frac{E22(t)\ W\ 100}{v_{cast}\ t} \qquad (101A)$$

Where E22(t) is time dependant total transverse strain, W=1m is the width of the wide mold face, v_{cast} is the casting velocity, and t is the current time bellow the meniscus. These results are

compiled in one graph in Fig. 6.17 where the time dependence is replaced by the distance bellow the meniscus and plotted along the mold length of 0.7m.

It can be observed from Fig 6.17 that increasing casting speeds tends to decrease the ideal taper due to less time spend in the mold, hotter shell, and less shrinkage. The steel tends to shrink most in the upper region of the mold where taper should be high. In lower portion of the mold the thermal resistance of the thicker shell combined with a thicker mold power layer lower the heat flux and shell shrinkage, so the taper should be smaller. The results indicate that taper should decrease greatly from the top to the bottom of the mold, so a multifold taper is recommended rather than a linear one. The conclusions derived from this simple slice model are consistent with the findings of Li and Ojeda [109], who used CON2D model for prediction of ideal taper in high speed billet casting. Before implementing into the actual caster, further work would be needed to incorporate the effects of mold distortion, changes in heat flux with casting speed, and steel grade.

6.4 Figures and Tables

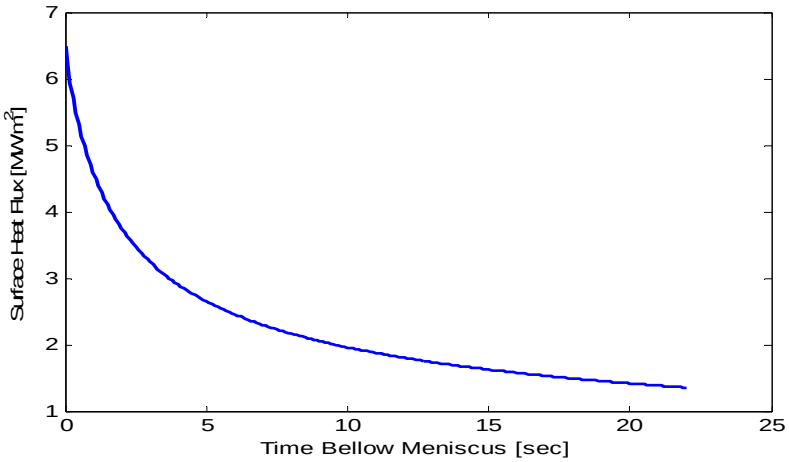

Figure 6.1 Instantaneous interfacial heat flux

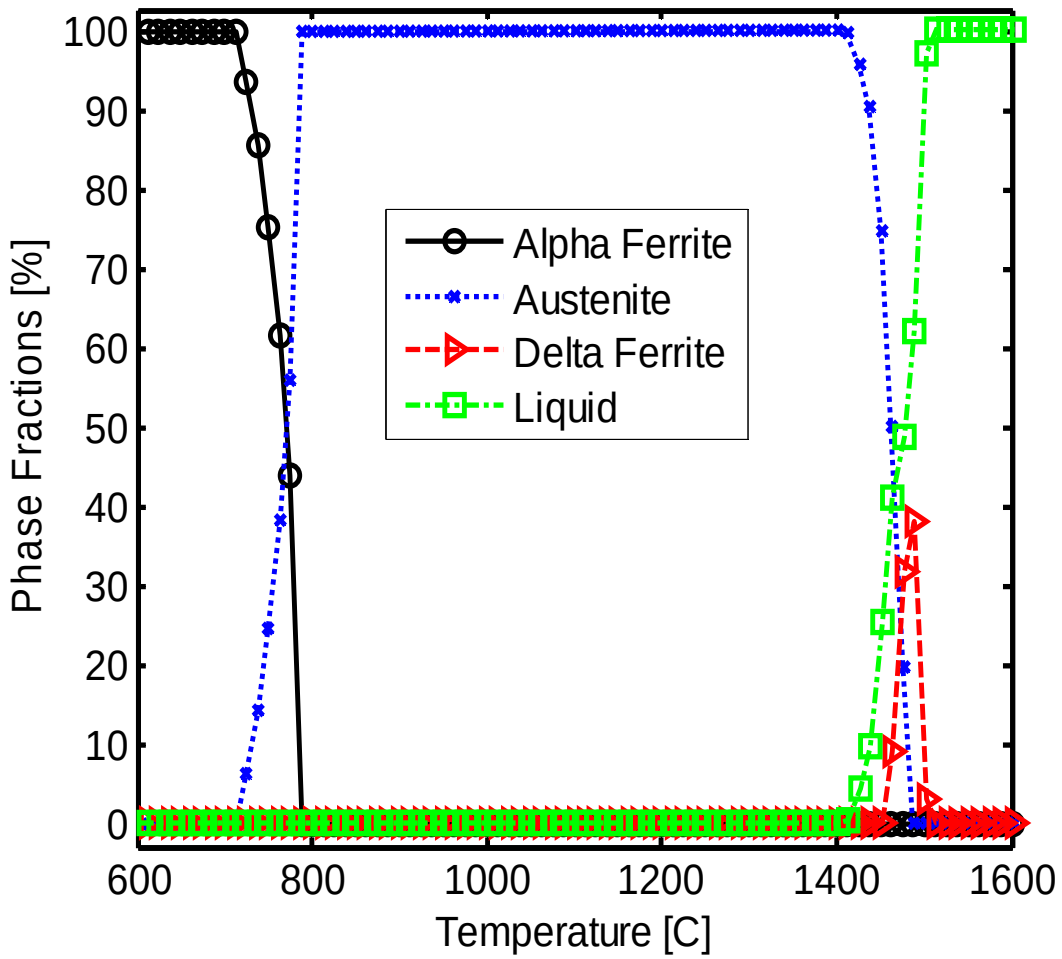

Figure 6.2 Phase fractions for 0.27%C carbon steel

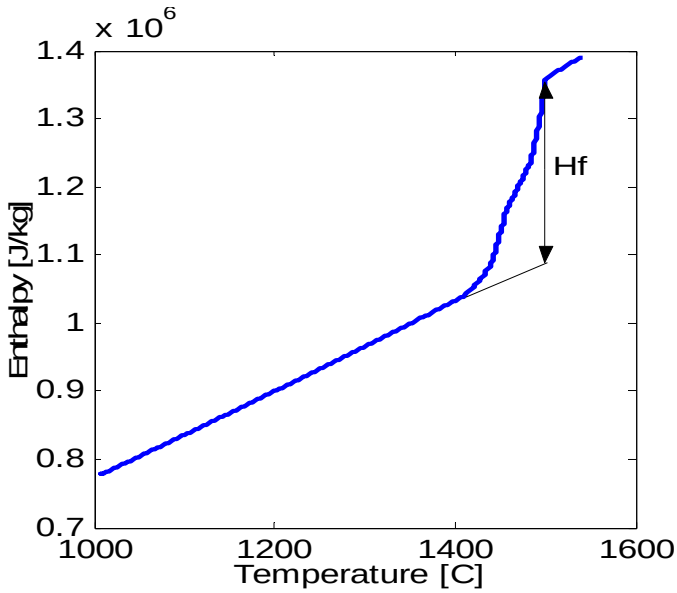

Figure 6.3 Enthalpy for 0.27 %C plain carbon steel

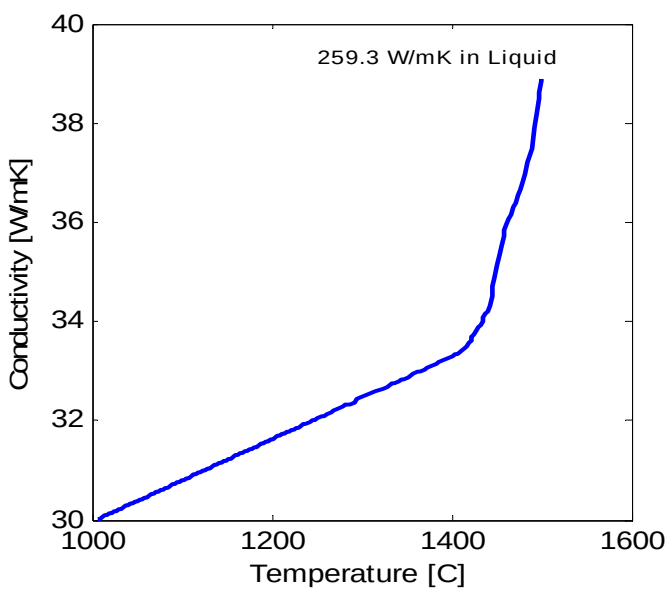

Figure 6.4 Thermal conductivity for 0.27%C plain carbon steel

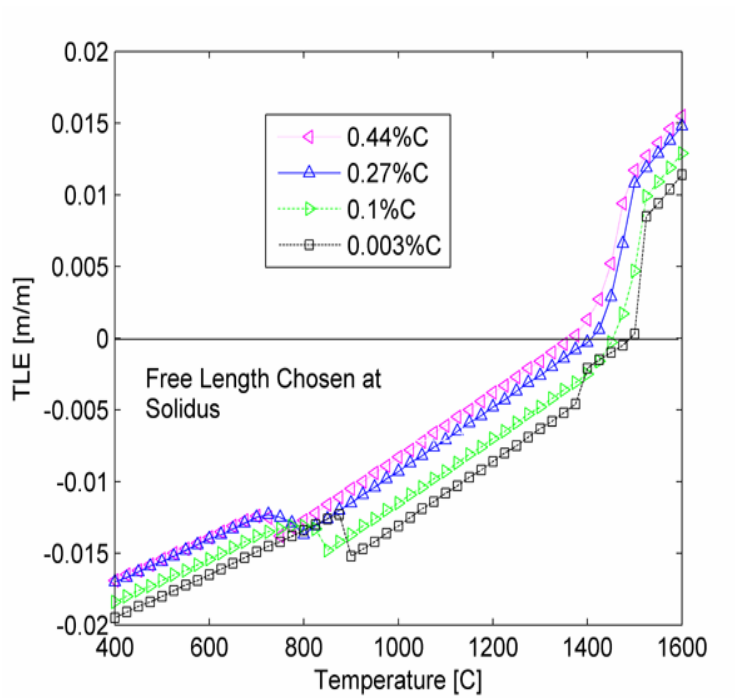

Figure 6.5 Thermal linear expansion (TLE) of plain carbon steels

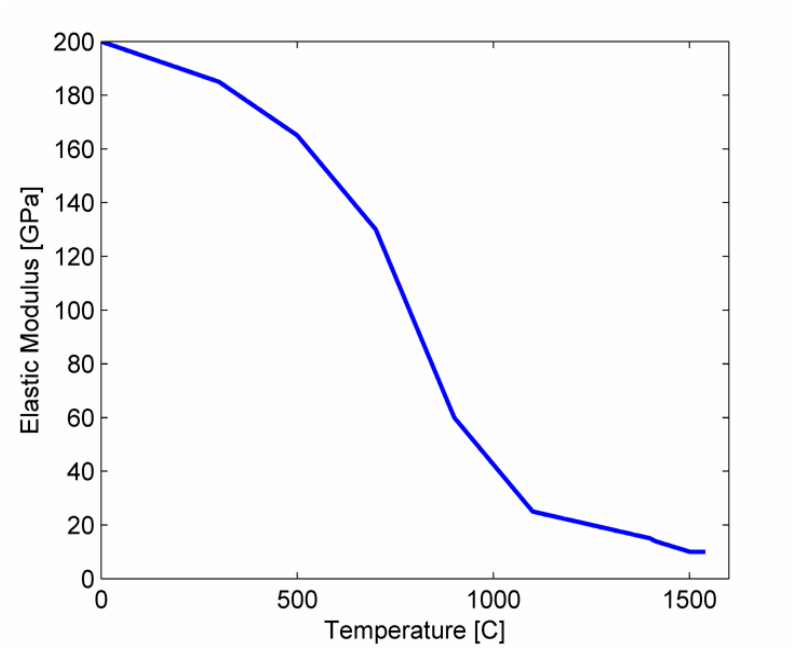

Figure 6.6 Elastic modulus for plain carbon steel

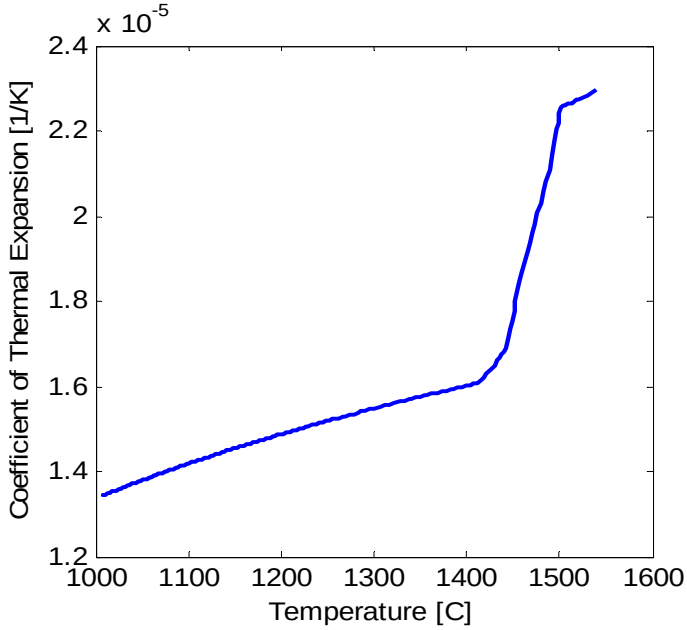

Figure 6.7 Coefficient of thermal linear expansion for 0.27%C plain carbon steel, T_{ref}=20C

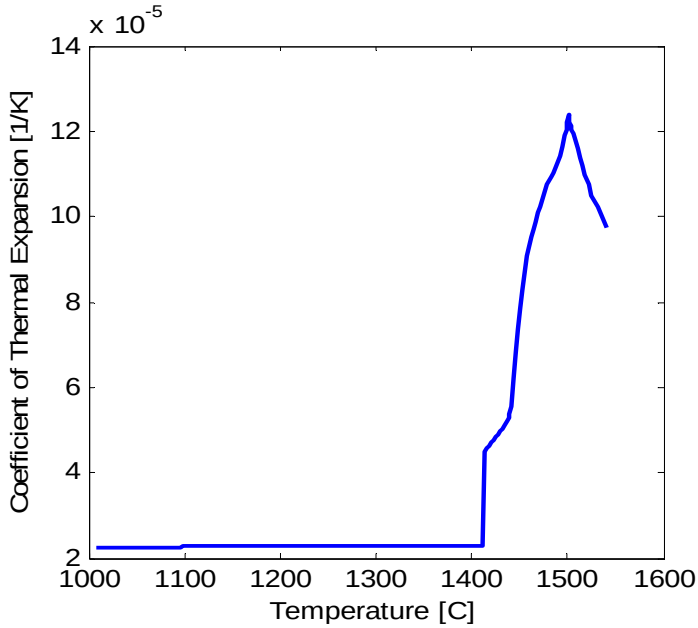

Figure 6.8 Coefficient of thermal linear expansion for 0.27%C plain carbon steel,

T_{ref}=T_{sol}=1411.79C

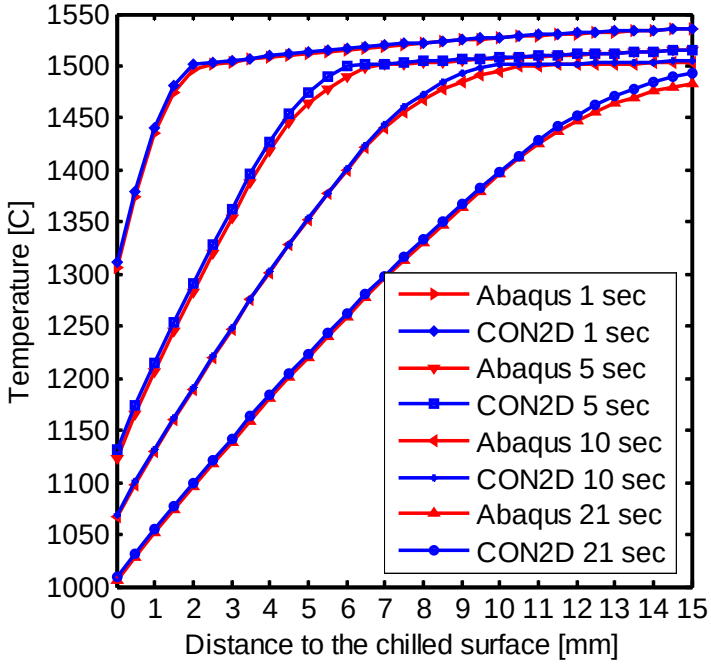

Figure 6.9 Temperature distribution along the solidifying slice in continuous casting mold

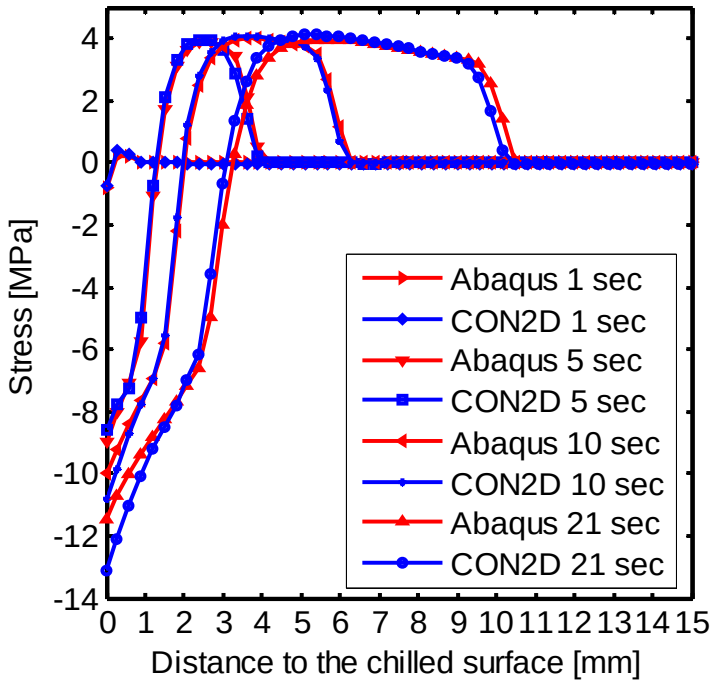

Figure 6.10 Lateral (y and z) stress distribution along the solidifying slice in continuous casting mold

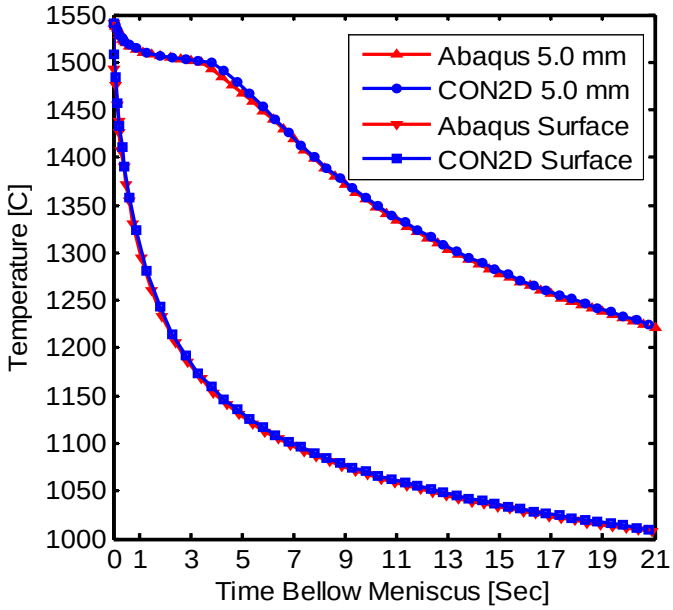

Figure 6.11 Temperature history for the surface material point and the material point 5 mm from the surface

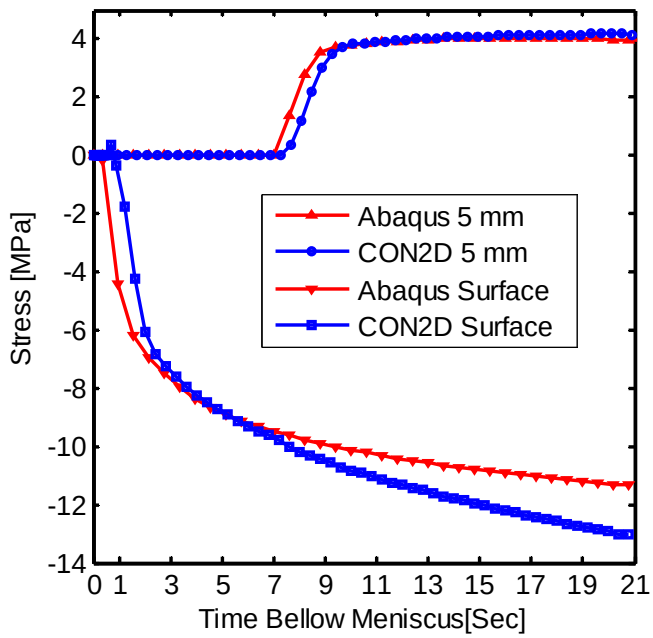

Figure 6.12 Lateral stress history for the surface material point and the material point 5 mm from the surface

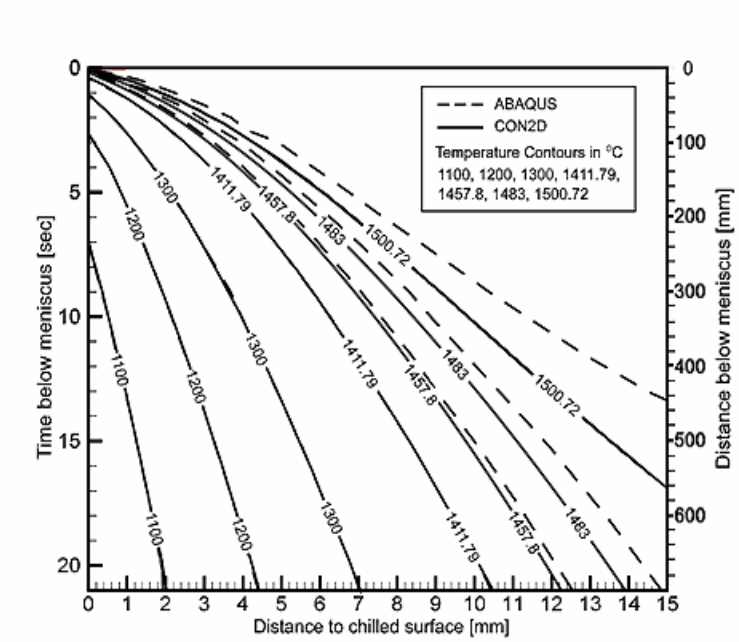

Figure 6.13 Temperature contours

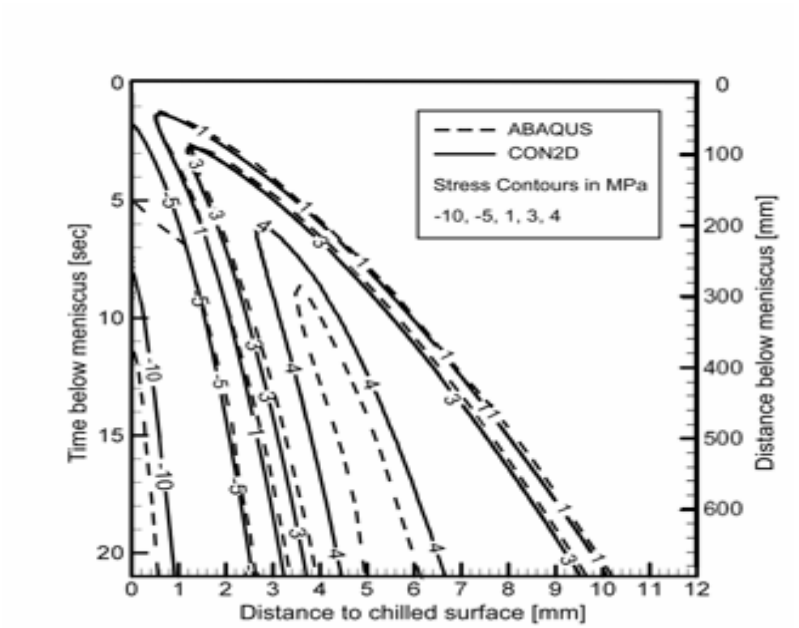

Figure 6.14 Stress contours

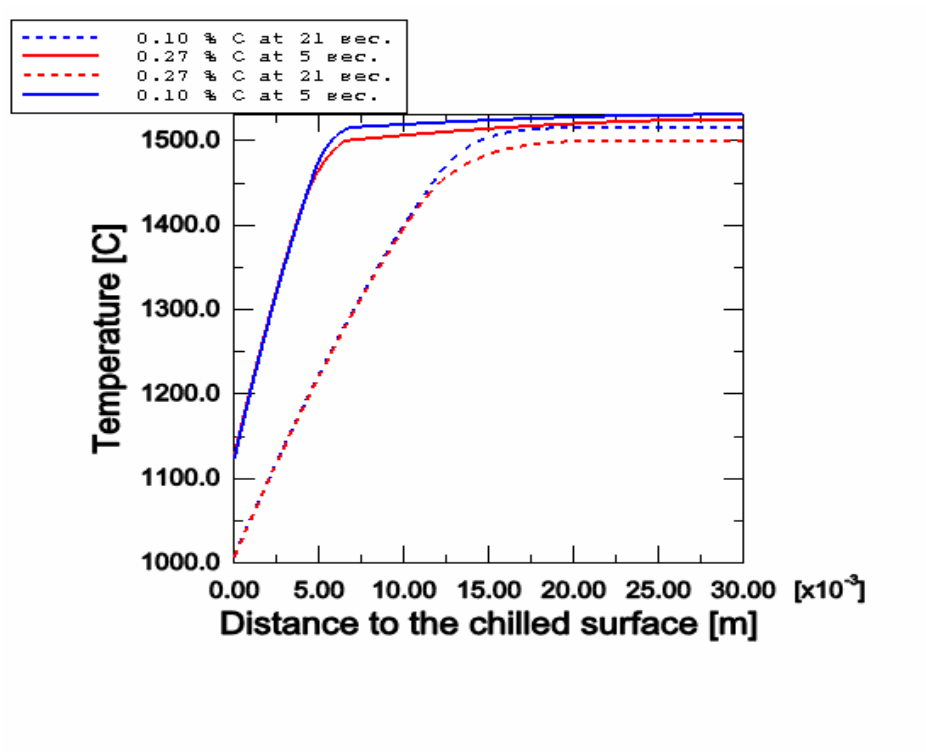

Fig. 6.15 Temperature distributions for 0.27%C and 0.10%C steel grades

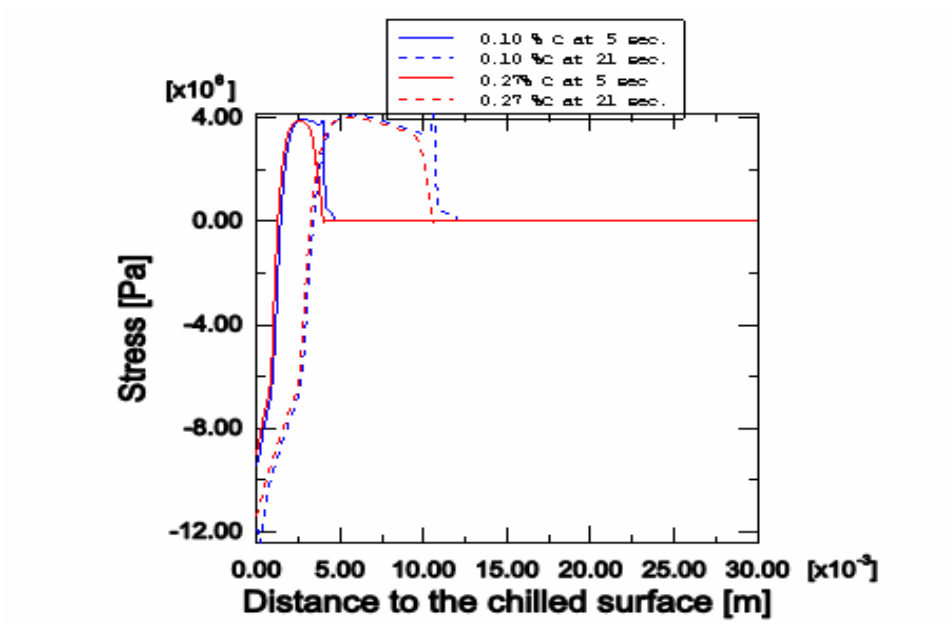

Fig. 6.16 Stress distributions for 0.27%C and 0.10%C steel grades, which have 2 different const. laws

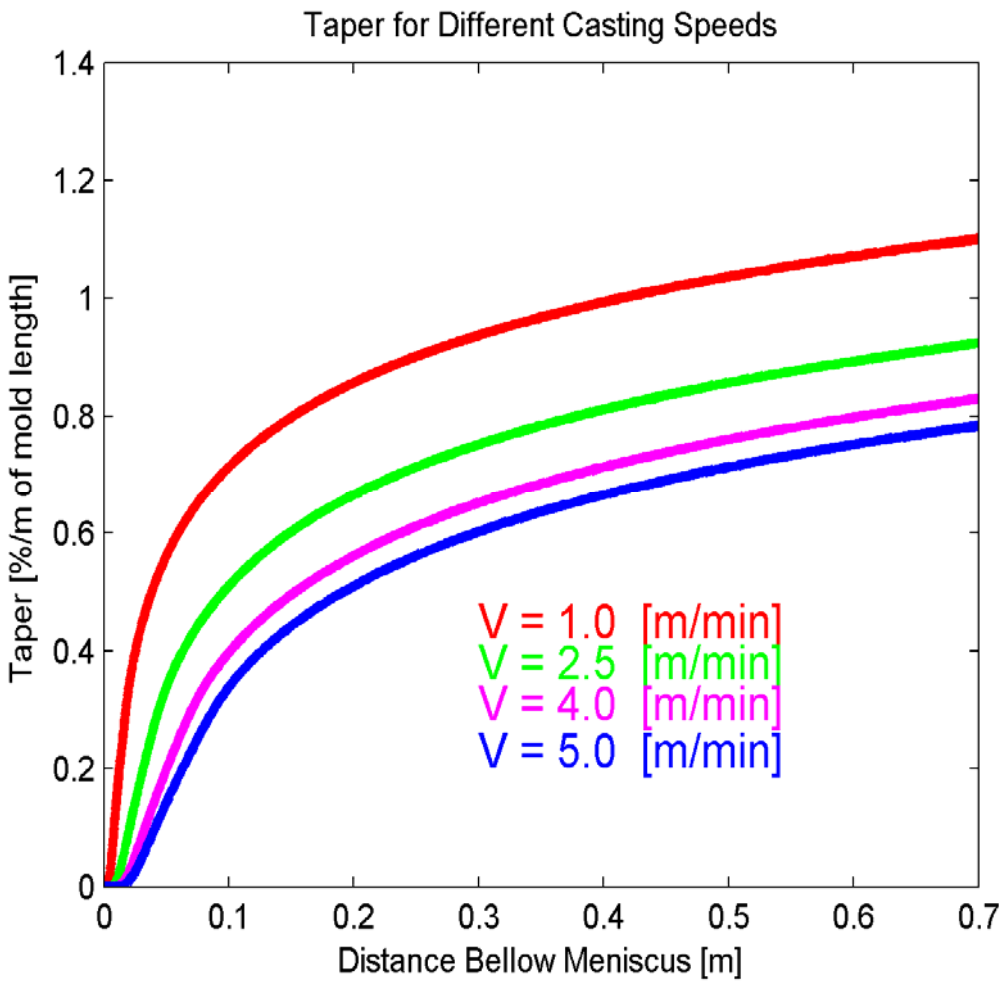

Figure 6.17 Ideal taper prediction for different casting speeds

Table 6.I Material constants

Density [kg/m^3]	7400.
Poisson's Ratio	0.3
Liquidus Temperature [^{o} C]	1411.79
Solidus Temperature [^{o} C]	1500.70
Initial Temperature [^{o} C]	1540.00
Latent Heat [J/kg K]	257,867
Reciprocal of Liquid viscosity [MPa^{-1}sec^{-1}]	1.5x10^8

Table 6.II CPU Benchmark results

CODE	**Global Method for Solving BVP**	**Local Integration Method**	**Treatment of Liq./Mushy zone**	**CPU time (Minutes)**
Abaqus	Full NR	Implicit followed by local Bounded NR	Liquid Function	55
Abaqus	Full NR	Implicit followed by Nemat-Nasser	Liquid Function	53
Abaqus	Full NR	Implicit followed by local Bounded NR	Radial Return	5.6
Abaqus	Full NR	Implicit followed by full NR (CREEP)	Radial Return or Liquid Function	Failed
Abaqus	Full NR	Explicit (CREEP)	Liquid Function	185
CON2D	Operator Splitting (Initial Strain)	Implicit followed by local Bounded NR	Liquid Function	6
CON2D	Operator Splitting (Initial Strain)	Implicit followed by Nemat-Nasser	Liquid Function	5.9

Chapter 7. Coupled Thermal Stress Analysis

Coupled thermal-stress analysis is needed when the stress analysis is dependant on the temperature distribution and the temperature distribution depends on the stress solution. Thermal stresses always depend directly on the temperature distribution obtained from transient heat transfer analysis through thermal strains (equations). The heat transfer model does not usually depend on the force equilibrium equation since the mechanical dissipation energy is negligible. If spatial and temporal distribution of thermal flux data leaving the shell is accurate, for example from plant measurements; than this fully uncoupled approach yields satisfactory results.

However, if thermal flux data is not available, then variable contact conditions exist between the strand and the mold where the heat is conducted between surfaces depends strongly on the distance separating the surfaces. Shrinkage of the shell will increase the thermal resistance across the gap and lead to hot and weak spots on the shell. This interdependence of the gap size and the thermal resistance requires coupling between the heat transfer and stress models solutions since as the gap is unknown in prior, the heat resistance in also unknown.

In this chapter, the UMAT is improved to enable thermo-mechanical coupling. The simple slice domain from chapter 6 is used one more time for qualitative validation of coupled results. The coupled thermo-mechanical model developed in this chapter along with Abaqus contact capabilities is than applied in the next two chapters to the two casting processes with thermo-mechanical coupling due to contact with the mold wall.

7.1 Modeling Thermo-Mechanical Coupling with Abaqus and UMAT

Abaqus provides two choices to conduct coupled thermo-stress analysis with its *COUPLED TEMPERATURE-DISPLACEMENT procedure, either fully coupled analysis, or incrementally coupled where each increment is solved for temperature distribution first and then for stress. The first approach was found to be insufficiently robust and expensive for our highly nonlinear solidification phenomena, so a second approach with incrementally coupled analysis was adopted and used throughout this work. Abaqus distinguished incremental coupled from the fully coupled analysis via the key words *SOLUTION TECHNIQUE, TYPE=SEPARATED.

Newton's Method is again used to solve the nonlinear system in the following matrix representation of the fully coupled equations in eq. (102).

$$\begin{bmatrix} \mathbf{k}_{uu} & \mathbf{k}_{uT} \\ \mathbf{k}_{Tu} & \mathbf{k}_{TT} \end{bmatrix} \begin{Bmatrix} \Delta\mathbf{u} \\ \Delta\mathbf{T} \end{Bmatrix} = \begin{Bmatrix} \mathbf{R}_u \\ \mathbf{R}_T \end{Bmatrix} \tag{102}$$

Where $\Delta\mathbf{u}$ and $\Delta\mathbf{T}$ are the respective corrections to the incremental displacements and temperature, $\mathbf{k}_{ij}$ are submatrices of the fully coupled global stiffness matrix, and $\mathbf{R}_u$ and $\mathbf{R}_T$ are the mechanical and thermal residual vectors respectively. Often solving this system requires a costly unsymmetric solver scheme which is additional factor of at least two [80].

In the case of incrementally coupled analysis, the off-diagonal components in submatrices $\mathbf{k}_{uT}$ and $\mathbf{k}_{Tu}$, are small compared to the components in the diagonal submatrices $\mathbf{k}_{TT}$ and $\mathbf{k}_{uu}$ so less costly solution may be obtained by setting the off-diagonal matrices to zero so that an approximate set of equations is obtained in equation (103):

$$\begin{bmatrix} \mathbf{k}_{uu} & \mathbf{0} \\ \mathbf{0} & \mathbf{k}_{TT} \end{bmatrix} \begin{Bmatrix} \Delta\mathbf{u} \\ \Delta\mathbf{T} \end{Bmatrix} = \begin{Bmatrix} \mathbf{R}_u \\ \mathbf{R}_T \end{Bmatrix} \tag{103}$$

Even though Abaqus still uses the coupled procedure with coupled elements and coupled dofs, as a result of this approximation, the thermal and mechanical equations can be solved with significantly less CPU time using the symmetric solver for each increment. This is similar to the step-wise coupling in CON2D [3,4,8] where thermal and mechanical equations are solved separately for each increment (step).

Abaqus provides a rich library of 2D and 3D coupled temperature-displacement elements. Besides having coupled procedure and coupled elements, all other mechanical and thermal boundary and initial conditions as well as temperature dependant material properties from previous separate transient heat transfer and quasi-static input decks need to be merged. An existing user subroutine UMAT needs to be reconfigured for coupled analysis, and a new user subroutine called GAPCON needs to be coded to define the conductance between the mold and shell contact surfaces.

Along with mechanical consistent tangent operator (CTO) described in sections 3.6 and 4.3, the CTO with respect to temperature needs to be derived accurately to provide a fast convergence for coupled analysis, even when increment-wise coupling is used. Taking (46) and (47), Lush [62] in his work has represented the equation (44) as:

$$\sigma_{ij}^{t+\Delta t} = \sigma_{ij}^{*t+\Delta t} - \sqrt{6}\,\mu\,\Delta t\, f(T^{t+\Delta t}, \bar{\sigma}^{t+\Delta t}, \bar{\varepsilon}_{ie}^{t+\Delta t}, \%C)\frac{\sqrt{3}}{\sqrt{2}}\frac{\sigma_{ij}^{*'t+\Delta t}}{\bar{\sigma}^{*t+\Delta t}} \tag{104}$$

This is a convenient form for deriving CTO with respect to temperature. The above equation is differentiated with respect to temperature in (105)

$$\frac{\partial \sigma_{ij}^{t+\Delta t}}{\partial T^{t+\Delta t}} = -3\mu\,\Delta t \frac{\sigma_{ij}^{*'t+\Delta t}}{\bar{\sigma}^{*t+\Delta t}} \frac{\partial f}{\partial T} \tag{105}$$

Due to the complex nature of equation (96), the term $\partial f / \partial T$ is found by forward finite difference in (106).

$$\frac{\partial f}{\partial T} = \frac{f^{t+\Delta t} - f^{t}}{T^{t+\Delta t} - T^{t}} \tag{106}$$

A separate Abaqus subroutine GAPCON [1] is coded adapting the calculations from CON2D [3,4,5,6] which models heat transfer across the interfacial gap governing the heat flux leaving the steel to enter the mold. The GAPCON fortran code is given in the Appendix.

The Abaqus main code is providing GAPCON with a calculated gap – a separation distance between surfaces in contact for each contact node at every increment. The thin layer of mold powder film, which is used as a lubricant to alleviate friction between mold and strand, is present in the gap. The heat transfer resistor model from Fig. 7.1, consisting of a radiation and four conduction terms, is used to calculate total interfacial heat transfer coefficient h_T.

$$h_T = \frac{1}{R_T} + h_{rad} \tag{107}$$

Radiation heat transfer coefficient h_{rad} is calculated from equation (108)

$$h_{rad} = \frac{5.67*10^{-8}}{\frac{1}{\varepsilon_m}+\frac{1}{\varepsilon_s}-1}\left(T_{shell}+T_{mold}\right)\left(T_{shell}^2+T_{mold}^2\right) \tag{108}$$

Where $\varepsilon_m = \varepsilon_s = 0.8$ are emissivities of the mold and shell surface, and T_{shell} and T_{mold} are their current temperatures. The conduction resistor, R_T, given in equations (107) and (108) consists of four terms. The first term, 1/ h_{mold}, is the contact resistance between mold wall surface and the powder film. The contact heat transfer coefficient h_{mold} ranges between 2500 W/m^2 and 7500 W/m^2 [49,42]. The second resistance, d_{air}/k_{air}, is conduction through the air gap whose conduction is k_{air}=0.06 W/mK, and the thickness of air gap, d_{air}, is determined by mechanical contact analysis[49]. The third resistance, d_{pow}/ k_{pow}, is conduction through the powder film with a thermal conductivity, k_{pow}=1 W/mK. Calculations of powder film thickness, d_{pow}, are adapted from a CON1D model [7] as a function of the distance bellow the meniscus. The final term, 1/ h_{shell}, is the contact resistance between powder film and the strand, where shell contact heat transfer h_{shell} coefficient depends greatly on temperature, due to large change in viscosity of the powder film over the temperature range of strand surface [49]. The temperature dependency of h_{shell} is given in table 7.I.

$$R_T = \frac{1}{h_{mold}} + \frac{d_{air}}{k_{air}} + \frac{d_{pow}}{k_{pow}} + \frac{1}{h_{shell}} \tag{109}$$

Finally the heat flux across the interfacial gap flux between the mold wall and steel surface is calculated from Eq. (110)

$$q''_{gap} = -h_T \left(T_{shell} - T_{mold} \right) \tag{110}$$

where minus sign is given since heat is leaving shell surface.

7.2 Abaqus Coupled Model Verification

Since the solidifying slice model from chapters 5 and 6 has a very well defined thermal flux boundary data and has no contact modeled, the uncoupled approach works well for it. Also this model has been rigorously validated against analytical and CON2D results.

Because this model represents the center of the shell, which contacts the mold at all times, contact does not need to be modeled. This model thus can serve as an excellent starting validation model for Abaqus coupled heat transfer and stress analysis that works in conjunction with extended UMAT accommodating coupling. The 2D models of wedge and beam blank that follow in next chapters depend greatly on contact with the mold wall, however, so have contact features added to the coupled models.

Instead of 2 separate input decks, one for transient heat transfer and one for stress, a single input deck is present which calculates temperature and mechanical (displacement, strain, and stress) results for every time increment. Coupled and uncoupled temperature and stress results are plotted for 2 times along the solidifying slice on figures 7.2 and 7.3.

As expected the results are virtually identical, a clear sign that the extended UMAT works properly along with Abaqus increment-wise coupling.

Total CPU time for the coupled analysis was larger than that for the combined uncoupled heat transfer and stress analysis. It took ~40 minutes to complete the coupled model on IBM p690 versus 25 minutes for heat transfer followed by 3 minutes for stress analysis on the same computing platform.

The 2D coupled models of wedge and beam blank that follow in the next chapters will have many more dofs along with contact features enabled that will largely increase the numerical complexity of these calculations, and further emphasize the need for large modern parallel computing platforms.

7.3 Figure and Tables

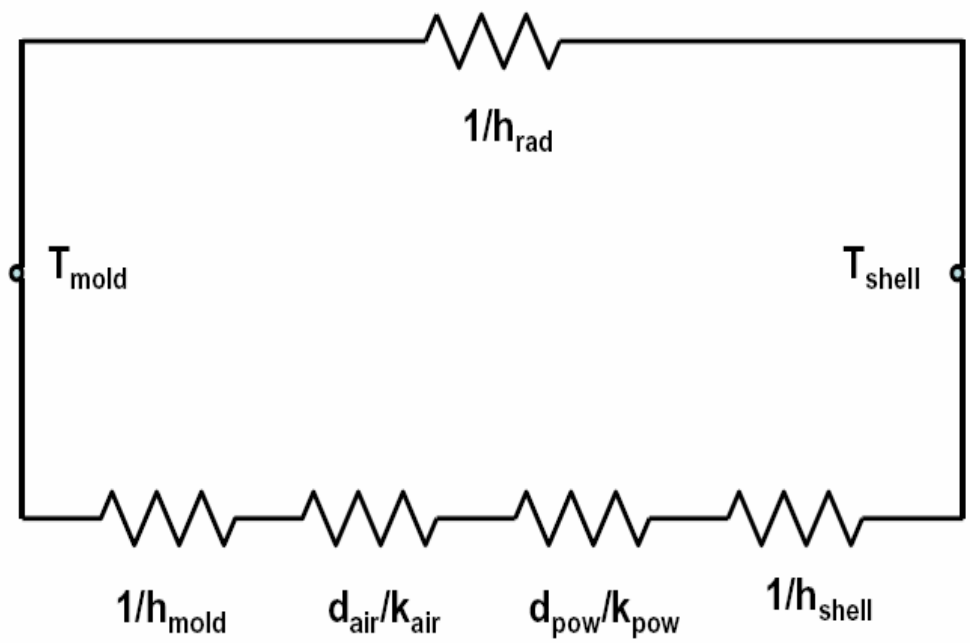

Figure 7.1 Heat resistor model

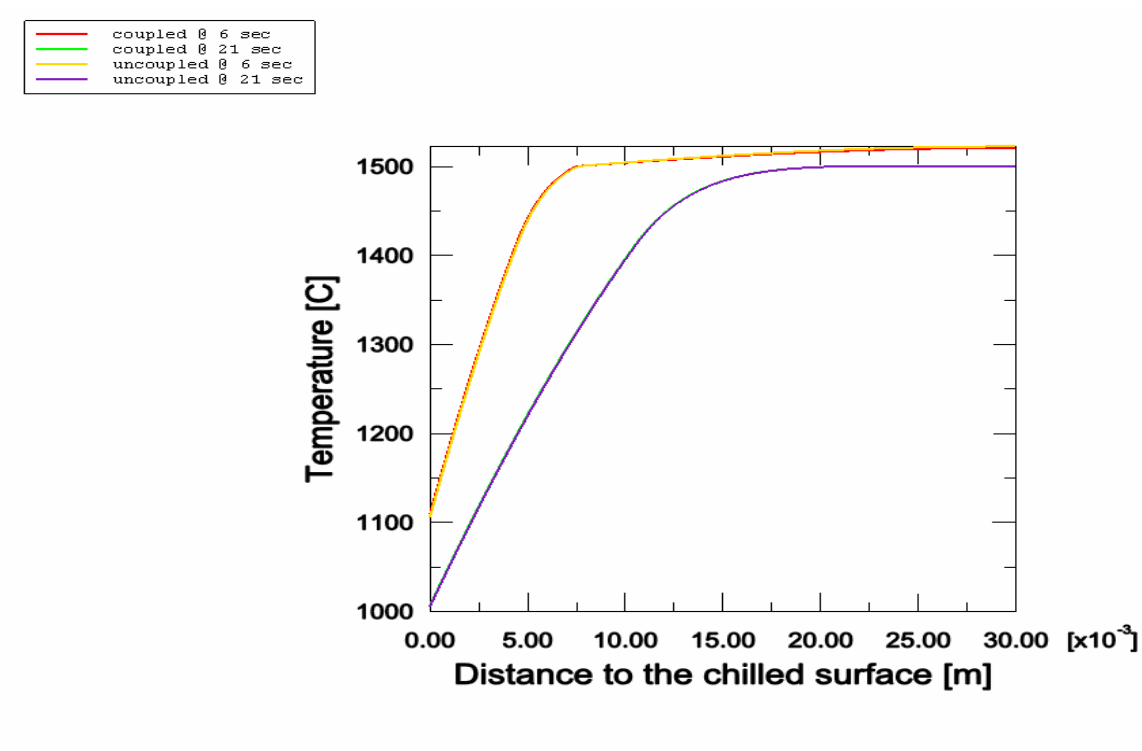

Figure 7.2 Abaqus coupled and uncoupled temperature slice distributions

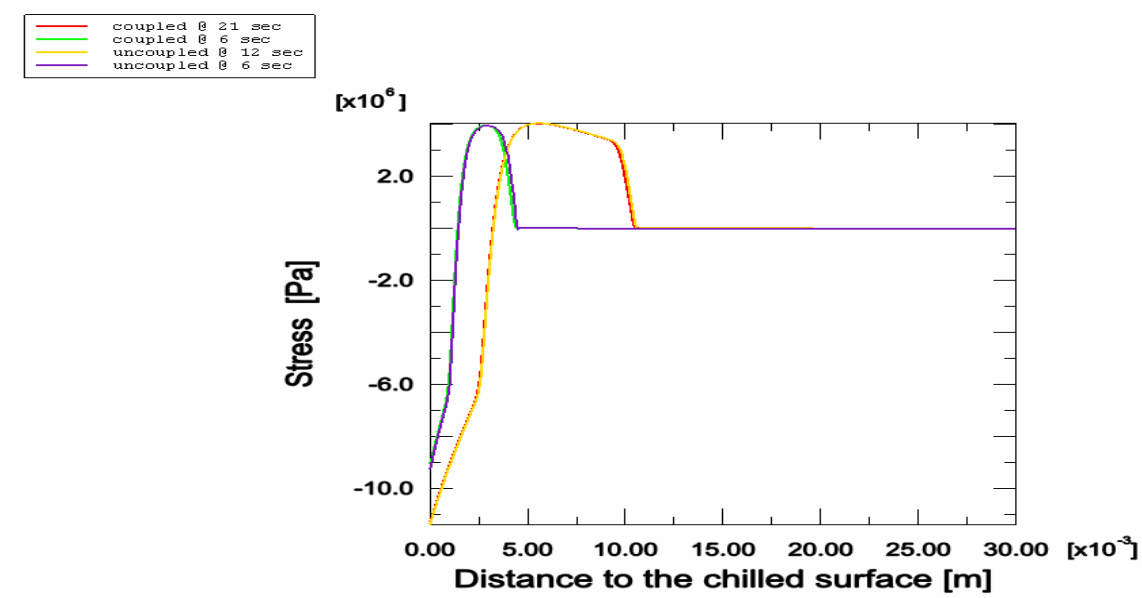

Figure 7.3 Abaqus Coupled and Uncoupled Stress Slice Distributions

Table 7.I Temperature dependence of h_{shell} [49]

Temperature, °C	**h_{shell}, W/m^{2}K**
1030	1000
1150	2000
1511	10,000
1530	20,000

Chapter 8. 2D Model Validation: Billet Continuous Casting

In previous study [3,8], a transient, thermal-elastic-visco-plastic finite element code, has been developed to follow the thermal and mechanical behavior of a section of the solidifying steel shell, as it moves down the mold at the casting speed. It is applied here to simulate temperature, stress, strain and deformation in a 2D section of a continuous casting billet for the same conditions used in the previous simulation in the mold. Having CON2D temperature and stress contour results available from this work yields a great opportunity to quantitatively verify our new coupled Abaqus model along with its contact features by modeling this real world complex 2D phenomenon.

8.1 CON2D Model of Billet Continuous Casting

The modeling domain for CON2D is a L-shaped region in one quarter of a transverse 120 mm square section from continuous casting steel billet assuming symmetrical temperature and stress distributions about the billet center lines, as shown in Figures 8.1 and 8.2. Generalized plane strain condition from the section 4.4 is enforced in the casting (Z) direction.

While the heat transfer and mechanical FE implementations in CON2D are briefly explained in the sections 3.2 and 3.6, the details about its step-wise coupling and its simple but efficient contact algorithm can be found somewhere else [8]. CON2D has a special internal boundary condition algorithm which tracks the position of the solidifying front and applies the ferrostatic pressure to newly solidified material points as an internal load that pushes the shell toward the mold wall. The ferrostatic pressure, F_p, is calculated by equation (111).

$$F_p = \rho g z \tag{111}$$

Where ρ is density, g=9.81m/s^2 gravitation acceleration, and z is a current distance below the meniscus, which can be easily calculated from a current time bellow meniscus and casting velocity.

The mold taper has the task to partly compensate for the shell shrinkage yielding good contact between strand shell and copper wall. By describing the displacements of the mold contact surface, the mold taper is taken into account. This displacement for linear taper, d_{taper}, can be calculated as:

$$d_{taper} = \frac{(\%taper/m)}{100} \frac{W}{2} v_c \; t_{mold} \tag{112}$$

where W, vc, and t_{mold} are the mold width, casting speed, and the time that domain spends in the mold or the time below the meniscus while (%taper/m) is the percentage of taper per meter of mold length.

The strand material for both models in this chapter is a mild carbon steel 0.27% C, with the identical temperature-dependant mechanical and thermal properties along with the Kozlowski III constitutive model from previous chapters. The initial temperature of the strand is 1540 C, while the initial temperature of the mold is 150 C.

8.2 Abaqus Model of Billet Continuous Casting

Instead of L-Shape used with CON2D, a 1/8 of a transverse 120 mm section (or ½ of L-Shape) from continuous casting steel billet is modeled with Abaqus, a domain so called a wedge, given in Fig. 8.3. Similarly to L-shape the steel is not modeled/simulated over the entire area, since only a small part will solidify. A boundary condition of a symmetry line of an L-Shape represents no movement allowed normal to the symmetry line. This is imposed by using Abaqus *Equation option [1] to enter linear multi-point constrains in the form of an equation to all nodes belonging to the symmetry line. A linear multi-point constraint requires that u_1 and u_2 displacement components be equal for all symmetry line nodes, or in terms of *Equation definition, that a linear combination of nodal displacement components is equal to zero, ie:

$$u_1^{symm\_node\_set} = u_2^{symm\_node\_set} \quad \text{or} \quad u_1^{symm\_node\_set} - u_2^{symm\_node\_set} = 0 \qquad (113)$$

The copper mold is represented with a much coarser mesh with linear elastic material properties. The temperature history of the mold hot and cold surfaces are taken from the previous work [8] in Fig 8.4. Since the goal of this analysis is to validate the mechanical and thermal behavior of the 2-D solidifying shell, the temperature history of the mold hot surface was imposed to all mold domain nodes.

Each potential mechanical contact in Abaqus is defined in terms of a “slave” and master surfaces. The nodes from a slave surface are constrained not to penetrate into the master surface; however the nodes of the master surface can, in principle, penetrate into the slave surface, Fig 8.5. Generally, the master surface should be chosen as the surface of the stiffer body or as the

surface with the coarser mesh. The clear choice in this case is that the master surface should be mold and the slave surface is strand. The default hard contact in Abaqus is defined when separated surface come in contact when the clearance between them reduces to zero and any contact pressure can be transmitted. The surfaces separate if the contact pressure reduces to zero Fig. 8.6 In this simulation, the slave (strand) surface is very soft (it is in liquid state) in the beginning and Abaqus is recommending its softened contact instead, Fig 8.7, which indeed turned out to be a much more robust and efficient. The key word in Abaqus for softened contact is *SURFACE BEHAVIOR, PRESSURE-OVERCLOSURE=EXPONENTIAL. The softened contact pressure-overclosure relationship has an exponential form defined by two parameters c_0 and p_0. In this relationship the surface begin to transmit contact pressure once the clearance between them reduces to c_0. The contact pressure transmitted between the surfaces then increases exponentially as the clearance continues to diminish. Contact pressure at zero clearance is p_0. Abaqus is recommending a small fraction of a typical slave element size for c_0 and typical pressure value transmitted for p_0, so $c_0=10^{-5}$ and $p_0=10^5$ values are adopted in this work. In addition to softened contact, automatic contact stabilization is added which adds a very small amount of viscous damping to contact nodes and helps eliminating a rigid body motion, which is present in early times of simulation before the contact is fully established.

The friction between surfaces in contact is modeled by using the Abaqus native Coulomb friction model. The strand and mold contacting surfaces can carry shear stress up to a certain magnitude across their interface before they start sliding relative to one another; this state is know as sticking. The Coulomb friction model defines this critical shear stress τ_{crit}, at which sliding of the surfaces starts as a fraction of the contact pressure p_{cont}, between the surfaces as given in the equation (114).

$$\tau_{crit} = \mu_{frict} p_{cont} \tag{114}$$

The fraction μ_{frict} is known as the coefficient of friction and a relatively small value of 0.1 is chosen in all 2D and 3D models in this work since friction between contacting strand and mold surfaces is alleviated by the powder film. In case of higher than 0.2 friction coefficient, the ansymmetric solver algorithm is necessary which is at least twice as much more cpu expensive than the default symmetric solver. Friction is not modeled in the CON2D code.

The thermal contact interactions are modeled by means of an external subroutine GAPCON, whose features as well as thermal properties specific to continuous casting are explained in the chapter 7.

Ferrostatic pressure is applied through the use of another external user subroutine DLOAD. It is a simple linear function of the distance bellow the meniscus Eq. (111), which is in turn is a linear function of time with given casting velocity. Applying ferrostatic pressure to the outer liquid free surface did not work and generated all kinds of convergence problems. This is understandable since liquid elements have a very small stiffness with elastic-perfectly plastic constitutive law with very low yield stress and an application of external load directly on them have produced large uncontrolled motions. Since there is no easy way in Abaqus to apply ferrostatic pressure to newly solidified material points, it is found, with trail and error, that delayed application of DLOAD to the third row (counting from the contact surface) of completely solidified elements worked fine. It was found that delayed time to allow 3 rows of elements to solidify was ~2 sec.

Mold surface (wall) position that incorporates taper of 0.75%/m and a mold thermal distortion is available among CON2D results, Fig 8.8, and is being curve fitted in a user subroutine DISP and enforced for all Abaqus mold contact surface nodes.

The pre-processing with FE mesh generation is originally performed with MSC Patran 2001 [111]. Abaqus native CAE 5.5 [1] pre-processor is also tested later. While Patran pre-processing capabilities are very well known for years and generally applicable to many other FE software, Abaqus/CAE is a relatively new tool created for Abaqus software only. Abaqus/CAE seems to be slightly easier to use, and produced less convergence troubles with Abaqus main software (solvers). The FE mesh consist of 7686 coupled generalized plane strain hybrid elements with 15986 nodes for the total of 31,000 dofs. The element size for strand domain varies from 0.15 mm close to the contact surface to 0.4 mm at the free liquid surface. The mold has much coarser mesh. The hybrid element implementation is recommended for excessive plastic straining [80], and indeed has created much less convergence problems in the "volatile" perfectly-plastic liquid/mushy zone. The downside of hybrid elements is that they have an extra pressure dof per element, which means more cpu time for each global solution iteration.

The whole simulation was run for 21 sec bellow meniscus, which corresponds to a 0.87 m long mold with given the casting speed of 2.5 m/min. It took Abaqus 6.5-5 threaded direct solver between 20 and 25 hours to complete a 21 sec simulation on NCSA Intel linux Xeon cluster with 3.2 Ghz. In average it took Abaqus global NR method 4 iterations to achieve global convergence, though there were periods when even 12 iterations were exceeded in some critical early periods and Abaqus has to cut back on the increment size. The increment sizes varied from 10^{-4} sec. to 0.01 sec. towards the end of the simulation.

C Li at al. [8] is reporting 24 hours cpu time with CON2D and L-shape on his 1GHz PC with similar number of nodes and elements, but CON2D approach, which avoids equilibrium iterations on a global level, instead can be prone to some stress oscillations [50].

8.3 2D Billet Results and Comments

Figure 8.9 shows the deformed mesh at the Mold Exit for the ABAQUS simulation. The shell moves away from the mold most at the corner area, which is an area with the lowest temperatures where the effect of shrinkage due to thermal contraction is strongest. The lower part, far away from the corner, stays in touch with the mold. Temperature contours from Abaqus and CON2D are given on Fig. 8.10 and 8.11 respectively. Temperature drops toward the corner due to the 2D heat transfer effect in this region. A very good quantitative match up between temperature contour lines can be observed, though codes are using slightly different contour line values. Unfortunately there are currently no capabilities in Abaqus postprocessor to enforce specific values for contour lines, and Abaqus/CAE is rather choosing them arbitrary based on number of contour intervals and maximum and minimum values.

The stress contours at mold exit are given on Fig. 8.12 and 8.13. C Li al at with CON2D [8] reports “hoop stress” contours, which consist of stress in x direction within the horizontal portion of the domain and the y direction stress within the vertical portion. In the single region of the Abaqus domain, the hoop stress is simply the y direction stress. Considering that two codes are using different contact and coupling algorithms and that the stress results are even more burdened with different stress values and colors, a closer look reveals that the prominent tensile and compressive stress areas are situated in approximately the same places. The lowest values of

hoop stress of -8 MPa are found at the shell contact area bellow the corner where the “cold” part of the solidified shell is compressed due to the faster surface shrinkage. The large island of tensile stress whose peak reaches ~ 4 MPa is found on both contours at the warmest part of newly solidified shell which is under tensile conditions. This agrees with the analytical and numerical stress solutions from previous chapters where surface shell compression and sub-surface shell tension close to solidification front are revealed. There are strong spikes of both tensile and compressive stresses reported by Abaqus and concentrated to the small peak-corner area zoomed in the Fig 8.14. It is likely that these extreme stress values are produced by some numerical error as similar spikes of stress are observed in CON2D. Considering that CON2D results are often validated against plant measurements and experiments [8, 3 9], and given such a reasonable match up of temperature and stress results between the codes; it is clear that Abaqus with UMAT can be used relatively easily in future as another tool to accurately investigate many other 2D solidification applications that require coupling like: longitudinal and transversal crack formation with appropriate failure mechanisms, parameters studies of different casting speeds and tapers, bulging bellow mold, effect of geometry of mold and its design, and many other phenomena under a wide variety of casting geometries. One such coupled thermo-mechanical analysis of a challenging beam blank casting geometry is performed in the next chapter.

8.4 Figures and Tables

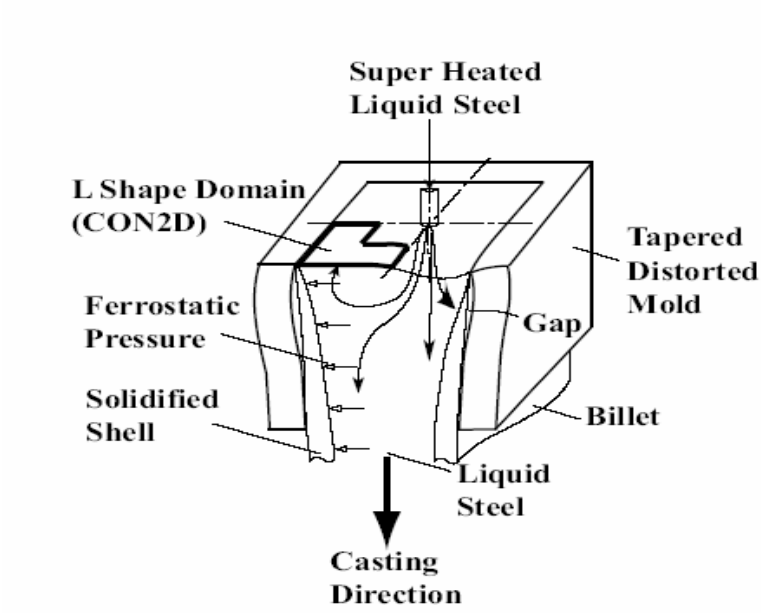

Figure 8.1 Schematic of the CON2D modeling domain [8]

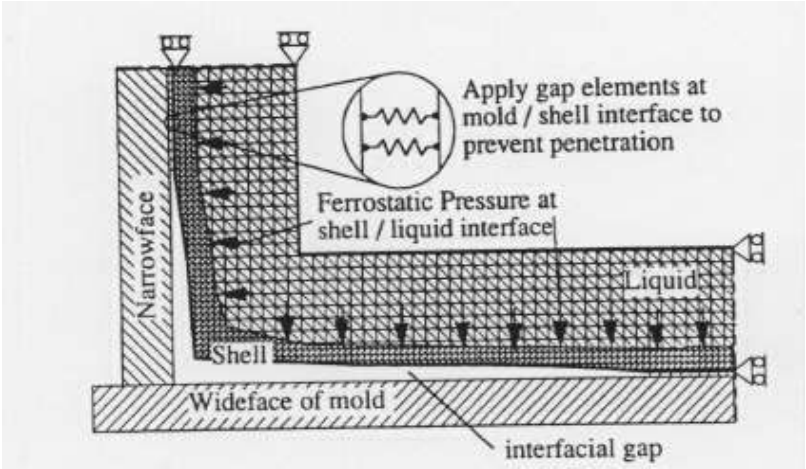

Figure 8.2 CON2D FE domain [3]

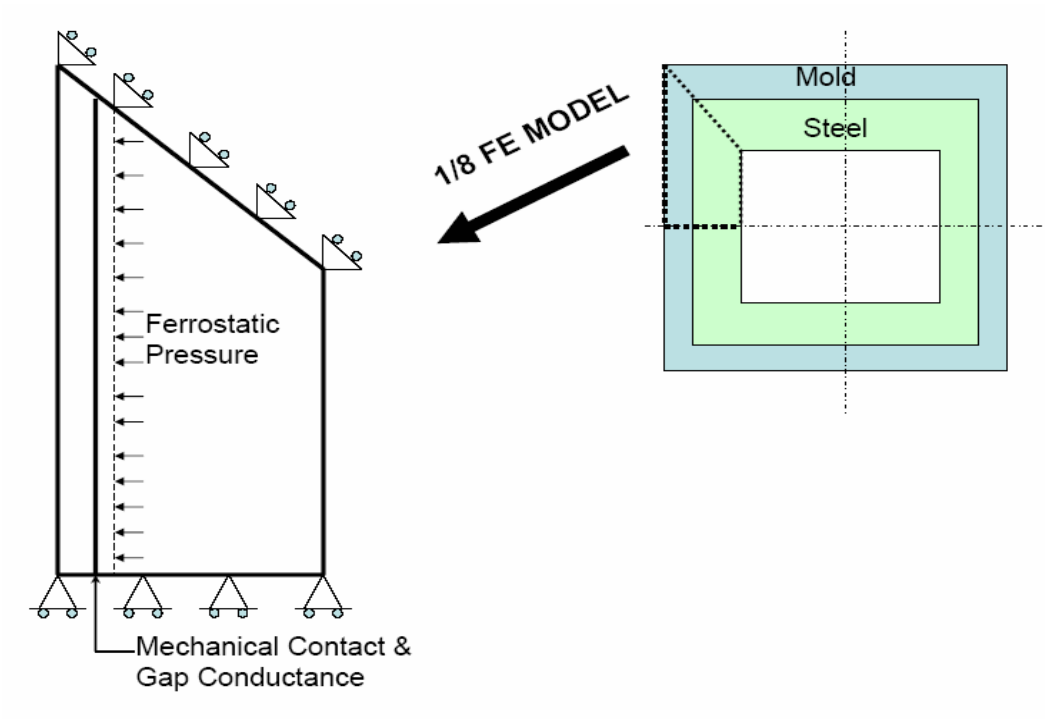

Figure 8.3 Abaqus modeling domain

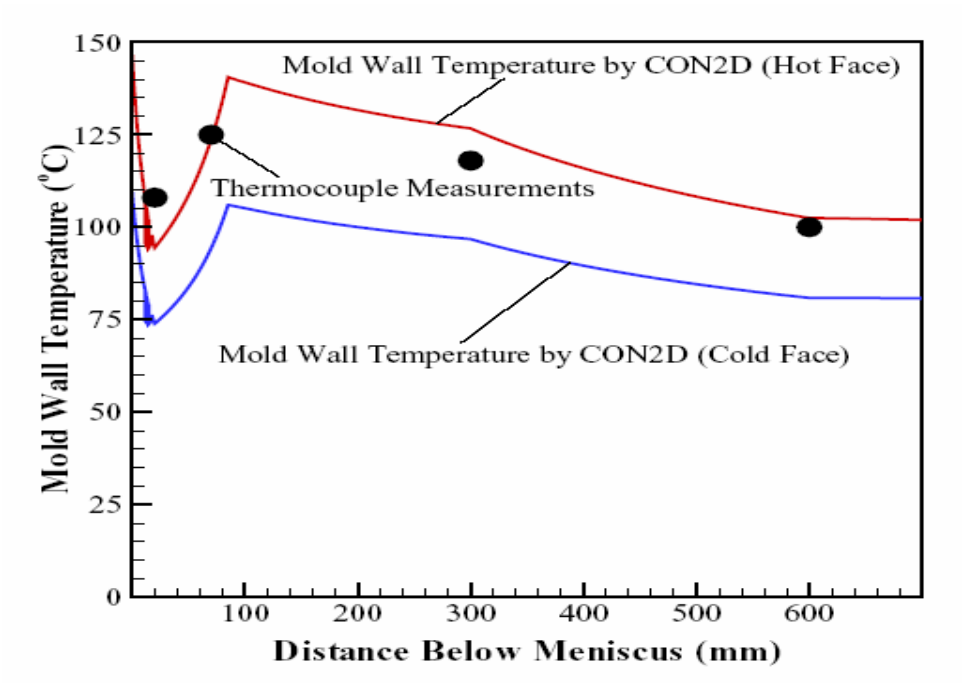

Figure 8.4 Mold wall temperature profiles from plant measurements [8], hot face temperature profile is imposed on the mold part of Abaqus model.

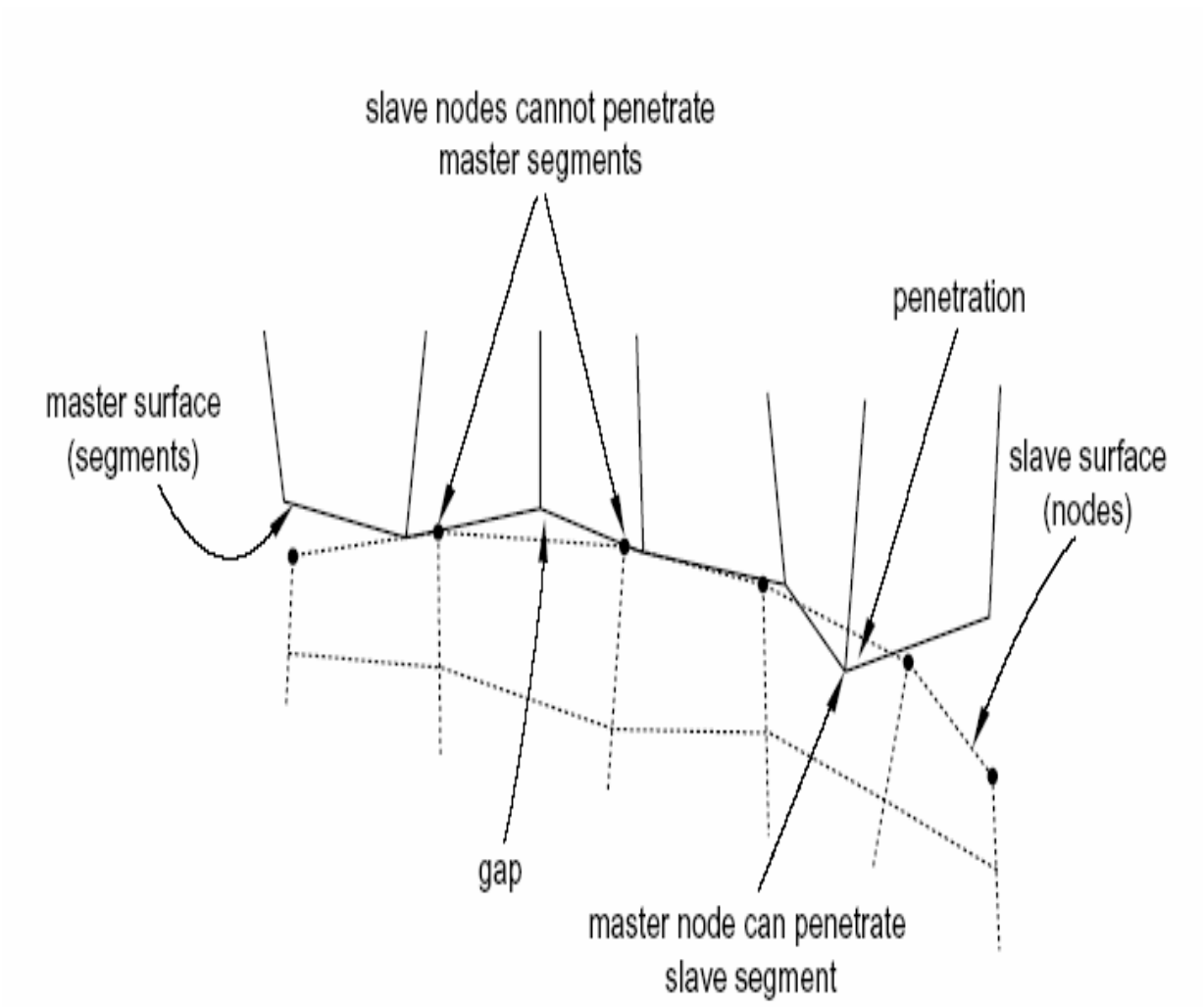

Figure 8.5 Abaqus slave-master contact definitions [1]

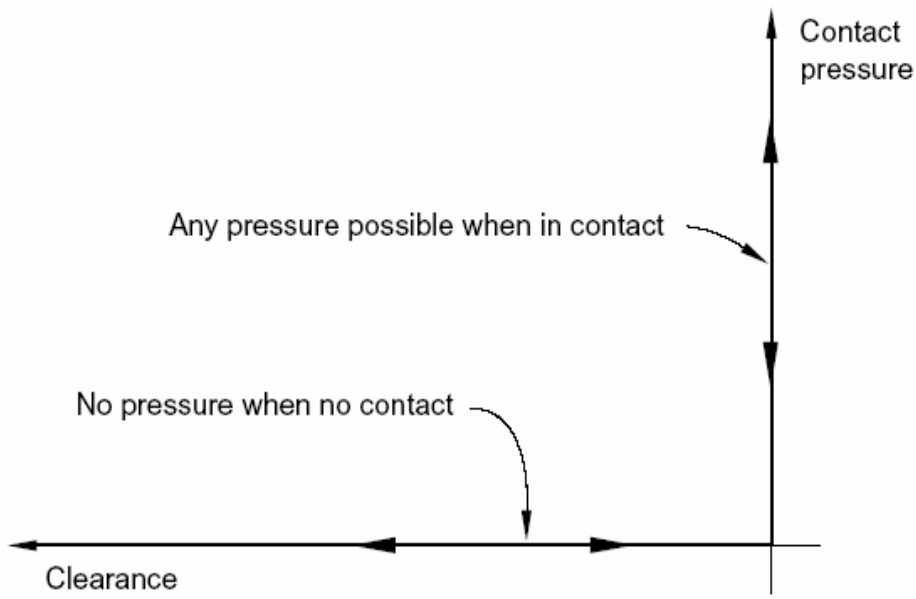

Fig. 8.6 Default (hard) contact in Abaqus [1]

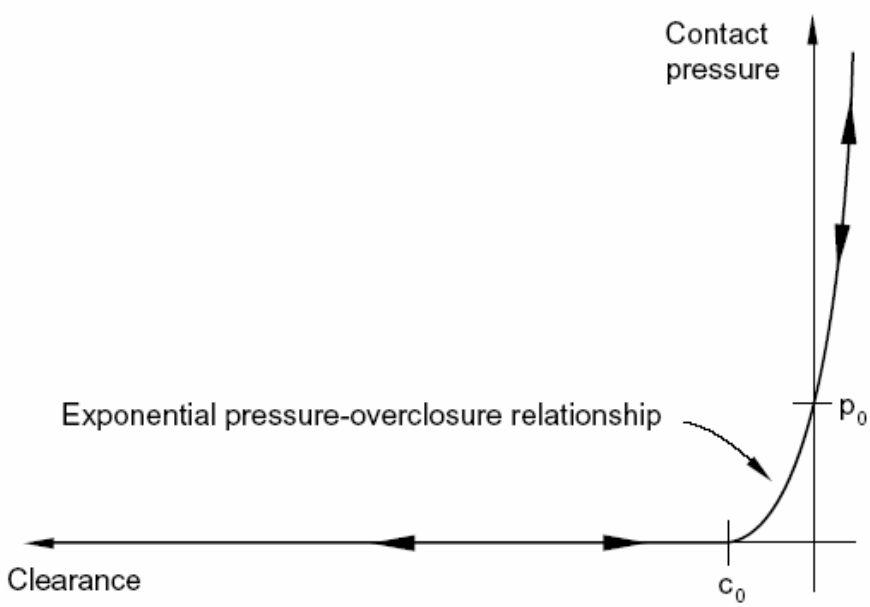

Fig. 8.7. Softened exponential contact in Abaqus [1]

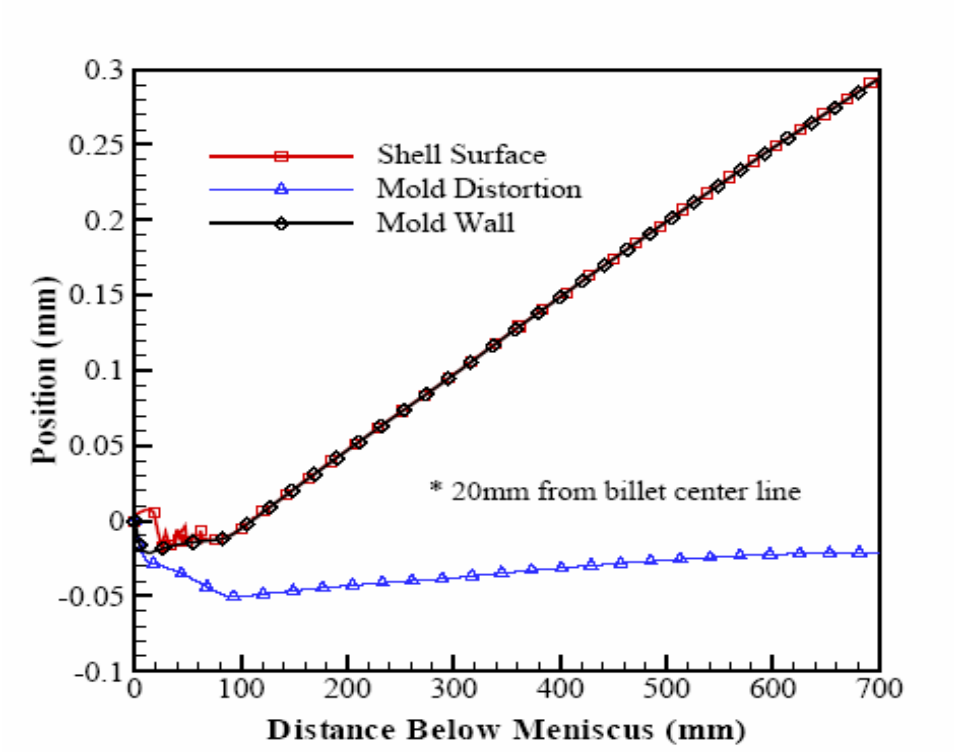

Fig. 8.8 Mold wall and shell surface position – CON2D result data [8], mold wall data is imposed on all Abaqus mold contact nodes to enforce 0.75%/m taper

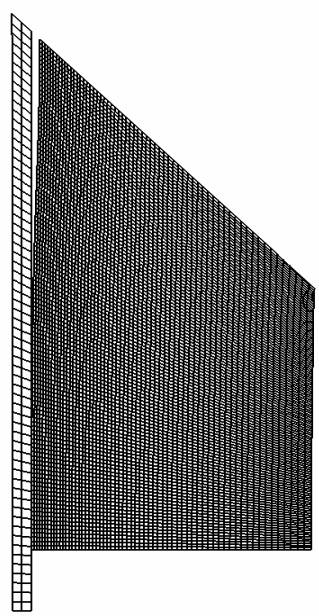

Fig 8.9 Abaqus deformed shape at mold exit

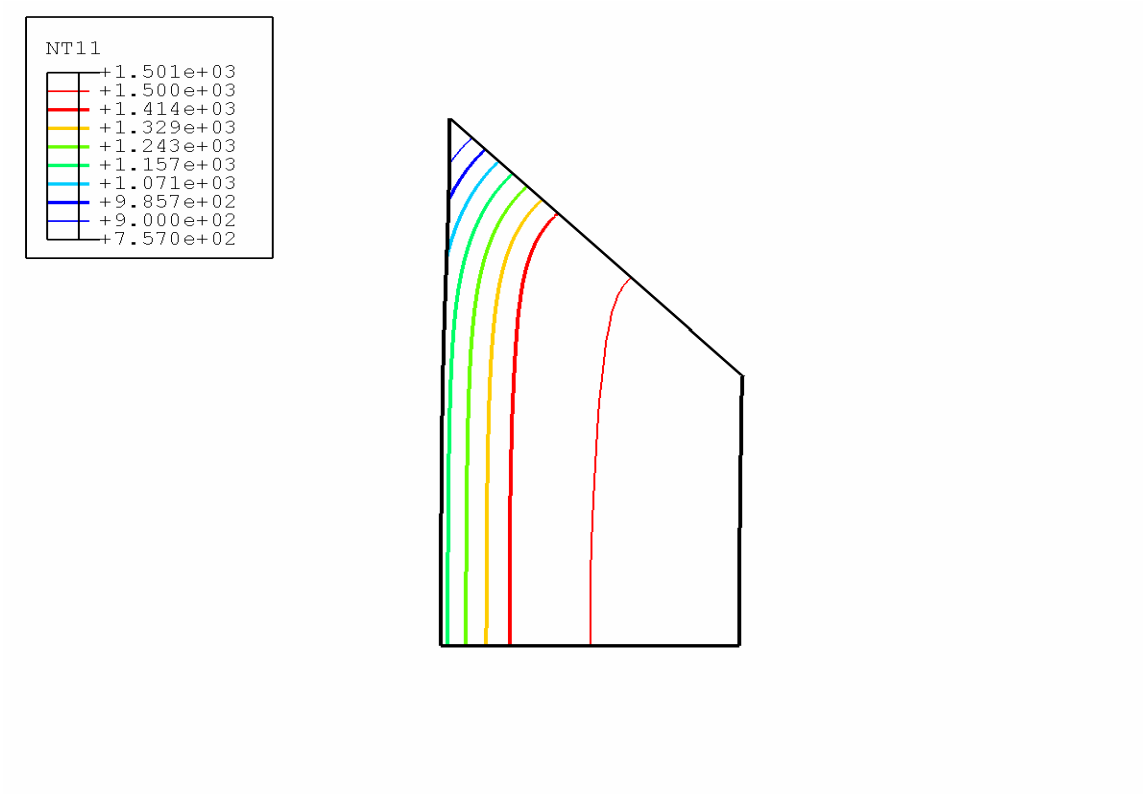

Fig. 8.10 Abaqus temperature contour results at mold exit

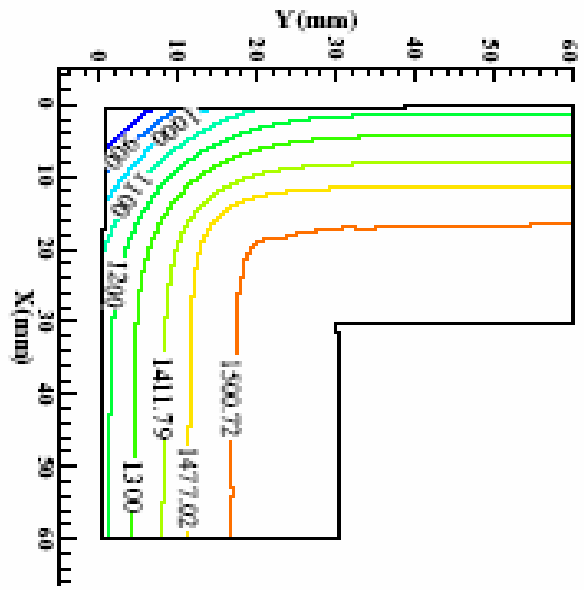

Fig. 8.11 CON2D temperature contour results at mold exit [8]

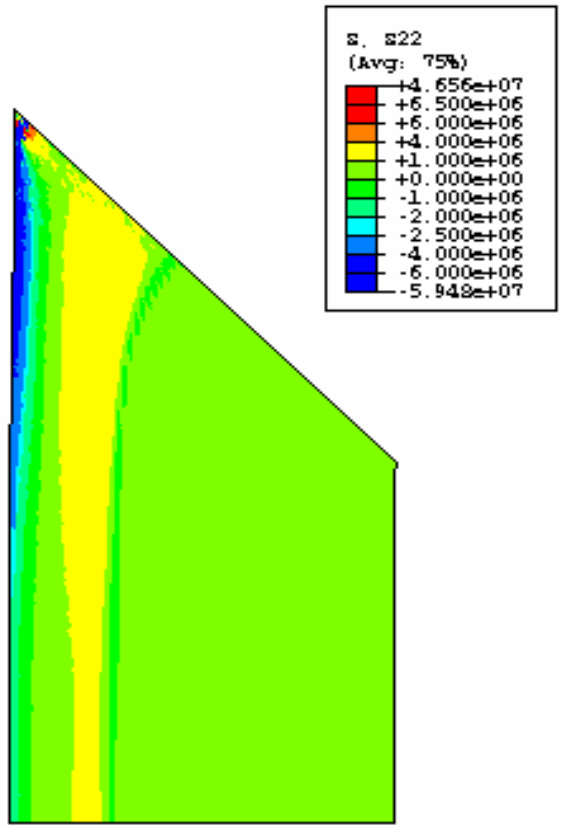

Fig. 8.12 Abaqus stress contour results at mold exit

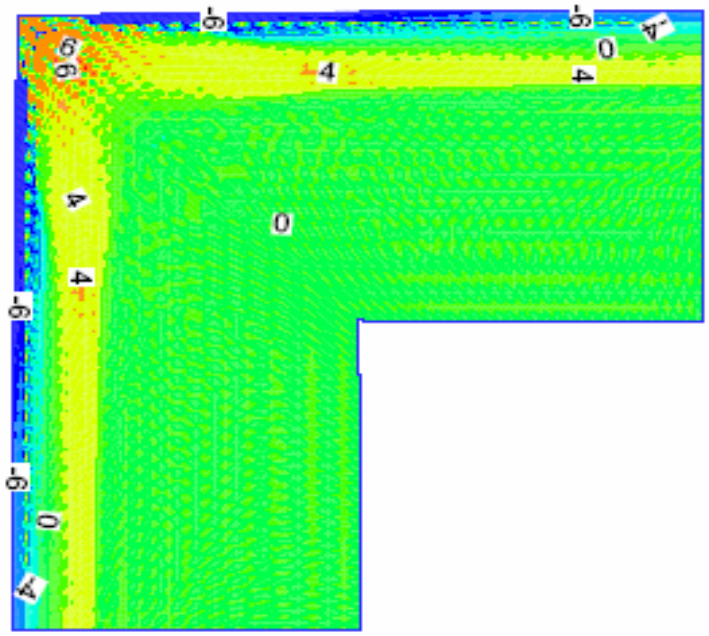

Fig. 8.13 CON2D stress contour results at mold exit [8]

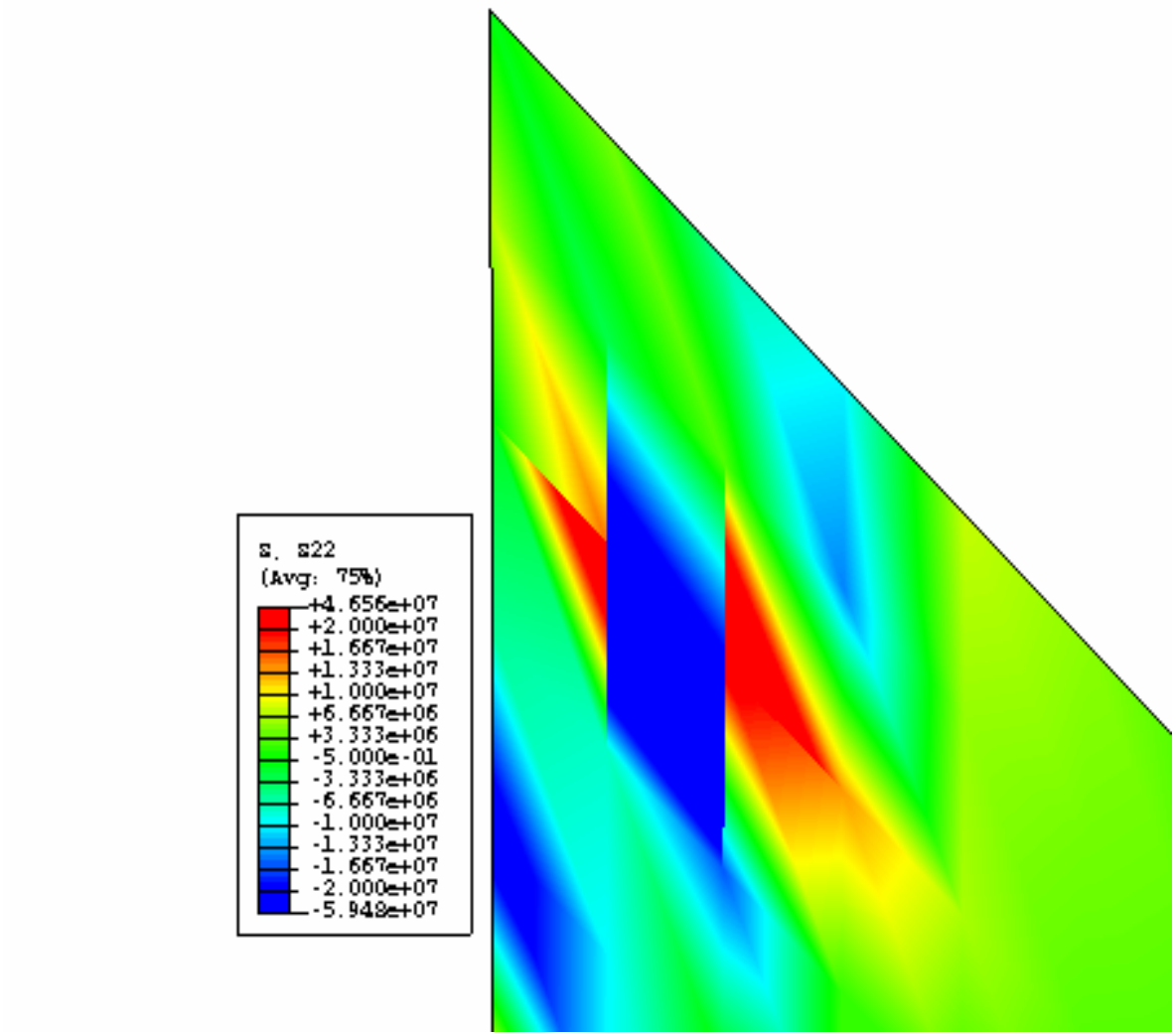

Fig. 8.14 Abaqus stress results zoomed at corner.

Table 8.I The billet simulation conditions

Casting strand [mm]	120 x 120
Working Mold length [mm]	870
Taper (wrt to W=90mm) [%/m]	0.75
Softened Contact Coefficients: c_0 and p_0	10^{-5}, 10^{5}
Mold Contact Resistance Heat Coefficient [W/m^2/K]	7500
Friction Coefficient Mold/Shell	0.1
Casting speed [m/min]	2.5
Steel grade [%C]	0.27
Initial temperature strand [C]	1540
Initial temperature mold [C]	150
Liquidus temperature [C]	1500.7
Solidus temperature [C]	1411.79
Time to apply ferrost. press. [sec.]	2.4
Number of elements	7686
Number of nodes	15968
Total number of dofs	31860

Chapter 9. Thermo-Mechanical Model of Beam Blank Casting

Beam blank casting is used in production of H and U beams as an alternative to conventional blooms. Economic advantages of beam blank casting are mainly due to lower rolling costs coming for its specific net shape where less mill rolling is necessary to achieve desired finished cross section. Beam blank casting has also higher productivity are requires less energy than billet casting. In recent years, the process has been optimized through careful integration of electro-mechanical sensors, computer-control, and production planning to provide a highly-automated system designed for optimal productivity [112,113]. The caster has to be directly coupled to the rolling mill in order to gain the most benefits. The beam blank caster has a complex geometry, called a "dog-bone" type. All failure mechanisms mentioned in Chapter 1 are present in beam blank casting, but its complex shape produces additional difficulty in numerical modeling. Consequently there are only a few numerical models of beam blank casting solidification reported [18,112]. Since Abaqus pre processing capabilities can effectively mesh this complex geometry while UMAT is providing accurate and efficient integration of viscoplastic laws, the Abaqus coupled thermo-mechanical model from Chapter 4 is a good tool for beam blank solidification modeling. Complex interactions between mold and solidifying shell will be again handled by the Abaqus mechanical and thermal contact capabilities.

9.1 Finite Element Model

Figure 9.1 shows a schematic of a cross section of the beam blank caster normal to the casting direction. The dimensions of the beam blank caster modeled in this work are 555mm (mold

width) by 420mm (flange thickness) by 90 mm, which is the thickness of the middle (narrow web) section of the mold. These values were taken at the height of the meniscus in the mold. The real mold has cooling channels at the outer edge of the mold. The generalized plane strain finite element domain used is this work is referred to here as a "snake" shape. It encompasses ¼ of the section with a slice of a simplified mold wall (neglecting the internal water slots) and the corresponding "stripe" of the strand adjacent to the mold wall, that is wide enough to allow solidification of expected shell thickens everywhere. This avoids expensive computation in the large, uninteresting liquid domain and contributes to significant savings in cpu time and also to the robustness of the model. It is similar to the cuts in liquid domain which are performed on the ¼ of the billet cross section in the last chapter yielding the L-Shape and Wedge-Shape models. This style of domain has the further advantage of allowing enlargement of the internal liquid domain (which would in reality become filled with new liquid metal), that would not be possible in a full domain.

The Kozlowski III model from Chapter 3 is used again as a constitutive law for a mild carbon steel grade 0.27C % whose temperature dependant thermo-mechanical material properties are listed in previous chapters. Copper is used as a mold material. All thermal and contact properties defined in section 7.1 with h_{mold}=3000 W/m^{2}K are enforced through the GAPCON subroutine along with softened mechanical contact coefficients $c_0=5*10^{-5}$ and $p_0=10^5$ from Fig. 8.7, and friction with the coefficient of friction set to 0.1. The FE domain with symmetric mechanical BC-s is given on a figure 9.2. Details of water channels are not modeled. Instead, the outer surface of the domain is tangential to the circular water channels, as shown in Fig. 9.1 The average convection coefficient of h=30,000 W/m^{2}K transferring the heat from this surface to the cooling water with 30 C. The structured mesh has 7500, 4-node generalized plane hybrid

elements with average size of 1 mm in strand, and 5 mm in mold. The total number of dofs counting Lagrangian multipliers for contact and extra pressure dof/element due to hybrid implementation is over 34,000.

By describing the displacements of the mold contact surface with respect to the time bellow meniscus, the mold taper of 1%/m is taken into account according to the equation (112) with respect to W=90 mm, which is the mold thickness in the middle (narrow) section of the beam mold. The casting speed v_c is 0.6 m/min. Thus, the angle of the slanted mold wall is constant. Since heat transfer through the mold is calculated in this model, the thermal distortion of the copper mold is also calculated.

The linearly increasing negative distributed load for the ferrostatic pressure Eq. (111) is applied to the contact shell surface starting at zero time. The negative sign is chosen to model the direction of ferrostatic pressure, which pushes the shell towards the mold. This approach is different than the one used by con2d and abaqus in chapter 8 where positive pressure pushes the "inner" side of the third row of solidified elements, with a delayed application time of 2.4 sec. Here, it rather pulls the shell towards the mold and produces less convergence problems and enables application of ferrostatic pressure at early times. The casting velocity is 0.6 m/min and therefore the time that the domain spends in the 0.45 m long mold is ~45 sec. It took Abaqus ~ 37 hours to finish this 45-sec simulation on NCSA's Intel Xeon linux cluster with 3.2 Ghz .

9.2 Results and Comments

The deformation (magnified three times) is given in Figure 9.3 for the whole domain at the mold exit, and it is zoomed to the flange region in Figure 9.4. Due to its geometry, the 2D heat transfer

effects are present in the flange region and the molten steel solidifies initially there faster, shrinking away from the mold wall and creating the gap. As the gap grows the heat extraction from the mold is more resisted by the gap thermal resistance elaborated in the chapter 7, eventually producing the retardation of the shell grow in the middle of the flange region. This can be seen at the temperature contour for the strand domain at the mold exit given in Fig. 9.5 where the middle of the flange surface shell area is mostly warmer then the rest of the shell surface which stays longer in touch with the mold. The exceptions are surfaces of the flange corners which are still colder due to the strong presence of the 2D conduction effects there, even with the increased heat resistance and the drop in the heat extraction from the mold. This is especially case for the "sharp" right flange corner which remains the coldest point of the shell domain.

The stress contour in y direction is the hoop stress for the narrow face and approximately for the vertical steep part of the wide face given in Fig. 9.6. It reveals expected compressive shell behavior at the "cold" surface and tensile stress in the warmer interior of the shell. Similar results were obtained for the horizontal sections of the domain whose hoop stress is in the x direction in Fig 9.7. These maximum hoop stress results can be used to predict the crack occurrence [42, 8].

Four points of interest, marked A,B,C,D (Fig. 9.2), on the shell surface were chosen for the history data. Point A is in the middle of the wide face (on the vertical symmetry plane BC), point B is in the middle of flange fillet, point C is at the left flange tip corner, and point D is at the right flange tip corner. The temperature history is given in Fig. 9.8 for these four points. The thermal flux that leaves the shell surface for these four points is given in figure 9.9. The gap evolution, which represents the air gap thickness between contact surfaces for these points, is given in figure 9.10. Points A and B stay in touch with the mold most of the time, and their flux

and temperature histories are fairly uniform without large jumps. Point C shrinks away at the fastest rate from the mold, facing rapidly increasing gap heat resistance, and having a sharp drop in the thermal flux between 4-6 sec. so that even the overheating can be observed at these times for this point. Point D at the very corner of the flange has a sharpest temperature drop at early times due to the 2D corner conduction effect. However, it stays closer to the narrow face of the mold during its shrinking and its gap is significantly smaller than for the point C resulting in a higher heat flux extraction than for the point C after 6 sec bellow the meniscus. This combined with the 2D corner cooling effect makes the point D the "coldest" point in the strand domain.

Figure 9.11 has the shell thickness evaluation history for the above four points along with the surface point in the middle of the flange, equally far away from the corners. As expected the coldest point D has the thickest shell. While the left corner flange point C has slightly thinner shell than the points A and B at early times due to the sudden shrinkage, later its shell thickness exceeds the thickness of points A and B due to the 2D corner effect. The middle flange point also shrinks away from the mold, but it is far away to feel any corner effect, and it stays warmest and therefore its shell thickness is the thinnest.

Figures 9.12 through 9.17 have temperature and hoop stress histories for points A, B, and the mid flange point at times 20 and 45 sec. They are similar to the realistic slice case profiles from Fig. 6.9 and 6.10 with compression on the surface and tensile stress close to solidifying front, except perhaps for the mid. flange point that has a very little compressive stress on the chilled surface due to the retarded shrinkage there.

Figure 9.18 shows a contour plot of equivalent inelastic strain at mold exit zoomed at the flange area. A corner point (D) and a subsurface, off-corner point, 16.7 mm from the corner, known for a strong alternating tensile/compressive inelastic strain history, are chosen and indicated in Fig.

9.18 Inelastic strain and temperature time histories for the corner point are given in Figures 9.19 and 9.20. The off-corner point inelastic strain history is given in Fig. 9.21, and its temperature history is given in Fig. 9.22. At 28.1s, the temperature is 1440 C, which corresponds with 0.03 value for inelastic strain, and experiences a sharp drop in inelastic strain to -0.03. From the temperature history graphs, the times when these material points are 90% or 1420.68 C, and 99% slid or 1411.7 C are 0.32 sec. and 0.349 sec. for the point D , and 29.63 sec. and 30.63 sec for the off-corner point.. These values are then used to read the inelastic strains corresponding to 90% and 99% solid from the Figures 9.19 and 9.21. Total inelastic strain minus the inelastic strain at 90% solid , represents the inelastic strain in the solid, and is included in Figs. 9.19 and 9.20. For the corner point, the inelastic strain for 90% solid is $6.37*10^{-4}$, and for 99% solid the value was $6.50*10^{-4}$, and inelastic strain in the solid is even smaller. For the off-corner point, the inelastic strain for 90% solid is -0.02970, and for 99% solid is -0.02971, and increases with time. The "damage strain" is the strain accumulated between 90% and 99% solid, and represents the most brittle material state during freezing, when liquid is still present, but when the dendrites are thick and preventing the surrounding liquid from compensating the strains from thermal stress, of solidification shrinkage. This measure of damage can be calculated for these material points from this data and compared with the empirical critical value to predict hot tearing. The results here indicate a damage strain of $-1.*10^{-3}$% at the off-corner point and $+1.3*10^{-3}$% at the corner, which are both very small and unlikely to hot tear. Details of this failure criterion can be found elsewhere [8].

This simulation provides the following insights into the continuous casting process for beam blanks:

- The coupled thermo-mechanical model developed in this work is capable of evaluating the simultaneous development of temperature, stress, strain and deformation in a 2D section of a continuous casting beam blanks with complex geometry.
- At the flange area, the taper of 1%/m wrt. to 90 mm thickness is insufficient to prevent a large interfacial gap from forming.
- The middle of the flange remains the warmest point in the domain at mold exit and has thinnest shell, while the neighboring right flange corner, point D, is the coldest point with the thickest shell. This highly uneven shell development concentrated in this small area of flange might cause quality problems, such as shell failures at this location. This agrees with reported experimental observations in the beam blank cast strand [18].
- Hoop stress results are showing expected compression on the surface and tension close to the solidifying front, as observed in the previous solidifying slice simulations.
- The inelastic strain in the mushy zone, accumulated over the critical time between 90% and 99% solid, can be extracted from these results and used with the proper fracture criteria to predict hot-tear cracks.

9.3 Figures and Tables

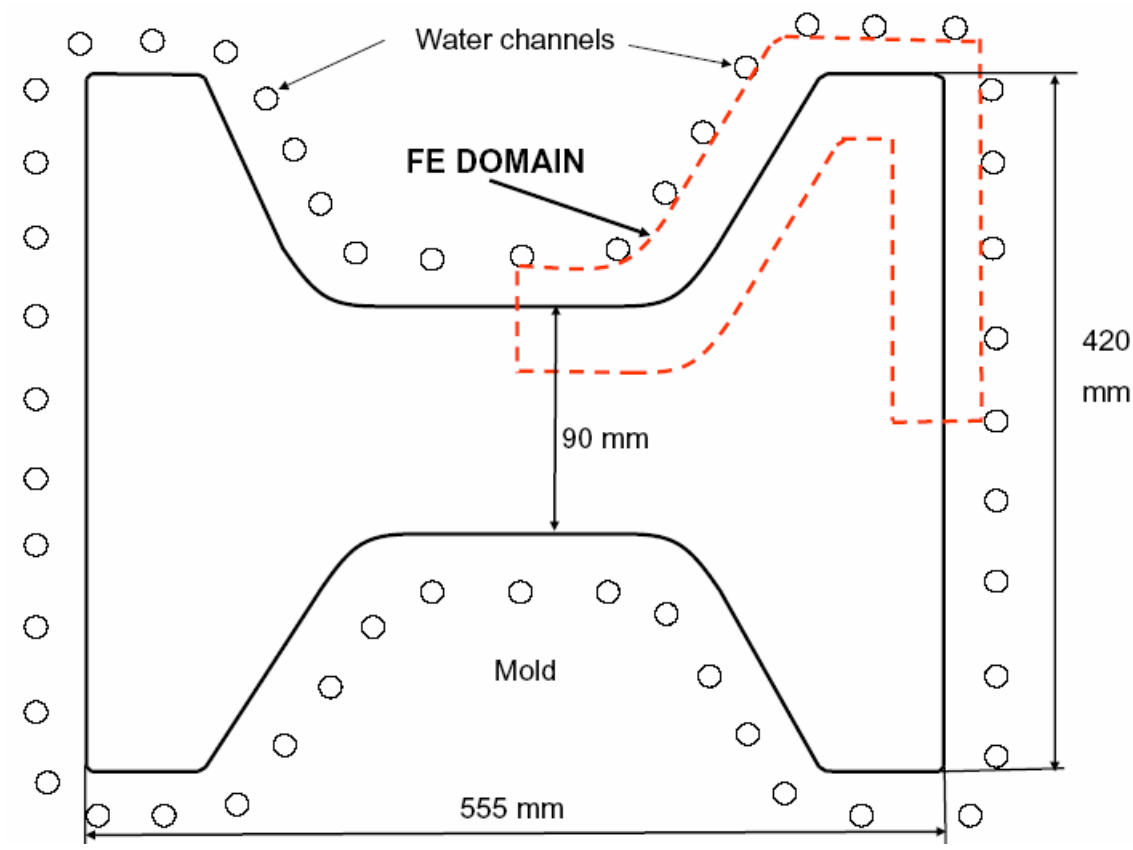

Figure 9.1 Schematic of a cross section of a beam blank caster with FE domain

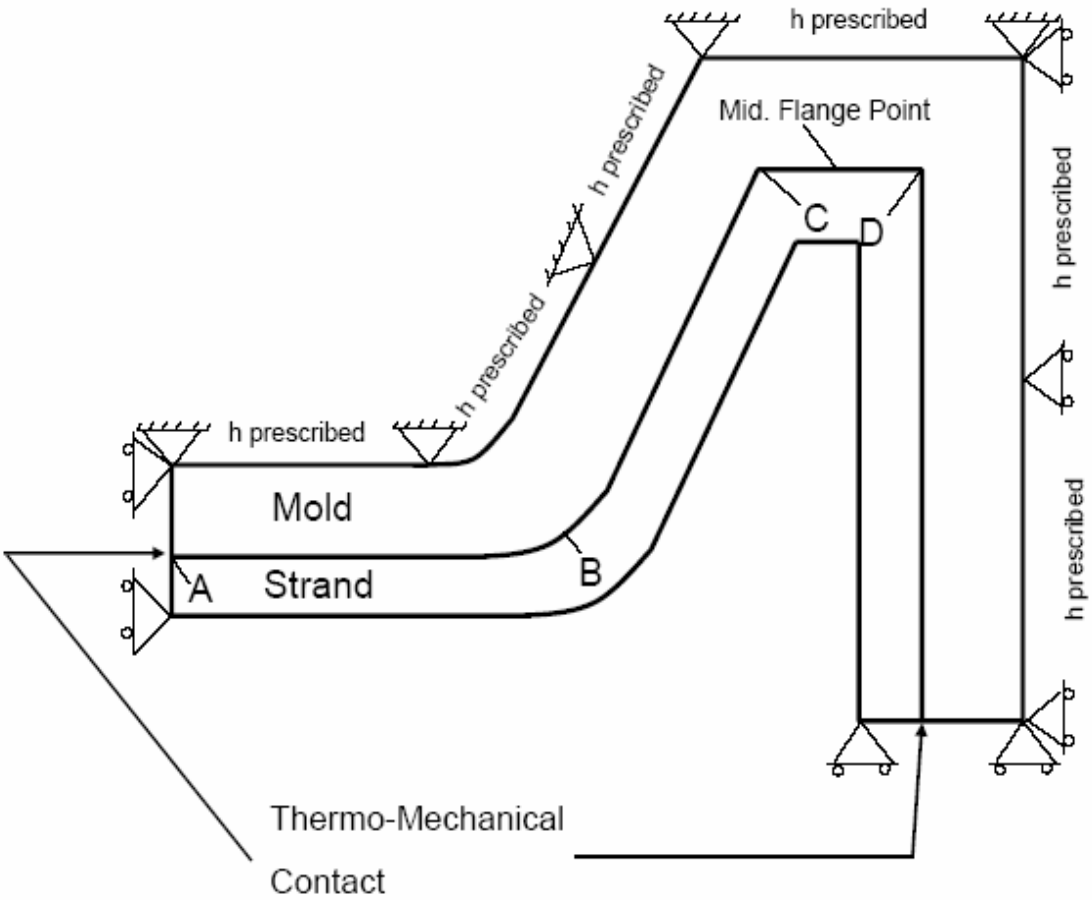

Fig 9.2 Thermo mechanical boundary condition applied to snake FE domain

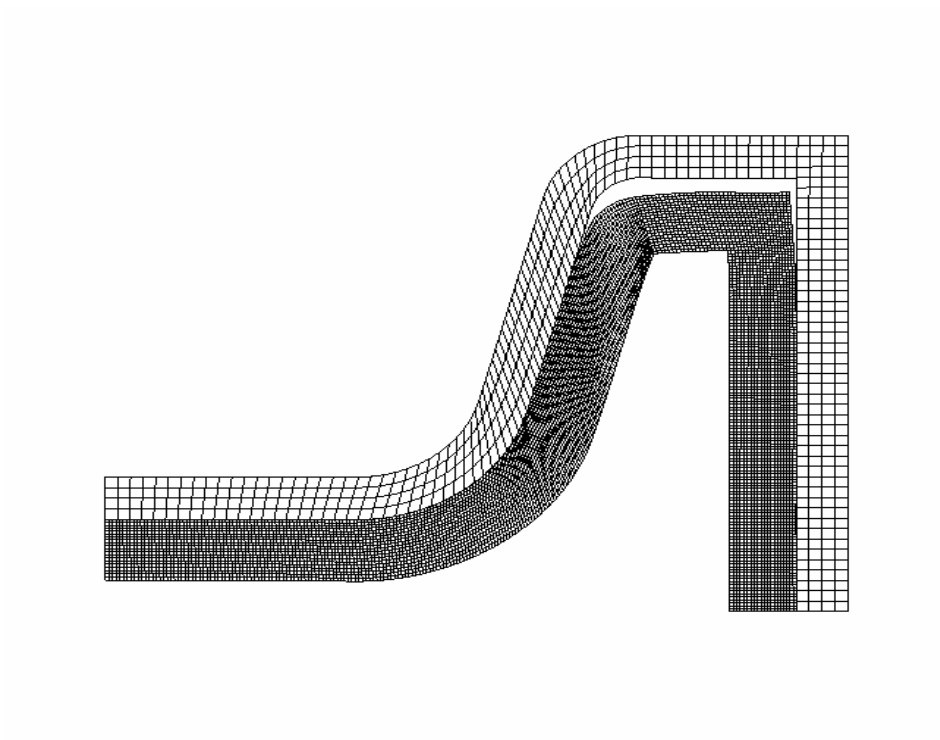

Fig 9.3 Deformation at the mold exit-whole domain (magnified 3 times)

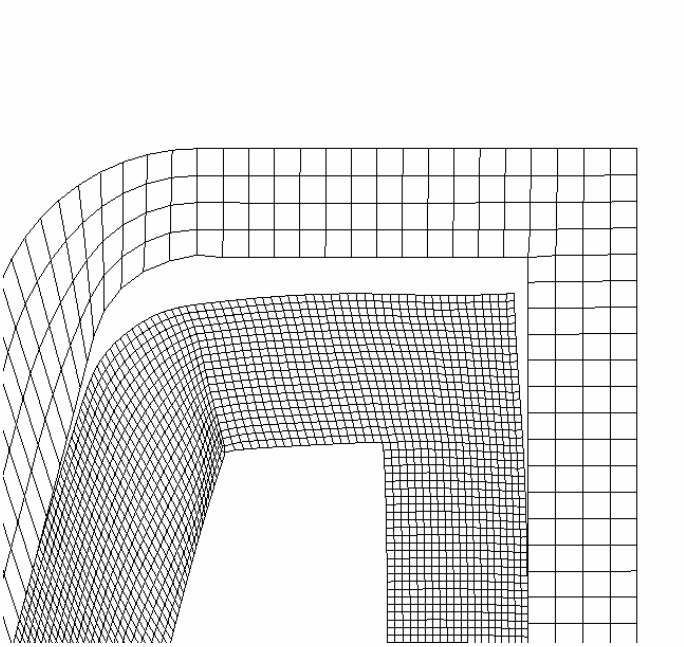

Fig 9.4 Deformation detail- Flange area (magnified 3 times)

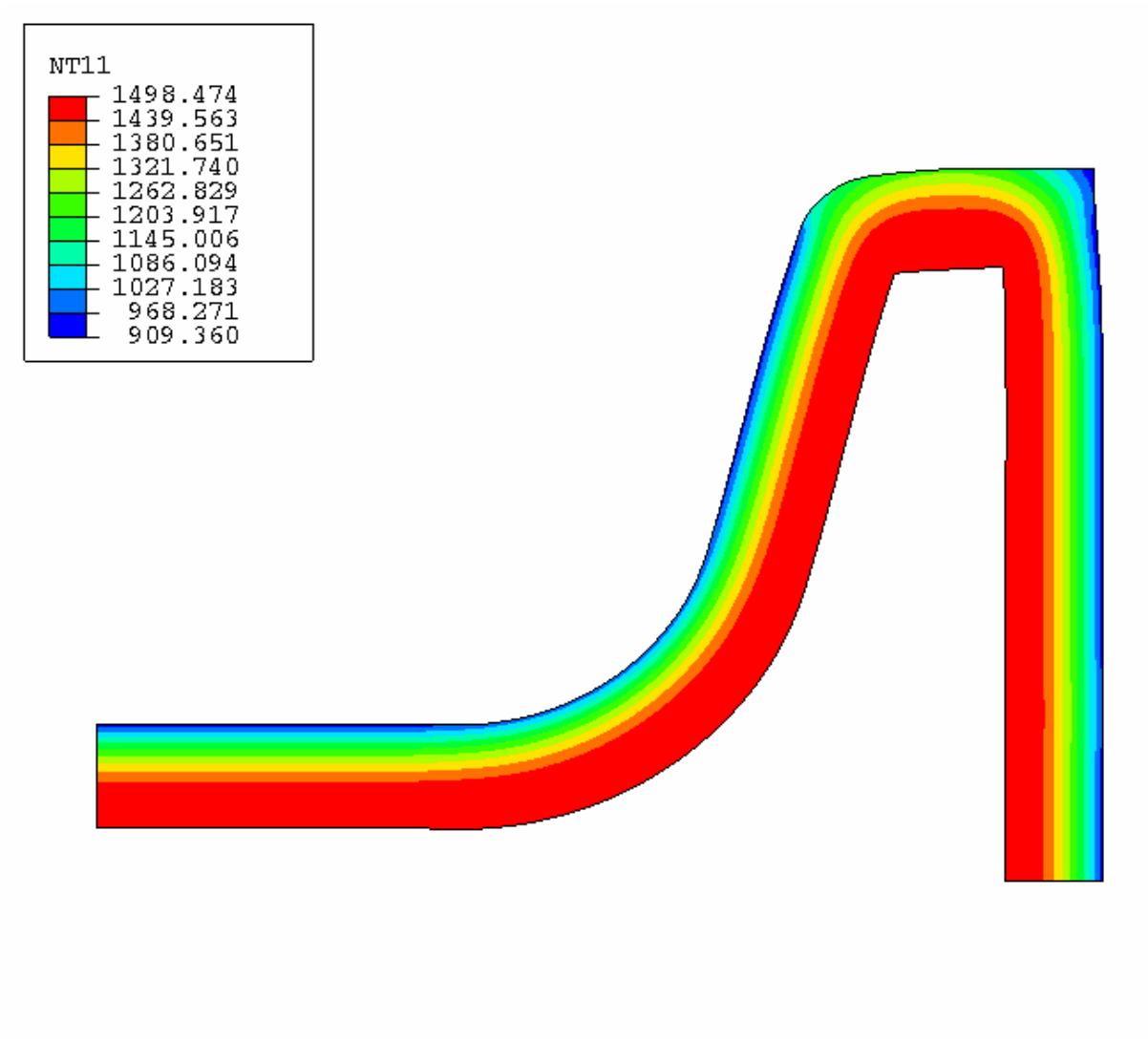

Fig. 9.5 Strand temperature contour at the mold exit

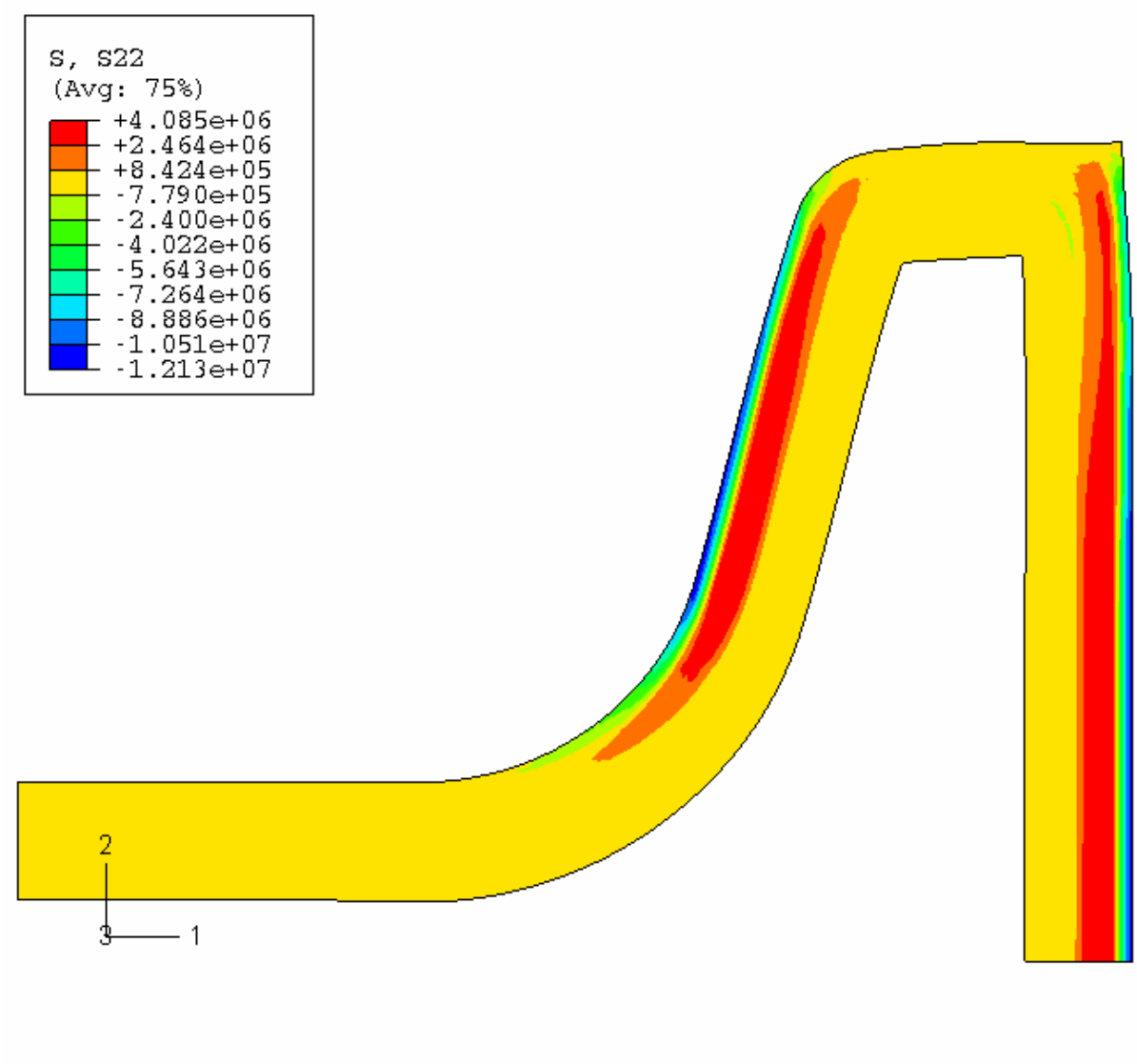

Fig. 9.6 Strand stress22 contour at the mold exit

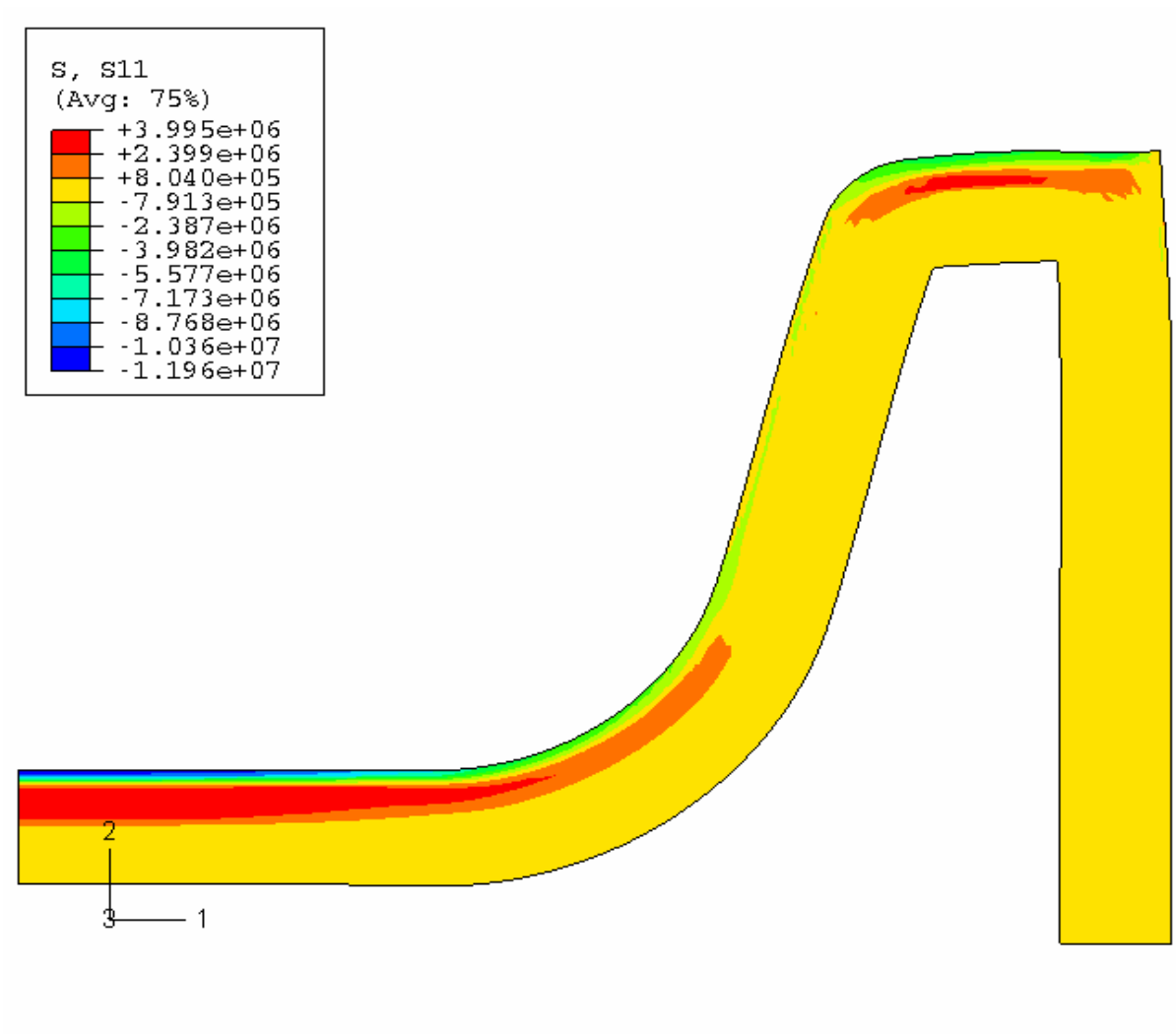

Fig 9.7 Strand stress11 contour at the mold exit

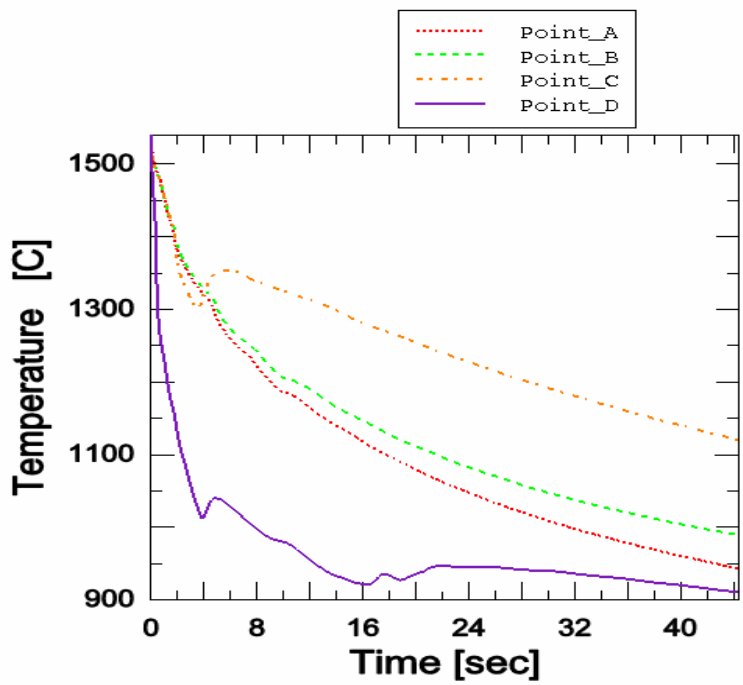

Fig. 9.8 Temperature history for points A, B, C, D

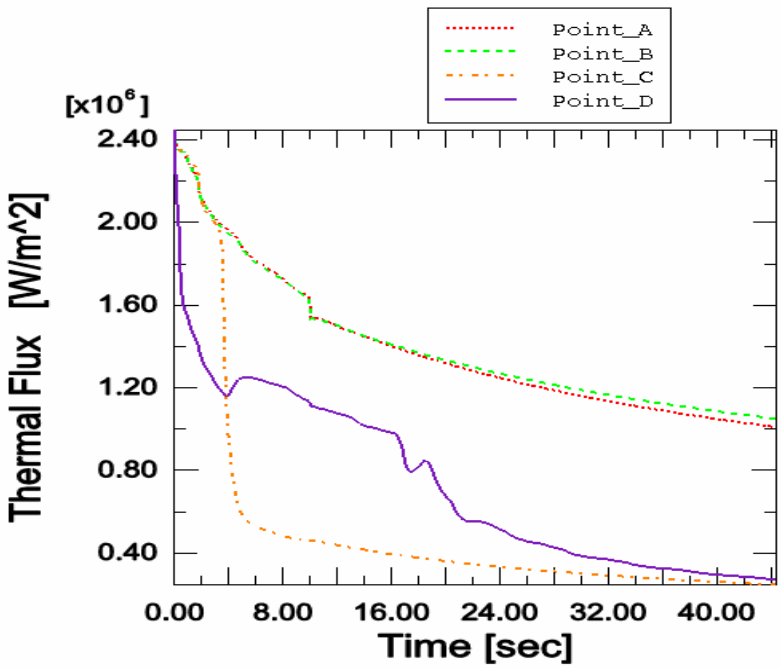

Fig. 9.9 Heat flux history for points A, B, C, D

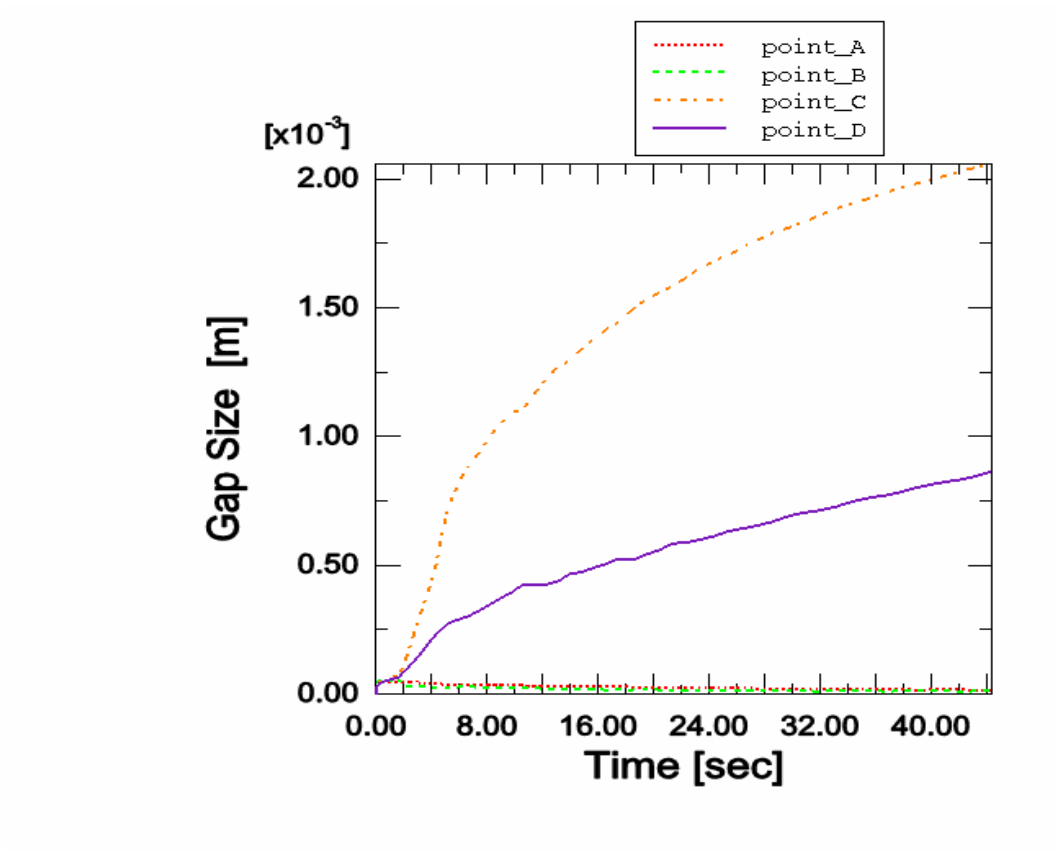

Fig. 9.10 Gap evolution history for points A, B, C, D

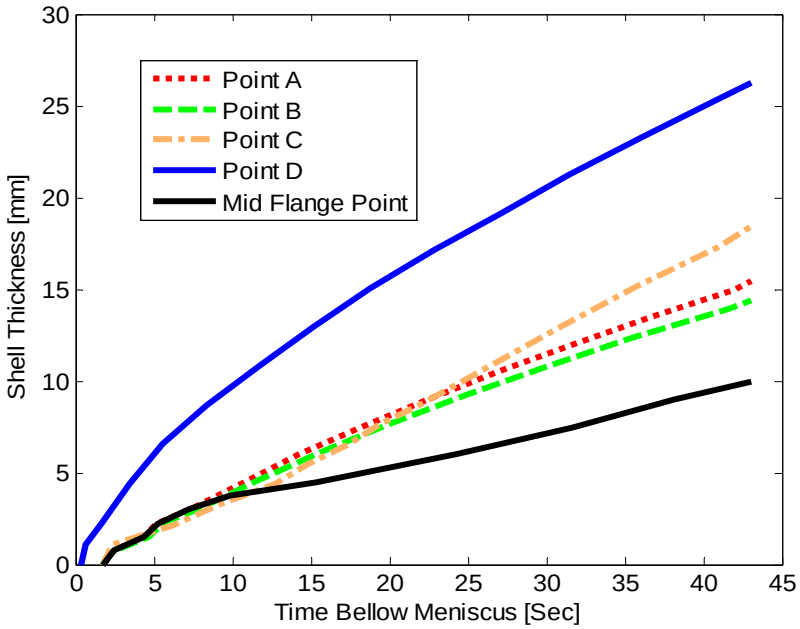

Fig 9.11 Shell thickness evolution history for points A, B, C, D, and the mid flange

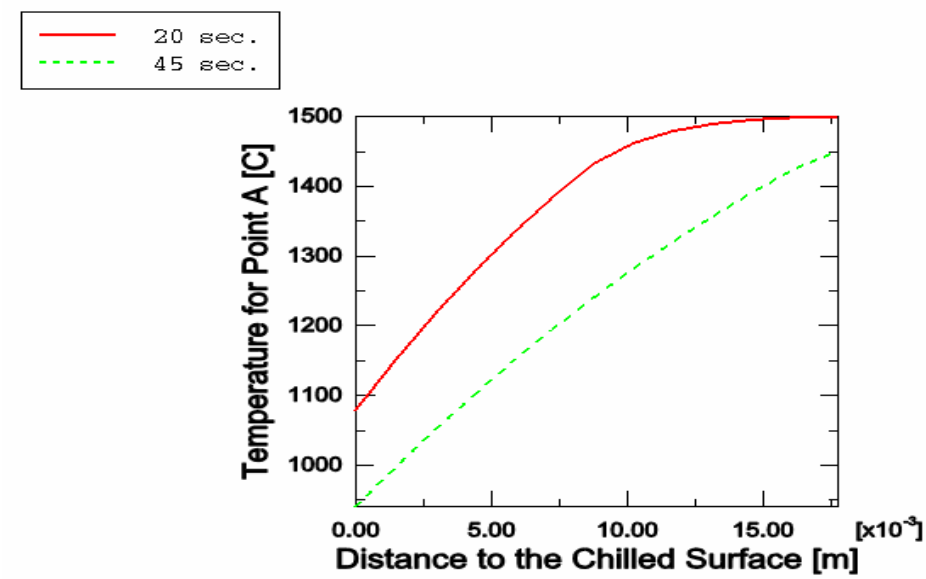

Fig. 9.12 Temperature profile through strand thickness for Point A

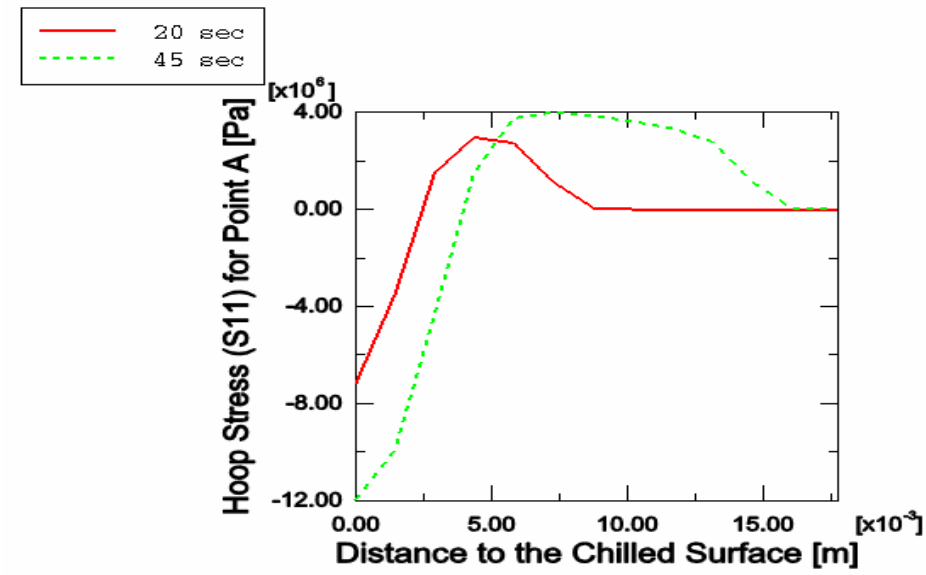

Fig. 9.13 Hoop stress profile through strand thickness for Point A

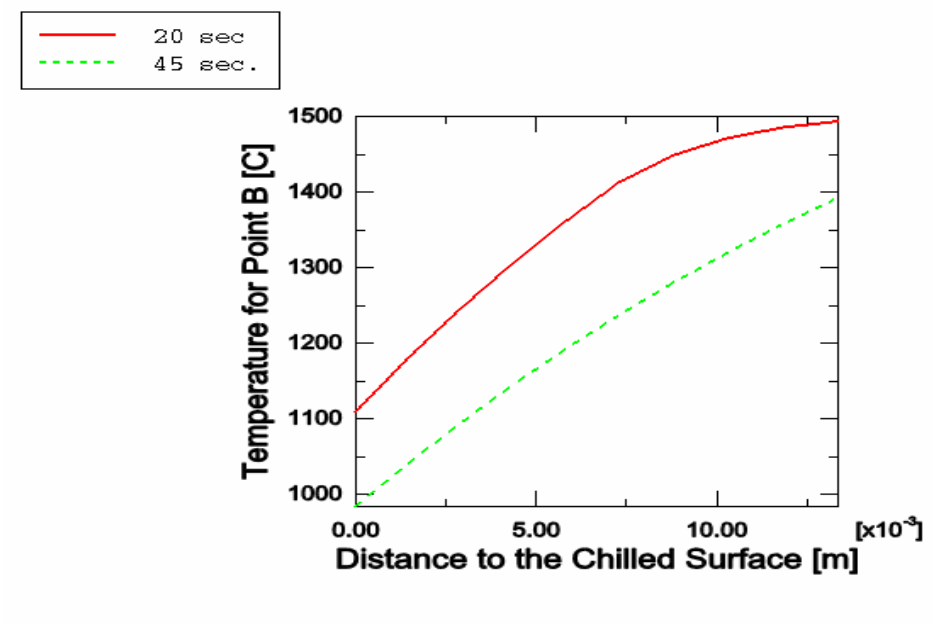

Fig. 9.14 Temperature profile through strand thickness for Point B

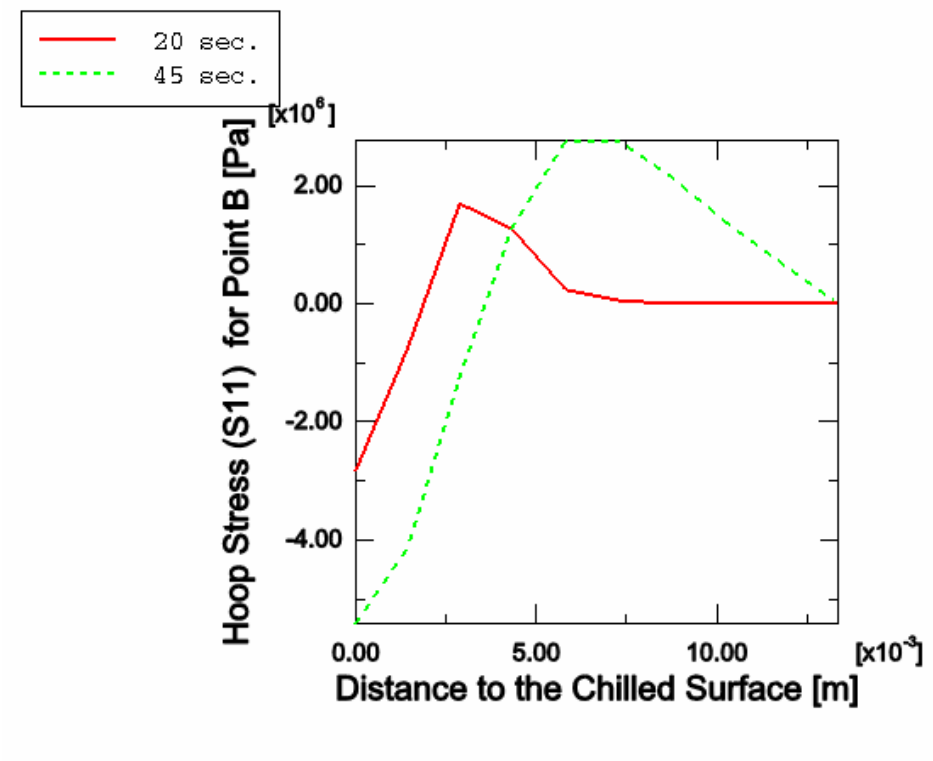

Fig. 9.15 Hoop stress profile through strand thickness for Point B

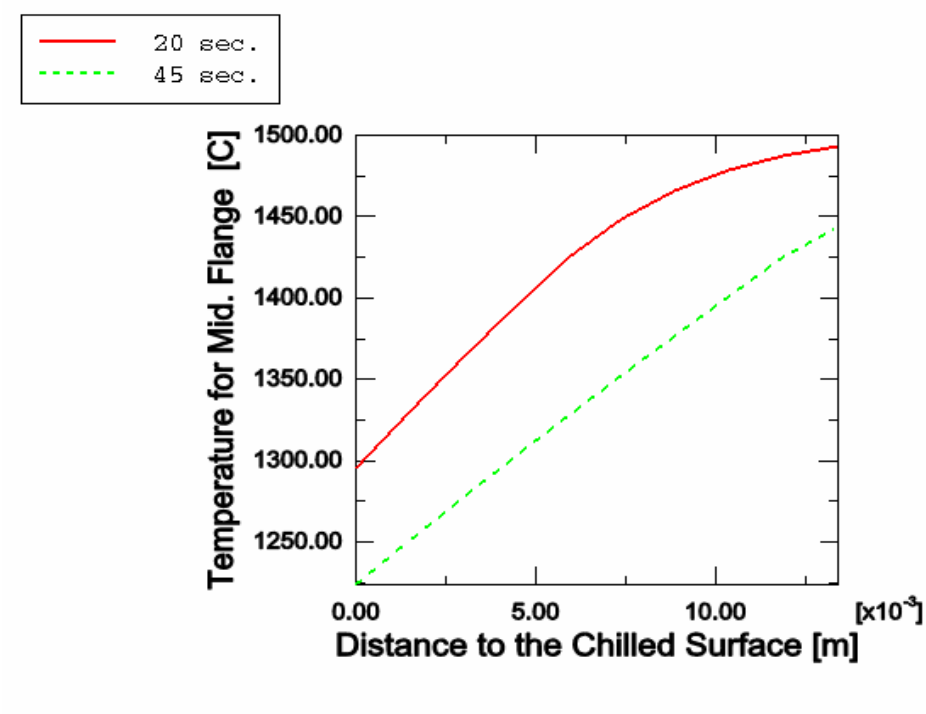

Fig. 9.16 Temperature profile through strand thickness for mid. flange point

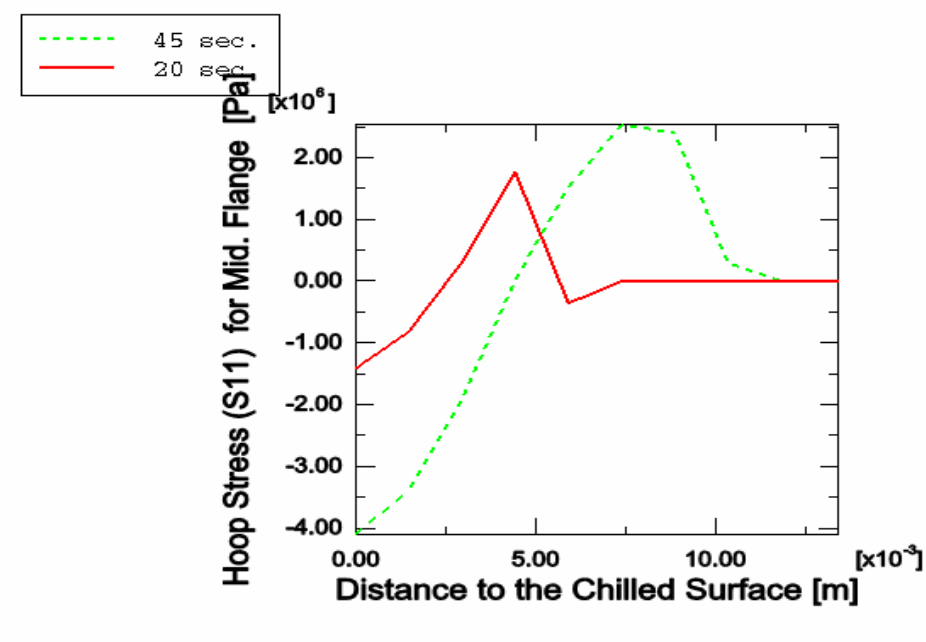

Fig. 9.17 Hoop stress profile through strand thickness for mid. flange point

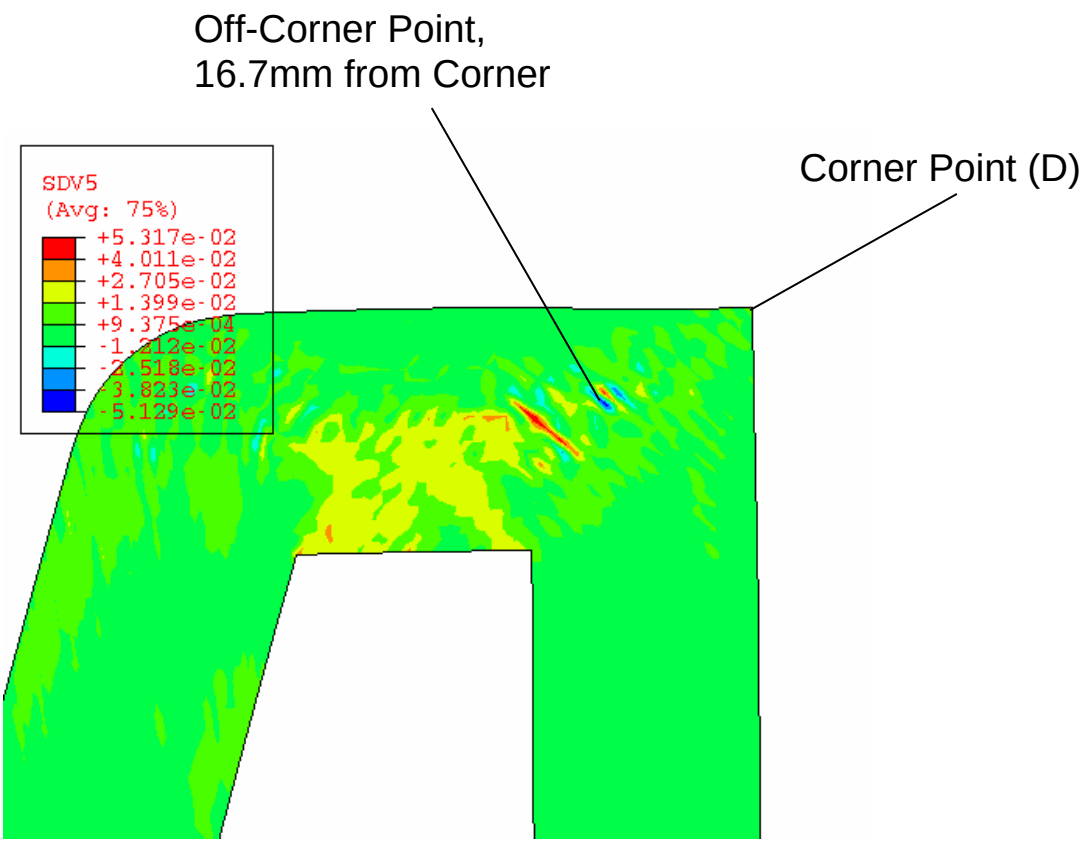

t

Fig. 9.18 Inelastic strain contour for flange area at mold exit

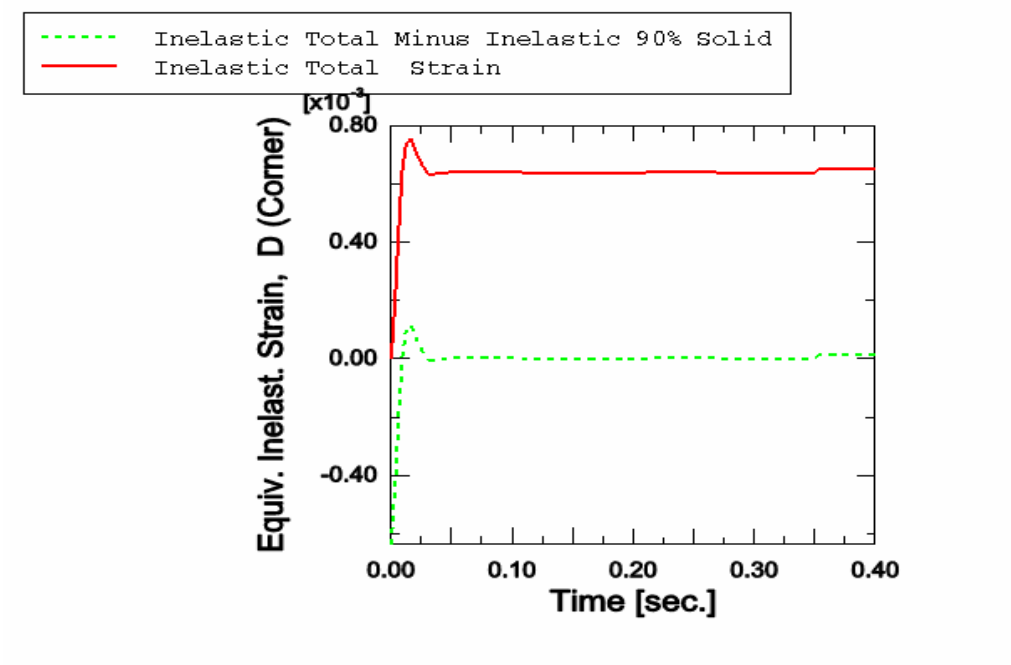

Fig. 9.19 Inelastic strain history for corner (Point D) at early times

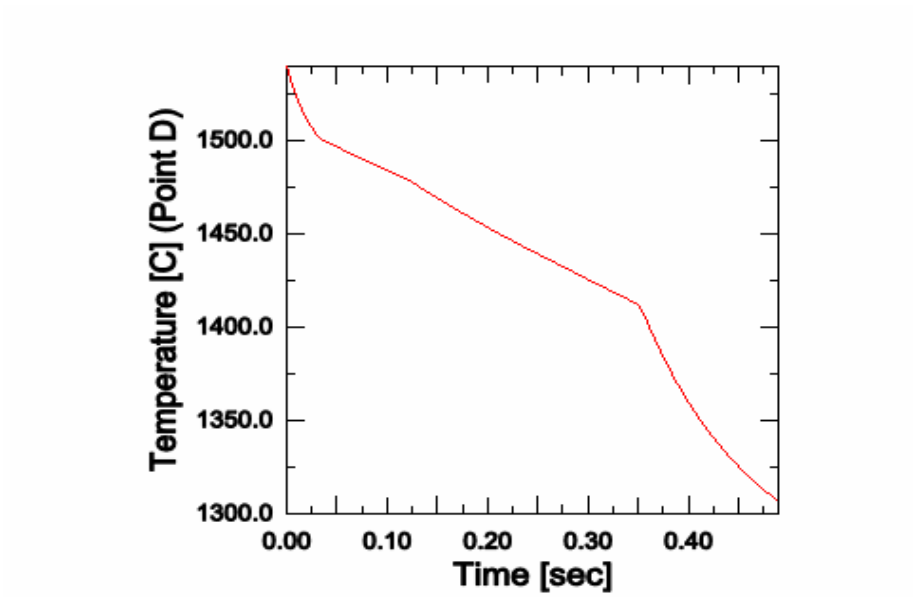

Fig. 9.20 Temperature history for corner (Point D) at early times

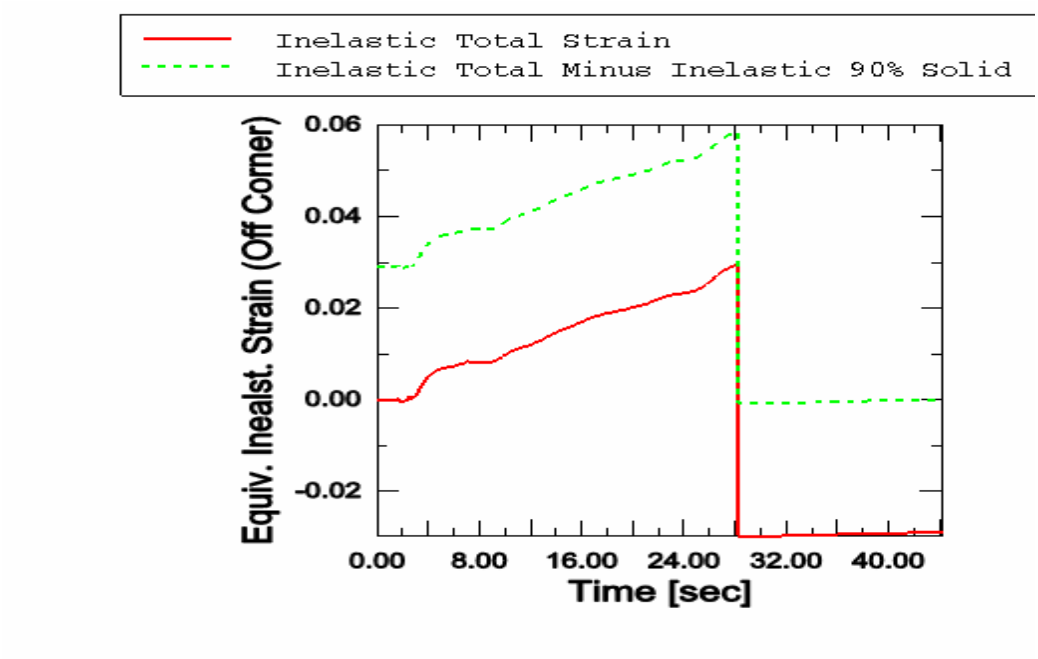

Fig. 9.21 Inelastic strain history for the off-corner point.

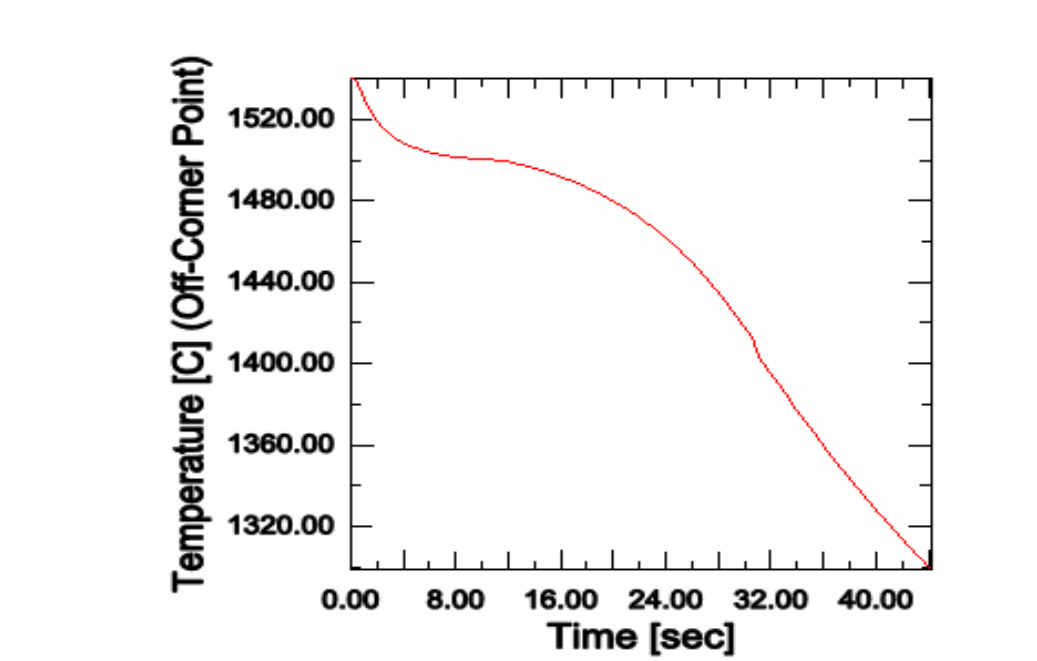

Fig 9.22 Temperature history for the off-corner point

Table 9.I The beam blank simulation conditions

Casting strand [mm]	555 x 420 x 90
Working Mold length [mm]	450
Taper (wrt to W=90mm) [%/m]	1
Softened Contact Coefficients: c_0 and p_0	$5*10^{-5}$, 10^5
Mold Contact Resistance Heat Coefficient, hmold [$W/m^2/K$]	3000
Friction Coefficient (Mold/Shell)	0.1
Casting speed [m/min]	0.6
Steel grade [%C]	0.27
Initial temperature strand [C]	1540
Initial temperature mold [C]	150
Liquidus temperature [C]	1500.7
Solidus temperature [C]	1411.79
Water side heat transfer coefficient [W/m^2K]	30000
Cooling water temperature [C]	30
Time to apply ferrost. pressure [sec.]	3
Number of elements	8805
Number of nodes	18438
Total number of dofs	35512

Chapter 10. Thermo-Mechanical Model of Thin Slab Casting

Thin slab casting was first introduced in 1986 in Nucor Steel's plant in Crawfordsville Indiana. This technology features casting of about 50-mm thick slabs, which are 1/3 thinner than convectional cold cast rolled slab. The economic advantages of thin slab casting technology make them significantly more attractive to build than the large expensive conventional steel plants that must produce 4-5 million tones of steel per year to be profitable [114]. Moreover, when thin slab casting is combined with hot direct rolling the final coiled products can be removed from the mill within 20 minutes after leaving the caster, while with conventional "thick" slab casting the slabs can be held for more than 20 hours before being reheated, and reheating itself requires additional time and energy.

Thermo-mechanical modeling of thin slab casting has received much less attention than conventional thick casting. The main additional modeling complication comes from the computational difficulty faced when modeling transient geometry of the funnel shape as the strand domain travels in the mold. A. Cristallini et al. [115] developed a two-dimensional transient thermal and stress analysis assuming elastic-plastic behavior of shell to design new funnel geometry. Park et al. [116] implemented a 2D generalized plain strain approach with elastic-viscoplastic constitutive model by imposing a severe taper in the funnel area to emulate the slope of the funnel that pushes the strand. While this approach was able to predict temperature and transverse stress results, the axial stresses in the casting direction, which likely are responsible for internal transverse cracks, can only be calculated properly with a 3D model that has some thickness in the casting direction. In the final part of this thesis, a novel 3D thermo-mechanical analysis of a thin slab casting is performed with our Abaqus model with

UMAT on the latest parallel computing platforms. It was observed in chapter 6 that uncoupled analysis consisting of transient heat transfer followed by thermo-stress analysis requires 5-10 times less total cpu time than a corresponding coupled thermo-mechanical analysis. Since a proper mesh refined enough to capture solidification phenomena in a 3D world consists of 300,000 to 500,000 dofs, it is a natural choice to perform uncoupled analysis in this case. However, with the constant increase in the computational speed of the newest hardware and possible improvements in the efficiency and stability of the software and numerical parallel algorithms, the coupled 3D analysis of continuous casting will probably follow in years to come.

10. 1 Geometry and FE Model

Fig. 10.1 shows a schematic of thin slab casting [117]. Aside from a thinner mold width than conventional thick caster, one additional significant difference is a funnel shape section across its central upper part. This design provides sufficient space for the introduction of a large size bifurcated submerged entry nozzle. The rest of the wide mold faces out of funnel region stays straight and parallel like any other rectangular mold. The funnel section narrows down gradually into a rectangular cross section which gives the final shape to the slab casts. Figure 10.2 has geometry of a thin mold used in this work. Generally, the shape of funnel can be characterized by the width and depth of funnel. The total width of the funnel is 750 mm consisting of two bends. The inside concave funnel bend is 400 mm wide where there is an inflection point that changes funnel curvature from concave to convex., the rest of the funnel is a convex outside bend. At the lower part of mold the wide faces at the funnel region becomes almost parallel, ie. the funnel depth tapers away linearly from 40 mm at the top of the mold to 6 mm at 900 mm

down from the mold top. The meniscus plane is 100 mm lower than the mold top so that working mold length is 1100 mm. The slab thickness varies for the center of the funnel from 170 mm at mold top to 108 mm at mold exit, for the concave/convex inflection point from 148 mm at mold top to 93.1 at mold exit, and stays the same at 90 mm for the straight part of the mold.

Similar to the previous model ¼ of the mold and the strand in it is modeled. The liquid domain is highly reduced again to save cpu time and to reduce possible convergence problems in the volatile liquid/mushy region. Unlike any other 2D models, this FE model has a thickness of 100 mm in the casting direction; see Fig 10.3 of the 3D FE domain viewed from the bottom of the mold. The usual symmetry BC-s are enforced on the central planes normal to the wide and narrow faces. In addition, the symmetry BC in the axial direction z is enforced on the bottom surfaces of the mold and strand.

Due to the axial movement of 3D domain in Lagrangian frame of reference, the different material points and nodes in axial direction have different local times. Equation (115) is used to calculate the local time that a material point spends in the mold.

$$t_{local} = \frac{L_Z}{\frac{v_c}{60}}\left(\frac{Z}{L_Z} - 1\right) + t_{ref} \qquad (115)$$

where L_Z is the thickness of 0.1 m of the domain in casting direction, v_c is the casting velocity of 3.6 m/min, Z is the axial coordinate of a material point in the local coordinate system sitting on the top plane and traveling with the domain, and t_{ref} is the time of the reference plane which is chosen to be a bottom plane and is the time that Abaqus is passing into UMAT. In the other words, Eq. (115) calculates the delayed time that different material particles above the reference bottom plane spend immersed in the mold. The bottom of the domain is the first plane to enter

the mold. All time dependant properties like: imposed thermal flux BC, ferrostatic pressure, imposed displacement of mold contact nodes to emulate funnel taper, and time dependant constitutive law are calculated with respect to local material point time.

The domain is meshed with 8-node linear brick elements, which experience less convergence problems than higher-order elements in Abaqus for contact problems. Special attention is given to a proper element sizes in the strand domain especially on the contact surface to accurately model solidification front in a 3D fixed mesh, while avoiding cost-prohibitive mesh size. The strand elements are biased from 1.3 mm average element size on the contact surface with the mold to 5 mm deep in the liquid/mushy zone. The total number of dofs in stress analysis including additional Lagrangian contact dofs and hybrid pressure dofs was ~430,000 for the most refined case. A mesh refinement study with 2 meshes has been conducted to verify that this mesh size is capable of reproducing a correct state of temperature and stress. A slice is formed with exactly the same element sizes used through the strand thickness in the 3D analysis. Then the coupled analysis is run with the identical properties and conditions used for a coupled slice from the chapter 7. The temperature and stress profiles at 21 sec. are compared in Fig. 10.4 and 10.5 with the results from the original coupled slice which has much more refined mesh. An excellent correspondence of temperature results was found. Though the stress result for a slice produced from a 3D mesh is not exactly matching the refined slice stress result, it is still capable of correctly reproducing a state of stress of a solidifying slice.

The transient heat transfer analysis is first run for the strand domain to calculate its spatial and temporal temperature fields. Conductivity, specific heat, and latent heat data are used from the chapter 6. The thermal boundary condition at the shell surface is modeled by use of a heat flux which is obtained from the plant measurements [118] down the mold. This flux data is curve

fitted and prescribed as a function of the local time bellow meniscus in Fig. 10.6. The previous work from chapters 8 and 9 revealed a formation of air gaps in the mold/shell interface in the corner region due to 2D heat flow corner effects. Therefore in order to avoid corner overcooling, the heat flux profile is reduced to 60% of its nominal value. This reduction is applied linearly starting 20mm from the corner on both wide and narrow strand surfaces. The Fig. 10.6 has also a reduced flux curve history imposed to the corner.

The result temperature file is used for a subsequent stress analysis. The mechanical contact between 3D surfaces of the shell and the mold wall is modeled with Abaqus softened contact capabilities from chapter 8. Since temperature field of the strand is already completely determined from the transient heat transfer analysis, no heat transfer across the interfacial gap is modeled. Elastic modulus, and expansion coefficient data are used from chapter 6. Viscoplastic constitutive law from equation (96) is implicitly integrated and solved with the local bounded NR procedure in UMAT from chapter 4. Elastic-perfectly plastic law from section 4.2 is used to model liquid/mushy zone. All previous UMAT coding has been already accommodated for the 3D state of stress and only a minor change in the number of state dependant variables, which are components of inelastic strain, has to be adjusted for 3D case in Abaqus input deck. Ferrostatic pressure is modeled again by means of DLOAD subroutine linearly increasing with respect to the local time for each material point on the shell surface pulled towards the mold wall. The funnel taper is modeled with the imposed displacement history to the funnel mold contact nodes. The total displacement is calculated from the difference between the funnel mold surface profiles at the top and the bottom of the mold, (see Fig 10.2), for a few points along the funnel mold surface. This displacement data is curve fitted with the third order polynomial to yield the x

directional (transverse) dependence. Finally this displacement function is linearly scaled with respect to the local total time bellow the meniscus.

10.2 Results and Comments

Results are given for three times bellow meniscus: 5 sec when the whole domain is already deep in the mold, 12 sec when the bottom plane of the domain is almost exiting the tapered part of the funnel, 15.8 sec when the shell in the funnel just went through the transition from tapered to the straight mold walls, and 19 sec when the domain is exiting the mold. The models with the coarser meshes have encountered floating exception convergence problems and could not run longer than 12 sec., even when the maximum time increment was limited to 0.006 sec. The most refined mesh with over 430,000 dofs did not encounter these problems, and it made it to 15.8 sec. with the max. time increment size restricted to 0.006 sec when the Abaqus solver reported memory problems and exited on a 32-bit NCSA's tungsten cluster. This late simulation memory problem was reported to Abaqus Inc., and we were advised to re-run the whole simulation on a 64-bit cluster with more available memory. Recently the whole simulation succeeded on an experimental AMD Opteron 64-bit box with dual core cpus, and the results at 19 sec. have been included in this work. It took more than 8 days of the wall clock time to complete this simulation on the Opteron box.

A final shape of the bottom shell surface at mold exit is imposed on the corresponding initial shape at meniscus in Fig 10.7. It shows a correct application of mold displacement BC which is correctly pushing out shell in the funnel into its final shape. Fig 10.8A has a detail corner bottom shell surface distortion in the mold with the corner gap formed at 12 sec with temperature contours imposed. Since this model does not have taper modeled, the real shell would not

probably form such a big gap, if the taper of the narrow face was put into the simulation. Another gap at the center of the wide face has quickly opened when the shell reached the mold wall geometry transition, and stayed opened for the rest of the analysis. Evolution of this gap viewed from the center section side view is sketched in Fig.10.8B.

Temperature contours are given in Fig 10.9, 10.10, 10.11, and 10.12. Parallel isotherms normal to the casting direction confirm validity of the assumption used in all 2D cases that heat conduction in casting direction is negligible. Temperature profiles along wide bottom edge face for surface and 2 sub-surfaces are compiled in Fig 10.13, 10.14, 10.15 and 10.16. Subsurface1 is 1.73 mm bellow the shell surface; while subsurface2 is 3.4 mm bellow the shell surface. Complicated geometry of the funnel region does not seem to produce any unexpected temperature results. Most of the shell surface is still cooling uniformly with respect to the local time it spends in the mold except in the corner and a small spot where funnel turns into straight part. Even though there is a drop of heat extraction from the shell in the corner due to the imposed flux drop, the immediate corner area still gets moderately cooled due to the 2D heat flow corner effect while the rest of the corner flux drop area stay warmest in the domain with as much as 120 C higher temperature than the rest of the domain and immediate corner. This is quantitatively very similar to the temperature corner profile from 2D coupled simulations from earlier chapters. Early attempts to run heat transfer analysis without a flux corner drop have produced severe overcooling of the corner area with as low as 400C, which is not real. Higher temperature subsurface profiles are mostly parallel to the surface profile indicating expected linear increase of the temperature through the shell thickness. Shell thickness evolution for bottom surface is given in Fig. 10.17. Most of wide face reaches ~9mm shell thickness at the mold, while corner has a thicker shell of 16 mm at mold exit.

There are three major contributions to the generation of stress in this model. Besides usual thermo-visco-plastic stresses coming from solidification due to the uneven cooling through shell thickness, there is a strong pure mechanical component coming from the funnel geometry pushing and bending solidified shell. Often mechanical component is dominant in funnel region and stress sign is opposite of expected compression on shell surface and subsurface tension common for pure solidification of a straight shell.

Transverse stress contour σ_x are given in Figs. 10.18, 10.19, 10.20, and 10.21 at 5, 12, 15.8, and 19 sec. Corresponding transverse stress distributions graphs along the wide face bottom edge for the same surface and two subsurface paths are given in Figs 10.22, 10.23, 10.24, and 10.25. They reveal an interesting transverse stress distribution. Most of the wide face, and especially in the funnel region, is in the state of tensile stress on the surface early in the simulation at 5 sec. This can be explained by the significant deformation of the shell as it gets pushed by the funnel and straightened in the funnel region increasing its length. The shell transverse elongation is even larger than its corresponding shrinkage due to the cooling, and the tension occurs on the shell surface. This is opposite of usual compression on the shell surface for the parallel molds without funnel. At later time of 12 sec. situation changes and most of wide face bottom edge is in compression except the funnel outer bend region that stays in the tensile state. Between 13.5 and 17 sec. most of the funnel shell surface goes into another period of tension, which is even stronger than at early times. That is the time when the shell in the funnel goes through the funnel mold wall transition region from the tapered to the straight. Finally, when the whole domain is deep in the lower part of the mold at 19 sec, surface compression dominates everywhere again except in the small area around the center of the funnel where some residual tensile surface stress is still present. Generally subsurface stress lines are showing usual tensile stress close to

solidification front when compression is on the surface, but opposite is also true for the most of the surface in tension.

Axial (casting direction) stress contours σ_z are given on Fig 10.26, 10.27, 10.28 and 10.29. Axial stress distribution along the bottom funnel edge for a shell surface and the two subsurface at 5, 12, and 15.8 sec are given on Figs 10.30, 10.31, 10.32 and 10.33. Axial stresses distributions and histories are quantitatively similar to the transverse stresses and characterized again by the two stress reversals. At 5 sec high tensile stress areas are recorded close to symmetry planes, while in the corner area both tensile and compressive stresses are present next to each other due to the strong thermal strains coming from temperature corner variations. Most of shell surface is in compression due to its axial shrinkage at 12 sec except a tiny tensile strip at the corner edge At the time of 15.8 sec. surface tension is present in most of the funnel region which is left from the axial unbending that shell undergoes after transition from tapered to straight part of the funnel mold wall. At the mold exit, surface compression dominates again.

Transverse and axial stress histories are given for the three interesting points on the bottom surface edge. Fig. 10.34 has stress histories for a center funnel point, Fig. 10.35 has stress histories for a point 0.3 m from center which is in the funnel outer bend region known for a strong showing of tensile stress from contours, and Fig. 10.36 has stress histories for a point 0.58 m from a center in a straight part of wide face. The stress histories for two funnel points are nicely depicting the two periods of stress reversals that solidifying shell in the funnel part of mold goes through, and they are common for both transverse and axial components of stress. The surface point history of the point in the straight part of funnel feels very little of a stress reversal from the funnel and mostly behaves in an expected surface compression fashion observed from the previous chapters.

To summarize: using a 3-dimensional uncoupled thermo-mechanical finite element model, the thermo-mechanical behavior of strand in a thin funnel mold has been analyzed. The transient heat transfer analysis with the realistic heat flux BC was run first, followed by the mechanical analysis with 3D softened mechanical contact between the shell and the mold wall.

This simulation provides the following insights into the continuous casting process for funnel thin slabs:

- This model indicates a significant interfacial gap develops at and near the corner, on the narrow face, owing to the lack of mold taper. Realistic taper data is necessary to be included in the future models to compensate for the large gap formation. Another gap at the center of the wide face opens when the shell goes through the funnel mold wall transition, and stays open for the rest of the mold.
- Large gradients of temperature are recorded between the corner tip and wider corner area. This is causing uneven shell development in the corner area, similar to beam blank, making the corner area prone to the shell failures.
- Negligible temperature gradients are observed in the casting direction justifying the assumption used in all 2D models that the heat conduction in axial (casting) direction can be neglected due to the large Peclet number.
- Two periods of stress reversals, characterized by the surface tension and the subsurface compression, are revealed for both transverse and axial shell stresses in the funnel area. The transverse stress reversals are consistent with the findings of Park et. al. [116] who used a 2D generalized plane model to model thin slab casting with funnel, except that this model has predicted additional compressions at the two curvature transition areas. The axial stress results are novel and can be used to predict internal transverse cracks.

- Even though this pioneer attempt to model 3D solidification in a complex geometry environment of a thin slab continuous mold with funnel turned out to be a serious computational task, and there is some uncertainty in the stress results due to the extremely complex phenomena that influences it; it clearly shows that the model developed in UMAT in this work is efficient enough to perform it successfully on the newest computational platforms.

10.4 Figures and Tables

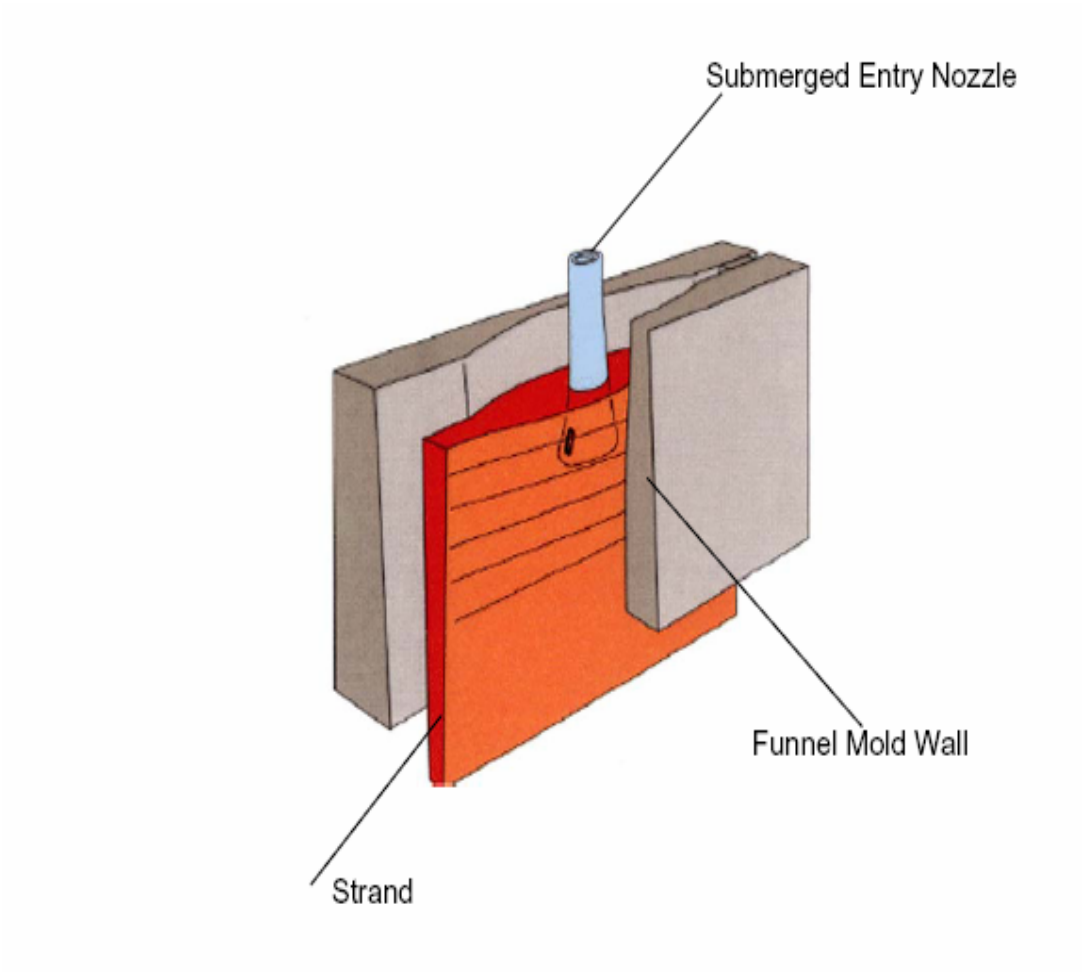

Fig 10.1 3D Schematic of thin slab casting [117]

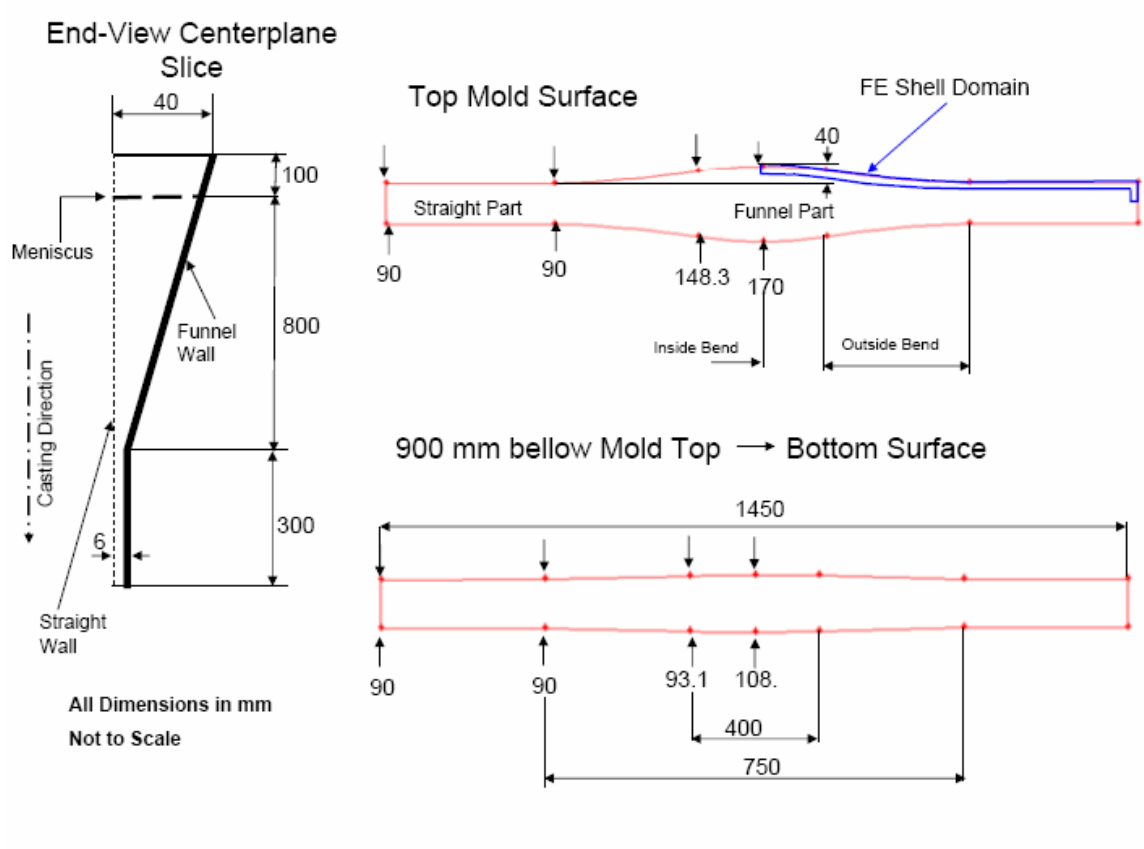

Fig. 10.2 Geometry of a thin slab casting mold

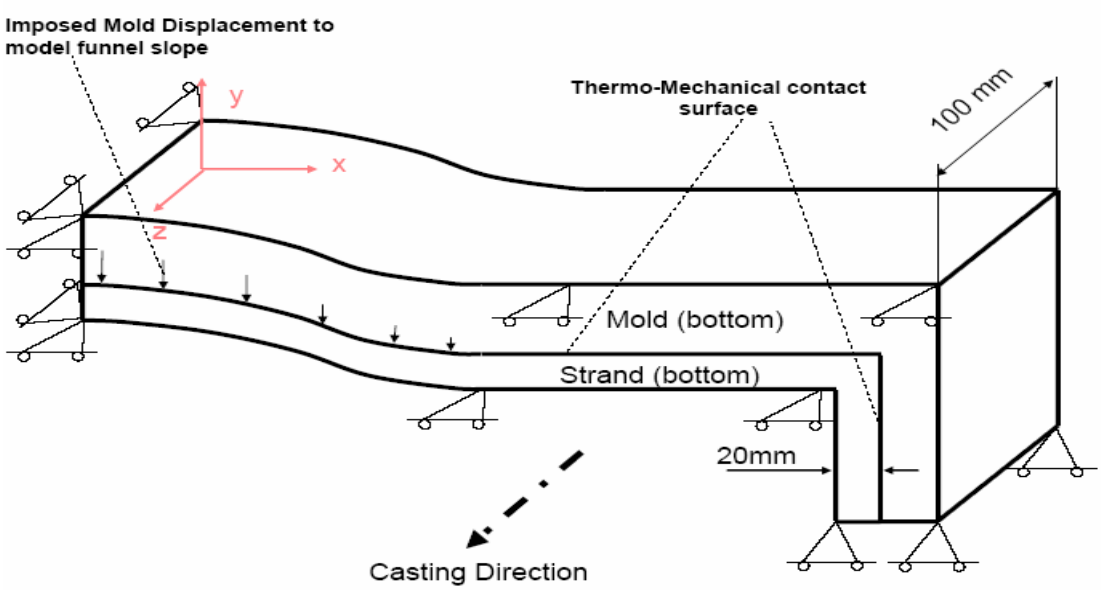

Fig 10.3 3D Model and BC-s

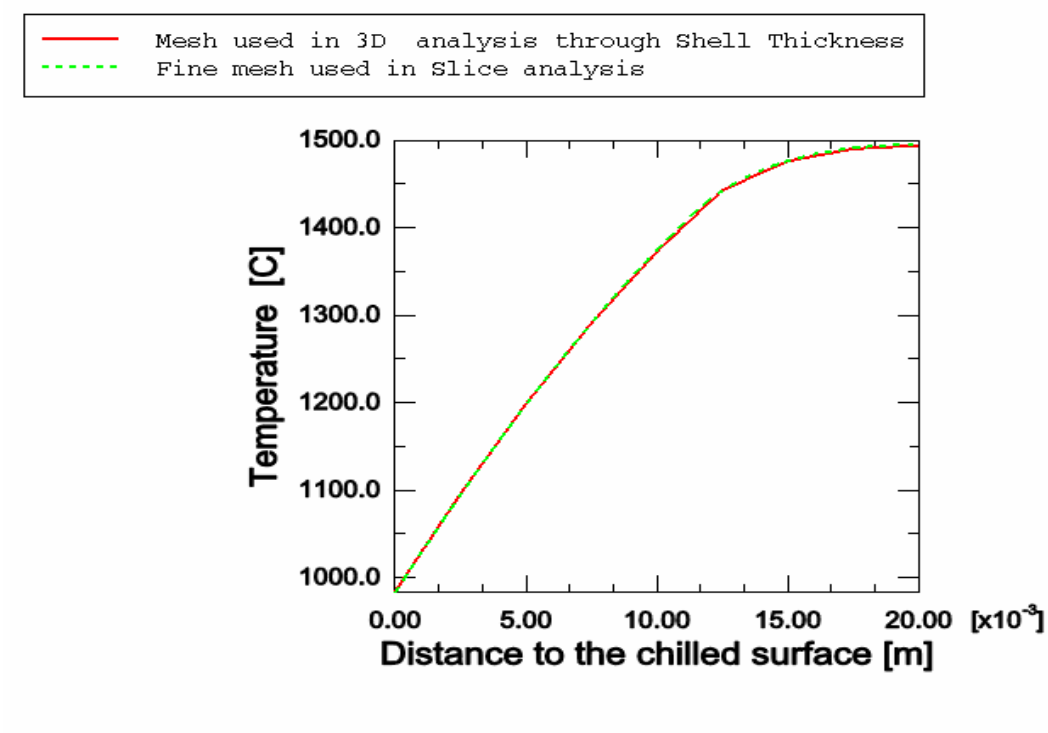

Fig. 10.4 Mesh refinement study, temperature results

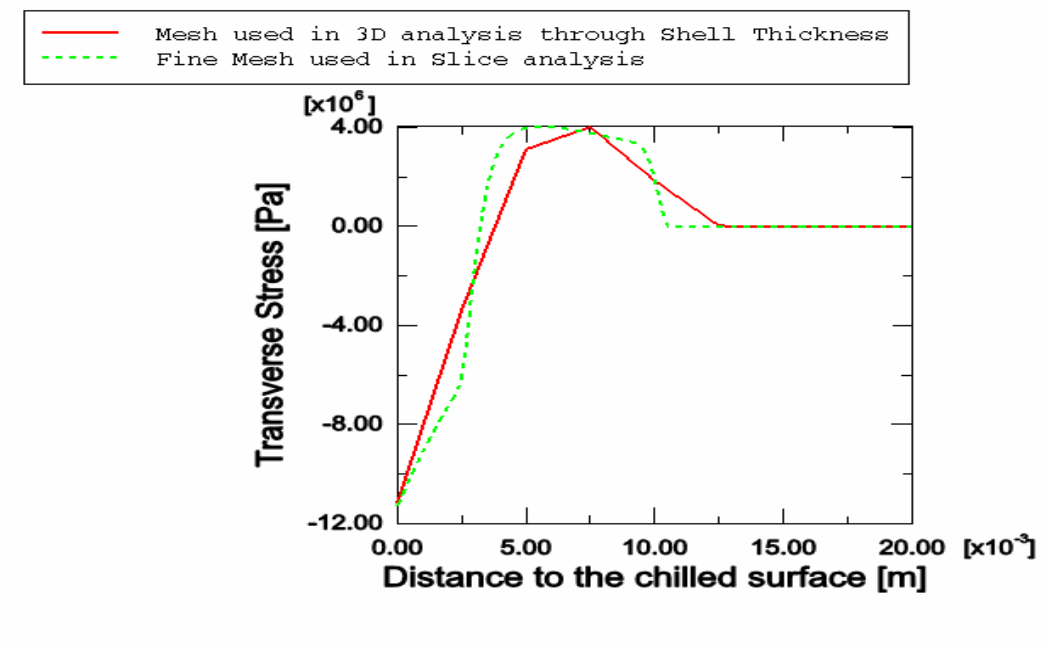

Fig. 10.5 Mesh refinement study, stress results

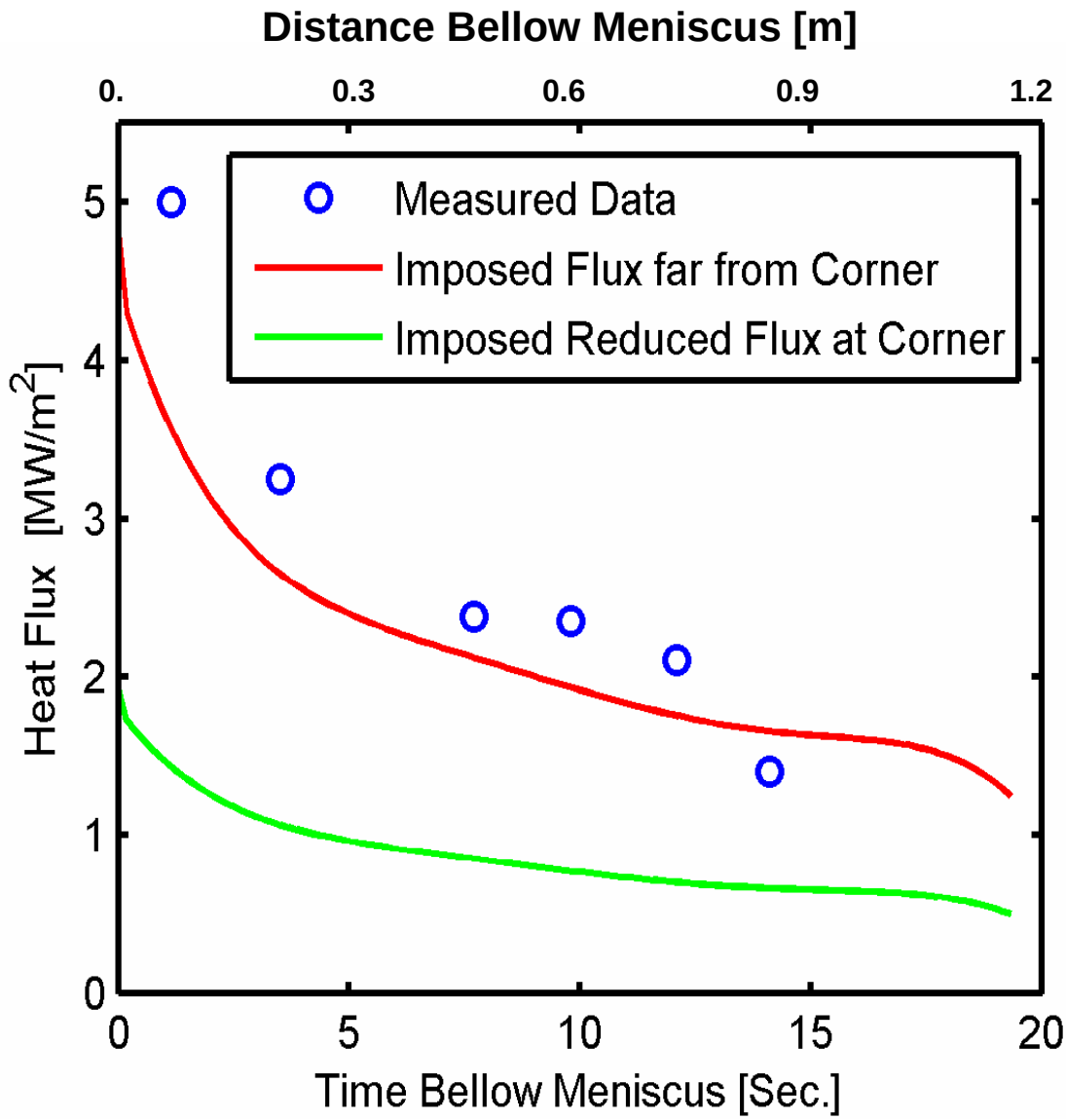

Fig. 10.6 Imposed heat flux BC

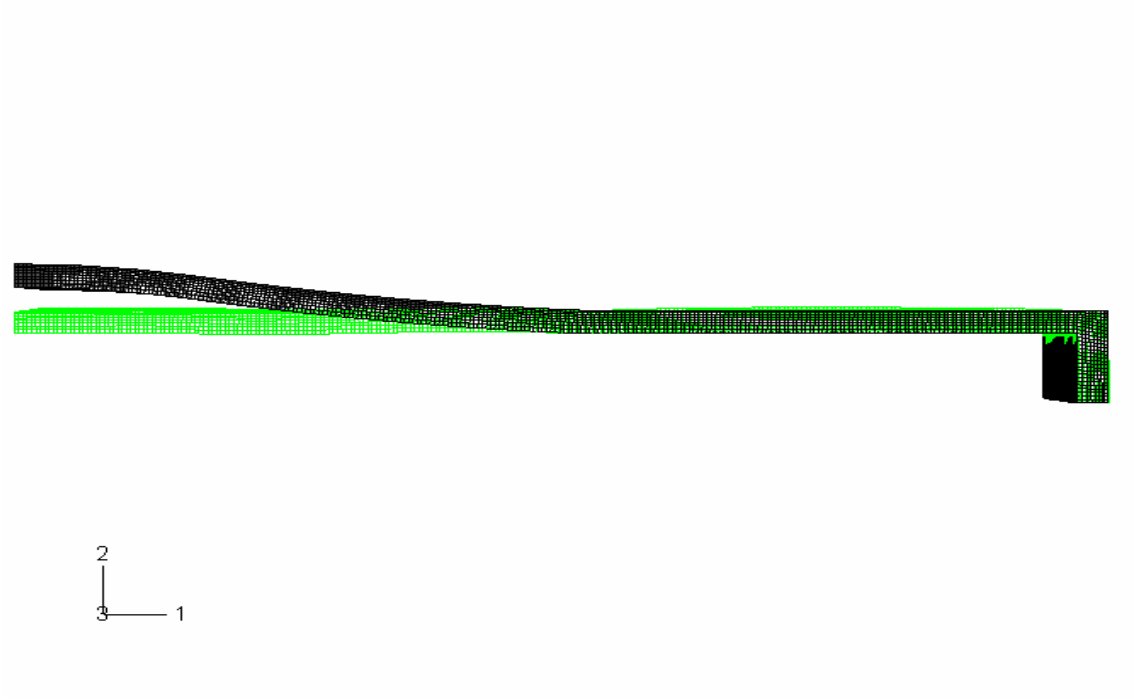

Fig. 10.7 Initial (black: at meniscus) and final (light green: at mold exit) shell shape 3-D view from bottom of mold (showing inside of NF wall in solid black at right)

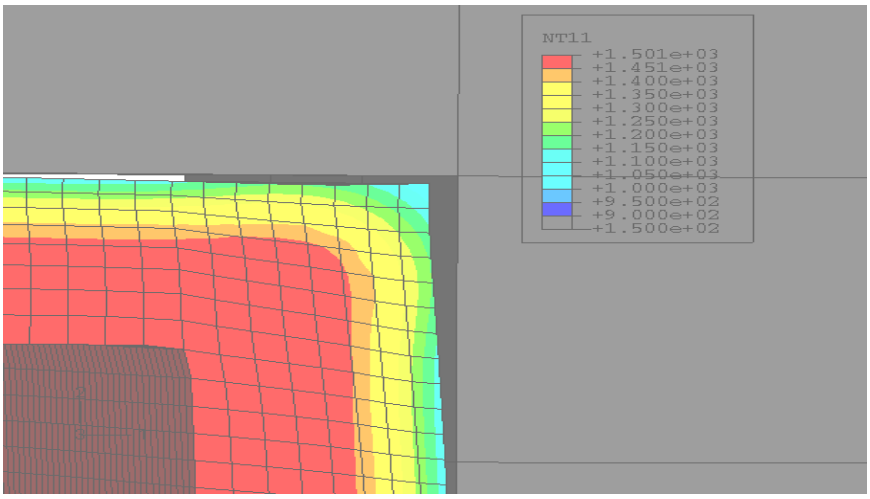

Fig. 10.8A Detail corner bottom shell surface distortion with temperature contour imposed at 12 sec. bellow meniscus

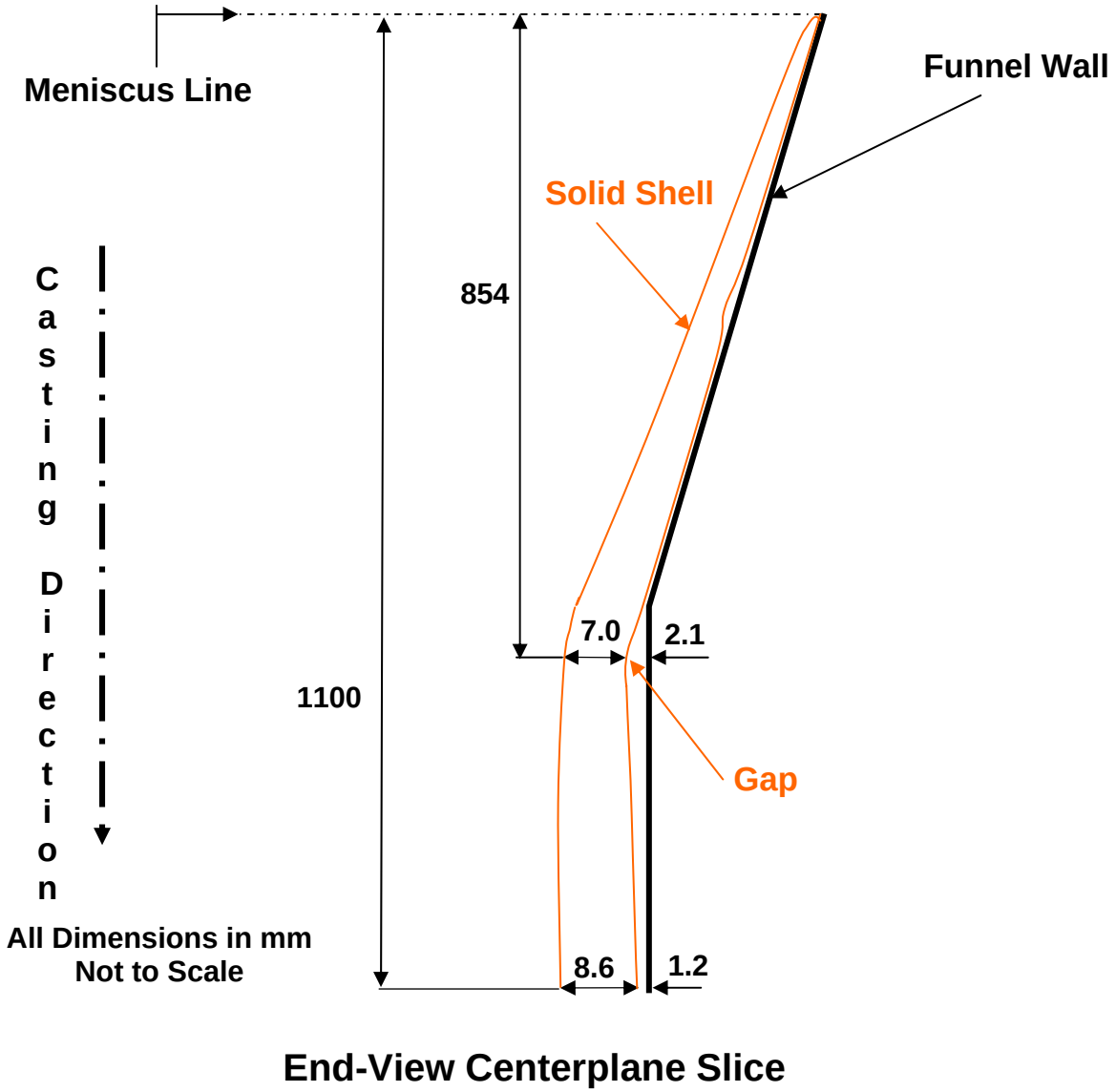

Fig. 10.8B Central gap evolution

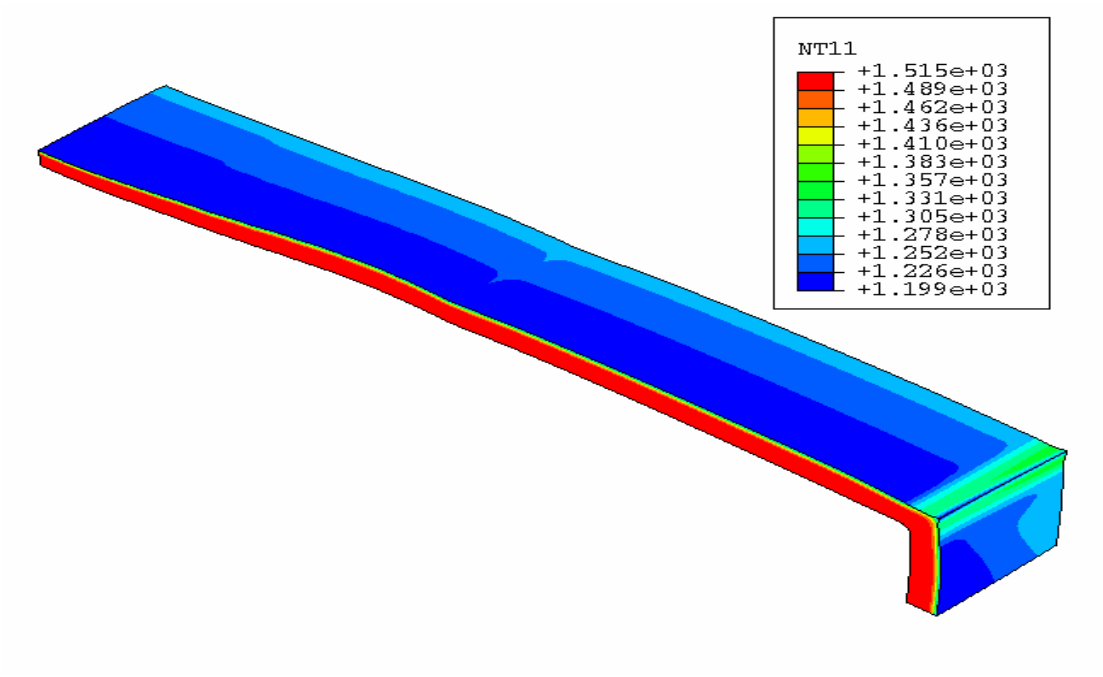

Fig 10.9 Temperature contour when domain bottom is 5 sec. below meniscus

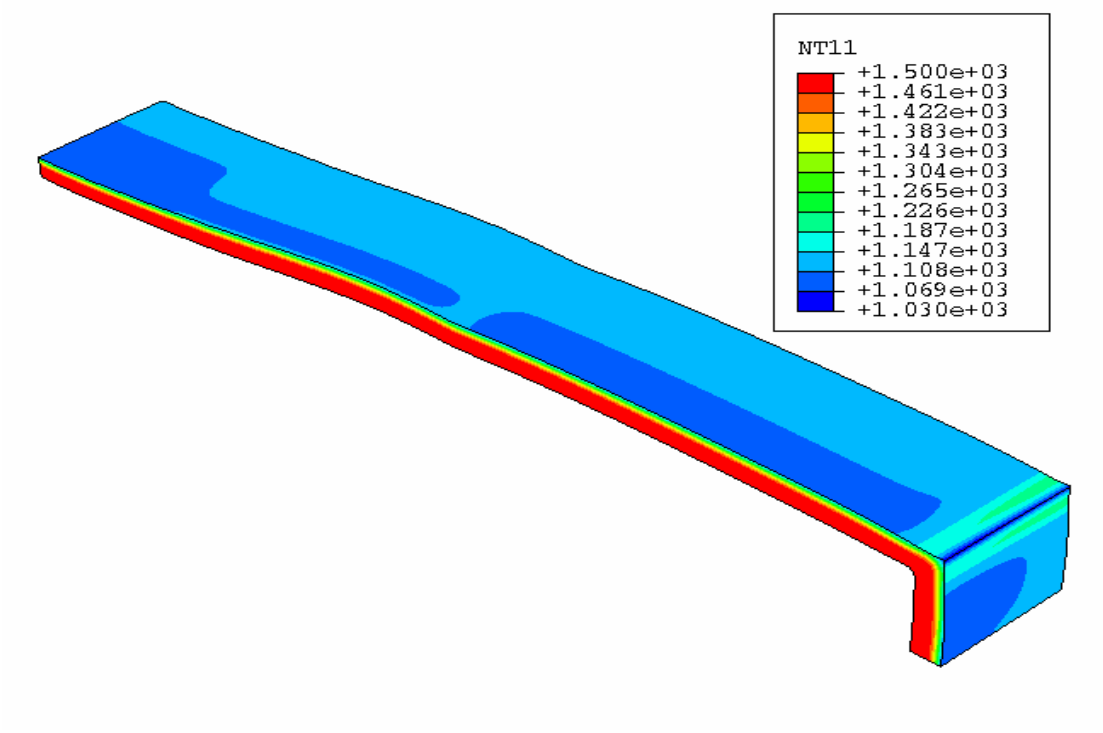

Fig 10.10 Temperature contour when domain bottom is 12 sec. below meniscus

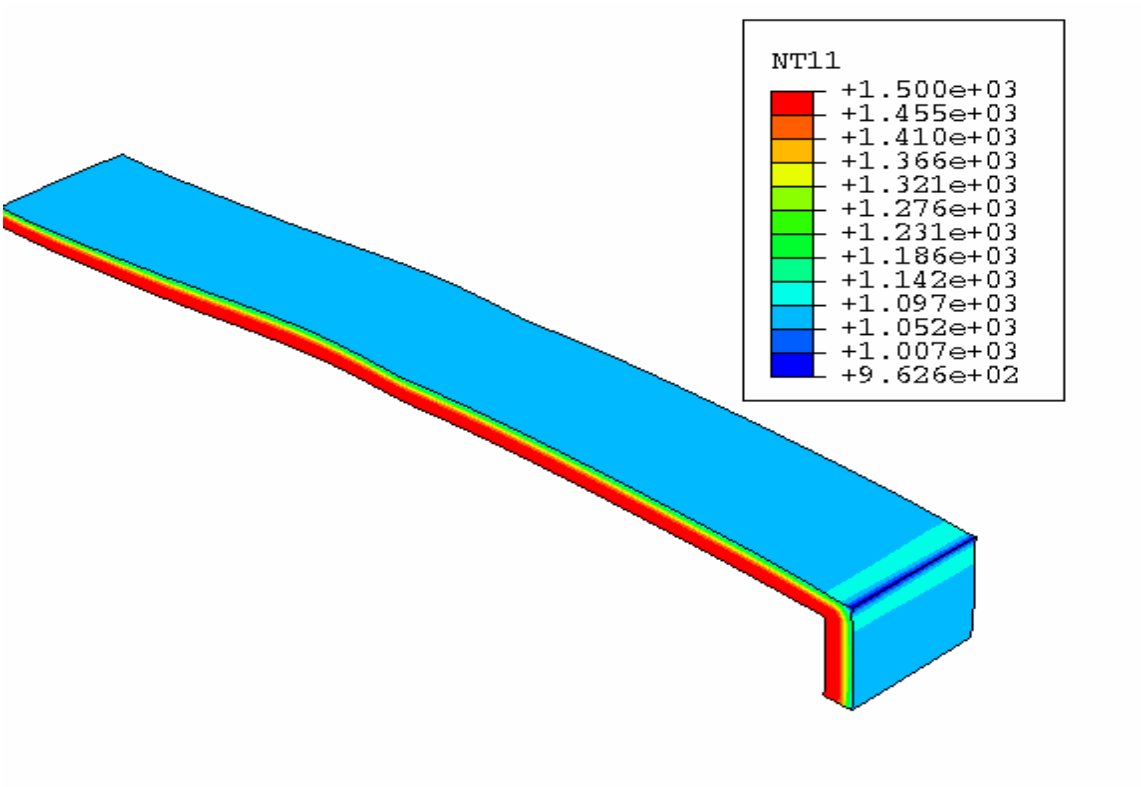

Fig 10.11 Temperature contour when domain bottom is 15.8 sec. below meniscus

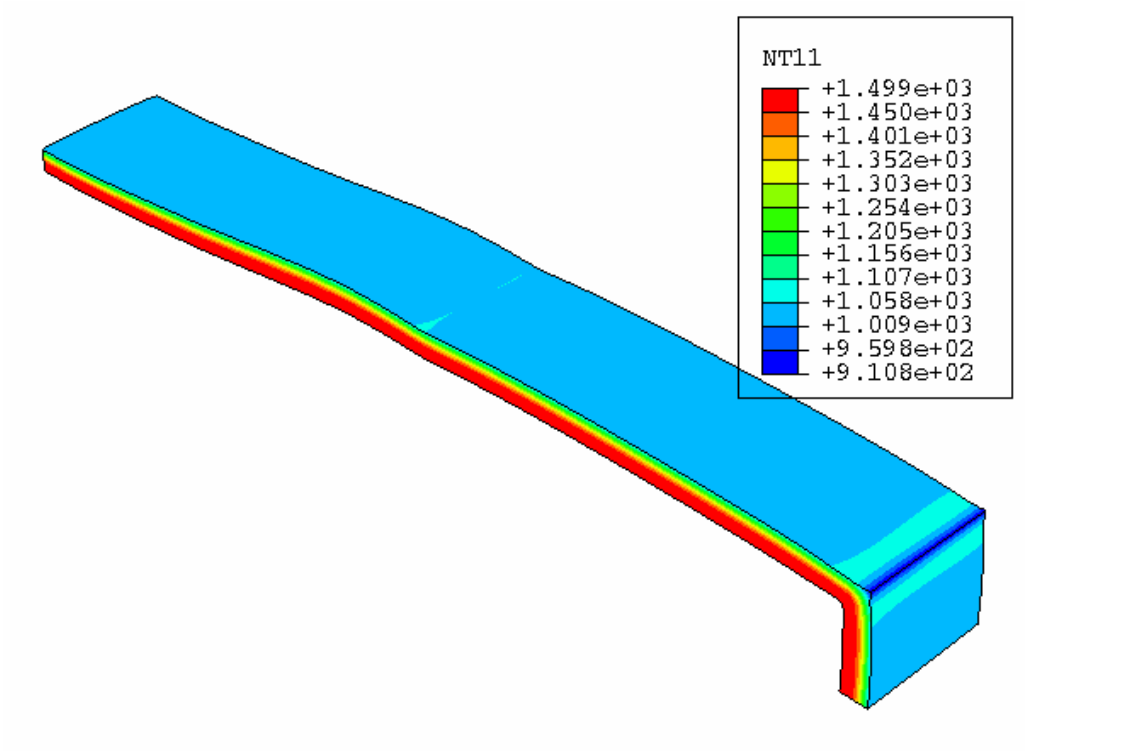

Fig 10.12 Temperature contour when domain bottom is 19 sec. below meniscus

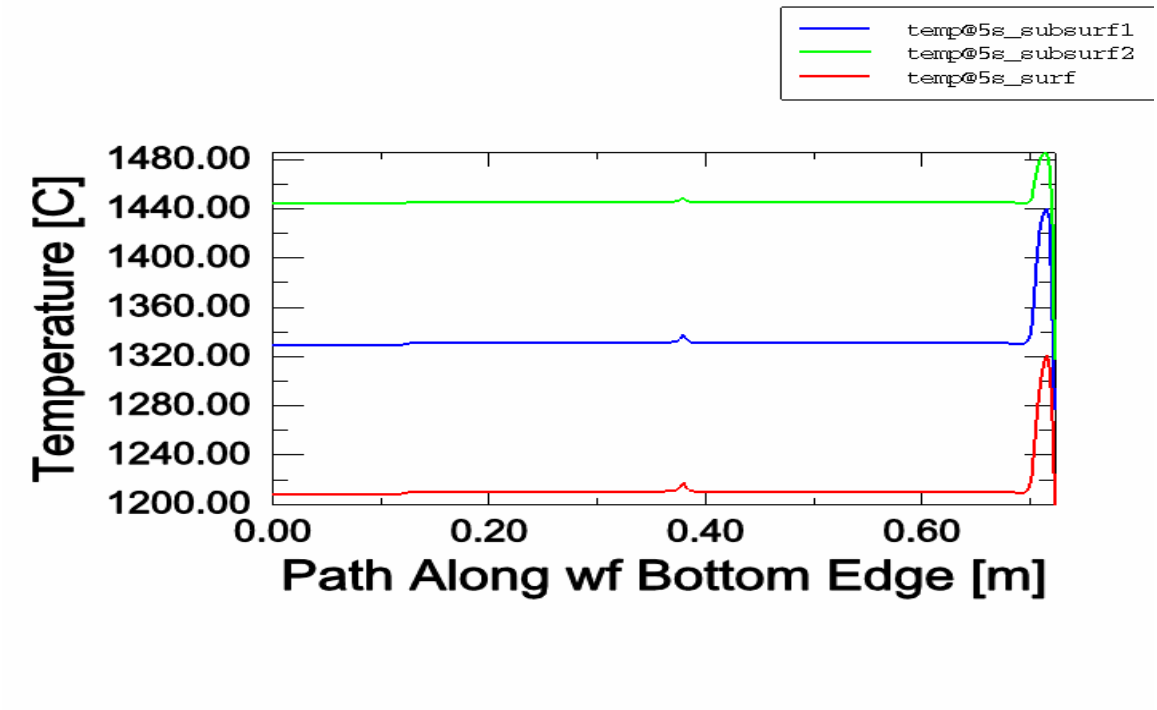

Fig. 10.13 Temperature profile along wide face bottom edge path at 5 sec.

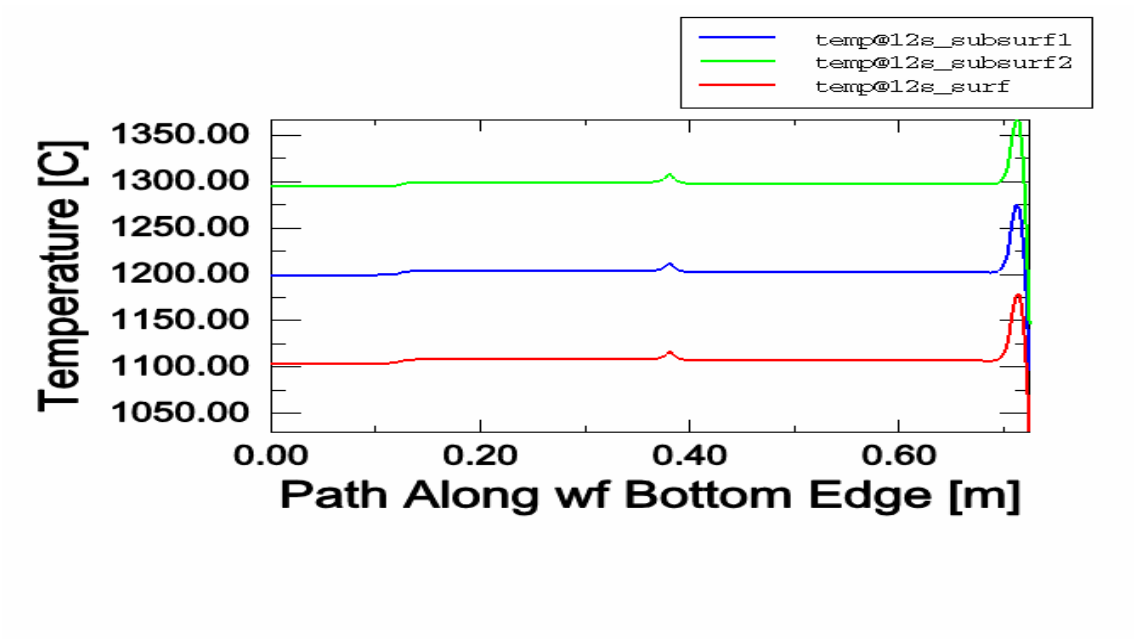

Fig. 10.14 Temperature profile along wide face bottom edge path at 12 sec.

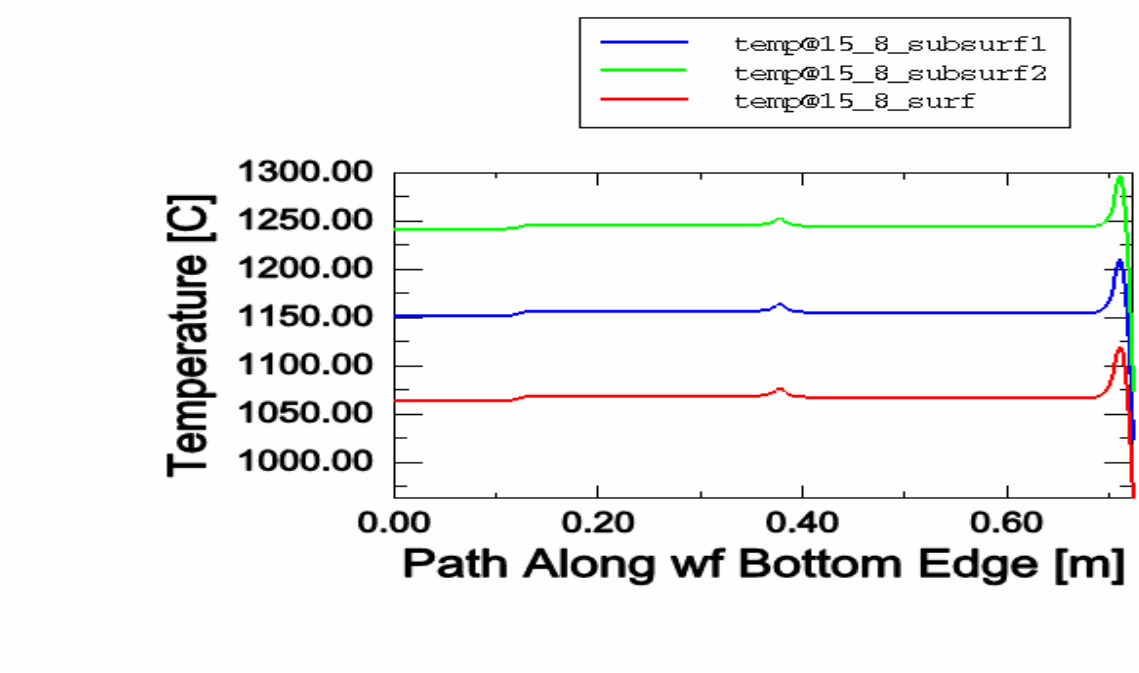

Fig. 10.15 Temperature profile along wide face bottom edge path at 15.8 sec.

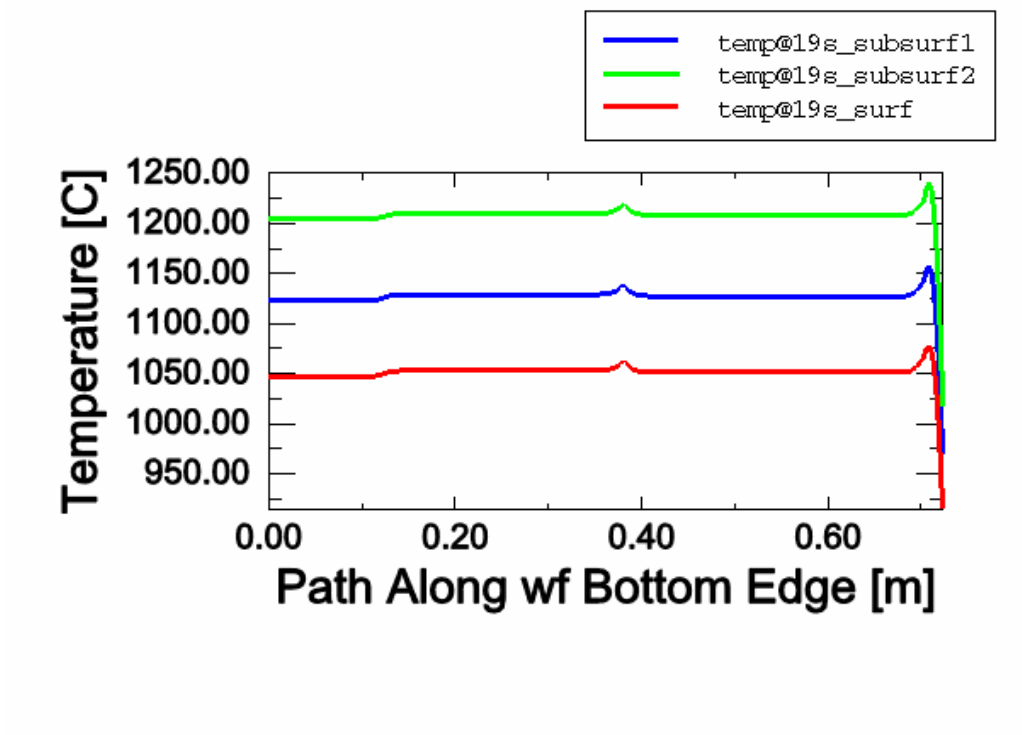

Fig. 10.16 Temperature profile along wide face bottom edge path at 19. sec.

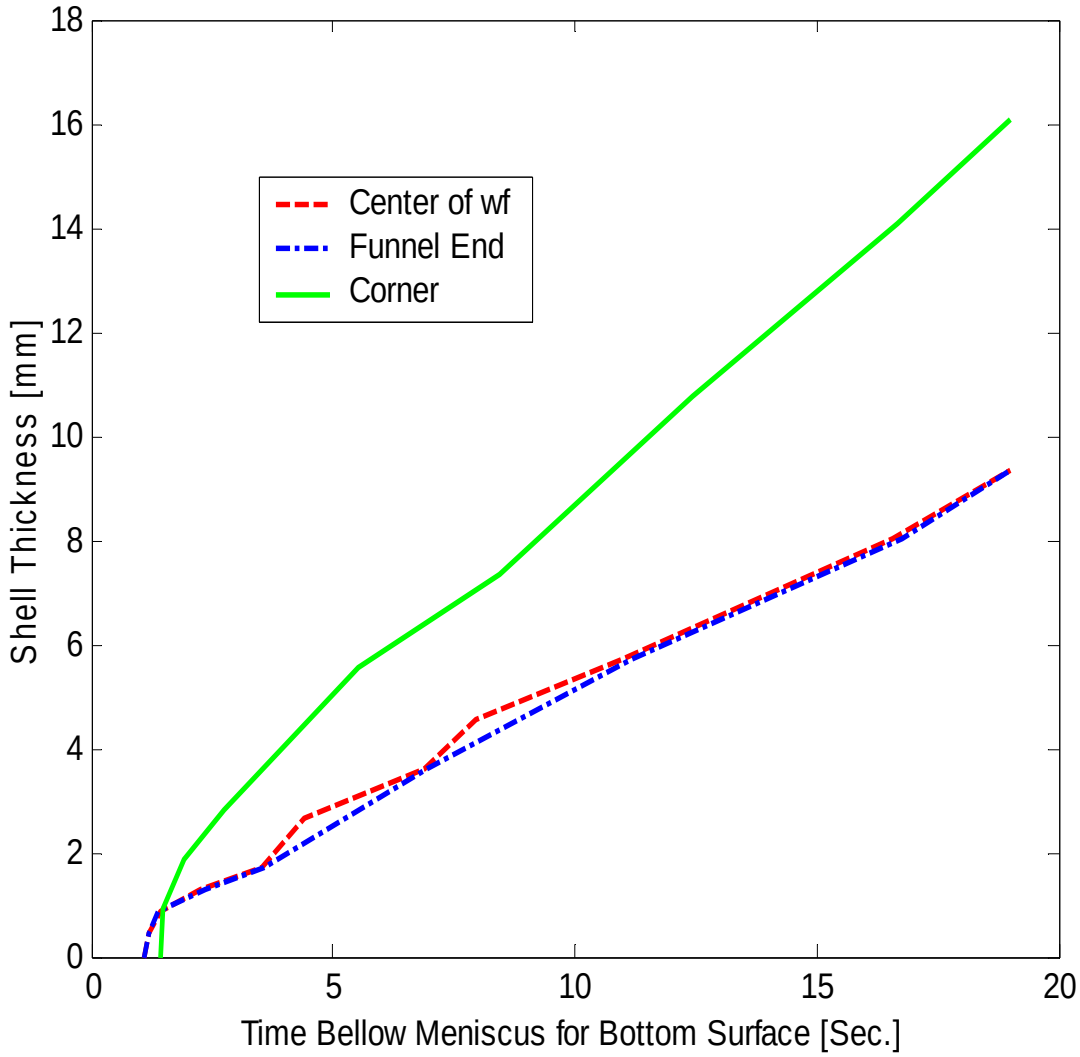

Fig. 10.17 Shell thickness history for bottom surface

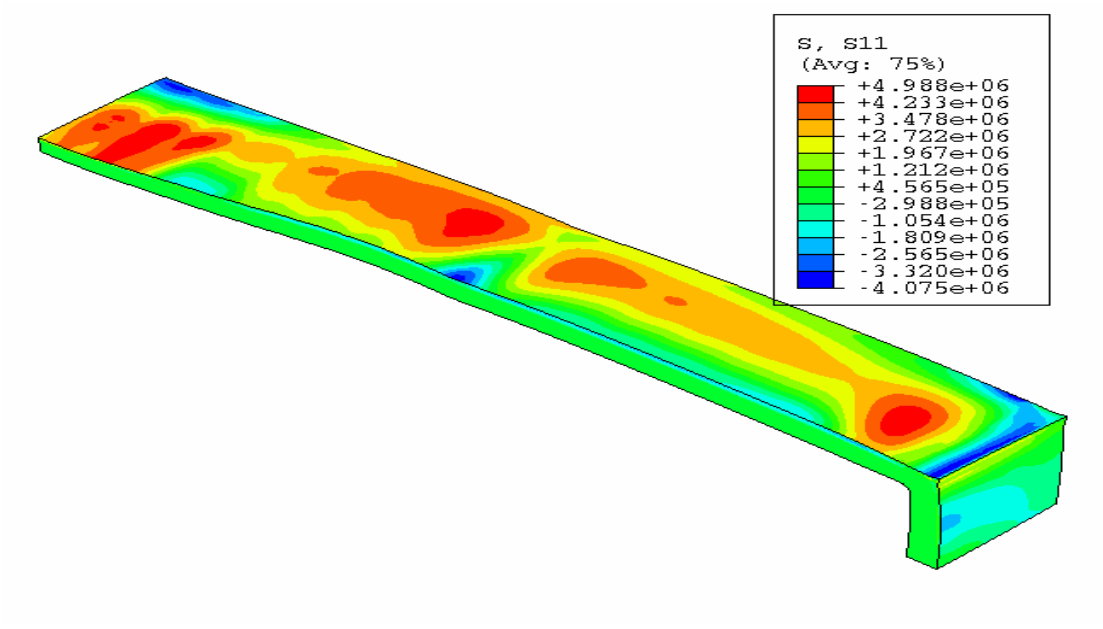

. Fig. 10.18 Transverse stress contour when domain bottom is 5 sec. below meniscus

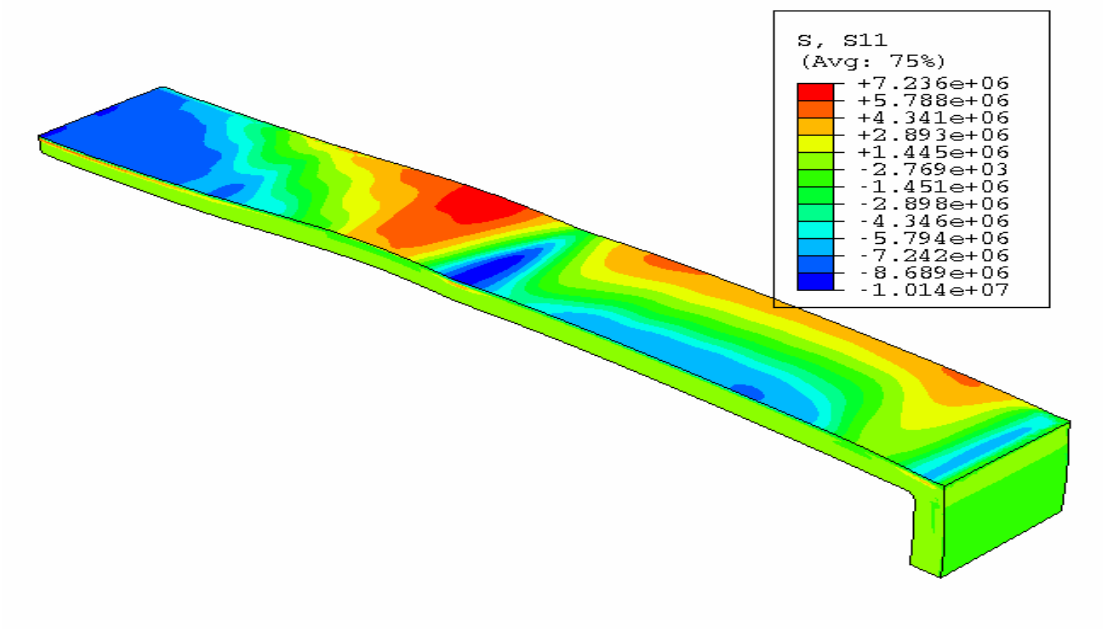

Fig. 10.19 Transverse stress contour when domain bottom is 12 sec. below meniscus

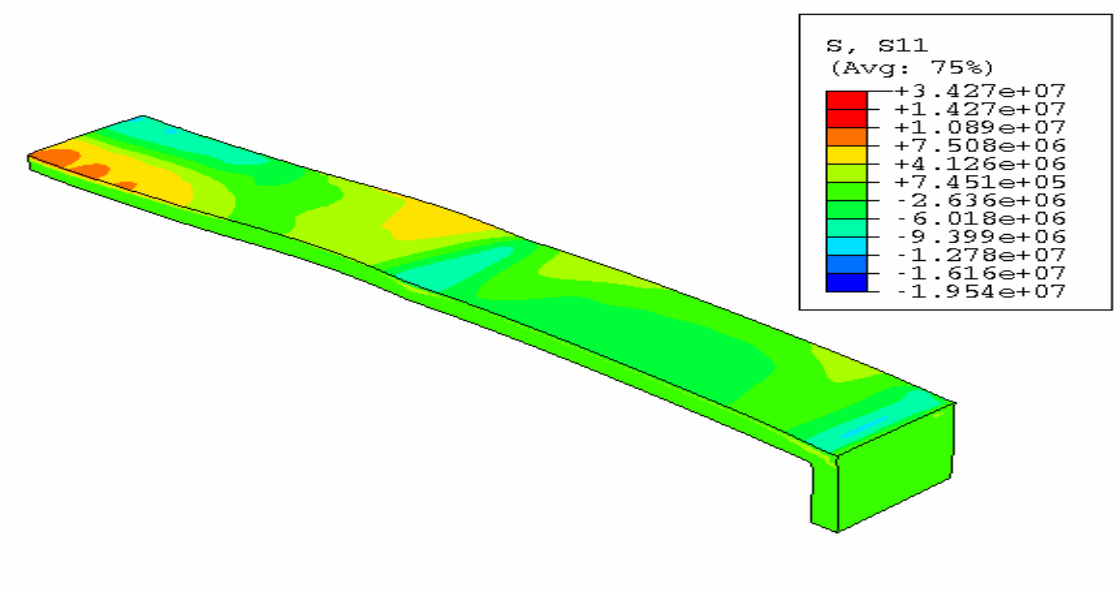

Fig. 10.20 Transverse stress contour when domain bottom is 15.8 sec. below meniscus

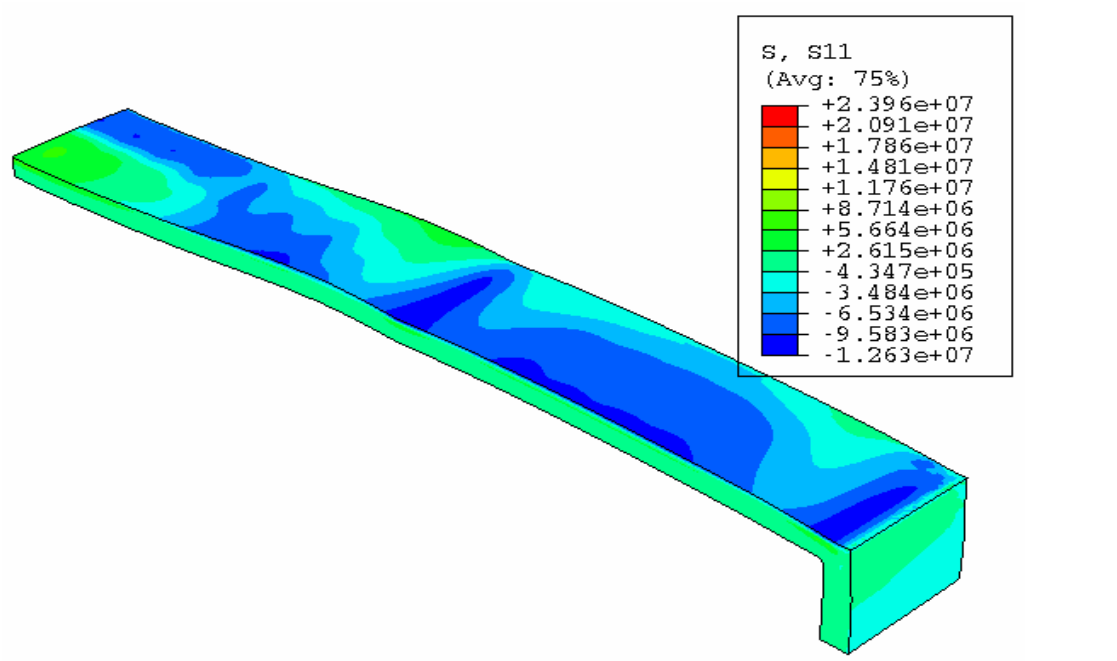

Fig. 10.21 Transverse stress contour when domain bottom is 19 sec. below meniscus

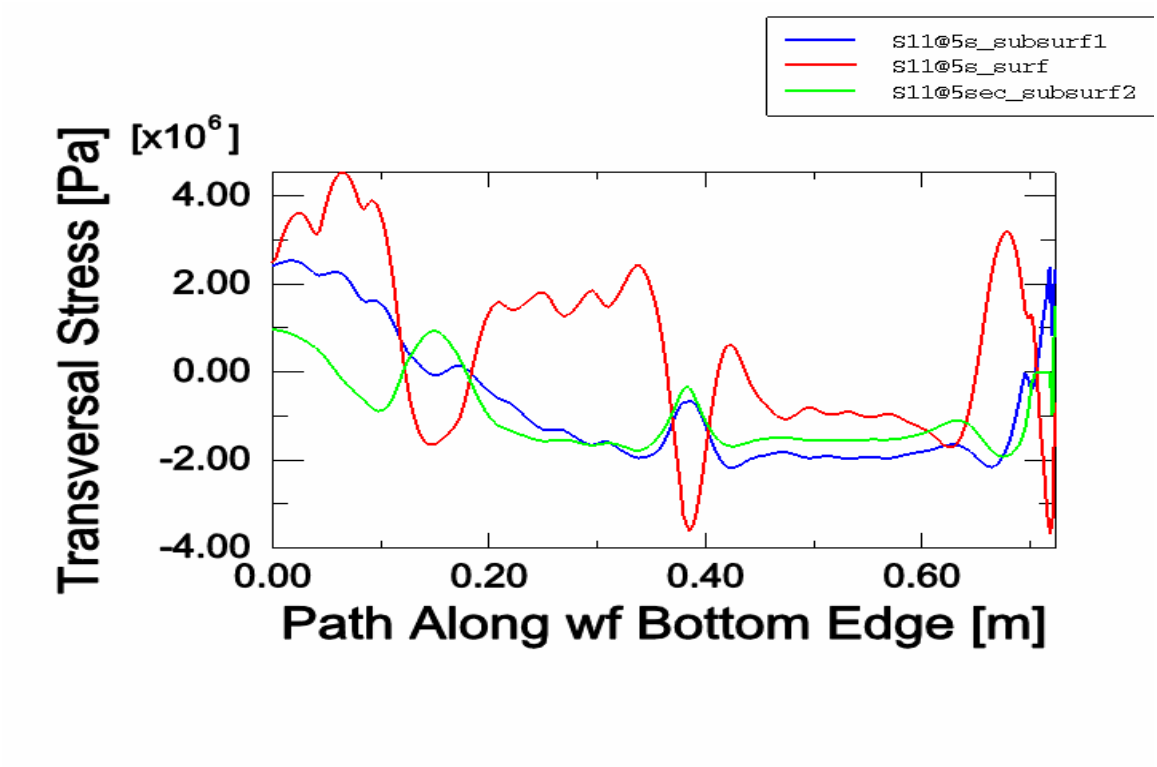

Fig. 10.22 Transverse stress profile along bottom edge wide face at 5 sec.

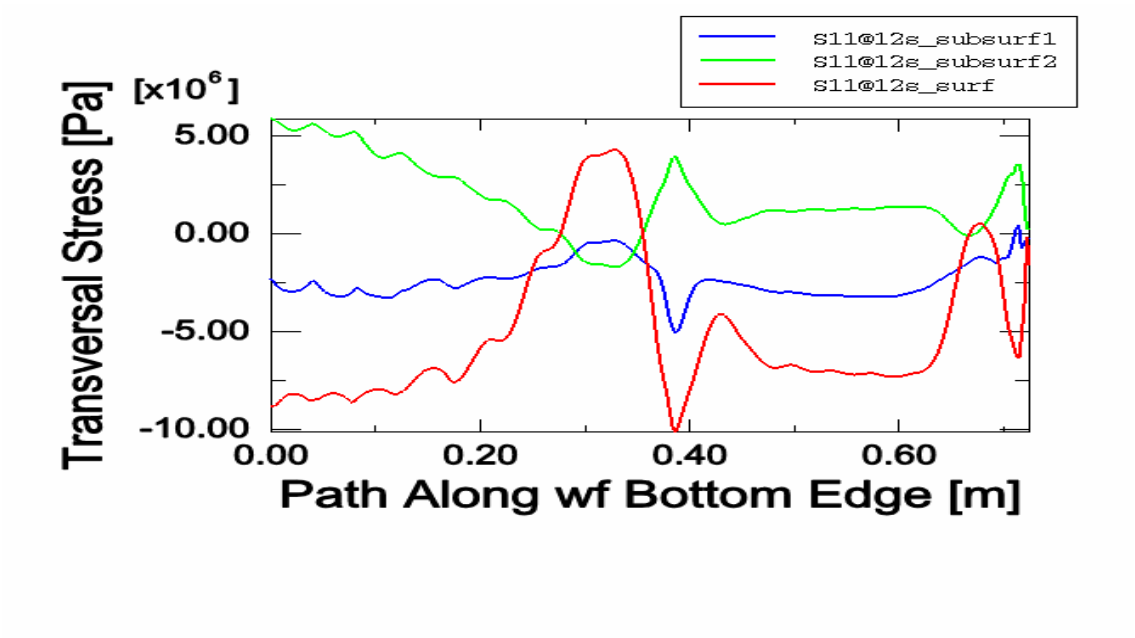

Fig. 10.23 Transverse stress profile along bottom edge wide face at 12 sec.

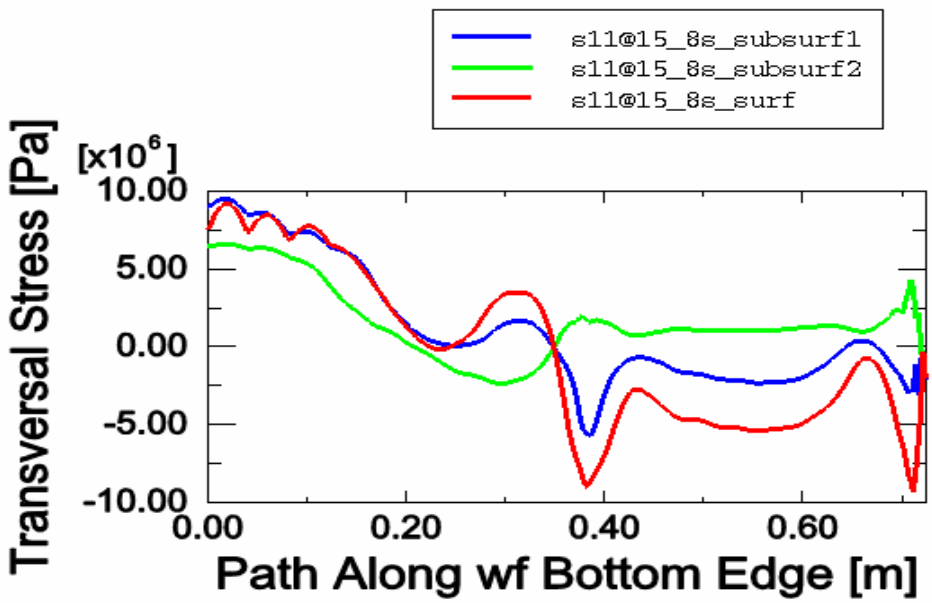

Fig. 10.24 Transverse stress profile along bottom edge wide face at 15.8 sec.

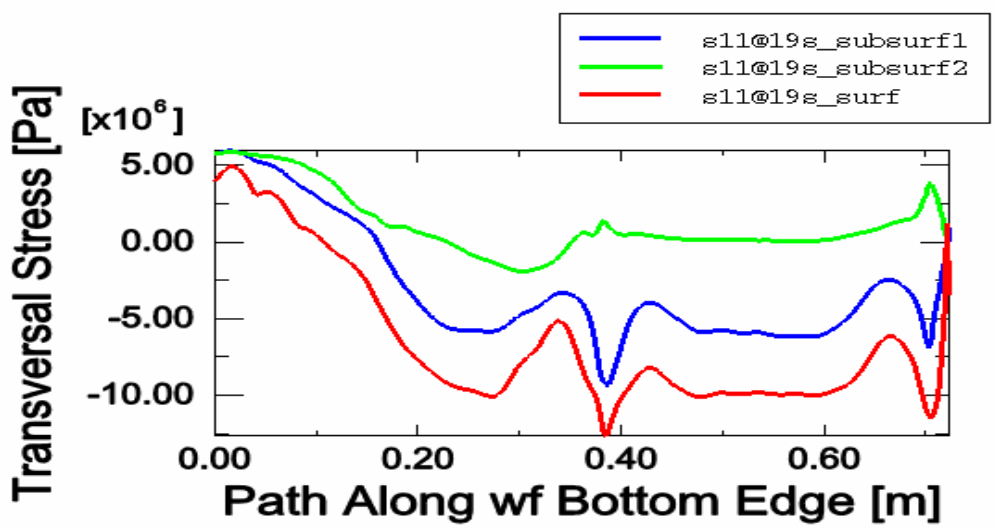

.Fig. 10.25 Transverse stress profile along bottom edge wide face at 19 sec.

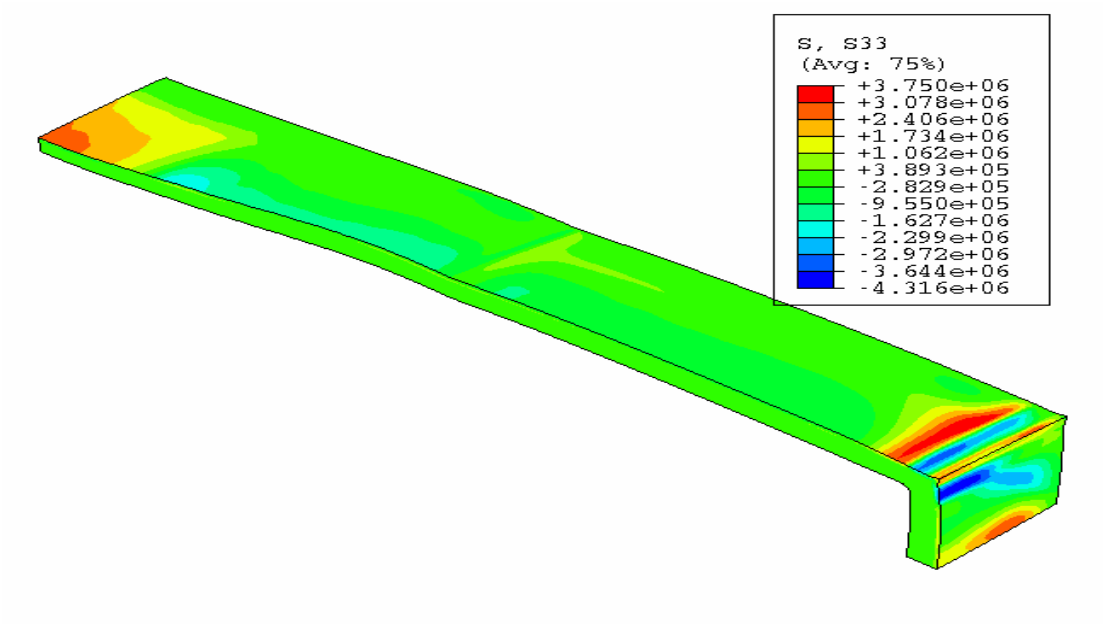

Fig. 10.26 Axial stress contour when domain bottom is 5 sec. below meniscus

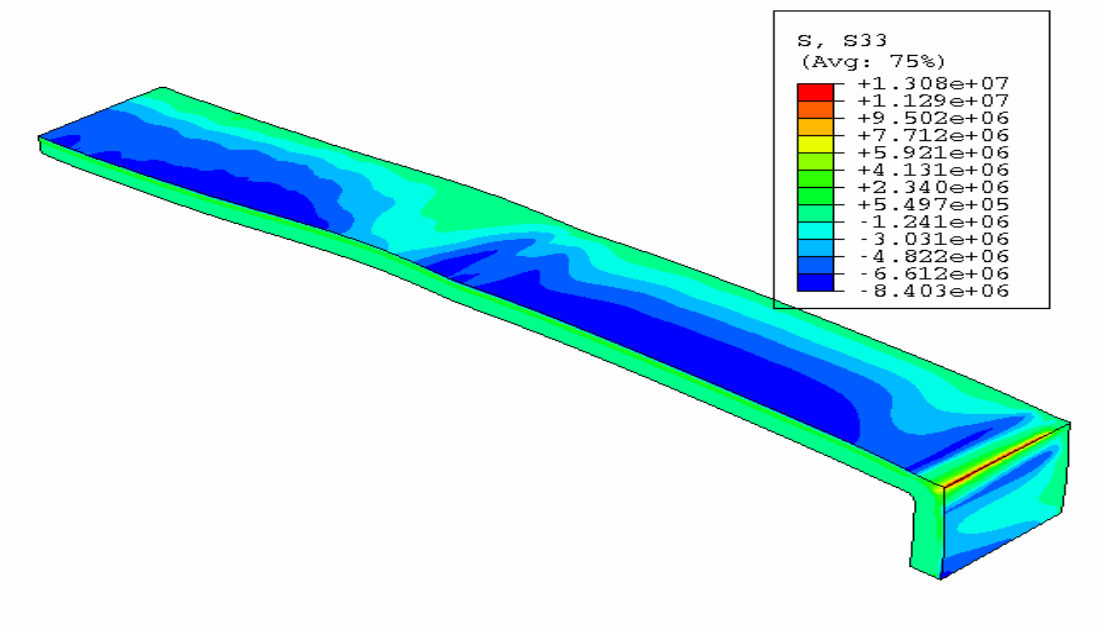

Fig. 10.27 Axial stress contour when domain bottom is 12 sec. below meniscus

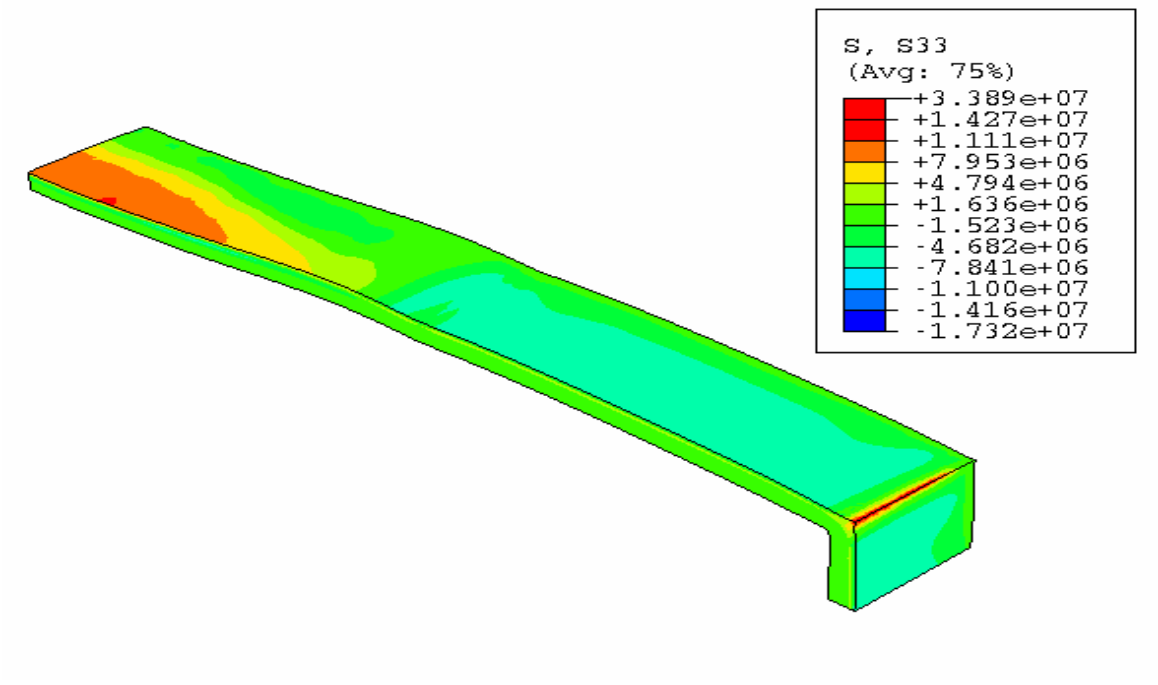

Fig. 10.28 Axial stress contour when domain bottom is 15.8 sec. below meniscus

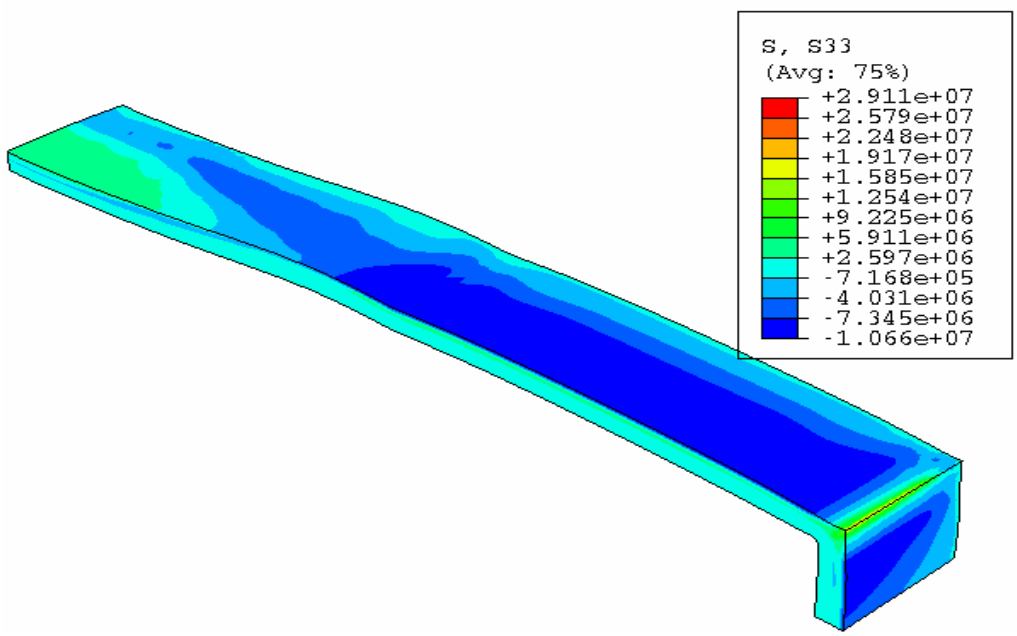

Fig. 10.29 Axial stress contour when domain bottom is 19 sec. bellow meniscus

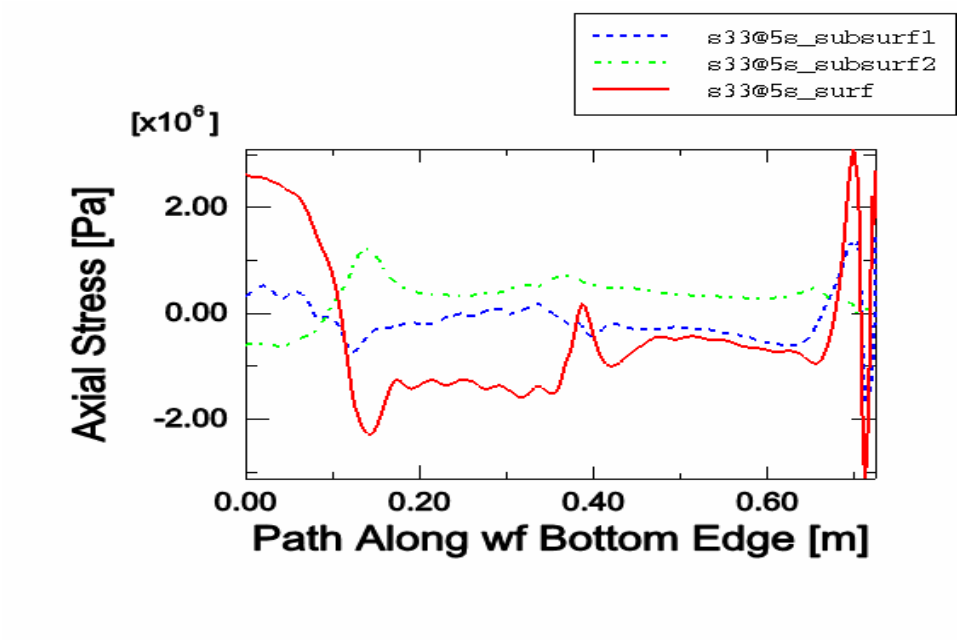

Fig. 10.30 Axial stress profile along bottom edge (wf) at 5 sec.

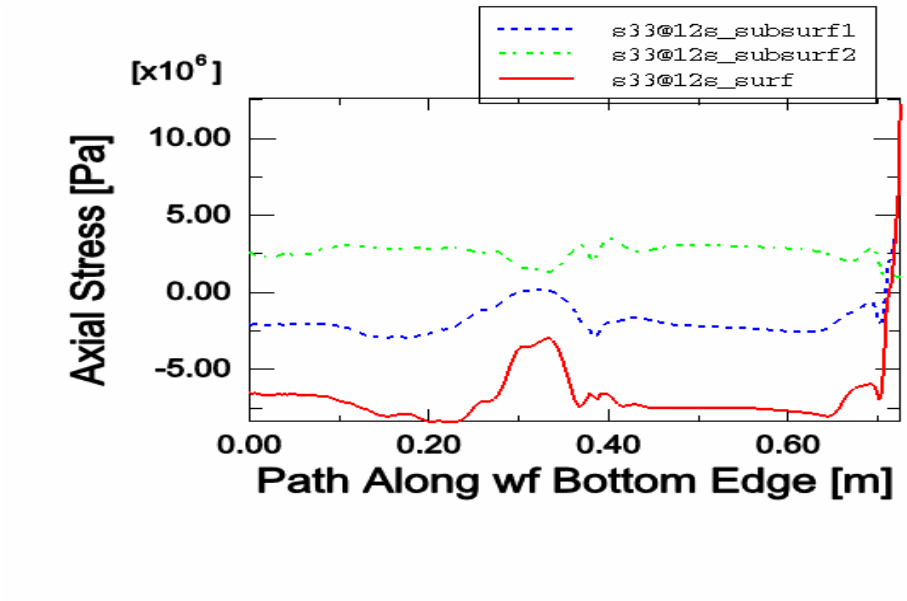

Fig. 10.31 Axial stress profile along bottom edge (wf) at 12 sec.

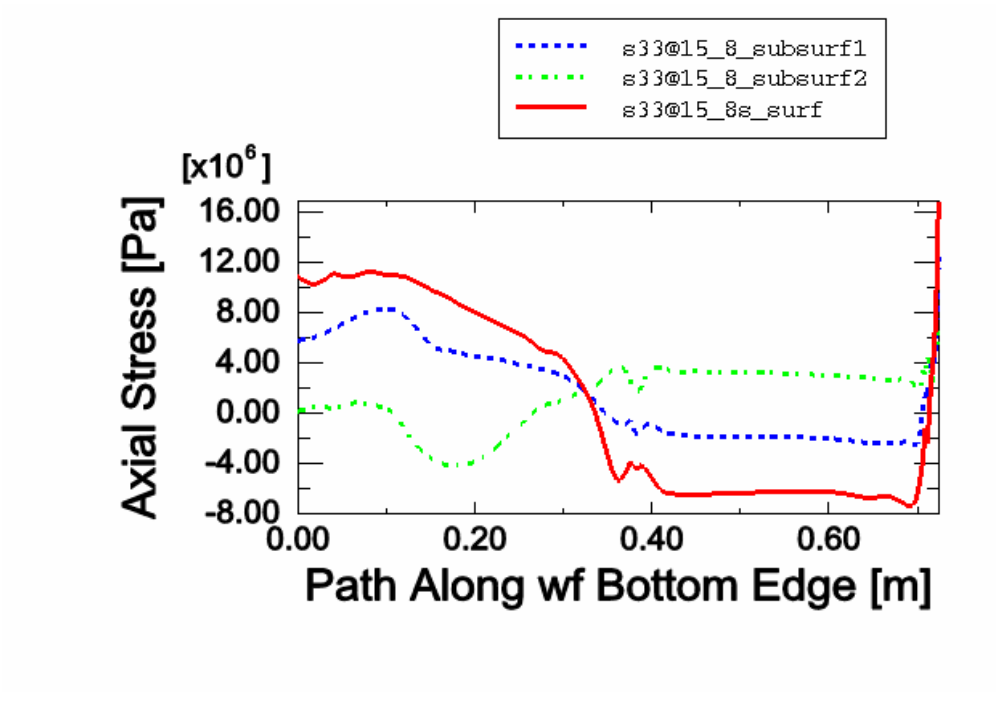

Fig. 10.32 Axial stress profile along bottom edge (wf) at 15.8 sec.

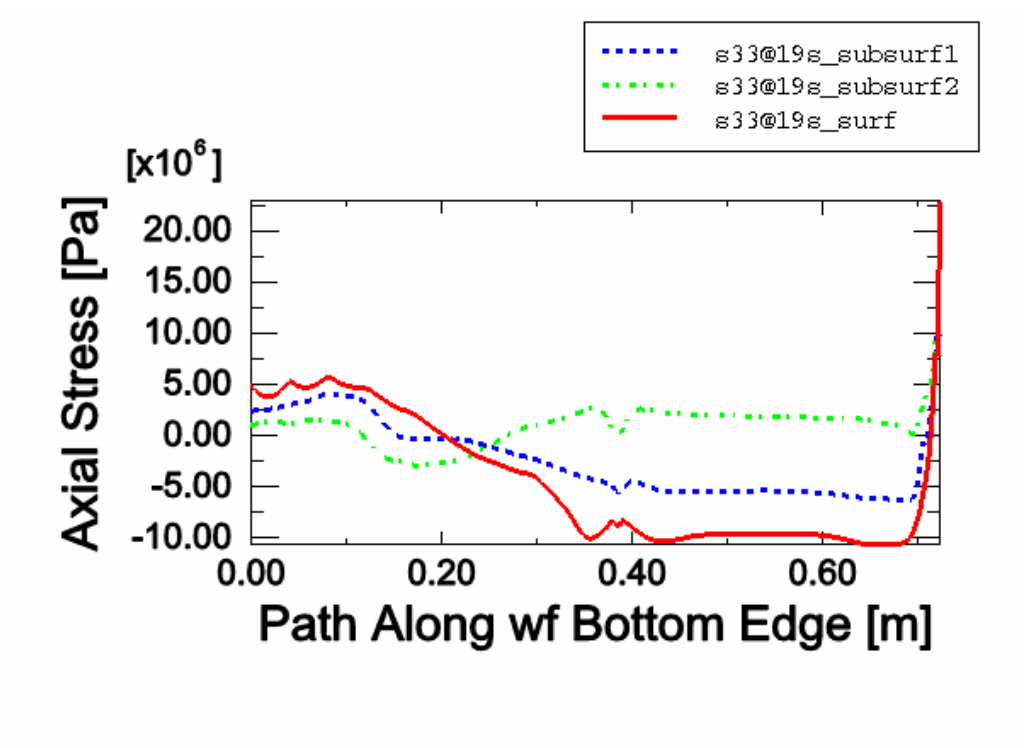

Fig. 10.33 Axial stress profile along bottom edge (wf) at 19 sec.

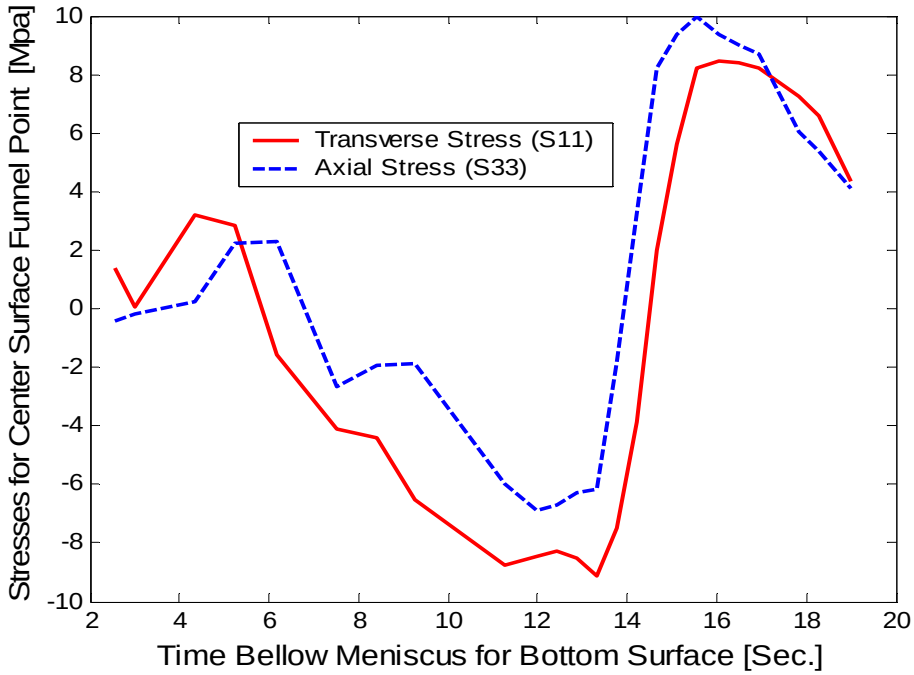

Fig. 10.34 Stress histories for a center bottom surface wf point.

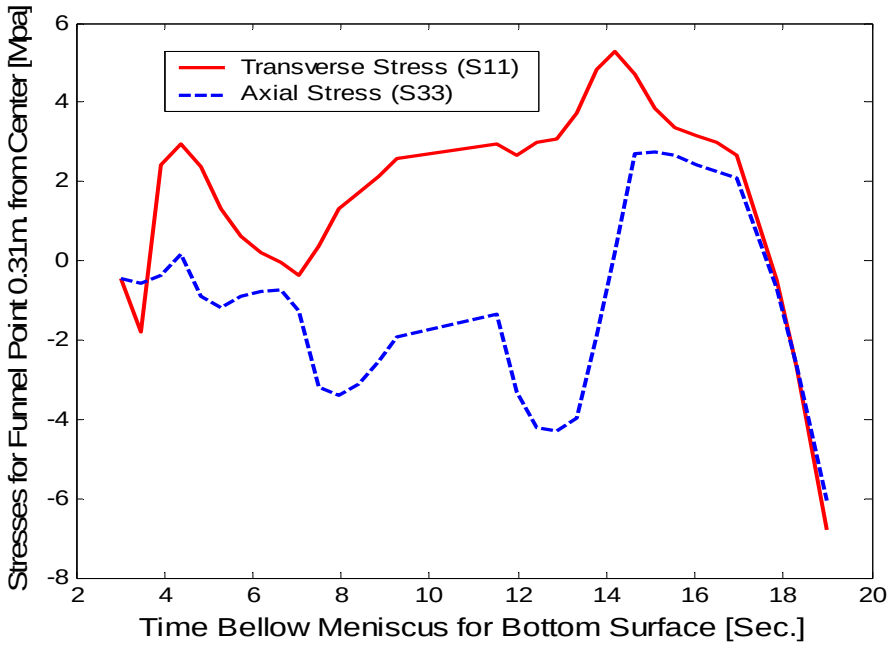

Fig. 10.35 Stress histories for a bottom surface wf Point, 0.31 m from a center, at the funnel outer bend.

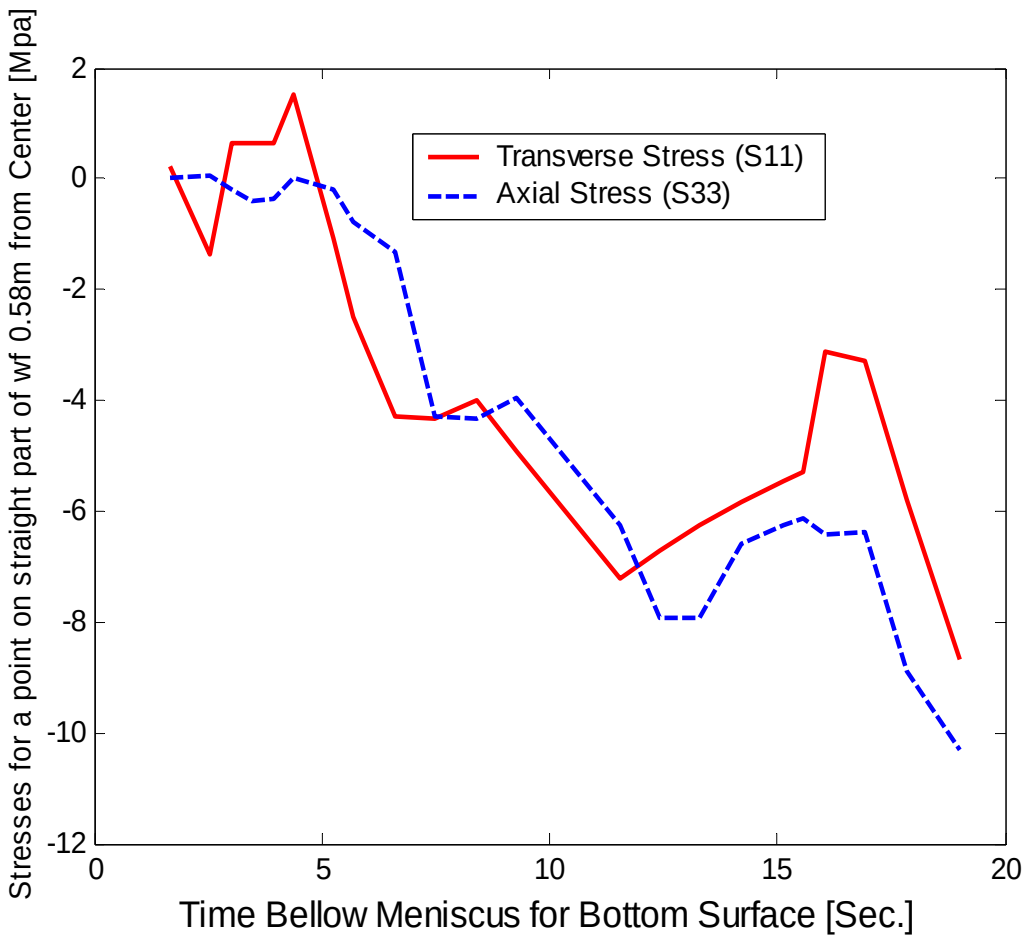

Fig. 10.36 Stress histories for a bottom surface wf point, 0.58 m from a center, at the straight part.

Table 10.I The thin slab with funnel simulation conditions

Strand Thickness [mm]	90
Slab width [mm]	1500
Working mould length [mm]	1200
Funnel depth at the meniscus [mm]	40
Funnel depth at bottom of mold [mm]	6
Casting speed [m/min]	3.6
Softened Contact Coefficients: c_0 and p_0	$5*10^{-4}$, 10^5
Friction Coefficient (Mold/Shell)	0.1
Steel grade [%C]	0.27
Liquids temperature [C]	1500.7
Solidus temperature [C]	1411.79
Initial strand temperature [C]	1540.
Time to apply ferrostatic pressure [sec]	0.
Number of elements	103182
Number of nodes	219332
Total number of dofs	430444

Chapter 11. Summary and Future Work

11.1 Summary of this work

A computationally efficient local integration algorithm from an in-house code CON2D has been implemented into a general purpose commercial finite element code Abaqus via user-defined subroutine UMAT to solve for thermal stresses, strains and displacement in realistic solidification process which involve highly nonlinear constitutive relations and temperature dependant material properties.

A class of highly nonlinear thermal-mechanical solidification problems is solved using several different local-global methods. The elastic-visco-plastic constitutive laws are integrated locally by using four different integration methods. In addition to the local integration methods built into Abaqus, two new integration methods are coded into Abaqus material user subroutine UMAT. Two special treatments for treating the liquid/mushy zone with a fixed grid approach are presented and compared. At the global level, the full Newton-Raphson method built into Abaqus finite element solution procedure is compared with the alternating implicit-explicit method of CON2D. Results of both numerical codes are validated against a semi-analytical solution. While the results are matching extremely well, the performance of Abaqus with the UMAT-coded methods is increased by ~ 20 times relative to the built-in methods and become comparable to CON2D.

This work has opened the door for large-scale realistic finite-element simulations of continuous casting and other solidification processes with highly nonlinear viscoplastic phenomena. More

features are implemented into Abaqus solidification models. These include: an increment-wise thermo-mechanical coupling, thermo-mechanical contact between mold wall and shell including gap dependant conductivity coded into Abaqus GAPCON subroutine, ferrostatic pressure on the solidifying shell coded into Abaqus subroutine DLOAD, taper and mold distortion coded into Abaqus subroutine DISP, and phase dependant constitutive laws (delta-ferrite and austenite). With the parallel solvers built into Abaqus on the latest computing platforms, this methodology has enabled realistic 2D generalized plane-strain coupled thermo-mechanical simulations of billet casting and later beam blank casting with complex geometry. Finally, a highly computationally intensive 3D solidification simulation of a thin-slab casting with funnel is performed. It has provided new valuable insights into a complex mechanical state of transverse and axial stress of the solidifying shell retracted by the funnel geometry.

11.2 Future Work Recommendations

- More realistic spatially and time dependant thermal flux boundary conditions from a real plant measurements along with proper steel grade and taper data should be used for the future 2D beam blank and 3D thin-slab simulations.

- Temperature and flux results from the beam-blank and thin-slab simulations should be verified against experimental plant measurements and used to further calibrate the models.

- Apply the model from this work to solve variety of practical continuous casting problems and improve the process efficiency and quality of the products such as:

  -taper optimization

  -prediction of breakouts due to shell thinning in hot spots

  -understanding the causes of surface depressions and longitudinal cracks

  -development of transverse. cracks due to withdrawal forces overcoming friction

  -hot tearing crack prediction in mushy/liquid zone

  -thermo-mechanical behavior of solidifying shell bellow mold and more.

- Gain more insights into some other solidification processes like aluminum continuous casting or welding.

- Follow the investigation of the memory problems that occurred late in the 3D simulation. Perhaps re-run the 3D simulation with the newest Abaqus distributed memory solver v6.6, which apparently scales better and uses memory more wisely, and which is scheduled for the release in late 2006.

- Use the stress and inelastic strain results from this work for failure predictions and improve UMAT to automatically calculate damage strains that can be contoured with Abaqus/CAE.

- Explore the ways to use Abaqus/Explicit based on an explicit finite element formulation. Though Abaqus/Explicit is primarily written for dynamics problems, it has been very

effectively used for highly nonlinear quasi-static problems with contact. The user subroutine UMAT developed in this work for implicit formulation should be re-written into VUMAT used to describe material constitutive behavior with explicit formulation. Abaqus/Explicit solver has showed almost an order of magnitude better parallel scaling than implicit parallel solvers. If this transition to Abaqus/Explicit is successful, coupled thermo-mechanical simulations of even larger 3D domains will be realistic.

- Abaqus Inc. is providing fluid-solid interface (FSI) capabilities. Since a large amount of CFD continuous casting research is preformed with Fluent, this will allow achieving an ultimate goal, a fully coupled 3D fluid-thermo-mechanical analysis of continuous casting and other related solidification processes.

Appendix. GAPCON Subroutine

```
      subroutine gapcon(ak,d,flowm,temp,predef,time,ciname,
     1  slname,msname,coords,noel,node,npred,kstep,kinc)
c
      include 'aba_param.inc'
c
      character*80 ciname,slname,msname
      dimension flowm(2),temp(2),predef(2,*),
     1          ak(5),d(2),coords(3),time(2)

c-------------------------------------------------------
CCCCCCCCCCCCCCCCCCCCCCCCCCCCCCC

      tshell= temp(1) + 273.15
      tmold = temp(2) + 273.15
cc
      vel = 0.6
      z = (vel / 60.d0) * TIME(1)
ccc
      rkair = 0.06
      rkpow = 1.00
      h0mold = 3000.
      tcrys = 1030.0 + 273.0
      tsoft = 1150.0 + 273.0
      hcrys = 1000.0
      hsoft = 2000.0
      hsol =  6000.0
      hliq =  3.e6
c
c     The values of powmax and powmin are obtained from CON1D
c
            if(z .gt. 0.1)   powmax = (0.408 + 0.613*z - 0.229*z**2)*1.d-3
            if(z .le. 0.1)   powmax = (0.3422 + 0.712*z)*1.d-3
            if(z .le. 0.018) powmax= (0.412-8.55*z+275*z**2)*1.d-3
            powmin = powmax - 0.05d-3
      e1 = 0.8
      e2 = 0.5
c
c           Calculate new emmissivity based on refractive index
c
            rindex = 1.5
            ad = 200
            emiss = rindex**2/(0.75*ad*powmax + 1./e1 + 1./e2 - 1.)
c
c     Calculates heat radiation of GAP
c
```

```
      hradgap = 5.669d-8*emiss*(tshell+tmold)*
     +         (tshell*tshell+tmold*tmold)
c
c     Linear interpolation with temperature for contact convection
c       coefficient with temperature
c
      h0shell = hsol + (hliq-hsol) * (tshell-tsol-273.)/(tliq-tsol)
      if(tshell.lt.(tsol+273.))
     +  h0shell = hsoft + (hsol-hsoft)*(tshell-tsoft)/(tsol+273.-tsoft)
      if(tshell.lt.tsoft)
     +  h0shell = hcrys + (hsoft-hcrys)*(tshell-tcrys)/(tsoft-tcrys)
      if(tshell.lt.tcrys) h0shell = hcrys
      h0shell = hliq
c-----------------------------------------------------------------------
cCCCCCCCCCCCCCCCCCCCCCCCCCCCCCCCCCCCCCCCCCCCCCCCCCCCCCCCCCCCCCCCCCCCCCCCCCCCcCC

c
        if(d(1).lt.powmin) d(1) = powmin
        if(d(1).lt.powmax) then
          powgap = d(1)
          airgap = 0.0
        else
          airgap = d(1) - powmax
          powgap = powmax
        endif
c
c       Determination of the contact resistance between the shell and
c       powder.
c
        reshell = 1./h0shell
c
c       Calculation of gap heat transfer
c
        rgap = 1./hradgap*(1./h0mold+powgap/rkpow+airgap/rkair+reshell)
     +         /(1./hradgap+1./h0mold+powgap/rkpow+airgap/rkair+reshell)


        AK(1) = 1.d0 / rgap
CCCCCCCCCCCC D E B U G CCCCCCCCCCCCCCCCCCCCC
        return
        end
```

References

1. Abaqus Standard User Manuals v6.5 *Abaqus Inc.*, 2005

2. J.H. Weiner and B.A. Boley, Elasto-plastic thermal stresses in a solidifying body, *J. Mech. Phys. Solids,* 11, 1963, 145-154

3. Li, C. and B.G. Thomas, Thermo-Mechanical Finite-Element Model of Shell Behavior in Continuous Casting of Steel, *Metal. & Material Trans. B.*, 2004. 35B(6): p. 1151-172.

4. Continuous Casting Consortium Website, ***http://ccc.me.uiuc.edu*** [30 October 2005]

5. H. Zhu, Coupled thermal-mechanical finite-element model with application to initial solidification, *Ph.D Thesis University of Illinois,* 1993

6. A. Moitra, B.G.Thomas and H Zhu, Application of thermo-mechanical model for steel behavior in continuous slab casting, *Proc. 76th Steelmaking Conference, ISS, 76*, 1993

7. Meng, Y. and B. G. Thomas, Heat transfer and solidification model of continuous slab casting: Con1d, *Metall. Trans. B* (In press).

8. Li C, Thermal-Mechanical Model of solidifying steel shell behavior and its applications in high speed continuous casting of billets, *Ph.D Thesis University of Illinois,* 2005

9. J. Parkman, Simulation of thermal-mechanical behavior during initial solidification of steel, *MS. Thesis University of Illinois,* 2000

10. Mizukami, H., S. Hiraki, M. Kawamoto, and T. Watanabe, Initial Solidification Behavior of Ultra Low, Low and Middle Carbon Steel, *ISIJ International, 1999*. 39(12): p. 1262-1269.

11. Bernhard, C., H. Hiebler, and M. Wolf, Simulation of Shell Strength Properties by the SSCT Test, *ISIJ International., 1996.* 36: p. S163-S166.

12. Suzuki, M., M. Suzuki, C. Yu, and T. Emi, In-Situ Measurement of Fracture Strength of Solidifying Steel Shells to Predict Upper Limit of Casting Speed in Continuous Caster with Oscillating Mold, *ISIJ International, 1997*. 37(4).

13. Moitra, A., B.G. Thomas, and W. Storkman, Thermo-mechanical model of Steel Shell Behavior in the Continuous Casting Mold, *in Proceedings of TMS Annual Meeting. 1992. San Diego, CA*

14. B.G. Thomas, Continuous Casting, *The Encyclopedia of Materials: Science and Technology., D. Apelian, ed., Elsevier Science Ltd., Oxford, UK*, vol. 2, Oct. 31, 2000.

15. Tien R. and Kaump V., Thermal Stresses During Solidification on Basis of Elastic Model, *ASME Journal of Applied Mechanics* 36(1969) p763-767

16. Cross M., Control Volume Model of Fluid Flow, Solidification and Stress, *Thames Polytechnic, London* 1992

17. Hattel J., P. N. Hansen, and L.F. Hansen, Analysis of Thermal Induced Stresses in Die Casting Using a Novel Control Volume FDM-Technique, *Proceedings Modeling of Casting Welding and Advanced Solidification Process VI*, Palm Coast, FL, March 21-26 1993

18. J. Lee, T. Yeo, Kyu H. OH, J. Yoon, and U. Yoon, Prediction of Cracks in Continuously Cast Steel Beam Blank through Fully Coupled Analysis of Fluid Flow, Heat Transfer, and Deformation Behavior of a Solidifying Shell, *Metal. And Materials Transactions A*, 31A, January 2000

19. Heinlein M, S. Mukherjee, and O. Richmond, A Boundary Element Method Analysis of Temperature Fields and Stresses During Solidification, *Acta Mechanica* 59 (1986) p59-81

20. Barber, B. and A. Perkins, Strand deformation in continuous casting, *Ironmaking and Steelmaking* 16(6), (1989), p406-411

21. Yu, L., FEM Analysis of Bulging Between Rolls in Continuous Casting, *Master thesis, Mechanical and Industrial Engineering, University of Illinois* (2000).

22. Kelly, J. E., K. P. Michalek, T. G. O'Connor, B. G. Thomas and J. A. Dantzig, Initial development of thermal and stress fields in continuously cast steel billets, *Metall. Trans. A,* 19A(10), (1988), p2589-3602

23. Tatsumi, N., Z. G. Wang and T. Inoue, Simulation of temperature and elastic-plastic stresses in solid shell during continuous casting process, *TRANS. JAPAN SOC. MECH. ENG. (SER. A)* 55(514), (1989), p1389-1393

24. Grill, A., K. Sorimachi and J. K. Brimacombe, Heat flow, gap formation and break-outs in the continuous casting of steel slabs, *Metall. Trans. B* 7B(2), (1976), p177-189

25. Grill, A., J. K. Brimacombe and F. Weinberg, Mathematical analysis of stresses in continuous casting of steel, *Ironmaking and Steelmaking* 3(1), (1976), p38-47

26. Sorimachi, K. and J. K. Brimacombe, Improvements in mathematical modelling of stresses in continuous casting of steel, *Ironmaking Steelmaking* 4(4), (1977), p240-245

27. Sorimachi, K. and T. Emi, Elastoplastic stress analysis of bulging as a major cause of internal cracks in continuously cast slabs, *Tetsu-to-Hagane (J. Iron Steel Inst. Jpn.)* 63(8), (July 1977), p1297-1304

28. Rammerstorfer, F. G., D. F. Fischer and C. Jaquemar, Nonlinear analysis of the states of stress and deformation during a metal casting process, *MIT-Report (K. J. Bathe), MIT* (1979),

29. Rammerstorfer, F. G., C. Jaquemar, D. F. Fischer and H. Wiesinger, Numerical Methods in Thermal Problems, *Pineridge Press*, 1979, p712-722

30. Rammerstorfer, F. G., C. Jaquemar, D. F. Fischer and H. Wiesinger, Thermal and thermo-mechanical behavior in the shell of continuously cast strands – mathematical approach, In *Proc. CCC'79, Linz.* (1979).

31. Kristiansson, J. O., Thermal stresses in the early stage of solidification of steel, *J.Therm. Stresses* 5(3-4), (1982), p315-330

32. Kristiansson, J. O., Thermomechanical behavior of the solidifying shell within continuous-casting billet molds{a numerical approach), *J. Therm. Stresses* 7(3-4), (1984), p209-216

33. Kinoshita, K., T. Emi and M. Kasai, Thermal elasto-plastic stress analysis of solidifying shell in continuous casting mold, *Tetsu to Hagane,* 14, *(*1979), p2022-2031.

34. F. Wimmer, H. Thone, and B. Lindorfer, Thermomechanically-coupled analysis of the steel solidification process in continuous casting mold, *Abaqus Users Conference*, 1996, p749-769

35. Thomas, B. G. and W. R. Storkman, Mathematical models of continuous slab casting to optimize mold taper, In *Modeling and Control of Casting and Welding Process*, G. J. A. A. F. Giamei, ed., Palm Coast, FL (April 1988), p. 287 297

36. Thomas, B. G., W. R. Storkman and A. Moitra, Optimizing taper in continuous slab casting molds using mathematical models, In *6th International Iron and Steel Congress*, ISIJ, ed., Vol. 3, (ISIJ, Nagoya, Japan, 1990), p348-355

37. Thomas, B. G. and H. Zhu, Thermal distortion of solidifying shell near meniscus in continuous casting of steel, In *JIM/TMS Solidification Science and Processing Conference*. Honolulu, HI (Dec. 1995).

38. G.Thomas, B., A. Moitra and R. McDavid, Simulation of longitudinal off-corner depressions in continuously cast steel slabs, *Iron and Steelmaker* 23(4), (Apr.1997), p57-70.

39. Thomas, B. G. and J. T. Parkman, Simulation of thermal mechanical behaviour during initial solidification, In *Thermec '97 Intl. Conf. on Thermomechanical Proc. of Steel and Other Materials*, TMS, ed., Vol. II, (TMS, Warrendale, PA,Wollongong, Australia, 1997). P2279-2285.

40. Park, J. K., Analysis of thermo-mechanical behavior in billet casting, In *83rd Steel- making Conference*, ISS-AIME, ed., Vol. 83 (ISS-AIME, Warrendale, PA, 2001).

41. Park, J. K., C. Li, B. G. Thomas and I. V. Samarasekera, Analysis of thermo-mechanical behavior in billet casting, In *60th Electric Furnace Conference*, ISS-AIME,ed., Vol. 60, (ISS-AIME, Warrendale, PA, San Antonio, TX, 2002).

42. Park, J. K., B. G. Thomas and I. V. Samarasekera, Analysis of thermal-mechanical behavior in billet casting with different mould corner radius, *Ironmaking and Steelmaking* 29(5), (2002), p359-375.

43. Tszeng, T. C. and S. Kobayashi, Stress analysis in solidification processes: Application to continuous casting, *INT. J. MACH. TOOLS MANUF.* 29(1), (1989), p121-140.

44. Mizoguchi, T., S. Ogibayashi and T. Kajitani, Mathematical model analysis on the growth of initially solidified shell, *Iron and Steel* 81(10), (1995).

45. Boehmer, J. R., F. N. Fett and G. Funk, Analysis of high-temperature behavior of solidified material within a continuous casting machine, *Computer & Structures* 47(4-5), (1993), p683-698.

46. Funk, G., J. R. Bohmer, F. N. Fett and R. Hentrich, Coupled thermal and stress-strain models for the continuous casting of steels, *Steel Research (Germany)* 64(5), (1993), p246-254.

47. Funk, G., J. R. Boehmer and F. N. Fett, A coupled fdm/fem model for the continuous casting process, *Int. J. Comput. Appl. Technol.* 7(3-6), (1994), p214-228.

48. Boehmer, J. R., G. Funk, M. Jordan and F. N. Fett, Strategies for coupled analysis of thermal strain history during continuous solidification processes, *Advances in Engineering Software* 29(7-9), (1998), p679-697.

49. Han, H. N., J. E. Lee, T. J. Yeo, Y. M. Won, K. Kim, K. H. Oh and J. K. Yoon, A Finite element model for 2-dimensional slice of cast strand, *ISIJ International* 39(5), (1999), p445-455.

50. S. Koric, B.G. Thomas, Efficient Thermo-Mechanical Model for Solidification Processes, *International Journal for Numerical Methods in Engineering,* 2006, In Press.

51. Huespe, A. E., A. Cardona and V. Fachinotti, Thermomechanical model of a continuous casting process, *Computer Methods in Appl. Mech. & Engr.* 182(3), (Feb. 2000), p439-455.

52. V.D. Fachinotti and A. Cardona, A fixed-mesh Eularian-Lagrangian approach for stress analysis in continuous casting, *Instituto Argentina de Siderurgia, Argentina*, 2002.

53. Wray, P. J.. Plastic deformation of delta-ferrite iron at intermediate strain rates, *Metall. Trans. A* 7A, (1976), p1621-1627.

54. Wray, P. J., Effect of carbon content on the plastic flow of plain carbon steels at elevated temperatures, *Metall. Trans. A* 13A, (1982), p125-134.

55. Wray, P. J., High temperature plastic flow behavior of mixtures of austenite, cementite, ferrite, and pearlite in plain-carbon steels, *Metall. Trans. A* 15A, (1984), p2041-2058.

56. Seol, D. J., Y. M. Won, T.-J. Yeo, K. H. Oh, J. K. Park and C. H. Yim, Hightemperature deformation behavior of carbon steel in the austenite and ±-ferrite regions, *ISIJ International* 39(1), (1999), p91-98

57. Suzuki, T., K.-H. Tacke, K. Wunnenberg and K. Schwerdtfeger, Creep properties of steel at continuous casting temperatures, *Ironmaking and Steelmaking* 15(3), (1988), p90-100.

58. Kim, K., N. Han, T. Yeo, Y. Lee, H. Oh, and D. N. Lee, Analysis of surface cracks in continuously cast beam blank, *Ironmaking and Steelmaking* 24(3), (1997), p249-256.

59. Manes A. A. I., Thermo-elastic Stress Analysis to Predict Design Parameters of Continuous Casting, *Journal of Materials Sciences,* 27(1992), p4097-4106.

60. Thorborg, J. and J. Hattel, Thermo-elasto-plasticity in solidification process using the control volume method applied on staggered grid, In *Modeling of Casting, Welding and Advanced Solidification Processes* (2003).

61. P.F. Kozlowski, B.G. Thomas, J.A. Azzi, and H. Wang, Simple constitutive equations for steel at high temperature, *Metallurgical Transactions,* 23A, 1992, p903-918.

62. A.M. Lush, G. Weber and L. Anand, An implicit time –integration procedure for a set of integral variable constitutive equations for isotropic elasto-viscoplasticity, *International Journal of Plasticity,* 5, 1989, p521-49.

63. Fiaer H.G., and A. Mo, ALSPEN – A Mathematical Model for Thermal Stresses in DC-Cast Al Billets, *Metallurgical Transactions B*, 21 (1990), p0169-1061.

64. Zabaras N. Y. and O. Richmond, Front tracking thermomechanical model for hypoelastic-viscoplastic behavior in a solidifying body, *Computer Methods in Applied Mechanics and Engineering* 81 (1990) p333-364.

65. Hannart B., F. Cialti, and R. Schalkwuk, Thermal Stresses in DC Casting of Aluminum Slabs: Application of a Finite Element Method, *Light Metals* (1994), p879-887.

66. Smelser R.E., and O. Richmond, Constitutive Model Effects on Stresses and Deformations in a Solidifying Circular Cylinder, In: *Modeling and Control of Casting and Welding Processes –IV*, Palm Cast, FL, 1988, p313-328.

67. Chen Y., and I.C. Sheng, On the Solid-Fluid Transition Zone in Welding Analysis. *ASME Journal of Engineering Materials and Technology*, 115, (1993), p17-23.

68. Hughes, T. J. R., R. L. Taylor, J. L. Sackman, A. Curnier and W. Kanoknukulchai. A finite element method for a class of contact-impact problems, *Computer Methods in Applied Mechanics and Engineering* 8, (1976), p249-276.

69. Hallquist, J. O., G. L. Goudreau and D. J. Benson, Sliding interfaces with contact-impact in large-scale lagrangian computations, *Computer Methods in Applied Mechanics and Engineering* 51, (1985), p107-137.

70. Bathe, K. J. and A. Chaudhary, A solution method for planar and axisymmetric contact problems, *International Journal for Numerical Methods in Engineering* 21, (1985), p65-88.

71. Kikuchi, N. and J. T. Oden, Contact Problems in Elasticity: A Study of Variation Inequalities and Finite Element Methods*, SIAM, Philaddephia*, 1988.

72. Belytschko, T. and O. M. Neal, Contact-impact by the pinball algorithm with penalty, projection, and largrangian methods, *In Computational Techniques for Contact, Impact, Penetration and Performation of Solids*. San Francisco, 1989.

73. Simo, J. C. and T. A. Laursen, An augmented largrangian treatment of contact problems involving friction, *Computers and Structures* , (1992), p97-116.

74. Alart, P. and A. Curnier, A mixed formulation for frictional contact problems prone to newton like solution methods, *Computer Methods in Applied Mechanics and Engineering* 92, (1991), p353-375.

75. Wriggers, P., J. C. Simo and R. L. Taylor, Penalty and augmented largrangian formulations for contact problems, *In NUMETA Conference.* Swansea (1985).

76. ANSYS 9.0, 2005, *Swanson Analysis Systems, Inc*., Houston, PA

77. T Belytschko, W. K. Liu, B. Moran, Nonlinear FE for Continua and Structures, *Wiley*, 2000

78. R.W.Lewis, K. Morgan, H.R.Thomas, KN.Seetharamu, The Finite Element Method in Heat Transfer Analysis, *Wiley,* 1996

79. J. A. Dantzig and C. L. Tucker III, Modeling in Materials Processing, *Cambridge University Press,* 2001

80. Abaqus Theory Manual v6.4. *Abaqus Inc.*, 2004

81. Lemmon, E.C., Multidimensional Integral Phase Change Approximations for Finite Element Conduction Codes, in Numerical Methods in Heat Transfer, R. Lewis, Editor. 1981, *John Wiley and Sons Ltd.* New York, NY. p. 201-213.

82. Dupont, T., G. Fairweather, and J. Johnson, Three-level Galerkin Methods for Parabolic Equations, *Siam J. Numerical Analysis,* 1974. 11: p. 392-410.

83. G.E. Mase and G. T. Mase, Continuum mechanics for engineers, *CRC Press Second Edition*, 1999

84. Thomas, B. G., J. K. Brimacombe, and I. V. Samarasekera, The Formation of Panel Cracks in Steel Ingots, A State of the Art Review, Part I--Hot Ductility of Steel, *Transactions of the Iron and Steel Society*, Vol. 7, 1986, pp. 7-20.

85. L. Anand, Constitutive equations for the rate dependant deformation of metals at elevated temperatures, *ASME Journal of Engineering Materials Technology*, 104, 1982, p12-17.

86. A. Mendelson, Plasticity: Theory and Applications, *Krieger Pub. Co* 1983

87. J. Lemaitre and J.L. Chaboche, Mechanics of Solid Materials, *Cambridge University Press*, 2001

88. O.C. Zienkiewicz and R.L. Taylor, Finite element method: solid and fluid mechanics dynamics and non-linearity, *McGraw-Hill*, 1991

89. D.C Stouffer and L.T. Dame, Inelastic Deformation of Metals: Models, Mechanical Properties, Metallurgy, *Willey*, 1995

90. D. Tortorelli, ME 444 Class Notes, *http://acm9.me.uiuc.edu/me444.html*, [Spring 2004]

91. J. C. Simo and R. L. Taylor, Consistent tangent operators for rate independent elastoplasticity, *Computer Methods in Applied Mechanics and Engineering*, 48, 1985, p101-118.

92. M.A. Crisfiled, Nonlinear FEA of Solids and Structures, *Wiley*, 1991

93. Y. M.A. Hashash, Analysis of Deep Excavation in Clay, *Ph.D Thesis, Massachusetts Institute of Technology*, 1992

94. Glowinski R. and P.L. Tallee, Augmented Lagrangian and Operator-Splitting Methods in Non-linear Mechanics, *SIAM,Philadelphia, PA*,1989

95. O.C. Zienkiewicz and I. C. Cormeau, Visco-plasticity-plasticity and creep in elastic solids-a unified numerical solution approach, *International Journal for Numerical Methods in Engineering,* 8, 1974, p821-845.

96. R.W.Lewis, K. Morgan, H.R.Thomas, KN.Seetharamu, The Finite Element Method in Heat Transfer Analysis. *Wiley,* 1996

97. Guidelines for writing user subroutine CREEP, Attachment to answer #805 from abaqus online support system, *http://www.abaqus.com* , [May 2005]

98. Zabaras N. and A. B. F. M. Arif, A family of Integration Algorithams for Constitutive Equations in Finite Difference Deformations Elasto-Viscoplasticity, *Int. J. Numerical Methods in Engineering*, vol 33, (1992), p59-84

99. S. Nemat-Nasser and Y.F. Li, A New Explicit Algorithm for Finite-deformation Elastoplasticity And Elastoviscoplasticity: Performance Evalution, *Computers & Structures*, vol. 44 (5), (1992), 937-963.

100. S. Nemat-Nasser and D.T. Chung, An explicit constitutive algorithm for large-strain, large-strain-rate elastic-viscoplasticity, *Computer Methods in Applied Mechanics and Engineering*, vol. 95, (1992), p205-219.

101. M. Rappaz, J. Drezet, M. Gremaud, A new hot-tearing criterion, *Metall. Mater. Trans*. A, 30A (1999), p449-455.

102. R.D. Pehlke, A. Jeyarajan and H. Wada, Summary of Thermal Properties for Casting Alloys and Mold Materials, *Report No. NSF/MEA-82028, Department of Materials and Metallurgical Engineering, University of Michigan,* 1982, PB83 211003.

103. K. Harste, Investigation of the shrinkage and the origin of mechanical tension during the solidification and successive colling of cylindrical bars of Fe-C alloys, *PhD Thesis, Technical University of Clausthal,* 1989

104. X. Huang, B.G. Thomas and F.M. Najjar, Modeling superheat removal during continuous casting of steel slabs, *Metallurgical Transactions B*, 23B, 1992, p339-56

105. K. Harste, A. Jablonka and K. Schwerdtfeger, Shrinkage and Formation of Mechanical Stresses During Solidification of Round Steel Strands, *4th International Conference Continuous Casting. Preprints. Vol. 2, (Brussels, Belgium), Verlag Stahleisen, P.O. Box 8229, D-4000, Dusseldorf 1, FRG,* 2, 1988, p633-644.

106. I. Jimbo and A. A. W. Cramb, The density of liquid iron--carbon alloys, *Metallurgical Transactions B (USA*, 24B (1), 1993, 5-10.

107. H. Mizukami, K. Murakami and Y. Miyashita, Elastic Modulus of Steels at High Temperaure, *J. Iron Steel Inst. Japan*., 63 (146), 1977, S-652.

108. Li, C. and B.G. Thomas, Maximum Casting Speed for Continuous Cast Steel Billets Based on Sub-Mold Bulging Computation, *Steelmaking Conf. Proc. 2002, ISS, Warrendale, PA: Nashville, TN*, March 10-13, 2002. p. 109-130.

109. C. Li, B. G. Thomas and C. Ojeda, Ideal Taper Prediction for High Speed Billet Casting, *Continuous Casting Consortium Report,* 2002

110. Matlab User Manual-Version 14, Mathworks Inc, Natick, MA 2005

111. MSC Patran 2001 Manuals, MSC Software, Santa Ana, CA, 2003

112. H. Hoedl, F. Wimmer, and K.F. Mayrhofer. VAI Beam Blank Casting Technology-Fundamentals and examples of plant installations, *Voest-Alpine Industrieanlagenbau GmbH & Co (VAI), Linz, Austria*., 2002

113. H. Omori, T. Ueda, H. Mizota, M. Yao, Y. Shinjo, and T. Fujimura, *Tetsu-to-Hagane,* 67, 1981, p1321-1330.

114. Kristin Carpenter. The Influence of Microalloying Elements on the Hot Ductility of Thin Slab Cast Steel, *PhD Thesis, University of Wollongong, Australia*, 2004

115. A. Cristallini, M. R. Ridolfi, A. Spaccarotella, R Caposti, G. Fleming and J. Sucker, Advanced Process Modeling of CSP Design for Thin Slab Casting of High Alloyed Steels, In *12th IAS Steelmaking Seminar and 2nd ISS Argentina Section Meeting*, Nov. 1999

116. Joong Kil Park, Brian G. Thomas, and Indira Samarasekera, Analysis of Thermo-Mechanical Behavior in Thin Slab Casting, *Internal Report University of British Columbia*, 2002

117. Kowaski Steel, *Private Communications*, 1996-1999

118. J. K. Park, B. G. Thomas, I. V. Samarasekera, and U. S. Yoon, Thermal and Mechanical Behavior of Copper Molds during Thin-Slab Casting (I): Plant Trial and Mathematical Modeling, *Metallurgical and Materials Transactions* B, 33B, Jun 2002

Author's Biography

Seid Koric was born on September 8,1967 in Sarajevo, Bosnia and Herzegovina. In 1993 he received his B.S. Degree in Mechanical Engineering from the University of Sarajevo with high honors. The onset of the war in Bosnia stopped him to continue with his graduate study. Instead, he joined a team of humanitarian workers in the Research and Development Center for Gas Technology from Sarajevo, who despite bombing, worked along with some international organizations to design, deploy, and establish a natural gas distribution, the only source of energy in the besieged city of Sarajevo.

In July of 1995, Seid and his wife Sanja were accepted as legal immigrants in USA. In the Fall of 1997 Seid started his graduate study in the Department of Aerospace Engineering at the University of Illinois at Urbana-Champaign. He completed his Master of Science degree advised by professor Harry H. Hilton in 1999, working in the area of viscoelasticity.

Since July 1999, Seid has been working as an engineering applications analyst at the National Center for Supercomputing Applications at the University of Illinois. Seid is providing user support and consulting for national academic and industrial computational mechanics community on NCSA's high performance computing platforms.

In the Fall 2001, Seid has begun to pursue his professional Ph.D. at the Mechanical and Industrial Engineering department. Under the guidance of Professor Brian G. Thomas, he has worked on thermo-mechanical modeling of solidification processes and their applications in steel continuous casting. Seid has successfully implemented a new efficient integration method into a commercial finite element code that opened the door for large scale simulations of many solidification processes.